UNIVERSITAT DE BARCELONA

# Transport phenomena and anomalous diffusion in conservative systems of low dimension

Narcís Miguel i Baños

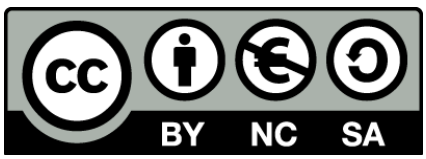

# Transport phenomena and anomalous diffusion in conservative systems of low dimension

Narcís Miguel i Baños
Deptartament de Matemàtiques i Informàtica
Universitat de Barcelona
Gran Via 585, 08007
Barcelona, Catalunya
narcis@maia.ub.es

**Transport phenomena and anomalous diffusion in conservative systems of low dimension**

Programa de doctorat de Matemàtiques.
Memòria presentada per aspirar al grau de Doctor en Matemtìques per la Universitat de Barcelona.

Certifiquem que la present memòria ha estat realitzada per en Narcís Miguel i Baños i dirigida per nosaltres.

Carles Simó i Torres

Arturo Vieiro i Yanes

# Agraïments

Vaig començar la llicenciatura en Matemàtiques el febrer de 2006 sense saber ben bé perquè, i crec que se me n'ha anat de les mans. Sobretot perquè encara hi ha moltíssima feina a fer. Durant la carrera em vaig encaminar cap a la geometria i la topologia, però vaig topar amb Càlcul Numèric, amb en Joaquim Font, en Carles Simó i en Joan Carles Tatjer. Les vaig passar més putes que Caïn. Res comparat amb els Mètodes de Simulació del màster. Res comparat amb el motiu pel qual escric això. Però ha valgut moltíssim la pena.

Des de Càlcul Numèric que en Carles Simó mereix de mi un agraïment sentit. Ja llavors ens deia que l'important era que aprenguéssim. D'ell he après més del que em podia imaginar que podria saber, i segur que molt menys del que m'ha intentat ensenyar. És increïble el que cap als marges de papers en brut! A l'Arturo el vaig conèixer com a company de despatx, des d'on sempre m'ha guiat i ajudat tan professionalment com personal. Als dos els agraeixo infinitament que hagin estat tan propers com exigents, i que m'hagin transmès la passió per la feina que fem. Qualsevol virtud que es pugui detectar en aquesta memòria se'ls ha d'atribuir a ells.

Vull agraïr especialment al Joaquim Font la seva guia en els primers passos que vaig fer en els sistemes dinàmics; i al Jaume Timoneda el manteniment de l'equip que ha fet possible aquesta feina (ja veureu).

I want to extend my most sincere thank-you to Professors Vassili Gelfreich (University of Warwick, UK) and James D. Meiss (University of Colorado Boulder, USA) for being such kind and patient hosts during my visits in their respective departments. From them I could get a deeper understanding of a lot of the topics that I deal with in this memoir. I really appreciate that they shared with me their knowledge and gave me lectures on very interesting techniques.

Tot això no hagués sigut possible si no hagués tingut sempre la squashi guerrera darrera. He estat i estic per déu blessed aka pec beneït. Els joves membres de la squad hem tingut com a seu el xalet aka krakhaus. Agraeixo especialment el temps que m'han dedicat: el Daniel Pérez, que ja era company de carrera, després de màster, i finalment de doctorat. Amb ell he compartit quilos de braves, edos (també es mesuren en quilos), dinàmica, i litres de fantes de taronja i birres. Amb l'Ari he tingut la sort de conèixer l'única persona que mola més que si mateixa #onlyAriiscoolerthanAri. Sempre present en els xaturangues. En Marc m'ha ensenyat que no estic sol a YouTube, l'importància del sharpness i mantenir el cercle petit des del dia 1. Anem lents pel carril de la dreta i que ells vagin fent nai, que ells vagin corrents, ells tindran l'accident. L'Eloi com a llegenda del metall i la seva correcció política. Quins esmorzars. I el jove Joan, que està pujant jovement fort, i se'l troba a faltar els divendres al Narin. Ah, i no li agraeixo res a en Jordi, però sí al seu canapè, al mosquit tigre de Cubelles i al hacker que el va estar martiritzant durant un temps. Està tocat del bolet.

També tinc presents (en un ordre absurd) als joves Àlex Haro, Marta, Meri, Carlos, Dani Sànchez, David R., David M., Roc, Marina, Àlex Luque, Jordi-Lluís, Ino, el joba sampera, el joba fusell, Àngel, Joan Carles, Susana, Maisa, Priscilla, Yu, Ting Ting, Fabrizio, Zubin, Ernest, Toni Benseny, Miquel, Gerard, Xavi Massaneda, Tomàs L., $R^3$, Isabel, Redouan i Giulia! I al Iago Giné, a l'Adrià Roig, al Dani Garrido, a la Roser Homs, a la Zaira Pindado, a l'Adrià Facchi, a la Julia Docampo, a la Xesca Amengual, a la Laia Fandos i a l'Oscar Sánchez. A special thank-you to Marta Civil, Jesús Acosta and Eniko Enikov who brought the balance to the force in Tucson, AZ, while I was in Boulder. And, obviously, also thanks to Giannis and Magda. Si m'he deixat algú, ho sento.

I ara toquen els de casa. Primer, gràcies als meus pares, per moltes coses. En particular per no haver-me abandonat mai a la meva sort en una benzinera. I per no haver-vos penedit mai de no haver-ho fet. No us ho hagués tingut en compte, sempre ha estat una opció molt raonable. Potser m'hagués convertit en un nen salvatge i hagués anat a la universidad de la calle i usaria l'infinitiu per parlar en imperatiu. Conyes a part. Moltes gràcies. Gràcies als meus germans Eva, Àngel Marc, Jepe, Montse, Andreu i Xavi. Per sobretot a en Jepe per aguantar-me (gairebé) a diari i fer-me algun dibuix per la tesi, sobretot a en Xavi per venir els caps de setmana a fer-nos companyia, sobretot a la Montse per trucar de tant en tant per skype i parlar-me de l'amor, sobretot a l'Àngel Marc per recordar-me que sóc un pesat, sobretot a l'Andreu per estar sempre massa apassionat i sobretot a l'Eva per enviar-nos fotos de'n Jimmy conduint. I gràcies a la Neus, també!

I finalment gràcies a la jove noieta, la Kaouthar. Hem compartit tota la carrera, màster i doctorat. Sempre has estat al meu costat. Hi ha massa coses que t'he d'agraïr. Podria fer-ne una llista, perdria tota la gràcia.

Durant els primers anys de tesi he gaudit d'una beca FPI del MINECO amb referència BES-2011-045439 i he pogut fer dues estades de recerca al Mathematics Institute de la University of Warwick, Coventry, UK i al Department of Applied Mathematics de la University of Colorado Boulder, USA amb l'ajut de les beques d'estades breus (també del MINECO) amb referències EEBB-I-14-09055 i EEBB-I-15-10119, respectivament.

# Contents

# Chapter 1

# Introduction

This introductory chapter is devoted to set the problems we are going to deal with, and to introduce the main concepts involved that will be systematically used throughout the text. The general framework is about the dynamics in chaotic zones of low dimensional conservative systems. For concreteness we will restrict ourselves to the analytical context. In what follows, $\mathbb{S}^1 = \mathbb{R}/\mathbb{Z}$, unless otherwise stated. More specifically, we will consider

1. 2D symplectic maps. More precisely, we will deal with real analytic diffeomorphisms $F : \Omega \to \Omega$ under which the usual area form $dx \wedge dy$ is preserved: $F^*(dx \wedge dy) = dx \wedge dy$. Here $\Omega$ will be the 2-torus $\mathbb{T}^2 = \mathbb{S}^1 \times \mathbb{S}^1$, but lifts of $F$ to the cylinder $\mathbb{S}^1 \times \mathbb{R}$ or the whole plane $\mathbb{R}^2$ may also be considered. These maps preserve both orientation and area, that is, $\det DF(x, y) = 1$, for all $(x, y) \in \Omega$, where $DF$ denotes the differential matrix of $F$. We will refer to these maps simply as area-preserving maps, or APM.

   This kind of maps typically arise as Poincaré maps in a fixed energy level of 2 degrees of freedom (dof) Hamiltonian systems, and also as symplectic discretisations of 1 dof Hamiltonian systems.

2. 3D volume preserving maps. We will consider real analytic diffeomorphisms $G : \Theta \to \Theta$ such that $\det DG(x, y, z) = 1$ for all $(x, y, z) \in \Theta$. Here again the usual domain of definition will be a torus, $\Theta = \mathbb{T}^3 = \mathbb{S}^1 \times \mathbb{S}^1 \times \mathbb{S}^1$, but we may lift $G$ either to the cylinder $\mathbb{T}^2 \times \mathbb{R}$ or to the full space $\mathbb{R}^3$ depending on our needs. For shortness we will refer to these maps as VPM.

   This kind of maps arises, for instance, as suitable discretisations of divergence free vector fields.

## 1.1 Notation and definitions

There are three concepts that are central in this thesis: the distinction between regular and chaotic orbits, the stickiness effect and anomalous diffusion. These two last (related) phenomena take place in zones in the phase space that can be considered as chaotic. All these concepts are introduced in this section.

In order to perform a proper study of stickiness and diffusion in the phase space, we need to set an adequate context. Roughly speaking, we need to have some regular component embedded in a compact seemingly fully chaotic phase space. This will be clarified in Sect. 2.6.

In the 2D case, it will come for free by considering the Chirikov standard map -or simply standard map- in $\mathbb{T}^2$ (1.13) in a special range of the parameter it depends on. This map and some of its main dynamical features will be introduced in Sect.1.2. Concerning the VPM case, as far as we are aware of, there are no analogous models, so a proper one should be constructed in Sect. 5.2. By this we mean the following:

1. The variables of the standard map can be understood as an action and an angle. In the VPM setting we will deal with 1-action and 2-angle maps.

2. The standard map depends on a single parameter $k$ such that, for $k = 0$, the phase space is foliated by horizontal invariant curves of the form $\{y = \text{ const}\}$, and the dynamics on each of them is conjugated to a rigid rotation. In the VPM case we will require the dependence on a parameter $\varepsilon$ such that for $\varepsilon = 0$ the phase space is foliated by horizontal invariant tori of the form $\{z = \text{ const}\}$, where also the dynamics on each torus is conjugated to a rigid rotation.

The situation described for $k = 0$ and $\varepsilon = 0$ in the APM and VPM cases, respectively, is what we will refer to as *integrable*, see Def. 1.

In what follows, we will deal with both 2D and 3D cases simultaneously to stress the similarities that these two settings have and those that we will try to mimic.

### 1.1.1 Integrable systems and perturbations

Typically, conservative systems are neither integrable nor fully chaotic, but exhibit a mixed phase space. In the systems we are going to deal with one of the variables can be interpreted as an action and the others as angles.

In the 2D symplectic case, the notion of integrability is inherited from the Arnol'd-Liouville sense in Hamiltonian systems[1]: all orbits lie on tori and the dynamics of the map restricted to each torus is conjugated to a rigid rotation. The notion of integrability we are going to use in the VPM case is analogous to this one. For 1-action 2-angle maps, we will consider integrable maps to be those that almost all orbits lie on 2D tori, and that the dynamics of the VPM on each torus is conjugated to a rigid rotation. This concept can be put together as follows.

**Definition 1.** *A conservative map with* 1*-action and* $d$*-angles is said to be* integrable *if it is topologically conjugated to the normal form*

$$H_0^{(d)} : \mathbb{T}^d \times [0,1] \to \mathbb{T}^d \times [0,1], \qquad H_0^{(d)} : \begin{pmatrix} \theta \\ r \end{pmatrix} \mapsto \begin{pmatrix} \theta + g^{(d)}(r) \\ r \end{pmatrix}, \tag{1.1}$$

*where* $g^{(d)}(r) : [0,1] \to \mathbb{T}^d$.

Here $d = 1, 2$ correspond to the APM and VPM cases, respectively.

We are going to consider maps that are area or volume preserving one-parameter perturbations of integrable systems as (1.1) of the following form:

$$H_\varepsilon^{(d)} : \mathbb{T}^d \times [0,1] \to \mathbb{T}^d \times [0,1],$$
$$H_\varepsilon^{(d)} : \begin{pmatrix} \theta \\ r \end{pmatrix} \mapsto \begin{pmatrix} \bar{\theta} \\ \bar{r} \end{pmatrix} = \begin{pmatrix} \theta + g^{(d)}(r) \\ r \end{pmatrix} + \varepsilon \begin{pmatrix} f_1^{(d)}(\theta, r) \\ f_2(\theta, r) \end{pmatrix}, \tag{1.2}$$

[1] An $n$-dof Hamiltonian system is said to be integrable in the Arnol'd-Liouville sense if there exist $n$ invariants functionally independent almost everywhere and in involution.

where

1. The functions $f_1^{(d)} : \mathbb{T}^d \times [0,1] \to \mathbb{T}^d$ and $f_2 : \mathbb{T}^d \times [0,1] \to [0,1]$ are analytic and 1-periodic in $\theta \in \mathbb{T}^d$,
2. The vector $(f_1^{(d)}, f_2)$ is normalized in such a way that has some norm equal to 1, and
3. The function $f_2$ has zero average, $\int_{\mathbb{T}^d} f_2(\theta, r)\, d\theta = 0$. This is the so-called zero-flux condition. It implies that each torus intersects its image under $H_\varepsilon^{(d)}$.

**Definition 2.** *A vector of irrational frequencies $\rho = (\rho_1, \dots \rho_n) \in \mathbb{R}^n$ is said to be a $(C, \tau)$-Diophantine number, $C > 0$, $\tau \geq n$, if it satisfies the following infinitely many inequalities: for all $k = (k_1, \dots, k_n) \in \mathbb{Z}^n \setminus \{(0, \overset{n)}{\dots}, 0)\}$, $k_0 \in \mathbb{Z}$,*

$$|(k, \rho) - k_0| \geq \frac{C}{|k|^\tau},$$

*where $|k| = |k_1| + \cdots + |k_n|$ and $(\cdot, \cdot)$ denotes the usual scalar product in $\mathbb{R}^n$. We will denote by $D(C, \tau)$ the set of $(C, \tau)$-Diophantine numbers.*

Let us restrict ourselves to $\rho \in (0, 1)$. One can represent $\rho$ in continued fraction expansion form:

$$\rho = \cfrac{1}{a_1 + \cfrac{1}{a_2 + \cfrac{1}{a_3 + \cfrac{1}{\dots}}}} =: [a_1, a_2, \dots],$$

where $a_j$, $j \geq 1$ are positive integer numbers, called *quotients*. In case $\rho \in (0,1) \cap \mathbb{Q}$, $\rho$ can be represented in this way with finitely many quotients, in two equivalent ways:

$$\rho = [a_1, a_2, \dots, a_n] = [a_1, a_2, \dots, a_n - 1, 1].$$

And if $\rho \in (0,1) \cap (\mathbb{R} \setminus \mathbb{Q})$, one needs infinitely many quotients. If $\rho = [a_1, a_2, \dots, a_n, \dots]$, one can consider the successive truncations of the continued fraction expansion. We obtain a sequence of irrational numbers called *approximants*:

$$\frac{p_n}{q_n} = [a_1, a_2, \dots, a_n].$$

It is important to remark the following, see [72].

**Remark 1.** *1. The sequence $p_n/q_n$ tends to $\rho$ as $n \to \infty$,*

*2. $|\rho - p_n/q_n| < |\rho - p_{n-1}/q_{n-1}|$ for all $n > 0$.*

*3. $(\rho - p_n/q_n)(\rho - p_{n-1}/q_{n-1}) < 0$, that is, successive approximants lie on different sides of $\rho$.*

The phase space of $H_0^{(d)}$ is rather simple. Each level set $\mathcal{M}_a = \{(\theta, r) : r = a\}$ is invariant under $H_0^{(d)}$, and the restriction of the dynamics of $H_0^{(d)}$ on $\mathcal{M}_a$, $H_{0|\mathcal{M}_a}^{(d)}$, is a rigid rotation $\theta \mapsto \theta + g^{(d)}(a)$. In this case, $\mathcal{M}_a$ are homotopically equivalent to $\{(\xi, 0) : \xi \in \mathbb{T}^d\}$. We are going to refer to these kind of tori as *rotational*, or simply RIC (rotational invariant curves) in the 2D case and RIT (rotational invariant tori) in the 3D case.

Each of these RIC or RIT are characterized by their rotation numbers. For maps of the circle it is defined as follows

**Definition 3.** *Let $\tilde{f} : \mathbb{S}^1 \to \mathbb{S}^1$ be a homeomorphism of the circle. The rotation number of $\tilde{f}$ is defined as the limit*

$$\rho(\tilde{f}) = \lim_{n\to\infty} \frac{1}{n} \left(f^n(x) - x\right), \tag{1.3}$$

*where $f$ is a lift of $\tilde{f}$ to $\mathbb{R}$.*

This limit exists for all $x \in \mathbb{S}^1$ and does not depend on the $x$ or lift of $\tilde{f}$ chosen. It measures the average rate of rotation of orbits along the circle.

This concept is transferable to APM and to VPM, but the corresponding limit (1.3) of either case can exist or not. Namely, if $\tilde{F} : \mathbb{T}^d \times [0,1] \to \mathbb{T}^d \times [0,1]$ is a conservative map, $d = 1, 2$, $F : \mathbb{R}^d \times [0,1] \to \mathbb{R}^d \times [0,1]$ a lift of $\tilde{F}$, and $\pi_1$ is the projection onto the torus $\mathbb{T}^d$, the rotation number or vector of an orbit starting at $(\theta_0, r_0)$ is the limit (if it exists)

$$\rho = \lim_{n\to\infty} \frac{\pi_\theta F^n(\theta_0, r_0) - \theta_0}{n}, \tag{1.4}$$

where $\pi_\theta$ denotes the projection onto $\mathbb{R}^d$. If this limit exists, it does neither depend on the choice of the initial point on the orbit nor on the choice of the lift of $\tilde{F}$. For APM, $\rho \in \mathbb{T}^1$ in (1.4) can either be rational or irrational, and for VPM $\rho \in \mathbb{T}^2$ is a 2-component vector whose entries can be both rational or irrational, or a rational and an irrational number. These distinctions give rise to different kinds of orbits. Note that, for the integrable maps (1.1), the rotation number is given by $g^{(d)}(r)$, but in this case all orbits lie on RIC or RIT.

Generically, in the twist APM case, RIC have irrational rotation number and can be represented as graphs of a continuous function [94]. But the converse is not necessarily true, since there are invariant sets of twist APM with irrational rotation number that are topologically a Cantor set, see Sect. 1.1.2.

**Effect of a small perturbation**. One expects some of this structure to be preserved once $\varepsilon > 0$, but some extra hypotheses apart from the smallness of $\varepsilon$ have to be considered. Namely

- In the APM case, *Moser's twist theorem* [108, 124] asserts that if $|\frac{dg^{(1)}(r)}{dr}| \geq K > 0$ (twist condition) and $g^{(1)}(a) = \rho \in [0,1)$ is $(C,\tau)$-Diophantine, then $H_\varepsilon^{(1)}$ has an invariant curve with rotation number $\rho$, provided $\varepsilon$ is sufficiently small. Of course, the better twist condition (larger $K$) and better Diophantine condition (larger $C$, smaller $\tau$), the larger $\varepsilon$ can be in the perturbation. The best $(C,\tau)$-Diophantine condition is that for the golden mean number, $\omega = (\sqrt{5}-1)/2$, for which $C$ is asymptotically $1/\sqrt{5}$ and $\tau = 1$.

- In the VPM case, we have an analogous result [24, 147]: for small enough $\varepsilon$, one can establish the existence of invariant 2D-tori provided the vector of frequencies $g^{(2)}(a) = \rho \in [0,1)^2$ is $(C,\tau)$-Diophantine, the rotation vector is non-degenerate, that is rank $D_r g^{(2)} = 1$ and the twist condition $\det(D_r g^{(2)}, D_r^2 g^{(2)}) \neq 0$ holds.

These results are KAM-like, where KAM stands for Kolmogorov-Arnol'd-Moser theory. Classical examples of this theory are the results for circle maps [4], twist APM [124], Hamiltonian systems [2], symplectic maps [6] and VPM [24, 147]. All of them essentially consist

in performing a sequence of changes of variables in such a way that, if we start with a perturbation of size $\varepsilon$, after $k$ steps we have an approximation of the invariant torus under study with an error $\mathcal{O}(\varepsilon^{\gamma^k})$, $\gamma \in (1,2)$, that is, we want to converge to the solution close to quadratically, as it happens for the Newton method, but in a functional space in the present case. To do so, the main requirements usually are

1. The Diophantine frequency. This is required to get rid of the dominant part of the perturbation in each change of variables, to avoid small divisor problems.

2. A non-degeneracy condition. This allows to slightly change the actions to recover the initial frequency using the implicit function theorem.

3. The smallness of the perturbation. This allows to use the implicit function theorem and to always stay in the complex strip of actions we started with. At each inductive step, the width of this strip decreases in a controlled way so that in the limit it does not shrink to zero.

In both cases the theorem asserts that the measure of the set of invariant tori that exist for $\varepsilon > 0$ small, tends to be total as $\varepsilon \to 0$. That is, the majority of orbits lie on invariant tori. But there is an important difference between these two results. In the 2D symplectic case one has one action and its corresponding angle. After each change of variables we can slightly change the actions to recover the initial frequency we are working with due to the twist (non-degeneracy) condition. Hence in this context it makes sense to talk about persistence of invariant curves. This also holds for general symplectic maps in any (even) dimension [6]. In the volume preserving case [24, 147, 76] since the map has more angles than actions, it is difficult to control the rotation frequencies of any prescribed torus: if the non-perturbed system $H_0^{(2)}$ has an invariant torus with rotation vector $\rho \in (0,1)^2$, it can not be predicted if $H_\varepsilon^{(2)}$ has an invariant torus with rotation vector $\rho$, even if it satisfies a Diophantine condition, see Def. 2. In the VPM case we only have a free parameter and hence we can not recover all frequencies but only those on a line among the frequencies we are dealing with. Hence, it only asserts that for any arbitrarily small perturbation size $\varepsilon$, in a neighborhood of where there used to be an invariant 2D torus with a given frequency $\rho$, there appear other invariant 2D tori with Diophantine frequencies, but it can not be determined if the torus with frequency $\rho$ reappears.

So, once $\varepsilon > 0$ the measure occupied by rotational invariant tori is no longer total and the topology of the phase space drastically changes. Namely, the measure of the complement of the phase space not occupied by KAM tori is $\mathcal{O}(\sqrt{\varepsilon})$, see [116]; and if one considers families of Lagrangian tori appearing in a neighbourhood of a simple resonance, one can improve it to $\mathcal{O}(\varepsilon)$, [96], that agrees with the conjecture in [7], that KAM tori leave a set of measure $\mathcal{O}(\varepsilon)$. The most fragile invariant tori upon perturbation are those called *resonant*.

**Definition 4.** *[6] The resonant module associated to $\rho \in \mathbb{R}^d$ is the sub-lattice of $\mathbb{Z}^d$*

$$\mathcal{L}(\rho) = \{k \in \mathbb{Z}^d \,:\, (k,\rho) \in \mathbb{Z}\}. \tag{1.5}$$

*Resonant RIC or RIT are those whose rotation vector $\rho = g^{(d)}(a)$ have* $\operatorname{rank} \mathcal{L} > 0$.

In the case of twist area preserving maps, resonant RIC are those with rational rotation number $p/q \in \mathbb{Q}$, $(p,q) = 1$. According to the Poincaré-Birkhoff theorem [16], they are

generically destroyed under perturbation giving rise to a pair of elliptic and hyperbolic orbits with this same rotation number, resembling a chain of $q$ penduli encircling the torus along the angle variable. These hyperbolic orbits have invariant manifolds that generically intersect transversally. This implies the loss of integrability [151, 33]. If the $q$th power of the map is close to the identity in a suitable annular region containing the separatrices and has a limit Hamiltonian with a homoclinic connection, the splitting angle between these invariant manifolds is bounded from above, as $\varepsilon \to 0^+$, by an exponentially small quantity of the form $A\exp(-B/\log(\lambda))$, where $A > 0$ is a constant, $B > 0$ is a constant related to the distance to the real axis of the singularities of the homoclinic solution in complex time of the limit interpolating Hamiltonian, and $\lambda$ is the dominant eigenvalue of $D(H_\varepsilon^{(1)})^q$ of the hyperbolic orbit, see [47]. It turns out that the area of the lobes created by the invariant manifolds is of the same order of magnitude of the splitting angle [26, 115, 135], see Fig. 1.2.

Inside the chaotic zone that includes the lobe area, a suitable power $N$ of $H_\varepsilon^{(1)}$ has an invariant hyperbolic Cantor set, a Smale horseshoe [138]. The restriction of the dynamics of $(H_\varepsilon^{(1)})^N$ to this Cantor set is topologically conjugate to a Bernoulli shift. In particular, it has positive topological entropy [6]. Hence, one expects orbits with unpredictable dynamics (meaning sensitive dependence with respect to initial conditions), although having zero measure. Actually, when performing numerical simulations, in the scale of the map, this whole lobe area is usually detected as chaotic, in a sense that we will explain in Subsect. 1.1.3. But if we take a closer look via suitable return models near the just splitted separatrices, one can prove that there are elliptic periodic points inside these lobes [132], and moreover that they appear in positive measure sets of parameters [136]. So, in general, one can not assert that this zone is fully chaotic.

In fact the *positive metric entropy conjecture* remains still open. It asserts that in symplectic maps, KAM tori coexist with ergodic components of positive measure [114]. In practice, we are going to consider fine grids on regions of the phase space and distinguish between regular and chaotic orbits as we will explain in Subsect. 1.1.3. This may lead to the visualization of connected positive measure regions that are seemingly fully chaotic, but there may be still islands of stability smaller than the pixel size. Namely, the orientation preserving Hénon map is obtained as a universal return map model for quadratic tangencies in area preserving maps, see for instance [59, 60, 61]. This phenomenon gives rise to periodic points of high period that exhibit a positive measure domain of stability but this region is extremely small. A related result is the one of Duarte [38], where it is proven that, for the standard map (1.13), there is a residual set of parameters (for large enough $k$) for which any point in the phase space is close to such a stability island, and that the distance between them tends to 0 as the parameter increases. Despite these facts, in our numerical experiments, the effect of tiny islands of stability is averaged out. And this is checked by performing the same experiments with different precision and checking that they strongly agree. Hence, we are going to deal with those regions that we detect as positive measure chaotic zones as if they were positive measure and chaotic.

In the 3D volume preserving case, we will refer to the case $\dim \mathcal{L}(\rho) = 1$ as simply resonant or rank-one resonant and $\dim \mathcal{L}(\rho) = 2$ as doubly resonant or rank-two resonant.

In the simply resonant case, in a proper basis of $\mathcal{L}(\rho)$ the frequencies can be written as having a rational and an irrational component, $\rho = (p/q, \rho_0)$, $p, q \in \mathbb{Z}$, $q \neq 0$, $\rho_0 \in [0, 1)$. If $\rho_0$ satisfies a $D(C, \tau)$ condition, there is a volume-preserving change of variables in a region around the resonant torus that decouples the fast angle dynamics $\rho_0$ and the remaining angle and its related action. This is done up to any order in an unfolding parameter that measures

the distance to the exact resonance. A truncation of this map is a decoupled skew product of an APM that describes the dynamics around the resonance in a long time scale but, of course, it has a remainder. There are two main cases, where this APM is either a twist or non-twist version of the Chirikov Standard map (1.13).

In the double resonant case, again one has to choose a proper basis of $\mathcal{L}(\rho)$. It can be done in such a way that, in this basis, $\rho = (n_1/k_1, n_2/k_2)$ where $k_1$ divides $k_2$. One can perform an averaging procedure to the $k_2$th power of the map. After this, one obtains a near identity map that depends on an unfolding parameter that also measures the distance to the resonance that, in first approximation, is a periodically forced version of the standard map, with two angles and an action. The dynamics of the action variable is the identity plus a forcing that is periodic in the two angles. Hence in this case the phase space is still 3-dimensional. See [41].

### 1.1.2 The Aubry-Mather theorem, Cantori and Turnstiles

We have just introduced the problem of the persistence of invariant tori of integrable 2D and 3D conservative maps, provided they satisfied some twist or non-degeneracy condition.

A natural question that arises in this context is if it is possible to establish the existence of orbits with a prescribed rotation number. In the area-preserving setting the answer is affirmative. It is fundamental result in the so-called Aubry-Mather theory [8, 93]. Namely, the existence of such orbits can be asserted in some interval of rotation numbers.

Consider an APM of the annulus $F : \mathbb{S}^1 \times [0,1] \to \mathbb{S}^1 \times [0,1]$ satisfying a twist condition,

$$\frac{\partial \pi_1 F}{\partial y}(x,y) \geq K > 0, \text{ for all } x \in \mathbb{S}^1 \times [0,1].$$

Assume that $F$ preserves the boundaries $\{y = i\}$, $i = 0, 1$. Denote by $F_i = F_{\{y=i\}}$ the restriction $F_i(x) = F(x,i)$, $i = 0, 1$, and assume that $\rho_0$ and $\rho_1$ are the rotation numbers of $F_0$ and $F_1$ respectively. Since $K > 0$, $\rho_0 < \rho_1$. Recall that

**Definition 5.** *A set $\mathcal{M}$ is is said to be monotone if for any $(x,y)$, $(x',y') \in \mathcal{M}$,*

$$\pi_1(x,y) < \pi_1(x',y') \Rightarrow \pi_1 F(x,y) < \pi_1 F(x',y'),$$

*where the projection is considered on the lift $\mathbb{R}$ of $\mathbb{S}^1$.*

**Theorem 1.** *[8, 93] For each $\rho$ such that $\rho_0 < \rho < \rho_1$, there exists a monotone invariant set under $F$, $\mathcal{M}_\rho$, whose rotation number is $\rho$.*

Note that theorem 1 was originally stated for homeomorphisms of the annulus satisfying the monotone twist condition:

$$\pi_1 F(x,y) > \pi_1 F(x,z), \quad \text{if} \quad y > z.$$

We can consider $\rho$ to be either rational or irrational. The rational case is actually the well known Poincaré-Birkhoff theorem [16]: for each rational $\rho = p/q$ such that $\rho_0 < \rho < \rho_1$, there are at least two period-$q$ orbits such that for each point in the orbit, it turns $p$ times around the annulus before coming back to it. This periodic orbits are usually called *Birkhoff periodic orbits*.

In case $\rho \in \mathbb{R} \setminus \mathbb{Q}$, it can either be a RIC or a Cantor set. These last are usually referred to as Cantori (or simply Cantorus in singular). We refer to the original papers [8, 93] and to the review [98] for further explanations.

The remarkable fact about this theory is that it is not perturbative, but it has a huge impact in the perturbative setting. For the map $H_\varepsilon^{(1)}$ as in (1.2), let $\rho \in \mathbb{R} \setminus \mathbb{Q}$ such that $\rho_0 < \rho < \rho_1$. If $\rho$ is $D(C, \tau)$-Diophantine, then Moser's twist theorem asserts that there exists $\varepsilon_0 > 0$ such that for all $0 < \varepsilon < \varepsilon_0$ there exists an invariant curve with rotation $\rho$. But it may still exist for larger values of $\varepsilon$ that can not be predicted by perturbative arguments. One expects that this invariant curve exists until some *critical* value of the parameter, $\varepsilon_{\text{crit}} > \varepsilon_0$ and it does no longer exist as a curve for $\varepsilon > \varepsilon_{\text{crit}}$. There are examples where these broken invariant curves reappear, see [22, 91, 49]. After the breakdown of the invariant curve, Theorem 1 ensures the existence of a monotone invariant Cantor set of rotation number $\rho$, that is usually understood as a 'remnant' of the RIC that existed for $\varepsilon < \varepsilon_{\text{crit}}$.

There are several proofs of this theorem. The original ones rely on a variational principle. But there are more geometrical proofs, see [70, 98]. These consist in constructing monotone sets with irrational rotation number $\rho$ as limit of monotone sets with rational rotation number $p_j/q_j$ such that $p_j/q_j \to \rho$ as $j \to \infty$. This stresses out the strong connection between periodic orbits and Cantori. Other remarkable results that also rely in this connection are, for instance:

1. Greene's conjecture [63, 43, 82], that relates the loss of stability of elliptic periodic orbits with rotation number $p_j/q_j \to \rho$ with the transition from RIC to Cantorus. This was partially justified in [82, 43].

2. The obstruction criterion of Olvera and Simó [112, 78], that gives geometrical conditions for the nonexistence of RIC based on the relative position of the invariant manifolds of hyperbolic periodic orbits, and

3. The Greene-MacKay renormalisation theory [83, 80], that also deals with the existence and nonexistence of RIC based on the relative position of some special families of periodic orbits. These concepts will be introduced with more detail in Chap. 4.

As an example, we illustrate in Fig. 1.1 the transition from RIC to Cantorus of the monotone orbit with the golden mean $\omega = (\sqrt{5}-1)/2$ as rotation number for the Chirikov Standard map (1.13), by following the two Birkhoff periodic orbits (hyperbolic and elliptic/reflection-hyperbolic) with rotation number 2584/4181, which is an approximant of $\omega$. This map will be introduced in Sect. 1.2. In this figure, we see the monotone set $\mathcal{M}_\omega$ for the values of the parameter $2\pi k = 0.971(0.001)1.1$. The breakdown occurs approximately at $k_G = 0.971635\ldots/(2\pi)$. In this picture one can observe how the points in the periodic orbit tend to approach each other once $k > k_G$, giving rise to gaps, and that the size of the largest gap increases as $k$ increases.

### Turnstiles and Mather's $\Delta W$

In [95], Mather gave a rigorous criterion for the nonexistence of RIC of a prescribed rotation number, based on a variational principle. The criterion states that a certain RIC exists if and only if some quantity, that he named $\Delta W$, vanishes. This quantity can be explicitly related to transport, since it is the area that is transported across a monotone orbit per iterate, [86].

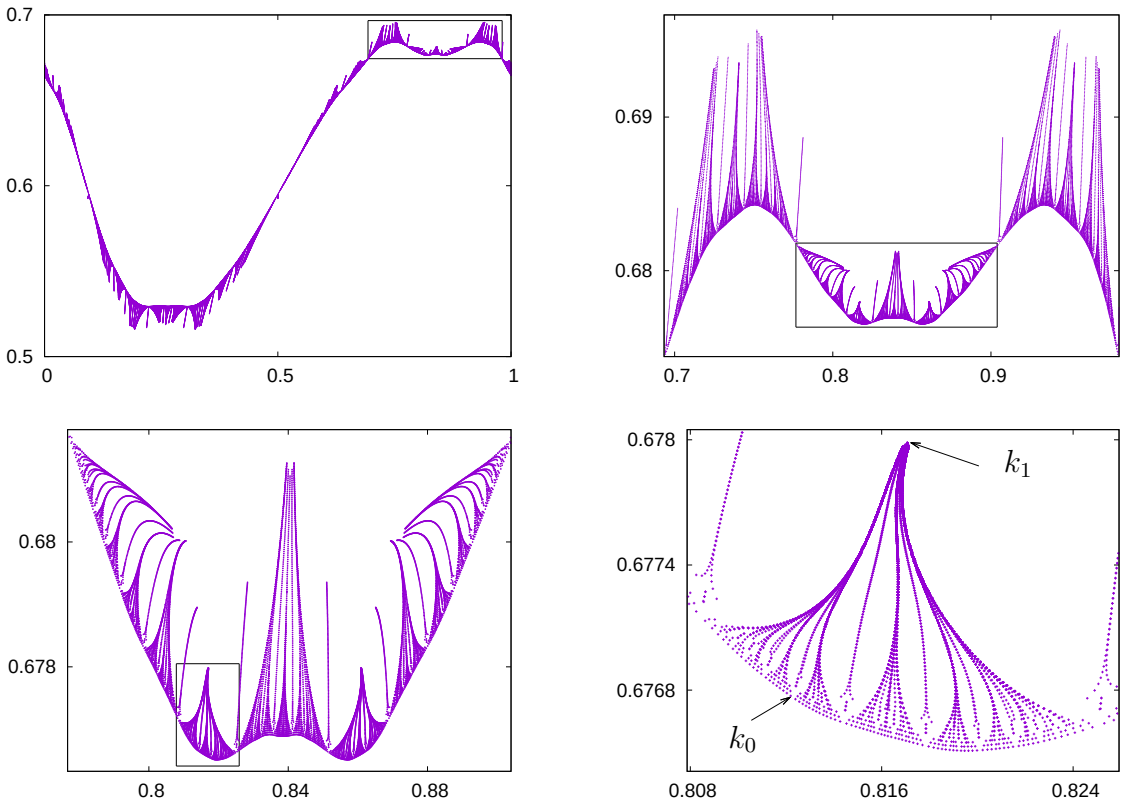


Figure 1.1: Sequence of magnifications in the marked boxes of the two Birkhoff periodic orbits with rotation number 2584/4181 of the standard map (1.13) for $2\pi k = 0.971(0.001)1.1$. For $k_0 = 0.971/(2\pi)$ they approximate a RIC while for all the other values of $k$ shown they approximate a Cantorus with $\omega = (\sqrt{5}-1)/2$ as rotation number. The first and last values of $k$ shown, $k_0$ and $k_1 = 1.1/(2\pi)$, are labelled in the bottom right plot.

Let $F : \mathbb{S}^1 \times [0,1] \to \mathbb{S}^1 \times [0,1]$ be a twist APM of the annulus, and let $\tilde{F}$ a lift to $\mathbb{R} \times [0,1]$. We can consider the following generating function $G(x,x')$ of $\tilde{F}$, defined as,

$$F(x,y) = (x',y') \Leftrightarrow y = \frac{\partial G(x,x')}{\partial x} = \partial_1 G(x,x'), \quad y' = -\frac{\partial G(x,x')}{\partial x'} = -\partial_2 G(x,x'),$$

that takes values in the set

$$B = \{(x,x') \in \mathbb{R}^2 \ : \ F(x,0) \le x' \le F(x,1)\}.$$

Of course, the generating function $G$ determines $F$ uniquely and $F$ determines $G$ up to an additive constant. It is easy to check that $\{(x_i,y_i)\}_i$, $i \in \mathbb{Z}$ is an orbit of $\tilde{F}$ (note that we also consider the pre-images), if and only if the bi-infinite sequence of angles $\{x_i\}_i$ (also called *configurations*) satisfies

$$\partial_2 G(x_{i-1},x_i) + \partial_1 G(x_i,x_{i+1}) = 0.$$

Such configurations are called *equilibrium sequences*. Consider a finite configuration with $q > 0$ elements, $\underline{x} = \{x_0, x_1, \ldots, x_{q-1}\}$. For $p \in \mathbb{Z}$, define the periodic action on $\underline{x}$ as

$$W_{p,q}(\underline{x}) := G(x_{q-1}, x_0 + p) + \sum_{i=0}^{q-2} G(x_i, x_{i+1}). \tag{1.6}$$

There exists a finite maximizing equilibrium sequence $\underline{x}_M$ of $W_{p,q}$, provided $p/q \in (\rho_0, \rho_1)$, that is, the rotation number lies between the rotation number interval defined by the rotation numbers of the boundaries, see [8]. And since any integer translate $\underline{x}' = \{x_0 + j, x_i + j, \ldots, x_{q-1} + j\}$, $j \in \mathbb{Z}$, of $\underline{x}$ also maximizes $W_{p,q}$, one can use a minimax principle to establish the existence of another equilibrium sequence $\underline{x}_{MM}$, that is a minimax orbit [95]. Note that these equilibrium sequences again correspond to the Birkhoff $p/q$-periodic orbits. Moreover, maxima of $\Delta W_{p,q}$ correspond to hyperbolic orbits and minimax equilibrium sequences correspond to periodic orbits that are either elliptic or reflection hyperbolic [85].

In [95], Mather defined the quantity

$$\Delta W_{p,q} = W_{p,q}(\underline{x}_M) - W_{p,q}(\underline{x}_{MM}). \tag{1.7}$$

And he proved the following result:

**Theorem 2.** *In the setting described above, let $\{p_i/q_i\}_i$ a sequence of rational numbers such that $p_i/q_i \to \rho \in \mathbb{R} \setminus \mathbb{Q}$ as $i \to \infty$. Then,*

1. *The sequence $\{\Delta W_{p_i,q_i}\}_i$ has a non-negative limit $\Delta W_\rho$ as $i \to \infty$, and*
2. *The APM $F$ has a RIC of rotation number $\rho$ if and only if $\Delta W_\rho = 0$.*

**$\Delta W_\rho$ as area**. For each $p, q \in \mathbb{Z}$, $q > 0$, the $p/q$ periodic orbits define a partial barrier for vertical transport. And the rate of transport, also called the *flux* or area per iterate that crosses these orbits can be explicitly related to $\Delta W_\rho$.

More concretely, consider any curve $C$ that interpolates the maximal and minimax orbits with rotation number $p/q$. This curve divides the cylinder. Fix a point in the maximal orbit, say $(x_0, y_0)$, and the one in its orbit that is closest to it to the right, $(x_i, y_i) = F^i(x_0, y_0)$, where $i$ is a Bézout coefficient in $ip + jq = 1$, $j \in \mathbb{Z}$.

The image $F^q(C)$ of $C$ also interpolates $\underline{x}_M$ and $\underline{x}_{MM}$. Generically, $F^q(C)$ does not coincide with $C$ but on $\underline{x}_M$ and $\underline{x}_{MM}$. In the segment from $(x_0, y_0)$ to $(x_i, y_i)$, the curves $F^q(C)$ and $C$ enclose a region $R$. If $F$ satisfies the zero-flux condition[2], the area of the part of $R$ that is above $C$ is the same as the area of the part of $R$ that is below $C$. Moreover, this is the area that crosses $C$ per iterate; and the structure that define $F^q(C)$ and $C$ acts as if it was a revolving door or *turnstile*. And in [86] the authors proved that this area is, precisely, $\Delta W_{p,q}$, and that it does not depend on the choice of the curve $C$. Moreover, from Theorem 2 we can take limits on sequences of periodic orbits converging to some irrational number $\rho$ to get the transport rate across Cantori.

We will illustrate this fact and provide further insight on the kind of orbits and the phase space structure inside the region that defines the area $\Delta W_{p,q}$ at the end of Subsect. 1.2 for the fixed points (with rotation number 0/1) of the Chirikov Standard map.

### 1.1.3 Regular and Chaotic orbits

Throughout the whole text, the lack of integrability or the amount of chaos in a system is measured as the amount of points (taken in a fine grid) that belong to orbits which we can consider that are *chaotic*, as we will define in this section. This will be done by considering an approximation of the maximal Lyapunov exponent, $\Lambda$.

[2]Recall that in our case this is guaranteed since the function $f_2$ in (1.2) has zero average.

The Lyapunov exponents are the generalisations of characteristic exponents of periodic orbits to general orbits, and measure the exponential rate of increase or decrease of the distance between nearby orbits. In our context, let $F : \mathbb{R}^n \to \mathbb{R}^n$ be a volume preserving map, that is, $\det DF(x) = 1$ for all $x \in \mathbb{R}^n$. To avoid technicalities, we are going to assume that

$$\sup \{\|DF(x)\| \ : \ x \in \mathbb{R}^n\} < \infty,$$

where $\|\cdot\|$ is any norm.

**Definition 6.** *Let $x_0 \in \mathbb{R}^n$, and $F^j(x_0) = x_j = F(x_{j-1})$. The* Lyapunov exponent *associated to $x_0$ and the vector $\xi_0 \in \mathbb{R}^n$, $\|\xi_0\| = 1$ (here $\|\cdot\|$ is any norm in $\mathbb{R}^n$) is the limit, if it exists,*

$$\Lambda(x_0; \xi_0) = \lim_{j\to\infty} \frac{1}{j} \log \left\|DF^j(x_0)\xi_0\right\| = \lim_{j\to\infty} \frac{1}{j} \sum_{i=0}^{j-1} \log \|DF(x_i)\xi_i\|, \tag{1.8}$$

*where $\xi_j = DF(x_{j-1})\xi_{j-1}$.*

The limit (1.8) exists for almost every $x_0 \in \mathbb{R}^n$ and $\xi_0 \in \mathbb{R}^n$. All points of the same orbit have the same Lyapunov exponent. For a given $x_0$, the limit $\Lambda(x_0; \xi_0)$ takes only finitely many values $l_1 < l_2 < \cdots < l_m$, $m \leq n$, and each of them occurs respectively with multiplicity $k_i$, where $k_1 + k_2 + \cdots + k_m = n$, see Chap. 1 in [13]. We will denote by $\Lambda(x_0) = l_m$ the *maximal Lyapunov exponent*. Moreover, volume preservation further implies that either $l_m > 0$ or $l_m = 0$, and $\sum_{i=1}^m k_i l_i = \log(\det DF) = 0$ .

The existence of positive Lyapunov exponents implies sensitive dependence with respect to initial conditions, and linear stability around invariant objects of the system requires $\Lambda(x) = 0$ for each $x$ in this invariant object. It is important to remark that there are examples of maps with zero Lyapunov exponent that exhibit sensitive dependence with respect to initial conditions [52], but this does not happen, generically, in our setting.

From a practical point of view, assuming $k_m = 1$, for each initial condition $x_0$, regardless of the initial vector $\xi_0$ chosen, $\xi_j$ tend to the maximal expanding direction with probability 1. So, the approximation of the limit (1.8) starting with a randomly chosen $\xi_0$ will give the maximal Lyapunov exponent $\Lambda(x_0)$ with probability 1. For a faster evaluation of $\Lambda(x_0)$, it is convenient to proceed as follows [126]

- Set $\eta_1 = DF(x_0)\xi_0$, $s_0 = \log \|\eta_1\|$, $\xi_1 = \eta_1/\|\eta_1\|$, and
- For $j > 1$, $\eta_j = DF(x_{j-1})\xi_{j-1}$, $s_j = \log \|\eta_j\| + s_{j-1}$, $\xi_j = \eta_j/\|\eta_j\|$,

and to compute an approximation of the limit

$$\Lambda(x_0) = \lim_{j\to\infty} \frac{s_j}{j}. \tag{1.9}$$

We will refer to the quantities $s_j$ as *Lyapunov sums*. When dealing with concrete examples, we will consider grids in regions of the phase space under study. Each initial condition in this grid $x_0$, and its orbit, will be considered to be regular if we can assume that the limit (1.9) is zero up to a reasonable threshold (that depends on the number of iterates of the map performed to approximate $\Lambda(x_0)$), and chaotic otherwise.

Note that in most cases it will be enough to study the growth of $s_j$ instead of approximating the limit to guess if we can consider it to be either positive or not.

For faster evaluations of the maximal Lyapunov exponent one can also use the so-called fast Lyapunov indicators (FLI), see the review [137], or the mean exponential growth factor of nearby orbits (MEGNO), see [23].

### 1.1.4 Stickiness

The stickiness problem is, roughly, that of measuring the time that chaotic orbits can spend near invariant objects of the system, where transport rates are expected to be slowed down. For Hamiltonian systems with 3 or more dof that are perturbations of Liouville-Arnol'd integrable systems, we have Nekhoroshev-like bounds: under steepness conditions, that refer to being unblocked at some order in resonance according to [125], it takes exponentially long times of the form $\mathcal{O}\left(c_1 \exp\left(c_2/\varepsilon^{c_3}\right)\right)$, $c_1, c_2, c_3 > 0$, in the distance-to-integrable parameter $\varepsilon$ to vary the actions by a quantity $\mathcal{O}(1)$. See [110, 56, 57]. Namely, in this situation, if one changes the small parameter to be the distance to an invariant KAM torus, put $\delta$, the speed of the diffusion close to this torus has super-exponential upper bounds of the form $\mathcal{O}\left(\exp(-\exp(1/\delta))\right)$, see [107]. This kind of drift of the action variables is the so-called Arnol'd diffusion and was first introduced in [3]. In this cited article, Arnol'd introduced the diffusion mechanism of transition chains: for a given Hamiltonian system, let $\phi_t$ denote its flow. The mechanism of transition chains consists in finding a sequence of invariant tori $T_1, \ldots, T_n$ such that for each $i = 1, \ldots, n$, the unstable invariant manifold of $T_i$, $W_i^u$ intersects the stable manifold of $T_{i+1}$, $W_{i+1}^s$ *transversally*. In this case, one can assure that if $\xi \in W_1^s$ and $\eta \in W_n^u$, for any neighbourhood $U$ of $\xi$ and $V$ of $\eta$, the flow $\phi_t$ connects both neighbourhoods, that is, $\cup_{t>0} \phi_t U \cap V \neq \emptyset$.

An illustrative example of exponentially long trapping times is [53], where the authors introduced a methodology to study the region in the phase space around a totally elliptic fixed point in a Hamiltonian system where invariant KAM tori are prominent. This methodology was based in the usage of normal forms and rigorous bounds. Around a totally elliptic fixed point, they were able to establish lower bounds for the diffusion time in this zone: they found that initial conditions taken in a poly-disk of radius $R_0$ were confined in a poly-disk of radius $\sigma R_0$, $\sigma > 1$ for exponentially long times.

But the setting we are dealing with differs essentially from this one since in our case stability can be established via KAM theory, since in either the 2D symplectic or 3D volume preserving (2-angle 1-action) cases invariant curves and 2D tori, respectively, are codimension 1 manifolds: total barriers to transport since they separate space. Hence, the stickiness problem has to be understood outside the region where these confining invariants of the system exist. Hence, despite being a different problem it is related to the effective stability of KAM tori in Hamiltonian systems in 3 or more dof.

The very first problem to deal with is what Chirikov called the structure of "the chaos border" [27], the boundary between regular and chaotic motion. Despite being an old problem it is highly intricate and yet unsolved and makes the stickiness problem extremely difficult to be approached in an analytic way. In the 2D setting there are intricate structures that coexist whose description is based on different renormalisation schemes. For instance, around a stability island one has the Hierarchical Island-Around-Island structure, that consists in partitioning the phase space using Cantori that are around either the main island or around satellites (and satellites of satellites, and so on), and that is conjectured to scale somehow [149]; and in turn, the destruction of each of these invariant curves and their evolution as Cantori can be explained via the Greene-MacKay renormalisation theory, see Sect. 3.5.6.

The 3D setting presents similar difficulties, but there is much less understanding on the geometry of the most prominent objects around 2D invariant tori. Yet it is a promising and interesting field of research that is being approached nowadays by several authors. See [40] in the conservative context, and [18, 19, 20, 21] in the dissipative setting.

In both 2D and 3D cases, one is lead to deal with this problem in a numerical way. In both cases, we will iterate maps defined on a torus $\mathbb{T}^{d+1}$ that can be lifted to $\mathbb{T}^d \times \mathbb{R}$, $d = 1, 2$. So, when we are on tori, it makes sense to consider an adequate compact neighbourhood $K$ of a sticky object and $K^c = \mathbb{T}^{d+1} \setminus K$, its complement to the torus. Then, diffusion properties are measured by studying, once either in $K$ or $K^c$, the probability to leave it after $t$ iterates. To fix notation, let $x_0 \in \mathbb{T}^{d+1}$ be an initial condition and we iterate it under a conservative map $F : \mathbb{T}^{d+1} \to \mathbb{T}^{d+1}$, $F^i(x_0) = x_i$,

- If for some iterate $i > 0$, $x_{i-1} \in K^c$ but $x_i \in K$, then $\mathcal{I}(t)$ measures the *trapping statistics*, that of being trapped in $K$ for $t$ consecutive iterates:

$$\mathcal{I}(t) = \text{Prob}\left(x_j \in K, \quad j = i, i+1, \ldots, i+t, \quad x_{i-1}, x_{i+t+1} \in K^c\right). \tag{1.10}$$

- And conversely, if for some iterate $i > 0$, $x_{i-1} \in K$ but $x_i \in K^c$, we will denote by $\mathcal{I}^c(t)$ the probability to remain outside $K$ for $t$ consecutive iterates

$$\mathcal{I}^c(t) = \text{Prob}\left(x_j \in K^c, \quad j = i, i+1, \ldots, i+t, \quad x_{i-1}, x_{i+t+1} \in K\right). \tag{1.11}$$

In the 2D case there is a general agreement that $\mathcal{I}(t) \sim t^{-b}$, where the symbol $\sim$ refers to this behaviour as being asymptotic. Usually in the literature people deal with

$$I(t) = \int_t^\infty \mathcal{I}(s)\, ds \sim t^{-b+1}$$

the cumulative distribution function (cdf from now on) of the trapping statistics. The very first numerical studies available were those of Karney et al. [69], who studied the stickiness effect of the main island of stability of the Hénon map (in a version that will be introduced in Chap. 2), where the authors found that $I(t) \sim t^{-1.45}$. Later, Chirikov and Shepelyanski [30] performed a study of the stickiness effect of the last invariant curve of the Chirikov Standard map, where they asserted $I(t) \sim t^{-1.34}$. The key fact is that both numerical simulations, that were independently performed, gave rise to statistics whose pdf is, asymptotically, a power law with $2 < b < 3$. Note that this fact implies that $\mathcal{I}(t)$ has bounded average but unbounded variance and, in turn, gives rise to anomalous diffusion, see Sect. 1.1.5.

Later on, Meiss and Ott [103] built a theory of stickiness around islands of stability that relied on the fact that there exist a hierarchical island-around-island structure and that the main obstruction to transport is the one caused by Cantori. Moreover, the leakage across these objects is given by Mather's $\Delta W$ [95], the flux or area in the phase space that crosses the Cantorus per iterate [86]. In this context, they interpreted the chaotic accessible zone close to islands as if it was partitioned by Cantori and the dynamics in it could be explained as a Markov process. The transition probabilities between neighbour states were the flux across these Cantori. For this model, if one considers hypotheses that arise from the Greene-MacKay renormalisation theory [80, 83], they found $I(t) \sim t^{-1.96}$, which still satisfies $2 < b < 3$ as before. It is worth noting that this model is the only one available that takes into account both Cantori and the Hierarchical Island-Around-Island structure.

In [32] it was conjectured that there exists a universal asymptotic exponent $b$, based on results for a Markov tree model, where the transition probabilities present random scaling factors. The authors give numerical evidence of this exponent in a 2-parametric family of cubic area-preserving maps with an elliptic fixed point, and compare it with the statistics in a simulated Markov model with random transition probabilities, where they get $b \approx 2.57 \pm 0.03$.

Concerning the 3D case, there is little literature on stickiness, from which we want to highlight the papers [109] where the authors detect an algebraic decay of $\mathcal{I}(t)$ (measured as the time needed to escape from a zone that contains a 2-torus) in the Küppers-Lortz state (as a volume preserving flow), and [141], where the authors place initial conditions near 2D tori and find exponentially long trapping times.

### 1.1.5 Anomalous diffusion

In a context where orbits can eventually become unbounded, one can study transport properties via the growth of the variance of trajectories. In the two cases we are going to deal with, we are going to consider lifts to the cylinders $\mathbb{T}^d \times \mathbb{R}$ of maps initially defined on the tori $\mathbb{T}^{d+1}$, $d = 1, 2$. So in either case we are going to have a 1-dimensional observable $\xi \in \mathbb{R}$ (the action variable) that will diffuse.

To give an explicit account on transport properties, we are going to compute the variance of a sample as

$$\mathrm{Var}_n = \left\langle (\Delta^n \xi)^2 \right\rangle - \left\langle \Delta^n \xi \right\rangle^2$$

where $\Delta^n \xi = \xi_n - \xi_0$ is the difference of the observable after $n$ iterations and its initial value, and $\langle \cdot \rangle$ means ensemble average, taken among a large number of initial conditions. In practice, the quantity $\mathrm{Var}_n$ will also depend on the parameters of the system under study and on $n$.

Under symmetric random walk hypotheses, one expects a behaviour such as $\mathrm{Var}_n \sim n^\gamma$, $\gamma = 1$. That is, after $n \gg 1$ iterates, one expects a set of values of $\xi$ initially distributed in any way, to become eventually distributed as a Gaussian, having as mean $\langle \Delta^n \xi \rangle$, that in the limit has to be 0; and variance $\mathrm{Var}_n$, that grows linearly in the number of iterates performed. In other words, an initial ensemble of orbits distributed according to a pdf $f = f(\xi, n)$ will evolve according to the heat equation

$$\frac{\partial f}{\partial n} = \frac{1}{2} D \frac{\partial^2 f}{\partial \xi^2}, \qquad D = \lim_{n \to \infty} \frac{\mathrm{Var}_n}{n}, \tag{1.12}$$

where $n \gg 1$ is considered a continuous variable and $D$ is the so-called *diffusion coefficient*. We will refer to this situation as *diffusive*.

The term *anomalous diffusion* refers to the cases where $\mathrm{Var}_n \sim n^\gamma, \gamma \neq 1$. In the literature, the case $\gamma < 1$ is referred to as *sub-diffusive*, and $\gamma > 1$ as *super-diffusive*. This last case is what we will deal with in chapters 3 and 5. Note that, $\mathrm{Var}_n \sim n^\gamma, \gamma > 1$ implies the divergence of $D$ in (1.12).

## 1.2 The Chirikov standard map

The main 2D example we are going to deal with in this thesis is the Chirikov (or Taylor-Chirikov) standard map [26, 27]. We are going to consider it in the following representation:

$$\tilde{M}_k : \mathbb{T}^2 \to \mathbb{T}^2, \qquad \tilde{M}_k : \begin{pmatrix} x \\ y \end{pmatrix} \mapsto \begin{pmatrix} \bar{x} \\ \bar{y} \end{pmatrix} = \begin{pmatrix} x + \bar{y} \\ y + k\sin(2\pi x) \end{pmatrix}. \tag{1.13}$$

We will denote by $M_k$ and $\bar{M}_k$ its lifts to the cylinder $\mathbb{S}^1 \times \mathbb{R}$ and the plane $\mathbb{R}^2$, respectively. Note that in the literature it is common to use the the scaled version $\bar{k} = 2\pi k$ of the parameter, and $\sin(x)$ instead of $\sin(2\pi x)$, that is, with the angle defined in $\mathbb{S}^1 = \mathbb{R}/2\pi\mathbb{Z}$.

The main reasons to use $\tilde{M}_k$ as key example are

1. Its dynamics for different ranges of the parameter $k$ provides a proper context where to study the two main problems we are going to deal with. First, for $k \geq 1$ one can study the effect of an island of stability in the statistical properties of the orbits in the chaotic zone (chapters 2 and 3) and for $k$ near $k_G \approx 0.156$ one can study the effect of a 'single' Cantorus in the transport rates across it.

2. It will serve as inspiration to construct a proper model for the study of the same problems in the 3D context (see chapter 5).

The map $\tilde{M}_k$ is one of the so-called standard-like maps also defined on the 2-torus $\mathbb{T}^2$,

$$(x, y) \mapsto (\bar{x}, \bar{y}) = (x + \bar{y}, y + kV(x)), \tag{1.14}$$

where $V(x)$ is an even 1-periodic function with zero average. Instead of taking $V(x) = \sin(2\pi x)$ one can consider other examples giving rise to different phenomena. See [9, 22, 91]. In this memoir we will only focus on the classical standard map with $V(x) = \sin(2\pi x)$. It is worth noting that it is a paradigmatic example as it appears in many contexts. For instance

1. It is a first order approximation of the dynamics around a generic $(p, q)$ resonant chain of islands in area preserving maps, see [26, 135],

2. It describes the dynamics both relatively far from the separatrix and around simple resonances in some return map models. The dynamics in a fundamental domain around the separatrices which emanate from a hyperbolic fixed point $P$ of an area preserving map $F$ can be described (in the simplest and symmetric case) by the Chirikov's Separatrix Map [26]

$$S_{a,b} : \begin{pmatrix} x \\ h \end{pmatrix} \mapsto \begin{pmatrix} \bar{x} \\ \bar{h} \end{pmatrix} = \begin{pmatrix} x + a + b\log|\bar{h}| \\ h + \sin(2\pi x) \end{pmatrix}, \quad b = -1/\log(|\lambda|)$$

where $(x, h) \in \mathbb{S}^1 \times [-\tilde{h}, \tilde{h}]$ are adapted coordinates. The variable $x$ moves along a fundamental interval of $W^s(P)$ (between two consecutive homoclinic points on the same orbit) and $h$ measures the distance from $W^s(P)$ in a suitable action variable. This action is not preserved under iteration of $F$ due to the splitting between $W^s(P)$ and $W^u(P)$. In the integrable case, this action can be understood as an energy that is zero along the separatrices (which coincide), and in such a case the dynamics on $h$ would simply be $\bar{h} = h$.

In the given formulation, $h$ has been scaled by the splitting size so that $\tilde{h}$ is $\mathcal{O}(1)$. The parameter $a$ is a necessary shift to have all iterates inside this fundamental domain, and $b = -1/\log(|\lambda|)$, where $\lambda$ is the dominant eigenvalue of $DF(P)$ [17].

To derive $S_{a,b}$, it is assumed that the first harmonic in the splitting function dominates. Furthermore, as we already said, it is assumed that the fixed point $P$ is hyperbolic. The term $\log|\bar{h}|$ actually comes from the passage close to this point. For parabolic points with invariant manifolds see [92].

If we are relatively far from the separatrix, take $h = h_0 + s$ in $S_{a,b}$, where $|h_0| \gg 1$ and expand the log term. If we consider $k = |h_0|/b$ and $y = a + b\log|h_0| + ks$ we recover $M_k + \mathcal{O}(|h_0|^{-2})$, see [142, 135].

We also recover the standard map by linearising around values $h = h_r$ where $b\log(h_r) = r \in \mathbb{Z}$, see [26, 27].

3. It is a conveniently scaled version the map obtained as a one step integration of the simple pendulum using a symplectic method of integration. Indeed, if we consider the equations

$$H = \frac{1}{2}\eta^2 + \cos\xi, \qquad \dot{\xi} = \eta, \quad \dot{\eta} = \sin\xi,$$

the map obtained by a single step of integration using the symplectic Euler method with stepsize $\varepsilon$ gives

$$P_\varepsilon : \begin{pmatrix} \xi \\ \eta \end{pmatrix} \mapsto \begin{pmatrix} \bar{\xi} \\ \bar{\eta} \end{pmatrix} = \begin{pmatrix} \xi + \varepsilon\bar{\eta} \\ \eta + \varepsilon\sin\xi \end{pmatrix}.$$

If we re-scale $P_\varepsilon$ via $C(\xi,\eta) = (2\pi\xi, 2\pi\eta/\varepsilon) = (x,y)$, we get

$$M_k = C \circ P_\varepsilon \circ C^{-1},$$

where $k = \varepsilon^2/(2\pi)$.

The overall dynamics of $\tilde{M}_k$ as a function of $k, k \geq 0$ (the case $k \leq 0$ is exactly the same by means of $k \to -k$) is fairly well known. At $k = 0$, $\tilde{M}_0$ is integrable. In fact it is of the form (1.2), $H_0^{(1)}$ with $g^{(1)}(r) = r$, and in this case the phase space is foliated by horizontal RIC. Once $k > 0$ some of this structure persists in virtue of Moser's twist Theorem, and the last RIC to be destroyed is the one with the golden mean $\omega = (\sqrt{5}-1)/2$ as rotation number, and it happens at the value of the parameter $k_G \approx (2\pi)^{-1}0.9716354061062\ldots$, called Greene's value of the parameter [63][3]. For $k > k_G$ the RIC is a Cantor set, according to Aubry-Mather theory [93, 8]. The actual value is rigorously bounded by $0.9716/(2\pi) < k_G < 63/(64\cdot 2\pi)$. The lower bound is a recently obtained value in [45], where the authors proved using computer assisted techniques that the golden mean invariant curve exists. The upper bound was provided in [88] where the authors did a computer assisted proof (CAP) for the nonexistence of any RIC in the standard family (1.13).

Since here RIC separate space, they do not permit vertical drift, but they do once destroyed. Taking this into account, we consider three main ranges of $k > 0$, according to the geometry of the phase space:

[3]The first approximation of this value is due to Greene, $k_G \approx 0.971635/(2\pi)$, but we will use the refined value of MacKay given in [80, 83]

- If $0 < k \leq k_G$, orbits of any point under $M_k$ are always bounded. It is remarkable that the measure of detectable chaos as a function of $k$ for $\tilde{M}_k$ (in the torus) is intimately related to the measure of the splitting of the invariant manifolds of the fixed point at the origin. The transversality of these invariant manifolds, including an asymptotic expansion of the splitting function, was rigorously obtained in [54]. In Fig. 1.2 we can see a comparison between the relative measure of the set of points with chaotic orbit (detected by computation of the Lyapunov exponent) and a multiple of the splitting angle of the manifolds of the hyperbolic fixed point, computed at the homoclinic point lying on the line $x = 1/2$. The agreement is good, even for large values close to $k = k_G$ of the parameter $k$, and it is specially accurate for small values of $k$.

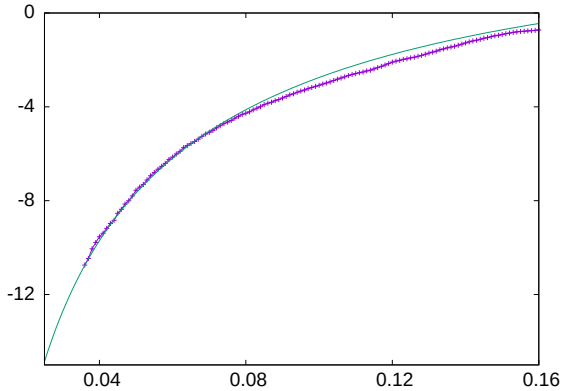


Figure 1.2: Fraction of points with chaotic orbit (line with points) and 50 times the splitting angle of the hyperbolic fixed point for the standard map (continuous line). Horizontal variable: the parameter $k$, see (1.13). In the vertical line the natural logarithms of the values are displayed.

- For $k_G < k < 0.903$, the nonexistence of RIC allows orbits to become unbounded under iteration of $M_k$ (now in the cylinder). But there is still some moderate regular area due to islands of stability, being the one around the fixed elliptic point the main source. In Fig. 1.3 we show the fraction of pixels in a fine grid (see the caption for detailed information) that are not visited by chaotic orbits, as a function of the parameter $k$. On the left we see that right after $k = 0.7$, less than a 2% of the pixels are not visited. Near $k = 0.9$ it seems that the regular area drops down to zero. But on the right we show a magnification of an region surrounding $k = 0.9$, that we recomputed in a finer grid. The value of the parameter for which we got the minimum fraction of non-visited pixels was for $k = 5.675/(2\pi) \approx 0.903$. For these value, after a total of $10^{12}$ iterates, only 3471 out of $2^{28}$ pixels were non-visited, that is, we detect a measure of regular area below 0.001% of the phase space. We remark that this detected area is not due to the satellites of the main elliptic island, but to other tiny elliptic periodic points.

- The case $k > 0.903$, corresponds to a range of the parameter where one expects that most of the phase space will be detected as fully chaotic. But still some moderate size islands appear. This case will be treated with detail in the next chapter.

In Fig. 1.4 one can see an example of how does the phase space of (1.13) look like from the point of view of regular-chaotic orbits. To generate them, we computed the Lyapunov exponent $\Lambda$ of each initial condition (in an equispaced $2048 \times 2048$ grid, keeping track on the pixels visited), and we plot them in light grey if we could assert, after $10^6$ iterates, that

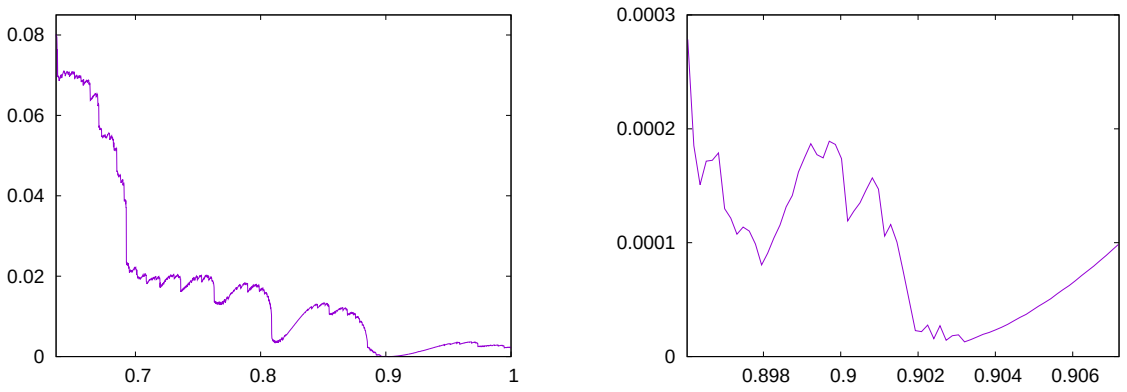


Figure 1.3: Fraction of pixels that correspond to orbits confined in islands as a function of $k$ in (1.13) in a $N \times N$ equispaced grid in the torus $\mathbb{T}^2$ that have not been visited by `ic` initial conditions iterated $T$ times. Left: $N = 2^{11}$, `ic` $= 100$ and $T = 10^8$. Right: $N = 2^{14}$, `ic` $= 1000$ and $T = 10^9$. The stepsize in $k$ is, in both plots, $10^{-3}/(2\pi)$. The reason for the sudden decreases is explained in Sect. 2.2.2. See also Fig. 5.2 for a related example.

$\Lambda > 0$. Roughly speaking, if one performs $T$ iterates of an initial condition, one can consider it to belong to a chaotic orbit if one gets an approximation of $\Lambda > \mathcal{O}(T^{-1})$. On top left, we plot the case $k = 0.5/(2\pi) \approx 0.0796$, where as commented above, the main source of chaotic orbits is due to the splitting of the invariant manifolds of the origin. Of course there is more chaotic area, but it is below pixel size. The picture on the top right is a magnification of the top left, where chaotic zones due to high period resonances are visible. In the bottom left, we plot the case $k = 0.9716/(2\pi) \approx 0.155$, right before the breakdown of the golden invariant Cantorus. Here we can see a complicated mixture of regular and chaotic orbits. The chaotic zone occupies approximately half of the phase space. There is numerical evidence that the relative size of the chaotic zone close to the breakdown of the last RIC is similar in larger family of standard-like maps (1.14), see [91]. Finally, on the bottom right we display the case $k = 2/\pi$, exactly at the period-doubling bifurcation of the main elliptic island. Here most of the phase space can be considered chaotic, and one expects it to become seemingly fully chaotic once $k \gg 1$. In this case, there are still plenty of elliptic islands in the phase space [38], but they are always below pixel size in the actual scale of the plot.

**An example of turnstile area: $\Delta W_{0,1}$**

Consider the map $M_k$, defined on the cylinder $\mathbb{S}^1 \times \mathbb{R}$. We are interested in the rate of escape of orbits from $T = \mathbb{S}^1 \times [0, 1]$ through the line $\{y = 0\}$ (or $\{y = 1\}$, by symmetry). We called this line $C$ in the discussion in page 18. Note that the hyperbolic and elliptic/reflection-hyperbolic fixed points of the standard map $M_k$ are located at $(0, 0)$ and $(0.5, 0)$, respectively, for all values of $k$. These points have rotation number $0/1$, that is, they are still fixed even if one considers lifts $\bar{M}_k$ of $M_k$ to the plane $\mathbb{R}^2$.

The orbits starting at $(x, y) \in T$ that escape this set in one single iterate are those that satisfy

$$y + k \sin(2\pi x) < 0.$$

That is, all points with $y \geq 0$ that are below the curve $-k \sin(2\pi x)$. One can also think

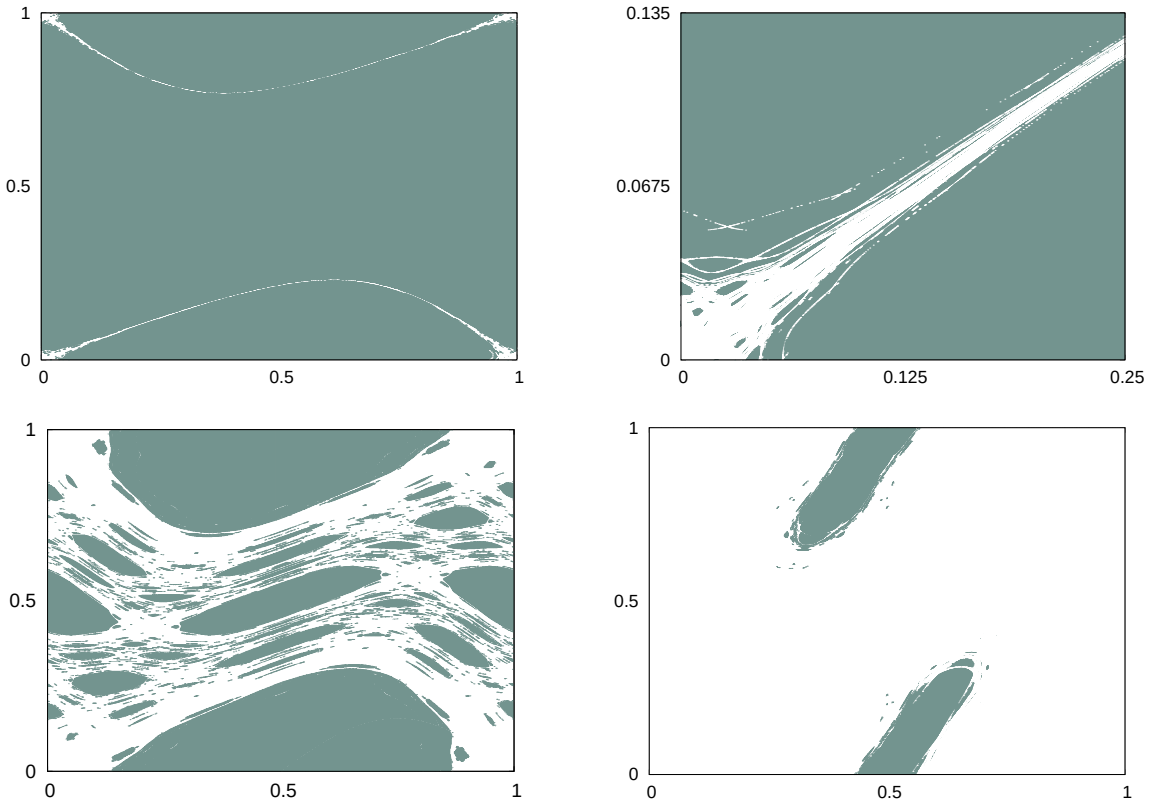


Figure 1.4: Distinction between regular and chaotic orbits in the phase space of (1.13) for $k = 0.5/(2\pi)$ (top, the right plot is a magnification of the left one), $k = 0.9716/(2\pi)$ (bottom left) and $k = 2/\pi$ (bottom right). Light grey pixels correspond to regular orbits while white pixels correspond to chaotic orbits.

in terms of escaping sets: all points escaping through $\{y = 0\}$ are those bounded by the pre-image of this line $M_k^{-1}(\{y = 0\}) = \{y = -k\sin(2\pi x)\}$ and the line $\{y = 0\}$ itself. First, we consider the case $k \leq 1$. The area of this set, that we are going to denote by $A$ is simply

$$A = \int_{0.5}^{1} -k\sin(2\pi x) = \frac{k}{\pi}.$$

From the point of view of Mather's $\Delta W_{0,1}$, we have to consider the generating function of the standard map. One can easily check that it is, up to a constant, of the form

$$G_k(x, x') = -\frac{1}{2}(x' - x)^2 + \frac{k}{2\pi}\cos(2\pi x).$$

The $(0, 1)$ periodic action is $W_{0,1}(\underline{x}) = G_k(x, x)$ where $\underline{x} = \{x\}$ is a finite sequence with one element, and the equilibrium sequences corresponding to the fixed points are constant equal to 0 and 0.5, that correspond to the fixed points at $(0, 0)$ and $(0.5, 0)$, respectively. Hence,

$$\Delta W_{0,1} = \frac{k}{2\pi}\cos(0) - \frac{k}{2\pi}\cos(2\pi 0.5) = \frac{k}{\pi} = A,$$

That is, the turnstile area $\Delta W_{0,1}$ grows linearly in $k$ for $k < 1$. Since we are restricting ourselves to the set $T$, for $k > 1$ (for $k = 1$, $y = -k\sin(2\pi x)$ is tangent to $\{y = 1\}$ at

$x = 3/4$), $\Delta W_{0,1}$ in $T$ will increase slower than linearly with slope $1/\pi$. In the case $k > 1$ the part of the domain between $\{y = -k\sin(2\pi x)\}$ and $\{y = 0\}$ which is on top of $y = 1$ must be skipped. Let $x^* \in (0.5, 0.75)$ be such that $-k\sin(2\pi x^*) = 1$. Then the value of $A$ will be twice the sum of the integral of $-k\sin(2\pi x)$ between 0.5 and $x^*$ plus $0.75 - x^*$. This gives

$$\frac{1}{\pi}\left(k - \sqrt{k^2 - 1}\right) + \frac{1}{2} - \frac{\arcsin(1/k)}{\pi}.$$

This behaves as $\frac{1}{2} - \frac{1}{2\pi k} + \mathcal{O}(k^{-3})$ for $k$ large and, hence we obtain

$$\lim_{k\to\infty} \Delta W_{0,1} = \frac{1}{2}.$$

Here we want to stress the fact that in the area $\Delta W_{0,1}$ we are including that occupied by points confined in islands (that can be either regular or chaotic) and points that are non-confined in stability islands. The islands of stability that can be included in the escaping set whose area is $\Delta W_{0,1}$ are essentially the main central island around the fixed point $(0.5, 0)$ and its satellites. This leads to the following considerations:

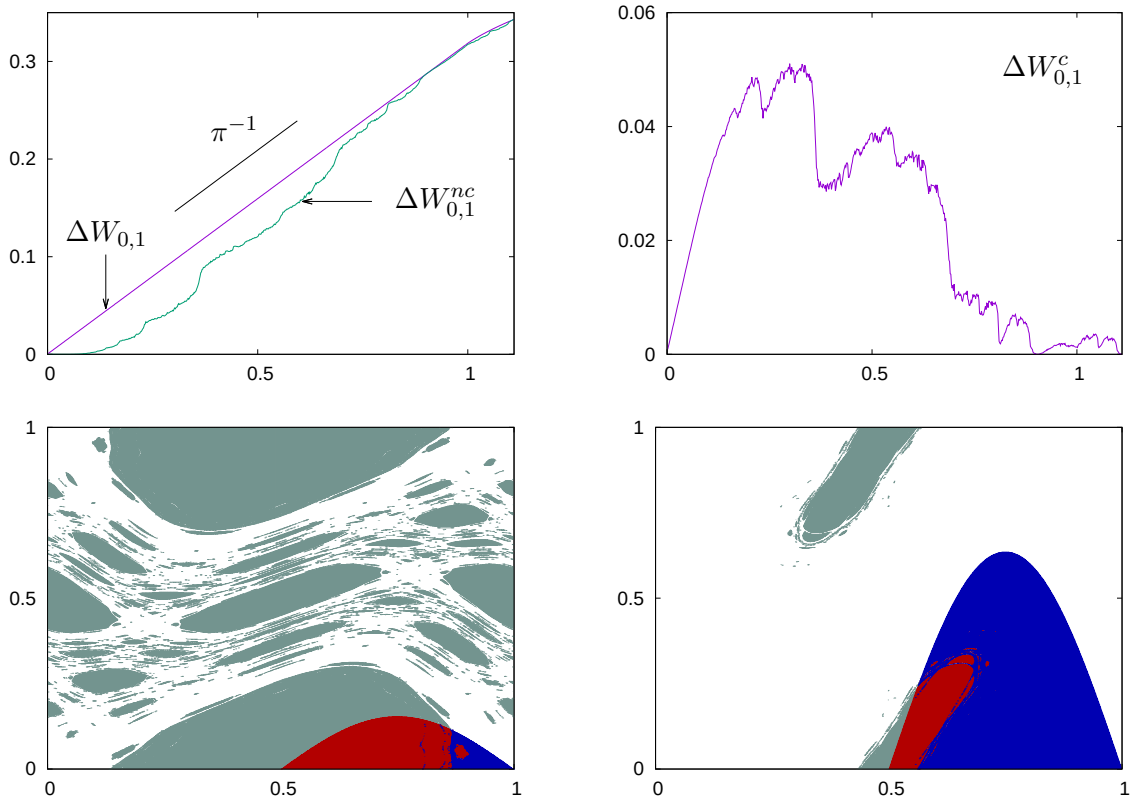


Figure 1.5: Turnstile area of the fixed points of the standard map (1.13). Top left: $\Delta W_{0,1}$ (purple) and $\Delta W^{nc}_{0,1}$ as a function of $k$. Top right: $\Delta W^{c}_{0,1}$ as a function of $k$. Bottom: phase space of $M_k$ for $k = 0.9716/(2\pi)$ (left) and $k = 2/\pi$ (right). The light gray pixels correspond to regular orbits, while those in white are chaotic. The area of the union of the red an blue regions is $\Delta W_{0,1}$, the red (resp. blue) pixels being regular (resp. chaotic).

1. For each $p, q \in \mathbb{Z}$, $q \neq 0$ such that we can assure that there exists a $p/q$-periodic orbit, the turnstile area $\Delta W_{p,q}$ can be written as the sum

$$\Delta W_{p,q} = \Delta W^c_{p,q} + \Delta W^{nc}_{p,q},$$

where the superscript $c$ stands for 'confined in an island' and $nc$ for 'non-confined in an island'.

2. Since $\Delta W^c_{p,q}$ can only consist in points whose rotation number in $\mathbb{S}^1 \times \mathbb{R}$ is $p/q$, we are lead to define the following set.

**Definition 7.** *The domain of stability of rotation number $p/q$ of an APM $F$ of the cylinder $\mathbb{S}^1 \times \mathbb{R}$ is the set of points*

$$\mathrm{DS}(p/q) = \left\{ (x, y) \in \mathbb{S}^1 \times \mathbb{R} \ : \ \lim_{n\to\infty} \frac{\pi_1 F^n(x, y) - x}{n} = \frac{p}{q} \right\},$$

*where $\pi_1$ denotes the projection onto the first component.*

Note that $\mathrm{DS}(p/q)$ not only contains the periodic orbits and regular points around the elliptic or reflection hyperbolic ones, but also chaotic confined points, satellite islands, and stable invariant manifolds.

Back to the example about the computation of $\Delta W_{0,1}$, for the standard map, the quantities $\Delta W^c_{0,1}$ and $\Delta W^{nc}_{0,1}$. In Fig. 1.5, top, we show $\Delta W_{0,1}$ as a function of $k$. On the left one can see both $\Delta W_{0,1}$ and $\Delta W^{nc}_{0,1}$. We indicated also the slope $\pi^{-1}$ to show the good agreement with the predicted behaviour. On the right, we show $\Delta W^c_{0,1}$. On the bottom of Fig. 1.5 we show the phase space of $M_k$ for $k = 0.9716/(2\pi)$ (left) and $k = 2/\pi$ (right). The union of the red and blue regions are the turnstile. The red part are regular initial conditions, while the blue region is formed of chaotic ones. It is important to remark that we will deal with transport in the chaotic zone. Hence, the rates of transport across periodic orbits will not be given by the relative area $\Delta W_{p,q}$ but by the relative area $\Delta W^{nc}_{p,q}$, both understood in adequate regions of the phase space, see Sect. 4.3.1.

## 1.3 Accelerator modes

Accelerator modes are a special kind of orbits that appear in maps $F(x, z)$ of the cylinder $\mathbb{T}^d \times \mathbb{R}^l$ to itself, where $x$ are angles and $z$ are actions, that are periodic in the action variables. In such a case, $F$ analytically projects onto the torus $\mathbb{T}^{d+l}$, and we shall denote it as $\tilde{F}$.

**Definition 8.** *A $q$-periodic point $(x_0, z_0) \in \mathbb{T}^d \times \mathbb{T}^l$ under such a map $\tilde{F}$, $\tilde{F}^q(x_0, z_0) = (x_0, z_0)$ is an accelerator mode if under iteration of the lifted map to the cylinder the action variables change by an integer quantity:*

$$F^q(x_0, z_0) = (x_0, z_0 + n), \qquad n \in \mathbb{Z}^l \setminus \{0\}.$$

In this section we present a simple way to generate area and volume preserving maps having accelerator mode orbits. Furthermore if we consider maps in this form, the stability of the accelerating orbits when we consider maps on the corresponding torus (when they

become fixed or periodic points), can be effectively computed, so that we can choose proper models in such a way that these associated orbits give rise to stable area or volume around them.

The structure around the stable accelerator modes is going to be the responsible for anomalous diffusion in the maps we are going to deal with.

### 1.3.1 Area-preserving maps as compositions of shears

The easiest way to generate area-preserving maps is by composing shears. The simplest nontrivial (in the sense of the dynamics) case corresponds to composing one shear in the $x$ direction and another one in the $z$ direction. Let $S_1$ and $S_2$ be shears represented as

$$S_1 : \begin{pmatrix} x \\ z \end{pmatrix} \mapsto \begin{pmatrix} x + g_1(z) \\ z \end{pmatrix}, \qquad S_2 : \begin{pmatrix} x \\ z \end{pmatrix} \mapsto \begin{pmatrix} x \\ z + g_2(x) \end{pmatrix}. \tag{1.15}$$

Since $\det(DS_i(x, z)) = 1$, the shears preserve both area and orientation. Two conjugate maps can be generated by composing them, $S_1 \circ S_2$ and $S_2 \circ S_1$. To fix ideas, let us consider the choice $\tilde{F} = S_1 \circ S_2$, which has the form

$$\tilde{F} : \begin{pmatrix} x \\ z \end{pmatrix} \mapsto \begin{pmatrix} x' \\ z' \end{pmatrix} = \begin{pmatrix} x + g_1(z') \\ z + g_2(x) \end{pmatrix}. \tag{1.16}$$

Maps of this form include Chirikov's standard map (1.13), non-twist standard maps (for instance taking $g_1(z) = z - z^2$), the Harper Map, Arnold's cat map, linked twist maps, etc. Note that these kind of maps are those with generating function

$$G(x, z') = xz' + \hat{g}_1(z') - \hat{g}_2(x), \qquad z = \frac{\partial G(x, z')}{\partial x}, \quad x' = \frac{\partial G(x, z')}{\partial z'}, \tag{1.17}$$

where $\hat{g}_i$ is a primitive of $g_i$, $i = 1, 2$.

Suppose that $\tilde{F}$ as in (1.16) is an analytic map on the torus, $\mathbb{T}^2$; in this case the shear functions $g_i$ should be analytic maps of the circle $\mathbb{S}^1$, or circle maps; without loss of generality, we can assume that each one is 1-periodic. An orbit of $\tilde{F}$ is periodic if a lift $\bar{F} : \mathbb{R}^2 \to \mathbb{R}^2$ of $f$ has orbits that return to some integer translate of its initial condition after a fixed number of steps, i.e., if $\bar{F}^q(x, z) = (x + m, z + n)$, for some $m, n \in \mathbb{Z}$ and $q \in \mathbb{N}$. Denoting points on an orbit by $(x_t, z_t) = \tilde{F}^t(x_0, z_0)$ periodicity implies that

$$m = \sum_{t=1}^{q} G_1(z_t), \quad n = \sum_{t=0}^{q-1} G_2(x_t), \tag{1.18}$$

where each $G_i$ is a lift of the corresponding $g_i$ to $\mathbb{R}$.

Such $(m, n, q)$-periodic orbits have different interpretations depending upon the degree of the circle maps $g_i$ and upon the physical interpretation of the phase space variables. For example, for standard-like maps, $x$ represents a physical angle and $z$ a momentum. In this case $g_1$ has degree-one—for Chirikov's case $g_1(z) = z \mod 1$—representing a twist, while $g_2$ represents a force and has degree zero. In this case, the map can be partially lifted to the cylinder $\mathbb{S}^1 \times \mathbb{R}$, and on this phase space it has zero net flux: the net area that crosses any non-contractible loop upon iteration, is zero. As commented above, the zero net flux condition is also necessary if one wants $\tilde{F}$ to have any invariant curves that encircle the cylinder, and is a requirement of KAM theory for preservation of such circles.

For this case, orbits with $n = 0$, correspond to periodic orbits on the cylinder, while those with $n \neq 0$, have momenta that grow (or decrease) linearly in time, that is, they are accelerator modes.

The simplest case corresponds to period one, $q = 1$, where (1.18) becomes

$$G_1(z+n) = m, \quad G_2(x) = n, \qquad n, m \in \mathbb{Z}. \tag{1.19}$$

Consequently, the set of fixed points,

$$\mathcal{A}_{m,n,1} = \left\{(x,z) \in \mathbb{T}^2 \ : \ G_1(z+n) = m \text{ and } G_2(x) = n\right\},$$

is the intersection of the level sets of the lifted shear functions.

The linear stability of a period-$q$ orbit of an area-preserving map $\tilde{F}$ is determined by the characteristic polynomial of $D\tilde{F}^q(x_0, z_0)$:

$$p_2(\lambda) = \lambda^2 - \tau\lambda + 1\,, \text{ where } \tau = \mathrm{tr}(Df^q(x_0, z_0)).$$

Hence, the multipliers $\lambda_1$ and $\lambda_2$ depend only on $\tau$: if $|\tau| < 2$, $\lambda_1 = \bar{\lambda}_2 \in \mathbb{C}$ and have modulus one, if $\tau = \pm 2$ then $\lambda_1 = \lambda_2 = \pm 1$ and if $|\tau| > 2$ then $\lambda_1 = \lambda_2^{-1}$ with the sign of $\tau$. For the form (1.16),

$$D\tilde{F}(x,z) = \begin{pmatrix} 1 + \dot{g}_1(z')\dot{g}_2(x) & \dot{g}_1(z') \\ \dot{g}_2(x) & 1 \end{pmatrix},$$

where we denote $\dot{g}(\xi) = dg/d\xi$. Thus

$$\mathrm{tr}(Df) = 2 + \dot{g}_1(z+m)\dot{g}_2(x) = 2 + \dot{g}_1(z)\dot{g}_2(x), \tag{1.20}$$

due to periodicity.

Suppose, e.g., that $G_2(x) = kp(x)$, where $k \in \mathbb{R}$, $p(x)$ is periodic, and $\|p\|_\infty = 1$. Then the condition (1.19) is equivalent to,

$$p(x) = \frac{n}{k}, \tag{1.21}$$

that only has solutions when $k \geq |n|$.

The period-one accelerator modes obtained from (1.21) are born at $k = |n|$, that is, at an extremum of $p(x)$. Hence, at this bifurcation, $\dot{g}_2(x) = 0$, so that $\tau = 2$. Consequently, the parameter $k$, unfolds generically an elliptic-hyperbolic bifurcation as it crosses $|n|$.

### Accelerator modes of Chirikov's standard map

Probably the most well-studied example with accelerator modes is Chirikov's standard map, $\tilde{M}_k$ (1.13), that has the form (1.16) where

$$g_1(z) = z \mod 1, \quad g_2(x) = k\sin(2\pi x).$$

Let us restrict ourselves to $k > 0$. In this case,

$$\mathcal{A}_{m,n,1} = \{x = \frac{1}{2\pi}\sin^{-1}\left(\frac{n}{k}\right), z = m - n\}. \tag{1.22}$$

Upon projection to the torus, one can set $n = m$ without loss of generality.

For each value of $n \in \mathbb{Z} \neq 0$ (1.22) only makes sense when $k \geq |n|$. So accelerator modes appear for $k = n$, at $(1/4, 0)$ jumping upwards and at $(3/4, 0)$ jumping downwards. Their stability is determined by (1.20) with

$$\tau = 2 + 2\pi k \cos(2\pi x).$$

A pair of accelerator modes are born at $x = \frac{1}{4}$ and $x = \frac{3}{4}$ with $\tau = 2$ when $k = |n|$.

As $k$ grows, generically, two branches emanate from each point, giving rise to hyperbolic and elliptic accelerator modes. Their position depends on the value of $k$, but they evolve along $y = 0$. Further details on the evolution of these accelerator modes as a function of $k$ will be given in Chap. 2.

### 1.3.2 Volume preserving maps as compositions of shears

A natural higher-dimensional version of (1.16) corresponds to a map on $\mathbb{T}^d \times \mathbb{T}^l$ with $d$-angles $x_1, x_2, \ldots, x_d$ and $l$ momenta $z_1, z_2, \ldots, z_l$, to be lifted to $\mathbb{T}^d \times \mathbb{R}^l$. This map is automatically volume and orientation preserving, $\det Df = 1$. The map is symplectic only if $d = l$ and each shear is a gradient, $g_1 = \nabla T(z)$ and $g_2 = \nabla V(x)$, and again in this case the map $f$ can be written similarly to (1.17) as coming from a generating function and the map is near the identity if $g_1$ and $g_2$ are small.

Alternatively one can consider shears $S_i$ along a single direction, that is, if $w \in \mathbb{T}^d$, then $S_i : \mathbb{T}^d \to \mathbb{T}^d$, let $S_i(w) = w + e_i g_i(w)$ where $e_i$ is the $i$th vector in the canonical basis of $\mathbb{R}^d$ as a vector space. If $g_i$ is independent of the $i^{th}$ component $w_i$, each shear is again volume and orientation preserving. Thus any map $f = S_{i_1} \circ S_{i_2} \circ \ldots \circ S_{i_j}$, $i_1, i_2, \ldots, i_j \in \{1, 2, \ldots, d\}$ is as well.

We are interested in the dynamics of a three-dimensional case, using angles $(x, y) \in \mathbb{T}^2$ and one action $z \in \mathbb{R}$. So the shears in these two directions will be periodic functions of their arguments. And we assume, as for the standard maps, that the vertical shear is a periodic function in $(x, y)$ with zero average, and hence it can be projected to the torus, $\mathbb{T}^3$. This implies, again, the possibility of periodic orbits on $\mathbb{T}^3$ that may not be periodic on $\mathbb{T}^2 \times \mathbb{R}$: the lifted $z$ variable may linearly increase or decrease by an integer amount for suitable $(x, y)$.

Mimicking the procedure of 1.3.1, we consider the composition of three shears, one in each direction

$$S_1 : \begin{pmatrix} x \\ y \\ z \end{pmatrix} \mapsto \begin{pmatrix} x + g_1(y, z) \\ y \\ z \end{pmatrix}, \quad S_2 : \begin{pmatrix} x \\ y \\ z \end{pmatrix} \mapsto \begin{pmatrix} x \\ y + g_2(x, z) \\ z \end{pmatrix}, \tag{1.23}$$

$$S_3 : \begin{pmatrix} x \\ y \\ z \end{pmatrix} \mapsto \begin{pmatrix} x \\ y \\ z + g_3(x, y) \end{pmatrix} \tag{1.24}$$

There are two sets of conjugate maps formed by composition of these three shears in some order, but the families are equivalent under permutations of the labels. To fix ideas, we take $\tilde{F} = S_2 \circ S_1 \circ S_3$, which gives

$$\tilde{F} : \begin{pmatrix} x \\ y \\ z \end{pmatrix} \mapsto \begin{pmatrix} x' \\ y' \\ z' \end{pmatrix} = \begin{pmatrix} x + g_1(y, z') \\ y + g_2(x', z') \\ z + g_3(x, y) \end{pmatrix}. \tag{1.25}$$

As done above, we are going to consider intersections of the level sets $\{g_i = n\}$, $n \in \mathbb{Z}$, $i = 1, 2, 3$. These are 2D-manifolds obtained by the corresponding level set times $[0, 1]$ on the missing variable.

Here we could deal with $q-$periodic accelerator modes, but we will restrict ourselves with fixed accelerator modes, $q = 1$. Denote the intersection of the level sets by

$$\mathcal{A}_{m,l,n} = \{g_1 = m\} \cap \{g_2 = l\} \cap \{g_3 = n\}, \qquad m, l, n \in \mathbb{Z}.$$

If $(x, y, z) \in \mathcal{A}_{m,l,n}$, $\tilde{F}(x, y, z) = (x, y, z)$ and when we lift it to $\mathbb{T}^2 \times \mathbb{R}$, $F(x, y, z) = (x, y, z + n)$.

We can also perform a similar analysis as for the 2D case concerning the linear stability of accelerator modes, when they appear. For a period-$q$ point of a volume and orientation preserving map $\tilde{F}$, $(x^*, y^*, z^*) = \tilde{F}^q(x^*, y^*, z^*)$, its linear stability is determined by the characteristic polynomial of $D\tilde{F}^q(x^*, y^*, z^*)$,

$$p_3(\lambda) = -\lambda^3 + \tau\lambda^2 - \sigma\lambda + 1, \tag{1.26}$$

where $\tau = \mathrm{tr}(D\tilde{F}^q(x^*, y^*, z^*))$ is the trace of the differential matrix at the periodic point and $\sigma = \frac{1}{2}(\tau^2 - \mathrm{tr}((D\tilde{F}^q(x^*, y^*, z^*))^2))$ is the second trace. The configurations of the three multipliers $\lambda_1, \lambda_2$ and $\lambda_3$ are generically in 8 regions in the $\tau - \sigma$ plane shown in Fig. 1.6.

Under the periodicity conditions on $g_1, g_2$ and $g_3$, we can determine the linear stability of accelerator modes when they appear. The values of the first and second trace are:

$$\begin{aligned} \tau &= 3 + g_2^{(2)} g_3^{(2)} + g_1^{(2)} g_3^{(1)} + g_1^{(1)} g_2^{(1)} + g_1^{(2)} g_2^{(1)} g_3^{(2)}, \\ \sigma &= 3 + g_2^{(2)} g_3^{(2)} + g_1^{(2)} g_3^{(1)} + g_1^{(1)} g_2^{(1)} - g_1^{(1)} g_2^{(2)} g_3^{(1)}, \end{aligned}$$

where $^{(i)}$ means the derivatives with respect to the $i$th position, $i = 1, 2$. If we write $g_3(x, y) = \varepsilon P(x, y)$, where $P(x, y)$ is a zero-average periodic function with $\|P\| = 1$, the condition $g_3(x, y) = \varepsilon P(x, y) = n$ only makes sense once $\varepsilon \geq |n|$. Again, the equality $\varepsilon = |n|$ is attained at extrema of $g_3$. Hence $g_3^{(1)} = g_3^{(2)} = 0$ at the birth of accelerator mode orbits, and then $\tau = \sigma = 3 + g_1^{(1)} g_2^{(1)}$. The configuration of the multipliers is on the saddle node line $\lambda_1 = 1$, so that $\lambda_2 \lambda_3 = 1$, as well. In practice, we are going to consider that, at $\varepsilon = |n|$, $g_1^{(1)} g_2^{(1)} = 0$, so a local parameter $\kappa = \varepsilon - |n|$ unfolds a Hopf-Saddle-Node bifurcation, see Chap. 5.

## 1.4 Objective and structure of the thesis

The main goal of this thesis is to contribute to the knowledge on how does the presence of some regular component affect the dynamics of a chaotic zone. The approach is to analyse the geometry of the phase space by means of the theoretical frameworks available. This is used to construct suitable models to explain the experimental data obtained via long-term and massive simulations. These simulations allow to check the feasibility of the hypotheses made, and to estimate parameters in the models.

Throughout the whole text, special emphasis is made on understanding and describing the geometry of the invariant objects that play a role, and on linking the previous results and predictions to the variation of their geometry as the parameters of the system vary.

More concretely,

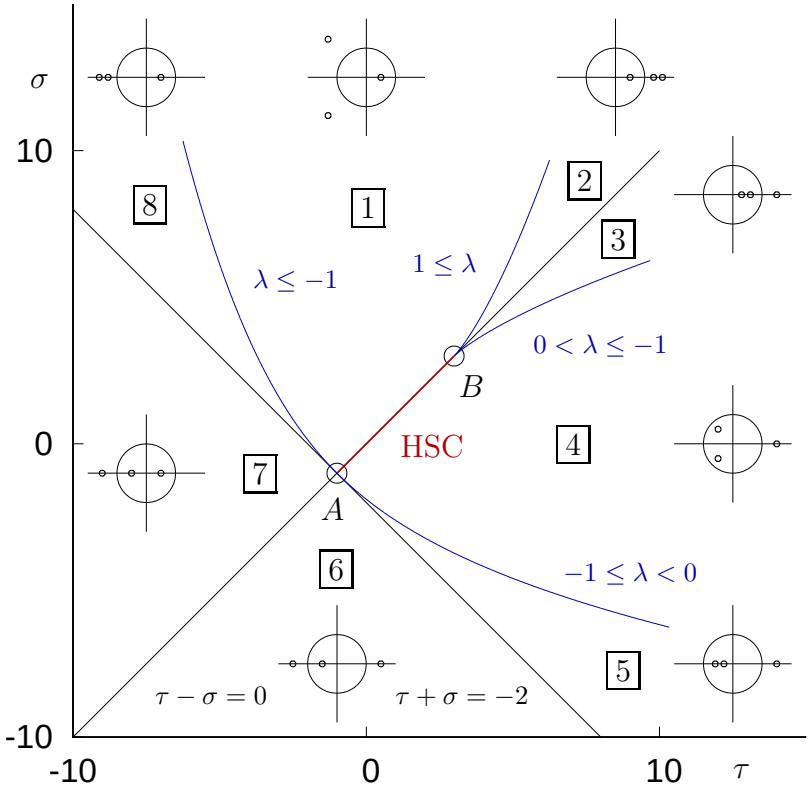


Figure 1.6: General stability diagram of periodic points of volume-preserving 3D maps, see [79]. The highlighted points have coordinates $A = (-1, -1)$ and $B = (3, 3)$. A Hopf-zero bifurcation occurs along the red segment, where $\tau = \sigma \in [-1, 3]$. The blue lines correspond to pairs $\tau, \sigma$ for which two eigenvalues $\lambda_1 = \lambda_2 = \lambda$ (solutions of (1.26)) collide. They are solutions of the algebraic equation $4\tau^3 + 4\sigma^3 - \tau^2\sigma^2 - 18\tau\sigma + 27 = 0$. The lines $\tau - \sigma = 0$ and $\tau + \sigma = -2$ correspond to saddle-node (one of the eigenvalues $\lambda = 1$) and to a period-doubling (one of the eigenvalues $\lambda = -1$) bifurcations, respectively.

1. In the Area-Preserving case, we will

   (a) Describe the most prominent objects of the phase space of the Standard map (1.13) for large values of the parameter $k$, from the point of view of the area that they occupy in the phase space of $\tilde{M}_k$ and also from the point of view of finding adequate models that describe their dynamics in some suitable compact domains containing them.

   (b) Probe the stickiness effect of some of these objects as $k$ varies to detect in which ranges of this parameter this effect is visible. When stickiness is detectable, under the hypotheses suggested by simulations, we give lower bounds on the mean squared displacement of some observable that ensures anomalous diffusion in the standard map.

   (c) This last part motivates to look for explicit quantitative information of transport rates across Cantori in APM. To do so, we will explore also the Standard map, for values $k > k_G$ but close to $k_G$, that is, right after the destruction of the

golden Cantorus. These transport rates will be explained (always giving adequate theoretical models) via the geometry of the zone surrounding this Cantorus, which can be predicted using the Greene-Mackay renormalisation theory. This theory predicts that the mean transport rate across the Cantorus, that we will denote as $\langle N_k \rangle$ in Chap.4, is such that $\langle N_k \rangle \, (k - k_G)^B$, where $B \approx 3$ tends to be 1-periodic as $k \to k_G$ in a suitable logarithmic scale. Despite being predicted, here we give the first evidence of the shape of this periodic behaviour. We also give some insight on the causes of this effect: namely on how it is related to the area $\Delta W$ and to the lobes defined by the invariant manifolds of hyperbolic periodic orbits whose rotation number are consecutive approximants of the golden mean.

2. And in the Volume-Preserving case, we will

   (a) Set up a problem where accelerator modes appear, so that a similar analysis of 1.(a) and 1.(b) above can be performed.

   (b) Select a relevant example and show the rich geometry of the stable region that this case presents. Special emphasis is made on the role each of these objects have on recurrence statistics. It turns out that there can be anomalous diffusion in the action also in this case.

### 1.4.1 Summary of the contents by chapters

Apart from this introductory chapter, the contents of the thesis is splitted among four more chapters. Chapters 2, 3 and 4 deal with the planar case, while chapter 5 deals with the 3D volume preserving case. More specifically,

⋆ In Chap. 2 we start by considering conservative quadratic Hénon maps (both orientation preserving and orientation reversing cases). First, we study the main features of the domain of stability of these two maps, mainly from the point of view of the area that they occupy, and how it does evolve as parameters change. To be as exhaustive as possible, we review the theory that allows to explain what one can observe in the phase space of these maps.

We finish the chapter by considering the Chirikov standard map (1.13) in the 2-torus $\mathbb{T}^2$ for large values of the parameter, $k \geq 1$. The most prominent sources of regular area in this setting are accelerator modes that appear periodically in $k$, and scaled somehow. We give numerical evidence of such a scaling, and guided by the experimental evidence, we derive limit representations for the dynamics in some compact set containing these islands, which turn out to be conjugated to the orientation preserving quadratic Hénon map or conjugated to the square of the orientation reversing quadratic Hénon map.

Some of these islands are the accelerator modes we checked that appeared in Sect. 1.3. This motivates the following chapter.

⋆ Chap. 3 is devoted to study the role of these islands of stability that 'jump' when the standard map is considered in the cylinder. The stability domain of these islands is determined and studied independently from the standard map $M_k$ in Chap. 2, and is recovered in some regions in the phase space of $M_k$ under suitable scalings. We focus in two main observables: the squared mean displacement of the action under

iteration of $M_k$ and the trapping time statistics. We study them both in an adequate range of the parameters, where we can see the effect of considering more and more iterations and the fact that we change parameters and the size of the gaps of a Cantorus change. We provide evidence of the fact that the trapping time statistics behave as the superposition of the effect of two distinctive phenomena: the one of the stickiness, detected as power-law statistics, and the one of the outermost Cantorus, detected as bumps. These bumps change their position in the time axis accordingly to the change of the size of the largest gap in the Cantorus.

First, assuming that the stickiness effect gives rise to power law statistics with a certain value of the exponent, and under some other mild conditions (that also are suggested by the simulations), we are able to give a lower bound on the growth of the mean squared displacement of the actions. This is the way these two phenomena are related to each other in this context.

Then, the fact that we can identify the source of the bumps as being due to the effect of the outermost Cantorus, motivates the topic of the next chapter: studying this effect by its own in a proper context.

⋆ In Chap. 4 we return to the Chirikov standard map, but for values of the parameter close to the destruction of the last RIC, that is, for value of the parameter close but larger than $k_G$ and approaching it from above. In this setting, we study escape rates across this Cantorus, and we deal with this problem from two different points of view.

First, as $k$ decreases to $k_G$. In this setting, it is known that the mean escape ratio across the Cantorus, that we will denote as $\langle N_k \rangle$, behaves essentially as $(k-k_G)^{-B}$, $B \approx 3$. The Greene-MacKay renormalisation theory, and the interpretation of $\Delta W$ as an area justify that, in fact, $\langle N_k \rangle (k - k_G)^B$ should eventually be periodic in a suitable logarithmic scale, as $k \to k_G$. In this chapter we give the first evidence of the shape of this periodic behaviour, and perform a numerical study of a region surrounding the Cantorus that allows to give a first (partial) explanation of it.

Second, we consider a problem related to the previous topic but for each fixed value of $k$: the probability that an orbit crosses the Cantorus in a prescribed time. We explain how to compute these statistics, and we show that in logarithmic scale in the number of iterates, as $k \to k_G$, they seem to behave the same way, but shifted in this log-scale in time.

⋆ Finally, Chap. 5 is devoted to study the stickiness problem in the 3D volume preserving setting. To do so, a map inspired in the Standard map is constructed following the scheme in Sect. 1.3. This map depends on various parameters, one of them, say $\varepsilon$, being a distance-to-integrable one. The map is considered in such a way that

1. Invariant tori subsist until moderate values of $\varepsilon$, and
2. At integer values of the parameter the origin becomes an accelerator mode, and that exactly at integer values it undergoes a Hopf-Saddle-Node bifurcation, giving rise to a stability bubble.

The normal form of the unfolding of this bifurcation justifies that, in fact, there are just two relevant parameters (since it is a co-dimension 2 bifurcation). An analysis inspired in that of Chap. 3 is performed by fixing one of them. Also in this case one can observe

a power law decay of the trapping time statistics, but with slightly different values of the exponent in different ranges of the number of iterates. Preliminary results of more massive simulations seem to indicate that the effect decreases as the number of iterates increases.

# Chapter 2

# From the Hénon conservative map to the Chirikov standard map for large parameter values

In this chapter we present a study of some dynamical properties of orientation-preserving and orientation-reversing quadratic Hénon maps concerning the stability region, the size of the chaotic zones, its evolution with respect to parameters and the splitting of the separatrices of fixed and periodic points plus its role in the preceding aspects.

Then the phase space of the standard map, for large values of the parameter, $k$, is studied. There are some stable orbits which appear periodically in $k$ and that present scalings in a way that depends on $k$. Using this scaling, we show that the dynamics around these stable orbits is the one of above Hénon maps plus some small error, which tends to vanish as $k \to \infty$.

We finish the chapter considering lifts of the Standard map to the cylinder, $M_k$, and studying the dynamics of these stable orbits under $M_k$. This will motivate the study presented in the next chapter.

The content of this chapter is already published in [105].

## 2.1 Introduction

The universal character of the Hénon map (2.1) is well-known since, in particular, it appears as a return map close to a quadratic tangency in the dissipative setting [111, 113]. Later the conservative orientation-preserving Hénon map (2.1) was obtained as a universal return map for quadratic tangencies of conservative maps preserving orientation, see, for instance, [55, 61]. Recently, it has been proved that the orientation-reversing Hénon map also appears as a universal return map in non-orientable cases, either for maps defined in non-orientable manifolds or for hyperbolic points with eigenvalues $\lambda$ and $\mu$ such that $\lambda\mu = -1$, see [62]. On the other hand, in [36] the authors consider non-transversal heteroclinic cycles for reversible maps having symmetric saddle fixed points, and they show that the corresponding return map can be written as the composition of either two orientation-preserving or two orientation-reversing Hénon maps.

In this chapter we investigate both orientation-preserving and orientation-reversing cases. Several properties concerning the stability region, the size of the chaotic zones, the splitting

of separatrices of the fixed/periodic points, etc, are presented in Sections 2.2 and 2.3.

In Section 2.4 we perform an extensive numerical exploration of the relative regular area of the phase space of Chirikov's standard map [26] for large values of the parameter, by means of the computation of Lyapunov exponents. This allows us to detect stable islands appearing periodically in the parameter that show some scaling properties.

In Section 2.5 we analyse the properties of such little islands, which are of period 1, 2 and 4. More concretely, we focus on the renormalisation properties of these islets and we derive suitable limit maps. It turns out that the obtained limit maps correspond to the orientation-preserving Hénon map, the composition of two of these and the composition of two orientation-reversing Hénon maps, respectively. The results obtained fit within the same spirit of previous results in [26, 69].

## 2.2 The Hénon conservative orientation-preserving map

In 1969 M. Hénon [65] started the study of quadratic area preserving maps in $\mathbb{R}^2$. He proved that quadratic maps with constant Jacobian can be reduced to the form

$$F : (x, y) \to (1 - ax^2 + y, bx) \tag{2.1}$$

for some constants $a, b \in \mathbb{R}$, with minors exceptions. If $b = -1$ the map is area and orientation-preserving. If $b = 1$ it is area preserving and orientation-reversing. The case $b = -1$ has a very simple geometric interpretation as the composition of two maps. The first one is $(x, y) \to (x, y + 1 - ax^2)$, one of the so-called "de Jonquières" maps, while the second is just a rotation by an angle of $-\pi/2$.

However, in what follows, we use another representation of the case $b = -1$ given by:

$$HP_c : \begin{pmatrix} x \\ y \end{pmatrix} \to \begin{pmatrix} x + 2y + \frac{c}{2}(1 - (x + y)^2) \\ y + \frac{c}{2}(1 - (x + y)^2) \end{pmatrix}, \tag{2.2}$$

where it is enough to consider $c > 0$. We name it *HP* which stands for Hénon orientation-preserving map. This representation is obtained from a minimal modification of the version given in [134]: $F_c : (x, y) \to (c(1-x^2)+2x+y, -x)$ after the change $(X, Y) = (x-y, x+y)/2$, and renaming $(X, Y)$ as $(x, y)$. The subscript $c$ in these maps is introduced to stress that they depend on this parameter. The map (2.2) has two fixed points. One of them, $H$, is located at $(-1, 0)$ and it is hyperbolic for all $c > 0$. The other one, $E$, located at $(1, 0)$, is elliptic for $0 < c < 2$, parabolic for $c = 2$ and reflection hyperbolic for $c > 2$.

### 2.2.1 Symmetries, reversors, limit flow and rotation number

The inverse map can be expressed as $HP_c^{-1} = S \circ HP_c \circ S$, where $S$ is the symmetry given by $S(x, y) = (x, -y)$. Defining $R = S \circ HP_c$, which is clearly an involution like $S$, we have $HP_c = S \circ R$ and $HP_c^{-1} = R \circ S$. Both $S$ and $R$ are called reversors. We can consider the sets, $\mathrm{Fix}(S)$ and $\mathrm{Fix}(R)$, of fixed points of both reversors, i.e., either points $z = (x, y)$ such that $S(z) = z$ (which are the points with $y = 0$) or points such that $R(z) = z$, which belong to a parabola.

A reversor like $S$ plays an important role to locate periodic points on $\mathrm{Fix}(S)$. If for a point $p \in \mathrm{Fix}(S)$ there exists $m \in \mathbb{N}$ such that $HP_c^m(p) \in \mathrm{Fix}(S)$, then $p$ is periodic, of period $m$ if $p = HP_c^m(p)$ and of period $2m$ if $p \neq HP_c^m(p)$. Furthermore, for any of these

periodic points, if it is hyperbolic, the image under $S$ of the unstable manifold $W^u(p)$ is the stable one $W^s(p)$. Similar properties hold for the reversor $R$.

For a preliminary study of the dynamics of an arbitrary map $F$, provided it is close to the identity map, it is quite useful to look for the existence of some ODE such that the time-1 map associated with the flow gives a good approximation to $F$. In the case of (2.2) this can be done by introducing the new variables $(\xi, \eta) = (x, 2y/\sqrt{c})$. Then, in the $(\xi, \eta)$ variables, $HP_c$ differs from Id by $\mathcal{O}(\sqrt{c})$. A scaling of time also by $\sqrt{c}$ leads to:

$$\frac{d\xi}{dt} = \eta, \quad \frac{d\eta}{dt} = 1 - \xi^2, \tag{2.3}$$

an ODE which is Hamiltonian with $H(\xi, \eta) = \frac{1}{2}\eta^2 - \xi + \frac{1}{3}\xi^3$. The solutions are contained in the level curves of $H$ and the main features are shown in the elementary Figure 2.1 left. It has also $H = (-1, 0)$ and $E = (1, 0)$ as fixed points, of hyperbolic and elliptic type respectively. The level $H^{-1}(2/3)$ contains the separatrix. Points inside the domain bounded by the separatrix belong to a foliation of periodic solutions. In the right side plot we show some confined orbits for $HP_c$, as well as the right branches of the invariant manifolds of the hyperbolic fixed point. They seem to be coincident but, of course, they are not (see Section 2.2.4). For this small value of $c$ the main difference between both plots is the change in the $y$ variable by a factor $\sqrt{c}/2$ when going from the left plot to the right one.

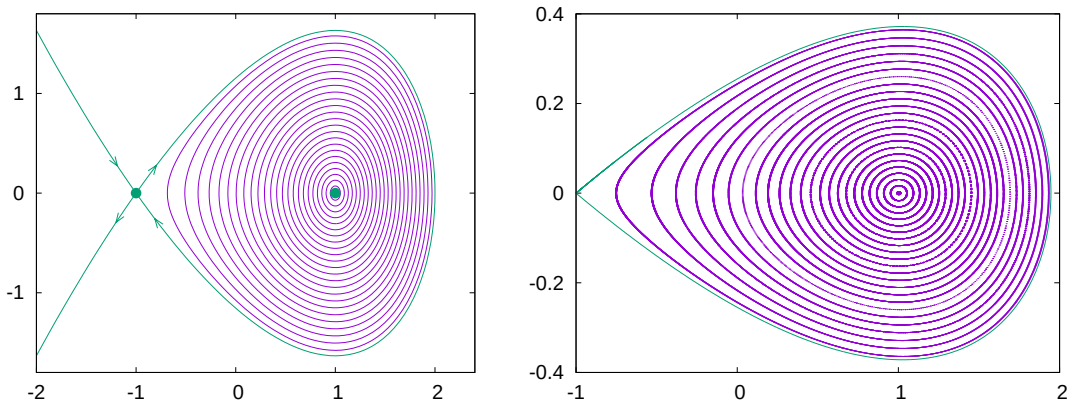


Figure 2.1: Left: the phase portrait of system (2.3). Fixed points are shown in blue, as are the invariant manifolds of the hyperbolic point. The periodic orbits are shown in red. Right: the right branches of the invariant manifolds of the hyperbolic point and (part of) the orbits of several initial points under $HP_c$, for $c = 0.2$.

An extremely relevant parameter is the rotation number (1.4). If we consider the time-$\sqrt{c}$ map associated to the flow, the rotation number corresponding to a periodic orbit of period $T$ is $\rho = \sqrt{c}/T$. It decreases monotonically from $\sqrt{c}/(\sqrt{2}\pi)$ to 0 when going from $E$ to $H$. The values agree very well with the corresponding rotation numbers for $HP_c$, for $c$ small, when $\rho$ is defined, i.e., on the curves invariant under $HP_c$.

For increasing values of $c$ the rotation number, when it is defined, gives a very good information on the dynamical properties. Figure 2.2 tells us about the value of $\rho$ on the $(c, x)$-plane, when the initial point to compute $\rho$ is in $\mathrm{Fix}(S)$, i.e., of the form $(x, 0)$. For the places in white the iteration of an initial point $(x, 0)$, under $HP_c$, leads to escape. In particular, for $c=3/2$, for which value the $E$ point has as eigenvalues $-1/2 \pm \mathrm{i}\sqrt{3}/2$, all other points on the $x$-axis, with $x > -1$, escape (unless they belong to some stable manifold).

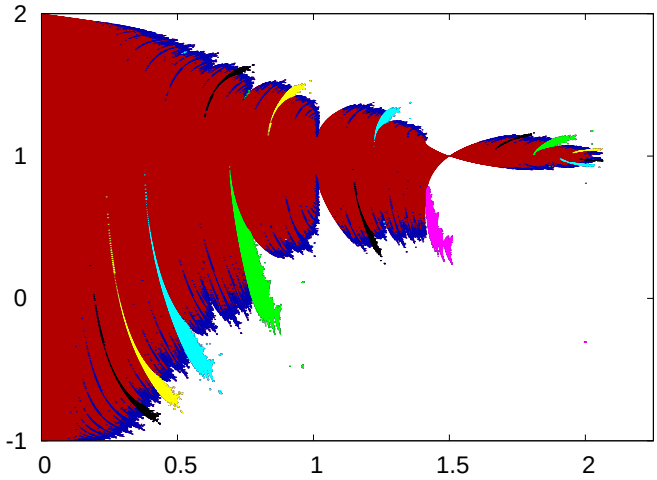


Figure 2.2: The plot shows, as a function of $c$ (horizontal variable), the values of $x$ (vertical variable) for points in Fix($S$) for which $\rho$ has been computed. The dots in red correspond to points for which there is good evidence that $\rho \notin \mathbb{Q}$. For $\rho = m/n$, $n = 3, 5, 9$ and 11 we used magenta, green, pale blue, yellow and black, respectively. Other rational values are shown in blue. See the text for details.

To compute $\rho$ we have used a topological method based on the order of the iterates on the curve, see, e.g., the Appendix in [123]. The tolerance used to stop the computation of $\rho$ is $10^{-10}$. Then, if the value of $\rho$ can be identified, with this tolerance, as a rational $m/n$ with $n < 10^4$, it is decided to consider $\rho \in \mathbb{Q}$ and, hence, they belong to islands with a period equal to the denominator. Otherwise we consider $\rho \notin \mathbb{Q}$. Points in light grey in Figure 2.2 are considered to have $\rho$ irrational. Points with $\rho$ of the form $m/n$, with $n \in \{3, 5, 7, 9, 11\}$ are shown in black, while points with other rational values of $\rho$ are shown in grey. The wedges in black, from left to right, have $\rho = 1/11, 1/9, 1/7, 2/11, 1/5, 2/9, 3/11, 2/7, 1/3, 4/11, 2/5, 3/7, 4/9$ and $5/11$, the last five showing up for $c > 3/2$. We note that all denominators are odd. A similar plot, but taking initial points in Fix($R$) would give even values for $n$, see [133].

We remark that most of the wedges associated with islands reach $x = 1$, but they are extremely narrow; below the pixel resolution. As rational numbers are dense, the light grey domains on the figure have, in fact, a Cantor-like structure. Furthermore, some of the island domains in the figure do not emerge from $x = 1$. They are related to satellites (and satellites of satellites, and so on) of the main islands. In some sense, the structure around each island and around its satellite islands repeats the structure of the full set, as a fractal object. This can be checked by magnifying the black domains in Figure 2.2.

### 2.2.2 Measure of the set of regular and chaotic confined orbits

In Figure 2.3 we show the measure, $\mu(c)$, of the set of bounded orbits as a function of $c$ for the map $HP_c$, as given in (2.2). Note that $\mu(c)$ also includes the measure of chaotic orbits within the island of stability that are bounded due to the existence of invariant curves that confine them. So, $\mu(c)$ is larger than the set of orbits whose Lyapunov exponent can be considered to be zero. We should stress that there are many other more general conservative models (e.g., Hamiltonian systems with two or three degrees of freedom, such as the Restricted Three-Body Problem, or traveling waves of some PDE, such as the Michelson system [129, 42])

which have many features in common with what we display for the Hénon conservative map.

To produce Figure 2.3 we compute the Lyapunov maximal exponent, $\Lambda(p)$, for initial points $p$ and for many values of $c$ and a narrow grid of points. A typical spacing in the coordinates $x$ and $y$ for the grid is 0.0005. In most of the cases we first compute a transient of $10^6$ iterates before starting to compute $\Lambda(p)$. In this way we detect most of the points which escape. A simple escaping criterion follows from the fact that if some forward iterate of $p$ has $x$-component with $x < -1$, it will escape. A number of iterates $m = 10^6$ is also used to produce an estimate of $\Lambda(p)$. If the value obtained is below $2 \times 10^{-5}$, the orbit of $p$ is considered to be regular and, hence, bounded. Otherwise it is considered to be chaotic. In the latter case, we continue with additional iterations (up to $10^8$ and in some cases up to $10^{10}$) to check if we can consider the chaos as confined or if the orbit of $p$ is finally escaping. The measure $\mu(c)$ is the fraction of points in the grid that are detected as regular and confined chaotic times the area of the rectangle where all bounded orbits of $HP_c$ lie.

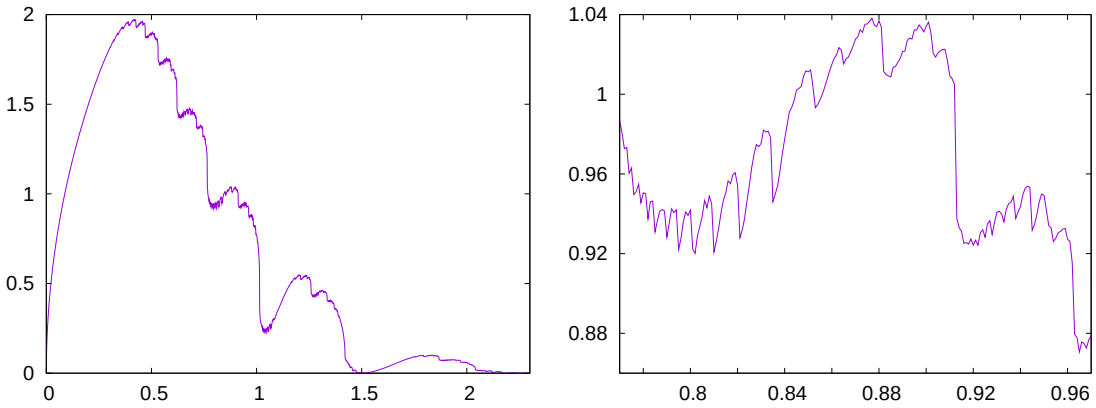


Figure 2.3: Left: measure $\mu(c)$ of the set of confined points as a function of $c$. Right: a magnification in the range $c \in [0.77, 0.97]$ to provide evidence of the self-similar properties of $\mu(c)$.

Note the sudden decrease of $\mu(c)$ at some values of $c$. Going from right to left one can see a first decrease near $c = 1.5$, a fact already mentioned in the discussion after Figure 2.2. The small confined area for $c = 1.5$ is due to the existence of tiny period-3 islands, that at $c = 1.5$ surround a 3-periodic orbit exactly at period-doubling, see [134]. Later on we see a sequence of sudden changes in $\mu(c)$ which correspond to the destruction of all the invariant curves surrounding the islands of periods 4, 5, 6 and so on.

The magnification shown in Figure 2.3, right, provides strong evidence of what happens with islands of a higher period and displays the self-similar properties of $\mu(c)$. As an example, the large jump near $c = 0.91$ corresponds to the breakdown of invariant curves around the islands of rotation number 2/9, while the jump shortly after $c = 0.96$ corresponds to the breakdown of invariant curves around the islands of rotation number 3/13. It is not difficult to identify all the jumps shown in these plots. The reason for the sudden decreases in confined area is that these broken invariant curves used to surround and hence confine some chaotic region, and once these invariant curves are broken, orbits in this region can eventually escape.

Among the points with bounded orbit there are, however, some which display chaotic behaviour. The Lyapunov exponent allows us to detect them. A natural question is, hence, how does the measure of this set change as a function of the value of $c$. This is shown in Figure 2.4. The plot shows quite a sharp change in its behaviour. This is to be expected, because

of the infinitely many chains of islands in the system (there are for any $\rho \in \mathbb{Q} \cap (0, 1/2]$, except for the case $\rho = 1/3$, see Appendix 7 in [5]). Each chain of islands has an associated hyperbolic periodic orbit, the splitting of whose invariant manifolds generates some amount of chaos. It is confined until the invariant curves, that surround these chaotic orbits, break down. Even considering that the computations shown in Figure 2.4 have been done with a $10^{-3}$ step in $c$, a careful examination of the data allows us to detect several hundreds of peaks. See Sections 2.2.3 and 2.2.4 for details on the splitting properties.

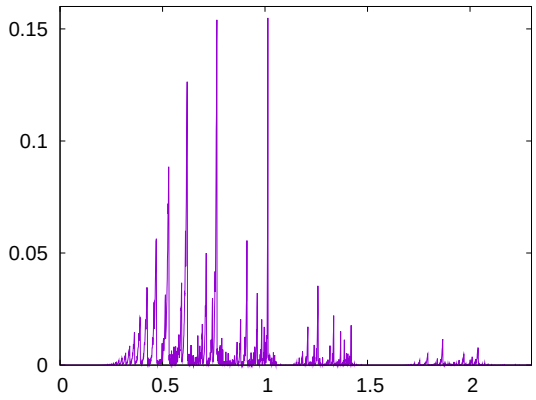


Figure 2.4: Measure of the set of confined points with chaotic dynamics as a function of $c$.

In Figure 2.5 we show three magnifications, computed with step $10^{-4}$ in $c$. They correspond to what happens before the breakdown of the invariant curves around the islands of periods 6, 5 and 4, respectively. For the moment, we do not consider the small jumps on these curves; just a kind of average or, better, a curve fitting the successive minima. For the left plot, for instance, this averaged shape is produced by the change in the size of the chaotic zone created by the homoclinic points associated to the period-6 hyperbolic orbit. But this orbit has been created at $c = c^0_{1/6} = 0.5$, while the destruction of all the invariant curves around the islands of rotation number $\rho = m/n = 1/6$ occurs for a critical value $c_{m/n} = c_{1/6} \approx 0.6204$. Hence, why does it take so long to see that the size of this zone is relevant? The answer will be give in Section 2.2.4. Similar things occur for the other two plots. The respective creation of islands and destruction of all the surrounding invariant curves occur, for period 5, at $c = c^0_{1/5} = 1 - \cos(2\pi/5) \approx 0.690983$ and $c = c_{1/5} \approx 0.7649$, and, for period 4, at $c = c^0_{1/4} = 1$ and $c = c_{1/4} \approx 1.0141$.

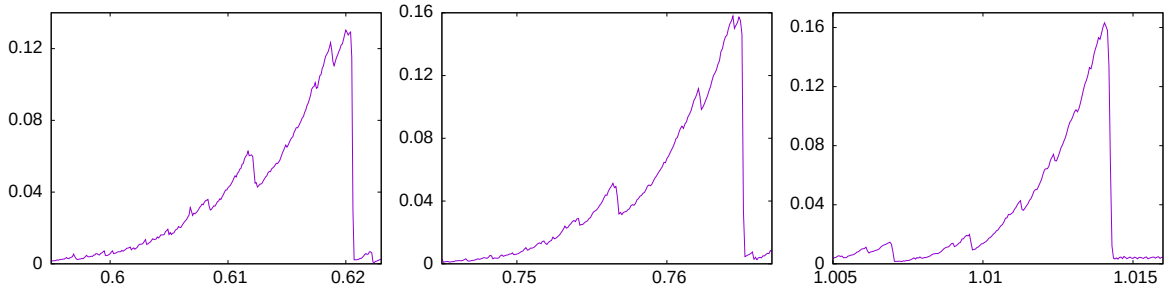


Figure 2.5: Magnification of Figure 2.4 corresponding to the breakdown of the invariant curves which surround the islands of period 6 (left), period 5 (centre) and period 4 (right).

The differences between an averaged behaviour of the rate of increase and the true behaviour in Figure 2.5 is due to the role of other minor islands. For instance, the jump seen

in the left plot shortly after $c = 0.61$ corresponds exactly to the same kind of phenomenon, created by the periodic orbit of rotation number $\rho = 3/19$. The measure of the chaotic zone associated with this periodic orbit has to be added, in some sense, to the largest chaotic zone due to the period-6 orbit.

### 2.2.3 Splitting of the invariant manifolds of the hyperbolic fixed point

For their intrinsic interest and to compare with the behaviour in Section 2.2.4, we shall consider now a measure of the lack of coincidence of the unstable and stable manifolds, $W^u_H, W^s_H$ of the hyperbolic fixed point. As a suitable measure we will use the splitting angle, that is, the angle between the manifolds, computed at the symmetric homoclinic point found on the first intersection with $y = 0, x > 1$. Let us denote the angle as $\sigma(c)$. A useful parameter to present the results is $h(c)$, defined as follows. Let $\lambda(c)$ be the dominant eigenvalue at $H$, which is equal to $1+c+\sqrt{2c+c^2}$ for $HP_c$. Then we define $h(c)$ as $\log(\lambda(c))$. We note that $h(c) = \sqrt{2c} + \mathcal{O}(c)$. If in the limit vector field (2.3) we scale time by an additional factor $\sqrt{2}$ then the map $HP_c$ will be well approximated by the $h(c)$-time map of (2.3). It is easy to check that the separatrix of the flow has the closest singularities to the real axis of the time, located at a distance $\tau = \pi$ of that axis. According to [46, 47], for any $\eta > 0$, there exists $N(\eta)$ such that the splitting angle is bounded by $N(\eta)\exp(-2\pi(\tau-\eta)/h(c))$. This type of result is true for general analytic area preserving maps close to the identity map. Formulas of the form $Ac^B \exp(-\text{ctant}/\lambda(c))$ refer to the dominant part of the splitting function. See [54], and [55] for additional examples.

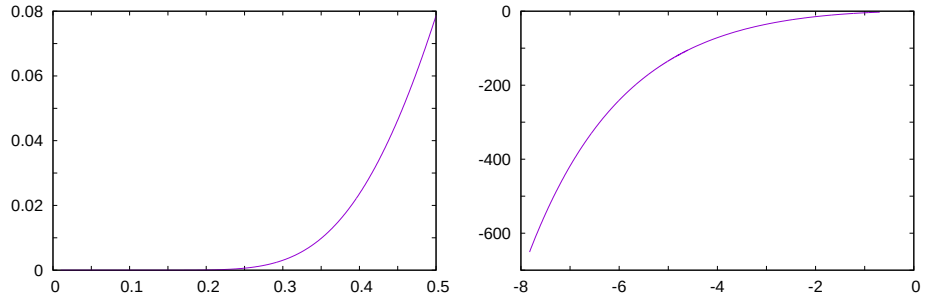


Figure 2.6: Different representations of the splitting angle $\sigma(c)$ between the manifolds at the first intersection with $y = 0, x > 1$. Left: $\sigma$ as a function of $c$, showing that $\sigma$ seems negligible for $c < 0.2$. Right: $\log(\sigma)$ as a function of $\log(c)$, which allows to see how small $\sigma(c)$ is for $c$ approaching zero.

For $HP_c$ we have computed $\sigma(c)$ for many small values of $c$ and the following formula fits the numerically computed data:

$$\sigma(c) = \frac{9}{2} \times 10^6 \pi^2 h(c)^{-8} \exp\left(-\frac{2\pi^2}{h(c)}\right) \times \Omega(h), \tag{2.4}$$

the factor $\Omega(h)$, or correcting factor, being of the form $\omega_0 + \mathcal{O}(h)$. Using a local representation of $W^u_H$ to order 400 and 500 decimal digits in the computations it is possible to compute $\sigma(c)$ and, hence, to derive from (2.4) values of $\Omega(h)$ and to look for a formal expansion in powers of $h^2$: $\Omega(h) = \sum_{m\geq 0} \omega_{2m} h^{2m}$. See more details in [128, 55], but in contrast to [55], in the present case we have computed the splitting angle instead of the homoclinic invariant and

derived the coefficients in $\Omega(h)$ using finite differences instead of polynomial fitting. The package PARI/GP [14] is useful for these simple problems.

As a result, the first digits of $\omega_0$ are 2.489312802936711962506598256012394999704 6 and, furthermore, there is a strong numerical evidence that the formal series is, in fact, a divergent one. However, the related series $\sum_{m\geq 0}\omega_m h^{2m}/(2m)!$ (i.e., the Borel transform of $\Omega(h)$) seems to be convergent. In Figure 2.7, left, we plot $\log_{10}(\omega_{2m}(2\pi^2)^{2m}/(2m+6)!)$ as a function of $m$ up to $m = 375$, i.e., up to the power $h^{750}$. The values seem to tend to a constant, a strong evidence of the Gevrey-1 character of $\Omega(h)$ and of the fact that its Borel transform seems to have radius of convergence equal to $2\pi^2$. If we assume that, despite the divergent character of $\Omega(h)$, a good approximation is obtained for small $h$, if we truncate the expansion at the smallest term (in absolute value), the relative errors are shown in Figure 2.7, right. They are acceptably small, even for $h = 1$.

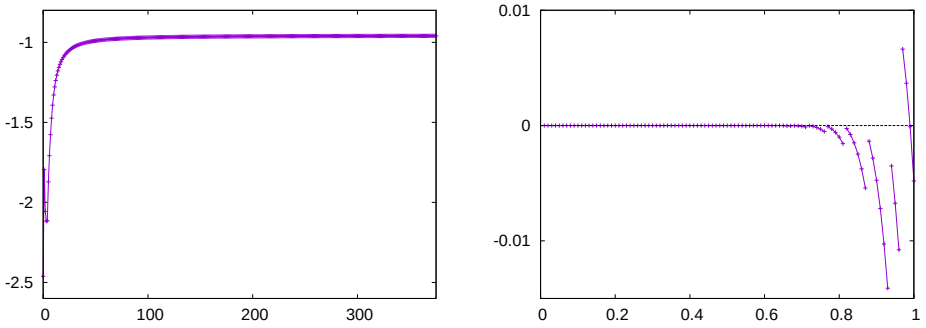


Figure 2.7: Left: $\log_{10}(\omega_{2m}(2\pi^2)^{2m}/(2m+6)!)$ as a function of $m$, which gives evidence of the Gevrey-1 character of $\Omega(h)$. Right: the relative errors $\Omega_{tr}(h)/\Omega(h) - 1$ as a function of $h$, with step 0.01, where $\Omega_{tr}(h)$ denotes the formal power series truncated at its smallest term, $m = m^*$. Note that this is achieved for different $m^* = m^*(h)$ depending on the value of $h$. The different pieces shown, from right to left, correspond to values of $m^*(h)$ equal to $4, 5, 6, \ldots$.

If we compare the left plot in Figure 2.3 with Figure 2.5 we check that up to $c = 0.35$ the behaviour of $\mu(c)$ just follows from the measure of the domain bounded by the separatrix in Figure 2.1 and the change of scale. It is proportional to $\sqrt{c}$. No sign of the effect of the splitting seen on Figure 2.6 shows up. But this has to be expected, because all the points with chaotic orbits created by the splitting of $W_H^{u,s}$ escape to infinity. In contrast, recall the case of the standard map, where there is no escape. In Fig. 1.2 we compared the relative measure of the set of chaotic points and a multiple of the splitting angle of the invariant manifolds of the origin, and the agreement was very good, even for relatively large values of the parameter.

### 2.2.4 Splitting of the invariant manifolds of periodic hyperbolic points

Consider a map $F$ having an elliptic fixed point $E_0$. Under generic conditions there is a domain of stability $D$ surrounding $E_0$. Inside $D$ the phase space has different Birkhoff resonant chains of islands of stability, located in an annular domain around $E_0$. Generically, these stability islands have a pendulum-like phase space structure formed by the invariant manifolds of the hyperbolic periodic points. Hence, for a concrete island, one can consider two "main" splittings of separatrices, geometrically related to the upper and lower separatrices of

the classical pendulum. We refer to the inner/outer splittings according to the distance to $E_0$ of the separatrices of the pendulum structure. It turns out that both splittings are generically different, being the outer one the largest [134]. Hence, the size of the confined chaotic zone is expected to grow, essentially, proportionally to the outer splitting of the separatrices of the main chain of islands inside the stability domain. And the distance between the main island of stability and the satellite stability islands is expected to behave also proportionally to the amplitude of the inner splitting. So, it has to be taken into account when dealing with transport rates and the stickiness effect.

In Figure 2.8 we show the behaviour of the outer splitting of separatrices of the islands with $\rho = 1/6$, $1/5$ and $1/4$ as the parameter $c$ of the Hénon map (2.2) changes. Consider that the periodic orbit with rotation number $\rho$ is created at the value $c = c_\rho^0$ (see Section 2.2.2). The fact that the invariant manifolds do not coincide creates a bounded chaotic region around the islands. However, the splitting of separatrices behaves in an exponentially small way in (maybe a power of) $\nu = c - c_\rho^0$. This means that the size of the splitting becomes large enough to be observable for relatively large values of $\nu$. Then, the effect of the chaotic zone around the island of rotation number $\rho$ contributes in a significant way to the total size of the confined chaotic region only for $\nu$ values for which the splitting can be observed. The Figure 2.8 shows the value of the splitting, for period 6, 5 and 4, from left to right, starting at the creation of the periodic island. Note the agreement with the Figure 2.5. The values of $c$ at which the splitting starts to be seen in Figure 2.8 agree very well with the ranges shown in Figure 2.5.

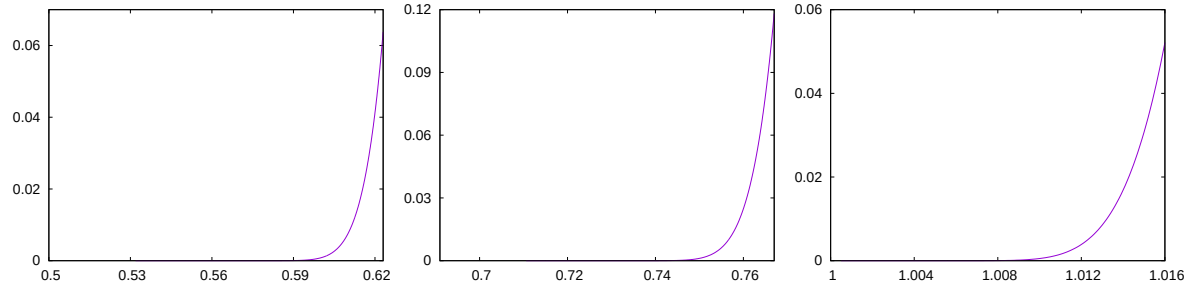


Figure 2.8: Behaviour of the outer splitting of the separatrices of the islands of period 6 (left), period 5 (centre) and period 4 (right). Compare with Figure 2.5.

The fact that the range in $c$, from the creation of the periodic islands of a given rotation number $\rho$, at $c = c_\rho^0$, till the destruction of the surrounding invariant curves, at $c = c_\rho$, becomes shorter when $\rho$ increases (as observed in Figure 2.8 for $\rho = 1/6, 1/5$ and $1/4$) has an easy explanation. The islands travel "faster" across the confined domain around the point $E$ because, when increasing $c$, the twist condition becomes weaker. A simple computation of the normal form around $E$ shows that $\rho$ changes from having the maximum at $E$ to have a local minimum at $E$ for $c = 5/4$.

### 2.2.5 The mechanism of destruction of invariant curves and the associated Cantor sets

The destruction of invariant curves can be seen, from an analytical point of view, as the lack of convergence of the sequence of iterations to obtain a conjugation between the dynamics on a candidate to be an invariant curve and a rigid rotation, with Diophantine rotation

number, in $\mathbb{S}^1$, following the KAM approach (see e.g. [6]). There are also criteria based on the blow-up of Sobolev norms of the hull functions, see [22].

Another approach, from a geometrical point of view, is the obstruction method [112]. We will illustrate this last approach with an example. The invariant curves surrounding period-6 islands are destroyed for $c = c_{1/6} \approx 0.6204$, as said in Section 2.2.2. In Figure 2.9 some orbits are shown. The period-6 islands would be found to the right of the displayed orbits.

In the left plot, to improve visibility, we skip some of the invariant curves around the elliptic periodic orbits of rotation number 3/19 (with one point on $y = 0$) and 4/25 (without points on $y = 0$ in the displayed domain). Beyond many other chains of little islands, some invariant curves (according to the value of the rotation number, using the criterion explained in Section 2.2.1) are found passing close to the point $(-0.138, 0)$. In the right plot one can see again the islands of rotation numbers 3/19 and 4/25. Furthermore, the large dots on the plot show the location of some of the points in the related periodic hyperbolic orbits (with the same rotation numbers than the elliptic ones). We also show part of the manifolds of these hyperbolic periodic orbits. On the points shown the unstable manifolds leave the points with positive slope. It is easy to see that $W^u_{3/19}$ (blue) intersects $W^s_{4/25}$ (green) (and, symmetrically, $W^s_{3/19}$ (magenta) intersects $W^u_{4/25}$ (red)). Hence, due to these heteroclinic intersections, there is no room for invariant curves with $\rho \in (3/19, 4/25)$.

A description of the destruction of invariant curves can also be found in [131].

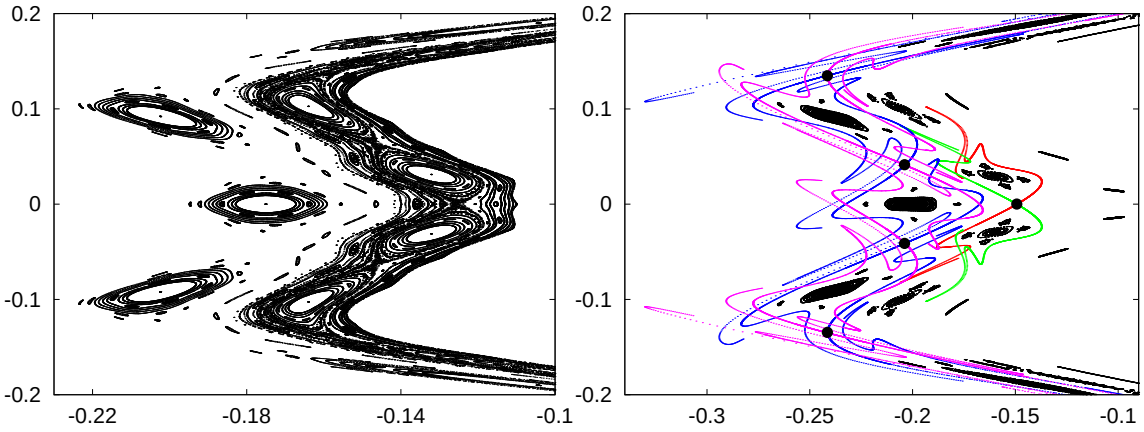


Figure 2.9: Several relevant orbits on the left part of the period-6 islands for values close to the destruction of the invariant curves around these islands. Left: Plot for $c = 0.618 < c_{1/6}$. Right: Plot for $c = 0.63 > c_{1/6}$. The colored manifolds are $W^u_{4/25}, W^s_{4/25}, W^u_{3/19}$ and $W^s_{3/19}$ in red, green, blue and magenta, respectively. See the text for details.

It can seem strange that we must go to $c = 0.63$ to discover the existence of these heteroclinic intersections, while we claimed before that the destruction has been found for $c = c_{1/6} \approx 0.6204$. Plots similar to Figure 2.9, right, for $c = 0.625$ or $c = 0.628$ do not provide evidence of the existence of heteroclinic points. The reasons of this are simple:

1) The arc length of the part of the manifolds shown in the figure is short. Much longer parts will show heteroclinic points for values slightly larger than 0.6204.

2) Beyond the hyperbolic periodic orbits with $\rho = 3/19, 4/25$ there are infinitely many other hyperbolic periodic orbits with intermediate values of $\rho$. It would be possible to find a long chain of heteroclinic connections between the ones we consider here.

The "gaps" produced by the heteroclinic intersections on the candidate to invariant object are the responsible for its Cantor-like structure. Therefore, the points with chaotic dynamics that were confined when the invariant curve still existed, can escape when the curve is destroyed and it is replaced by a Cantor set. If the gaps of that set are rather small, however, it will take a long time for the iterates to find their way to escape. We will deal with this problem in Chap. 4.

### 2.2.6 Explaining the birth and death of islands

In the previous subsections we presented some elements which allow to have a fairly good understanding of the changes in the measure of the set of confined points under iteration by $HP_c$. We give here the main items concerning the fate of the islands.

1) For small values of $c$ the map $HP_c$ has a dynamics quite similar to the flow (2.3). The measure of the confined orbits is very close to the measure in the case of (2.3), scaled by $\sqrt{c}/2$. Periodic orbits of rotation number $\rho \in \mathbb{Q}$ and the corresponding islands are born at $E$ for $c = c_\rho^0 = 1 - \cos(2\pi\rho)$ and travel away from $E$ when increasing $c$.

2) Simultaneously the hyperbolic periodic orbits with the same $\rho$ go also away from $E$, the splitting $\sigma_\rho(c)$ of their manifolds creates first tiny chaotic domains which, later on, increase with $c$ as $\sigma_\rho(c)$ increases. Finally the invariant curves surrounding the islands of a given $\rho$ are destroyed due to the existence of heteroclinic intersections of the manifolds of hyperbolic periodic orbits of slightly smaller $\rho$ and the confined chaotic domains can escape. The islands still exist for a while, until their central elliptic point becomes reflection hyperbolic.

3) For larger values of $c$ the mechanism of creation of islands is different. The value of $\rho$ at $E$ is a local minimum for $c > 5/4$. Then, periodic orbits of a given $\rho$ are created in pairs (two of elliptic type and two of hyperbolic type) near some place, away from $E$, close to a local maximum of the rotation number. This is related to the loss of the twist condition for a nearby integrable model and to the creation of the so-called meandering curves, see, e.g., [127]. When $c$ increases, one of the periodic islands approaches $E$ and the other approaches the boundary of the domain of confined orbits. As an example, for $\rho = 4/13$ the couple of periodic islands is created for $c \approx 1.345$. One of them ends at $E$ for $c \approx 1.3546$, while the other has surrounding invariant curves until $c \approx 1.369$ and, finally, the island is destroyed near $c = 1.391$.

To see the evolution of the set of confined orbits as a function of $c$, details on the evolution of an island and on the changes in the set of chaotic confined orbits the reader can have a look at some movies, available in `http://www.maia.ub.es/dsg/QuadraticAPM`.

## 2.3 The Hénon conservative orientation-reversing map

For our purposes, to study the islands in the standard map, it is also relevant to consider the Hénon conservative map, but with orientation-reversing, $HR_c$, which is given (using a setting similar to the one in (2.2)) by

$$HR_c \begin{pmatrix} x \\ y \end{pmatrix} \to \begin{pmatrix} x + \frac{c}{2}(1 - (x-y)^2) \\ -y - \frac{c}{2}(1 - (x-y)^2) \end{pmatrix}, \tag{2.5}$$

where, again, it is enough to consider $c > 0$. We name it $HR$ which stands for Hénon conservative-reversing map. It has two fixed points, $H_\pm$, located at $(\pm 1, 0)$, hyperbolic for all $c$. Because of the orientation-reversing character, they have a positive and a negative eigenvalue, given by $\lambda^u_\pm = \mp c \mp \sqrt{c^2+1}$, $\lambda^s_\pm = \mp c \pm \sqrt{c^2+1}$. Note that the absolute value of the unstable eigenvalues, coincides. Furthermore, it has a period-2 periodic orbit, whose points $E_\pm$ are located at $(0, \pm 1)$. They are elliptic for $c \in (0, 1)$, with limit rotation number $\rho(c) = \cos^{-1}(1 - 2c^2)/(2\pi)$, parabolic for $c = 1$ and reflection hyperbolic for $c > 1$.

The map $HR_c$ has a reversor $\hat{S}$, defined by $\hat{S}(x, y) = (-x, y)$ and, hence, an additional reversor $\hat{R} = \hat{S} \circ HR_c$. Both of them are involutions and satisfy similar properties to the $HP_c$ case. In particular $\hat{S} \circ HR_c \circ \hat{S} = HR_c^{-1}$, quite useful to obtain stable manifolds from unstable ones.

The square of the map can be approximated by a limit flow. No scaling of the variables is needed now. Only a scaling of time by a factor $2c$. The reason to select this scaling will be given later. Letting $c$ go to zero we obtain the limit flow

$$\frac{dx}{dt} = \frac{1}{2}(1 - x^2 - y^2), \quad \frac{dy}{dt} = xy, \tag{2.6}$$

whose Hamiltonian is $H = y(1 - x^2 - y^2/3)/2$. The separatrices are given by $y = 0$ and $1 - x^2 - y^2/3 = 0$. It is immediate to check that the separatrix going from $x = -1$ to $x = 1$ on $y = 0$ has a singularity for $t = \mathrm{i}\pi$, while the other separatrices, upper and lower, going from $(1, 0)$ to $(-1, 0)$ along $x^2 + y^2/3 = 1$, with extremal values $|y| = \sqrt{3}$, have singularities for $t = \mathrm{i}\pi/2$. The Figure 2.10 shows the flow of (2.6) and several iterates of $HR_c$ for $c = 0.2$. In the right part of the figure, the upper points (on top of what seems to be a connection between the saddles, close to $y = 0$) are mapped by $HR_c$ to the lower ones, and reciprocally. As in the case of $HP_c$, shown in Figure 2.1, for small $c$ the dynamics of the map is rather close to the one of the flow. No trace of chaotic behaviour is seen at the resolution level of the plot.

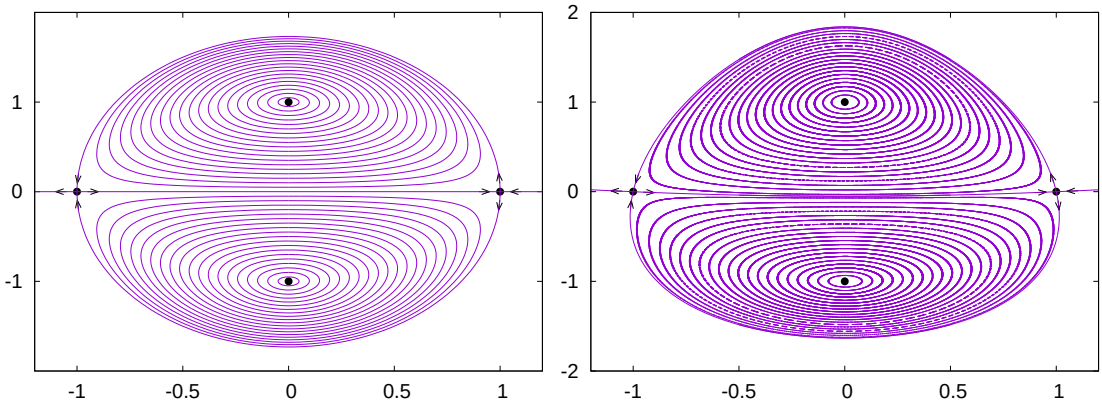


Figure 2.10: Left: Phase portrait of the limit flow given by (2.6). Right: Some orbits of $HR_c$ for $c = 0.2$, which seem to correspond to an integrable map. The invariant manifolds of the hyperbolic fixed points $H_\pm$ seem to be coincident.

However, there exist transversal heteroclinic points in $W^u_{H_-} \cap W^s_{H_+}$ (near the line $y = 0$) and in the upper and lower branches of $W^u_{H_+} \cap W^s_{H_-}$. Due to the symmetry $\hat{S}$ it is easy to locate these points on $x = 0$. In Figure 2.11 we use as parameter $h(c) = \log((\lambda^u_-)^2) = 2\log(c + \sqrt{c^2+1}) = 2c + \mathcal{O}(c^2)$. The reason to use the square is the fact that we are doing

the computations with the map $HR_c^2$. Furthermore, the fact that the dominant term in $h(c)$ is $2c$ is what justifies the time scaling done to obtain (2.6).

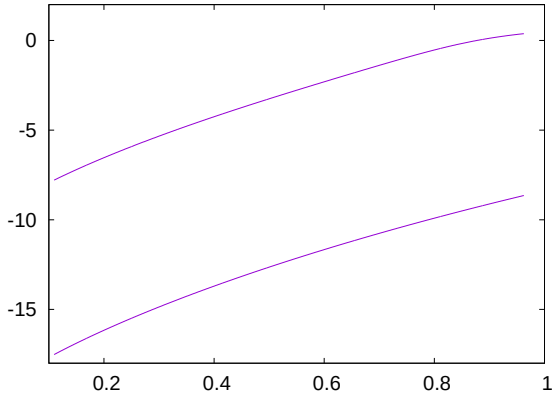


Figure 2.11: Values of the splitting angle for the separatrices in the case of $HR_c$. Here we plot $\log(\sigma(c))h(c)$ as a function of $h(c)$. The upper curve corresponds to the separatrix in the upper part of Figure 2.10, right, and the lower one to the separatrix near $y = 0$. For the separatrix in the lower part of Figure 2.10, right, the values are close to the ones in the upper part. See the text for details.

The splitting of the invariant manifolds has been measured by computing the splitting angle $\sigma(c)$ on $x = 0$, both at the heteroclinic point in $W^u_{H_-} \cap W^s_{H_+}$, that we denote as $\sigma_0(c)$, and at the one in the upper branches of $W^u_{H_+} \cap W^s_{H_-}$, that we denote as $\sigma_+(c)$. Assuming a behaviour similar to the one in (2.4), i.e., of the form $\sigma(h) = Ah^B \exp(-C/h)(1 + \mathcal{O}(h))$, for suitable constants $A, B, C$, suggests to plot $\log(\sigma(c))h(c)$ as a function of $h(c)$. This is done in Figure 2.11, the upper curve corresponding to $\sigma_+(c)$ and the lower one to $\sigma_0(c)$. A fit of the data gives values for the constant $C$ in the exponential term which clearly tend to $\pi^2$ and $2\pi^2$, when the data used are restricted to domains in the left part of the plot (i.e., smaller values of $h(c)$). This is in perfect agreement with the location of the singularities of the separatrices of the vector field in (2.6).

Finally, as we did in the $HP_c$ case in Section 2.2.2, we plot a measure of the set of confined points as a function of $c$ in Figure 2.12. One can check that the limit value, for $c \to 0$, is $\pi\sqrt{3}$, in agreement with the flow case in Figure 2.10, left. For $c = \sqrt{3}/2$, corresponding to elliptic fixed points with limit rotation number $1/3$, the measure goes to zero. It is easy to detect jumps near $c = 0.709, 0.608, 0.538, 0.487, \ldots$, corresponding to the destruction of invariant curves surrounding the islands of period $4, 5, 6, 7, \ldots$, respectively, under $HR_c^2$, both in the upper and lower part.

The behaviour of the measure of the set of confined chaotic points, the mechanism of destruction of invariant curves, etc, under the map $HR_c^2$ are similar to the ones described for $HP_c$.

## 2.4 The standard map for large parameter values

In this Section we consider Chirikov's standard map (1.13) in the 2-torus $\mathbb{T}^2$, $\tilde{M}_k$. As commented in Sect. 1.2, for large enough values of $k$ one would expect the chaotic sea to fill the whole phase space. When dealing with the problem of the relative measure of the stochastic zone, Chirikov and Izraelev in [28] and [26] proved the existence of some special

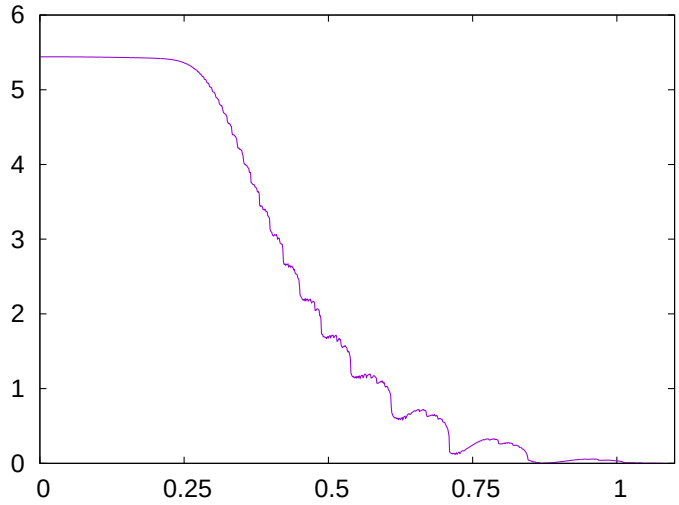


Figure 2.12: Measure of the set of confined points for $HR_c$ as a function of $c$.

stable fixed points and 2-periodic orbits in the torus $\mathbb{T}^2$ appearing near integer values of $k$, named by them as *islets of stability*. They also suggested that such orbits should scale both in area as $1/k^2$ and in the range of the parameter where they existed as $1/k$.

In Section 2.4.1 we give numerical evidence of the fact that these islets appear to be the largest islands in the phase space for large enough $k$, and that such scalings hold. Moreover, a similar structure is observed near half-integer values of the parameter, with similar scaling properties.

### 2.4.1 Measure of the set of regular points

In order to detect some regular area in the phase space of the standard map $\tilde{M}_k$, we have computed on a fine grid (typically with step $5 \times 10^{-5}$ both in $x$ and $y$) the measure of the set of points in the phase space which are regular, the ones for which we can consider the Lyapunov exponent to be zero [126] as a function of the parameter $k$, say $A_r(k)$. Note that it is a lower bound on the total regular area, since one could find other islands, islands below the pixel size, or even below the machine precision used. See [132] and [136].

In Figure 2.13 one can see the regular area of $\tilde{M}_k$ as a function of $k$ in the range $k \in [1.75, 10.75]$. In this figure one observes that the area seems to vanish everywhere but near integer and half-integer values of $k$, where some peaks show up. Moreover, the non-vanishing area seems to decrease as a negative power of $k$. The same seems to happen concerning the range in the parameter where these peaks appear.

In fact, it is easy to check that $\tilde{M}_k$ has, when considered on $\mathbb{T}^2$, the following remarkable orbits:

- If $k = n \in \mathbb{Z}$ it has 4 fixed points on the line $y = 0$: $x = 0, 1/2$ are hyperbolic and reflection hyperbolic respectively, and $x = 1/4, 3/4$ are unstable parabolic. In fact they are on an elliptic-hyperbolic (EH) bifurcation, where a fixed hyperbolic and a fixed elliptic point are born. These four fixed points and the two which are born at integer values of $k$ lie on $y = 0$ as $k$ varies. It also has a 2-periodic parabolic orbit at $(1/4, 1/2) \leftrightarrow (3/4, 1/2)$ at a period-doubling (PD) bifurcation. These points lie on symmetry lines of $\tilde{M}_k$ (see [63]), $y = 2x$ and $y = 2x - 1$ respectively.

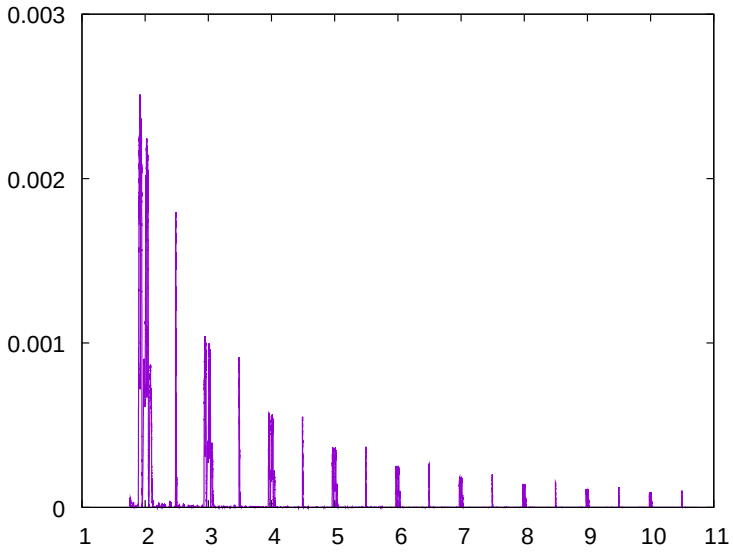


Figure 2.13: Relative measure $A_r(k)$ in the phase space of $\tilde{M}_k$ of the number of points with zero Lyapunov exponent as a function of the parameter $k = 1.75(0.00005)10.75$.

Let us denote these points as $p_1^1 = (1/4, 0)$, $p_1^2 = (3/4, 0)$ and $p_2 = (1/4, 1/2)$ when dealing with $k$ near integer. The subscript denotes the period.

- If $k = m+1/2$, $m \in \mathbb{Z}$ the map $\tilde{M}_k$ has a parabolic 4-periodic orbit at a PD bifurcation $(1/4, 1/2) \to (1/4, 0) \to (3/4, 1/2) \to (3/4, 0)$. The points on $y = 1/2$ lie on $y = 2x$ as $k$ evolves, and the other two points remain on $y = 0$.

  Let us denote $p_4 = (1/4, 1/2)$ when dealing with $k$ near to half-integer. Again the subscript denotes the period.

**Remark 2.** *Near half-integer values of $k$, there is another stable 4-periodic orbit of $\tilde{M}_k$ near $p_4$, but contrary to this last, its position in the phase space depends on the value of $k$. In Section 2.5.1 we are going to justify that, due to a symmetry, the structure and evolution of such orbit can be obtained directly from the study of the dynamics around $p_4$.*

Concerning the parameter, numerical continuation of some of these orbits suggests that the range in $k$ where the islands evolves scales as $1/k$, as predicted by Chirikov [26]. Namely,

- the island around $p_2$ is born at $k \approx n - 2/(n\pi^2)$, in an EH bifurcation, and passes through PD at $k = n$, $n \in \mathbb{Z}$,
- the islands of $p_1^{1,2}$ are born simultaneously at $k = n$ and have their PD at $k \approx n + 2/(n\pi^2)$, $n \in \mathbb{Z}$, and
- all islands of the orbit of $p_4$ are born at $k \approx m+1/2-1/(2\pi^2(m+1/2))$ where they have a degenerate saddle-centre bifurcation (see [136]), also referred as '0–4'-bifurcation in [36]), and have their PD at $k = m + 1/2$, $m \in \mathbb{Z}$.

All these items are summarized in Table 2.1.

In Figure 2.14 we have plotted magnifications near such values and we have superimposed them scaled as we have just suggested: we have plotted $n^2 A_r(k)$ as a function of $n(k - n)$, where $n$ is integer or half-integer. These plots show that these islands scale as predicted, and

| | **Position** | **Period** | $k$**-EH** | $k$**-PD** |
|---|---|---|---|---|
| $n \in \mathbb{Z}$ | $p_1^1 = (1/4, 0)$ | 1 | $n \star$ | $n + 2/(n\pi^2)$ |
| | $p_1^2 = (3/4, 0)$ | 1 | $n \star$ | $n + 2/(n\pi^2)$ |
| | $p_2 = (1/4, 1/2)$ $(3/4, 1/2)$ | 2 | $n - 2/(n\pi^2)$ | $n \star$ |
| $n' \in \mathbb{Z} + 1/2$ | $p_4 = (1/4, 1/2)$ $(1/4, 0)$ $(3/4, 1/2)$ $(3/4, 0)$ | 4 | $n' - 1/(2n'\pi^2)$ | $n' \star$ |

Table 2.1: Position, period and values of the parameter for which the orbits have elliptic-hyperbolic bifurcation (EH) and period-doubling bifurcation (PD). The inputs in the table labelled with $\star$ mean that it happens exactly at these particular values of $k$.

the larger is $k$, the better these scalings fit. This suggests the existence of a limit behaviour for $k \to \infty$, which is the contents of Section 2.5.

In the left plot in Figure 2.14 one can see that the fixed points and the 2-periodic orbit coexist in some range of the parameter close to integer, and that the evolution seems to repeat. This is to be clarified in Section 2.5.1. Moreover, a rougher version of each of them was previously computed by Karney et al. in [69], where the author study the effect of these islands in the overall diffusion of the standard map in the presence of noise.

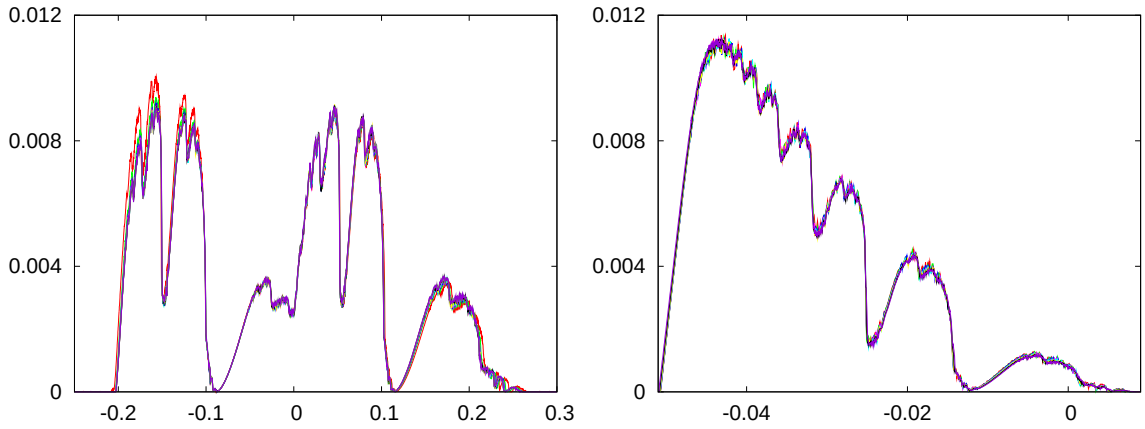


Figure 2.14: Superimposed scaled areas $n^2 A_r(k)$ as a function of the scaled parameter $n(k-n)$ near: Left: $n = 2, 3, \ldots, 10$. Right: $n = 2.5, 3.5, \ldots, 10.5$.

## 2.5 Relating the islands in the standard map to the Hénon map

The numerical results of the previous section suggest that the islands appearing near each integer and half-integer value of $k$ for $\tilde{M}_k$ (1.13) scale in the $x$ and $y$ variables, and in the range of the parameter $k$ where they subsist as $1/k$, and that this scaling becomes more exact as $k$ increases. In contrast with usual cases where the limit map is derived from a return map including a passage of the orbits near a homoclinic tangency, see, e.g., [111], now

it is obtained directly: no points of the relevant orbits come close to any saddle of the initial map.

In Section 2.5.1 we prove the existence of a limit behaviour of the dynamics around $p_1^{1,2}, p_2$ and $p_4$ as $k \to \infty$, and that such limits are, in fact, Hénon maps with a suitable reparametrisation. In Section 2.5.2 we compare the numerical results for the Hénon map given in Sections 2.2.2 and 2.3 and the ones in Section 2.4.1 for the standard map, using the scalings of Proposition 1.

### 2.5.1 Theoretical results

The contents of this subsection is summarized in the following

**Proposition 1.** *There exist a limit behaviour of the dynamics around $p_1^{1,2}$ and $p_2$ (resp. $p_4$) under scalings in $x, y$ and $k$ by $1/n$ for $n \in \mathbb{Z}$ (resp. $n - 0.5 \in \mathbb{Z}$). Moreover, these limit maps are conjugated to area preserving orientation-preserving (resp. composition of two or more orientation-reversing) Hénon maps, depending on a suitably scaled parameter.*

#### Proof of proposition 1 part I: Limit maps

In this subsection we derive limit maps for the dynamics around $p_1^{1,2}, p_2$ and $p_4$ by expanding $\tilde{M}_k^\nu$ (after a suitable scaling) in Taylor series around each $p_\nu$, where $\nu$ denotes its period. The symmetries of the standard map are used to reduce computations and to simplify the limit maps, but in any case one can obtain them without its aid. Let us introduce

$$E : \begin{pmatrix} x \\ y \end{pmatrix} \mapsto \begin{pmatrix} n^* x \\ n^* y \end{pmatrix},$$

where we will set $n^* = n \in \mathbb{Z}$ for $\nu = 1, 2$ and $n^* = m + 1/2, m \in \mathbb{Z}$ for $\nu = 4$. Consider also the translation and central symmetry

$$T_{(x_0,y_0)} : \begin{pmatrix} x \\ y \end{pmatrix} \mapsto \begin{pmatrix} x - x_0 \\ y - y_0 \end{pmatrix}, \quad S : \begin{pmatrix} x \\ y \end{pmatrix} \mapsto \begin{pmatrix} -x \\ -y \end{pmatrix}.$$

Let us start with $k$ close to $n \in \mathbb{Z}$ and set $n^* = n$. Consider a new parameter $k' = n(k-n)$, which controls the scaled distance to the closest integer.

1. Near $p_1^1 = (1/4, 0)$, consider the change of variables

$$L_1 = E \circ T_{(1/4,0)} \circ \tilde{M}_k \circ T_{(1/4,0)}^{-1} \circ E^{-1}.$$

This gives

$$\begin{aligned}
\begin{pmatrix} x \\ y \end{pmatrix} &\overset{\text{(i)}}{\mapsto} \begin{pmatrix} x/n + 1/4 \\ y/n \end{pmatrix} \\
&\overset{\text{(ii)}}{\mapsto} \begin{pmatrix} 1/4 + (x+y)/n + (k'/n + n)\sin(2\pi(x/n + 1/4)) \\ y/n + (k'/n + n)\sin(2\pi(x/n + 1/4)) \end{pmatrix} \\
&= \begin{pmatrix} 1/4 + (x + y + k' - 2\pi^2 x^2)/n \\ (y + k' - 2\pi^2 x^2)/n \end{pmatrix} + \mathcal{O}(n^{-3}) \\
&\overset{\text{(iii)}}{\mapsto} \begin{pmatrix} x + y + k' - 2\pi^2 x^2 \\ y + k' - 2\pi^2 x^2 \end{pmatrix} + \mathcal{O}(n^{-2}),
\end{aligned}$$

where (i) is the map $T^{-1}_{(1/4,0)} \circ E^{-1}$, (ii) corresponds to $\tilde{M}_k$ and (iii) is the map $E \circ T_{(1/4,0)}$. Then, near $p_1$ and for $k$ near integer we have the following behaviour:

$$L_1 : \begin{pmatrix} x \\ y \end{pmatrix} \mapsto \begin{pmatrix} \bar{x} \\ \bar{y} \end{pmatrix} = \begin{pmatrix} x + \bar{y} \\ y + k' - 2\pi^2 x^2 \end{pmatrix} + \mathcal{O}(n^{-2}). \tag{2.7}$$

The map around $p_1^2$ is the same as $L_1$, but composed with $S$.

2. Near $p_2 = (1/4, 1/2)$, if we perform the following change of variables

$$L_2 = E \circ T_{(1/4,1/2)} \circ S \circ \tilde{M}_k \circ T^{-1}_{(1/4,1/2)} \circ E^{-1}$$

we obtain

$$L_2 : \begin{pmatrix} x \\ y \end{pmatrix} \mapsto \begin{pmatrix} \bar{x} \\ \bar{y} \end{pmatrix} = \begin{pmatrix} -x + \bar{y} \\ -y - k' + 2\pi^2 x^2 \end{pmatrix} + \mathcal{O}(n^{-2}).$$

Here we have taken $S \circ \tilde{M}_k$ instead of $\tilde{M}_k^2$. This fact allows us to deal with a quadratic map instead of a quartic one. To obtain this expression one has to mimic the previous computation of $L_1$.

Now consider $n^* = m + 1/2, m \in \mathbb{Z}$. Here $k' = (m + 1/2)(k - m - 1/2)$ is the new parameter to be used.

3. Near $p_4 = (1/4, 1/2)$, the change of variables

$$L_4 = E \circ T_{(1/4,1/2)} \circ S \circ \tilde{M}_k^2 \circ T^{-1}_{(1/4,1/2)} \circ E^{-1}$$

gives

$$L_4 : \begin{pmatrix} x \\ y \end{pmatrix} \mapsto \begin{pmatrix} \bar{x} \\ \bar{y} \end{pmatrix} = \begin{pmatrix} -x - y - s_0 + \bar{y} \\ -y - s_0 - s_1 \end{pmatrix} + \mathcal{O}(n^{-2}), \tag{2.8}$$

where $s_0 = k' - 2\pi^2 x^2$ and $s_1 = k' - 2\pi^2 (x + y + s_0)^2$. Here we have also used $S \circ \tilde{M}_k^2$ instead of $\tilde{M}_k^4$. This allows to reduce the degree of the limit map from 16 to 4.

**Proof of proposition 1 part II: $L_1$, $L_2$ and $L_4$ are Hénon maps**

To find the conjugacies which relate our limit maps to a Hénon map $HP_c$ or $HR_c$ we shall just move their symmetry lines to $y = 0$ for $HP_c$ and to $x = 0$ for $HR_c$, and to make the position in the phase space of some particular orbits not to depend on the parameter. After these changes, a new parameter is going to be defined, plus some scalings in the $(x, y)$-variables, which coincide in all cases and depend on the new parameter. The results in Table 2.2 summarize the suitable scalings and reparametrisations.

Concerning the second 4-periodic orbit near $p_4$ (see Remark 2), it corresponds to the 2-periodic orbit of the orientation-reversing Hénon map $HR_c$. Such 4-periodic orbit can be found on the symmetry lines of $\tilde{M}_k$, $\{y = 2x\} \to \{y = 0\} \to \{y = 2x - 1\} \to \{y = 0\}$. Its position depends on the value of the parameter, but its distance to the 4-periodic orbit of $p_4$ scales as $1/k$ in distance measured on the symmetry lines.

With these results, up to terms of the order of $1/k^2$ for both integer and semi-integer values of the parameter, the scalings predicted by Chirikov and Izraelev in [28] and [26] are fully justified. Moreover, since the bifurcations of fixed points of conservative Hénon maps are well known, this allows to identify, up to some controlled error, the bifurcations of the orbits of $p_1^{1,2}$, $p_2$ and $p_4$.

This ends the proof of Proposition 1.

| Map | Sym. line | Hénon map | New parameter | Scaling |
|---|---|---|---|---|
| $L_1$ | $y=0$ | $HP_c$ | $c=\pi\sqrt{2k'}$ | $\sqrt{2}\pi/c$ |
| $L_2$ | $y=2x$ | $HP_c$ | $c=\sqrt{4+2k'\pi^2}$ | $\sqrt{2}\pi/c$ |
| $L_4$ | $y=2x$ | $(HR_c)^2$ | $c=\sqrt{1+2k'\pi^2}$ | $2\pi^2/c$ |

Table 2.2: Hénon maps to which $L_1$, $L_2$ and $L_4$ are conjugated. The new parameter and scalings in $x$ and $y$ are given in the last two columns.

**Bounds for the remainders of the limit maps in proposition 1**

The proof of this result follows from considering suitable Taylor expansions in $x$, $y$ and $k$ of $\tilde{M}_k$ around the orbits and values of the parameter in Table 2.1 labelled with $\star$, using suitable scalings for $k$ near an integer (or half-integer) value $n$. Concretely, in the case of $p_1^1$ for period $\nu=1$ in Table 2.1 we introduce new variables $X,Y$ defined by $x=1/4+X/n, y=Y/n$ and a new parameter $k'$ by $k=n+k'/n$. Expanding (1.13) we obtain a limit map $L_1$ (2.7) plus a remainder $\mathcal{R}$. In (2.7) we use again $x,y$ instead of $X,Y$ to denote the phase variables, while we keep the name of the new scaled parameter as $k'$ to stress out that it measures the scaled distance to the nearest integer.

Taking into account that the confined points under (2.7) are contained in a compact set, the remainder $\mathcal{R}$ has a bound of the form $|\mathcal{R}|<\mathcal{B}/n^2$, where $\mathcal{B}$ depends on $k'$. This follows immediately from the Taylor expansions and from the alternating character of the series.

For a given value of $k'$ we have estimated, numerically, the set of non-escaping points under $L_1$ using a fine grid. Given $n\in\mathbb{N}$ we compute $k=n+k'/n$, as said before. For each one of these points, the image under $\tilde{M}_k$ (using the above mentioned scalings) has been computed and compared to the one given by $L_1$. The value $\mathcal{R}$ is taken as a measure of the error and when multiplied by $n^2$, it gives a bound for $\mathcal{B}$. It is checked that this bound is essentially independent of the value of $n$.

For values of $k'$ such that the corresponding value of $c$ (see Table 2.2) belongs to $[0,1]$ (i.e., up to the value of $c$ for which the 1:4 resonance appears) one can take $\mathcal{B}=0.004$; for $c\in[1,1.5]$ (i.e., up to the 1:3 resonance) one can take $\mathcal{B}=0.02$, and up to $c=2$ (period doubling) one can take $\mathcal{B}=0.05$ (except, perhaps, at some tiny islands far away from the main confined domain). Higher bounds of $\mathcal{B}$ (up to 0.085) have to be taken at the end of the period doubling cascade. But this is quite irrelevant due to the tiny size of the islands.

The case of $p_1^2$ is identical to $p_1^1$ via a rotation of angle $\pi$ around the point $(1/2,0)$. For the case $p_2$ of period $\nu=2$ one can introduce new variables $X_1,Y_1$ around $(1/4,1/2)$ by $x=1/4+X_1/n, y=1/2+Y_1/n$ and $X_2,Y_2$ around $(3/4,1/2)$ by $x=3/4-X_2/n, y=1/2-Y_2/n$. As before, we introduce $k'$ by $k=n+k'/n$. Then the image of $(X_1,Y_1)$ under $\tilde{M}_k$ is expressed in the $(X_2,Y_2)$ variables as given by (2.8) plus a remainder $\mathcal{R}$ and the same happens for the image of $(X_2,Y_2)$ expressed in the $(X_1,Y_1)$ variables. In (2.8) we also rename the phase space variables as $x,y$. The bounds of the remainder are identical to the ones in the $\nu=1$ case.

For $\nu=4$ let us denote as $p_4^{(j)}, j=1,2,3,4$, the points which appear in Table 2.1, in the order given there. It turns out that the passage from a vicinity of $p_4^{(1)}$ to a vicinity of $p_4^{(3)}$ under $\tilde{M}_k^2$ is described by the map given in (2.8) plus a remainder $\mathcal{R}$. The value of $|\mathcal{R}|$ is bounded, similar to the above cases, by $\mathcal{B}/(n')^2$, where $n'$ is the closest element to $k$ in $\mathbb{Z}+1/2$. We assume $n'\geq 3/2$. The same expression is found for the passage from a vicinity of $p_4^{(3)}$ to a vicinity of $p_4^{(1)}$ under $\tilde{M}_k^2$.

To this end we introduce new variables $(X_1, Y_1)$, $(X_2, Y_2)$, $(X_3, Y_3)$ around $p_4^{(1)}$, $p_4^{(2)}$, $p_4^{(3)}$, respectively, by $x = 1/4 + X_1/n'$ $y = 1/2 + Y_1/n'$, then $x = 1/4 + X_2/n'$, $y = Y_2, /n'$ and, finally, $x = -1/4 - X_3/n'$, $y = 1/2 - Y_3/n'$. We also introduce a new parameter $k'$ given by $k = n' + k'/n'$. The passage from $(X_1, Y_1)$ to $(X_3, Y_3)$ is the one given in (2.8), again using $(x, y)$ for the variables, plus the remainder $\mathcal{R}$. In the range of interest of $k'$, from the elliptic-hyperbolic bifurcation at $-1/(2\pi^2)$ till the end of the period-doubling cascade at $\approx 0.00778$ one can take the bound $\mathcal{B} < 0.0251$.

**Remark 3.** *Karney et al. in [69] used the fact that the fixed point $p_1^{1,2}$ was in its EH-bifurcation to derive an approximate mapping to describe its dynamics, which they truncated at order 2. In this paper the authors also give the relation of such a map with $HP_c$, and give the scalings for $L_1$ as in Table 2.2, but there is no justification for the suppression of higher order terms in the limit $k \to \infty$.*

**Remark 4.** *The same procedure applies exactly for Zaslavsky's web map [150] whose most studied version is the so-called four-fold web map, which has the form*

$$W_k : \begin{pmatrix} x \\ y \end{pmatrix} \mapsto \begin{pmatrix} \bar{x} \\ \bar{y} \end{pmatrix} = \begin{pmatrix} y \\ -x - k\sin(2\pi y) \end{pmatrix}. \tag{2.9}$$

*Here again, we consider (2.9) in the torus $\mathbb{T}^2$. For values of $k$ near an integer there are two fixed points at $(1/4, 1/4)$ and $(3/4, 3/4)$ and a 2-periodic orbit $(1/4, 3/4) \leftrightarrow (3/4, 1/4)$, and for $k$ near a half-integer, there is a 4-periodic orbit $(1/4, 1/4) \mapsto (1/4, 3/4) \mapsto (3/4, 3/4) \mapsto (3/4, 1/4)$. Again, the dynamics around these orbits near integer and half-integer values of $k$ is a quadratic area-preserving Hénon map, which can be easily found with the aid of the symmetries of this map, $y = x$ and $y = -x$ and using exactly the same scalings as in Proposition 1.*

**Remark 5.** *As seen in item 2 in the enumeration of page 23, far from the separatrix, by setting $y = y_0 + s$, $y_0 \gg 1$ in the separatrix map model*

$$SM_{a,b} : \begin{pmatrix} x \\ y \end{pmatrix} \mapsto \begin{pmatrix} \bar{x} \\ \bar{y} \end{pmatrix} = \begin{pmatrix} x + a + b\log|\bar{y}| \\ y + \sin(2\pi x) \end{pmatrix}, \tag{2.10}$$

*the standard map (1.13) is recovered, depending on $k = b/|y_0|$, with an error $\mathcal{O}(y_0^{-2})$ (see [135]). The 2-periodic and 4-periodic stable islands of this section appear in the phase space of $SM_{a,b}$ for $b$ large enough (then the $SM_{a,b}$ is a good model of a close to integrable area-preserving map $F$, provided $b/y_0^2$ is small enough), see [136]. In particular the 4-periodic islet was shown to be born at a degenerate saddle-centre bifurcation, see Fig. 2.10.*

We also would like to note that in [122], both accelerator modes and ballistic modes are studied for the standard map and for the models in (2.9) and (2.10) related to the fixed and period-2 points.

### 2.5.2 Comparing numerical results

Proposition 1 tells us that the limit maps around $p_1^{1,2}$, $p_2$ and $p_4$ are Hénon maps (or compositions of Hénon maps) except for a controllable error. With the aid of the data in Table 2.2 we can recover the plots of the scaled regular area for the standard map as a function of

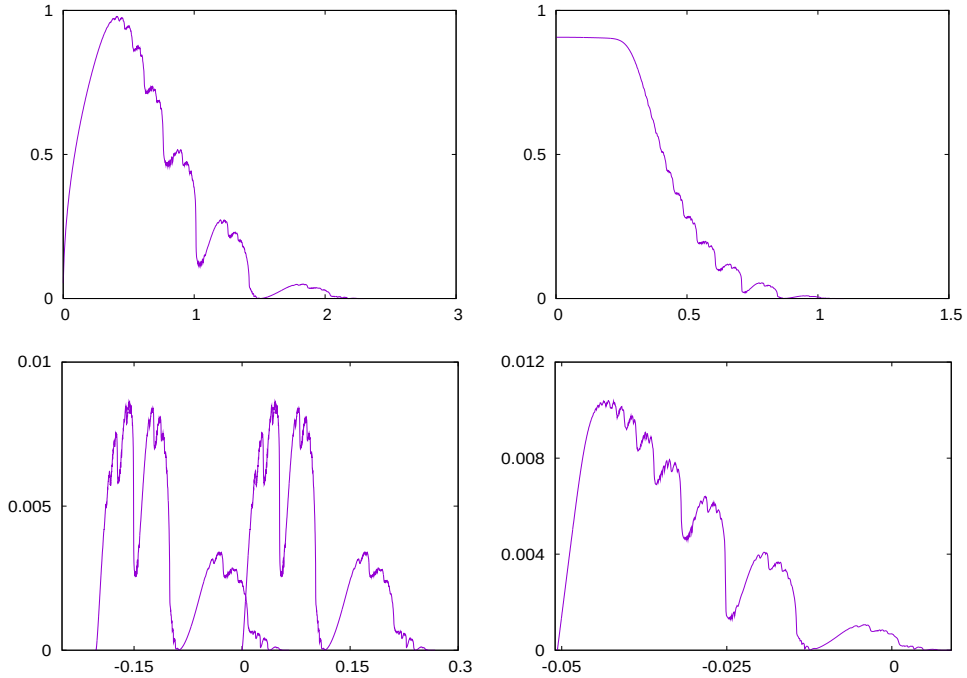


Figure 2.15: Evolution of the relative confined area of: Top: Left: $HP_c$, Right: $HR_c$. Bottom: Left: $L_1$, $L_2$. The resulting actual area in the phase space of $M_k$ is the addition of these two. Right: $L_4$. These last two figures are obtained from the evolution of the non-escaping points of the area preserving Hénon maps plus the scalings in Table 2.2. Compare the bottom plots with Fig. 2.14.

the scaled parameter from the numerical study we did for the Hénon maps in Sections 2.2.2 and 2.3. This is the contents of Figure 2.15.

From the expression of the limit maps $L_1$ (2.7) and $L_2$ (2.8) one can easily see that the relative regular area around the elliptic fixed point is the same, but shifted in the parameter. We have plotted the corresponding scaled relative regular area for both limit maps in Figure 2.15, bottom left. Note further that to recover the actual relative regular area (non-scaled) as in Figure 2.13 one has also to take into account that near integer values of the parameter there are two fixed points $p_1^1$ and $p_1^2$ and that $p_2$ is 2-periodic. Near half-integer values of the parameter there are two 4-periodic islands.

## 2.6 Dynamics of islets in lifts to the cylinder

We finish this chapter by considering the dynamics of the orbits of $p_1^{1,2}$, $p_2$ and $p_4$, once we lift $\tilde{M}_k$ to the cylinder $\mathbb{S}^1 \times \mathbb{R}$, $M_k$. Consider the data in Tab. 2.1. If we iterate the positions of $p_1^{1,2}$ and $p_2$ under $M_n$, $n \in \mathbb{Z}$, we get

$$\begin{array}{lcccccccc} p_1^1 & : & (1/4,0) & \mapsto & (1/4,n) & \mapsto & (1/4,2n) & \mapsto & \cdots \\ p_1^2 & : & (3/4,0) & \mapsto & (3/4,-n) & \mapsto & (3/4,-2n) & \mapsto & \cdots \\ p_2 & : & (1/4,1/2) & \mapsto & (3/4,1/2+n) & \mapsto & (1/4,1/2). & & \end{array}$$

And if we iterate $p_4$ under $M_{n+1/2}$, $n \in \mathbb{Z}$, we get

$$\begin{array}{lcccccc} p_4 & : & (1/4,1/2) & \mapsto & (1/4,n+1) & \mapsto & (3/4,2n+1+1/2) \quad \mapsto \\ & & & \mapsto & (3/4,n+1) & \mapsto & (1/4,1/2). \end{array}$$

There are 2 types of behaviours. According to the notation of [122], $p_2$ and $p_4$ are ballistic orbits, since despite travelling along the cylinder in the course of iteration, they return back to their initial position, and hence are bounded; while $p_1^{1,2}$ are accelerator modes, recall Def. 8. Note that these are precisely those we found in Sect. 1.3: the orbits of $(1/4, n)$ and $(3/4, n)$, $n \in \mathbb{Z}$ are not bounded under the iteration of $M_k$. In fact, since when we consider the dynamics on the torus, a local parameter $k' = k - n$ unfolds a saddle-center bifurcation, they hence show some bounded area surrounding them (and by this we mean both the main island and any satellites surrounding it). When lifted to the cylinder all points inside this area also behave in the same way: the momenta of any of them become unbounded by growing or decreasing linearly in the number of iterates.

What is also remarkable, is that this also happens for orbits not confined by (non-rotational) invariant curves. Orbits that get stuck around this structure also jump with the whole island. This suggests to detect orbits that got stuck around these islands by keeping track on the values of their momenta, $y$, after a long number of iterates.

As we commented in Sect. 1.1.5, in a phase space without any regular component, an ensemble of initial conditions (initially distributed in any way) in the chaotic zone and not confined in islands would tend to be Gaussian as we iterate, but the stickiness effect (if any) may destroy this behaviour.

Note that, since $p_2$ and $p_4$ are ballistic, orbits stuck around the islands of stability surrounding them would behave also as if they were ballistic for some number of iterates. So, unlike the orbits stuck around $p_1^{1,2}$ that would jump in the $y$ direction, being stuck around either $p_2$ or $p_4$ prevents to do so. Hence, we expect super-diffusive effects when dealing with $p_1^{1,2}$ and sub-diffusive effects due to $p_2$ and $p_4$, recall Subsect. 1.1.5.

As is visible in Fig. 2.15, bottom left, the islands of stability around $p_1^{1,2}$ and $p_2$ have positive measure in a compact neighbourhood of $k = n$. For small positive values of $k - n$, the islands of $p_2$ are already in the period doubling cascade, and in case the islands of $p_1^{1,2}$ affect the diffusive properties, this last effect is the dominant one.

As a final remark, we want to stress that this setting is ideal in the following sense: we have a seemingly fully chaotic phase space only affected by a single regular zone (there are actually two islands that evolve simultaneously and, according to the zero-flux condition, the area they occupy has to be identical). In this situation, if we want to study the effect of these islands, we only have to take initial conditions making sure that they lie in the chaotic zone outside a neighbourhood of the island. Choosing them close to the island may give rise to spurious data because the time spent inside strongly depends on the initial position. So if we take them outside the islands, all the initial conditions will be equally statistically relevant.

We will deal with this problem in Chap. 3. Namely, it will be devoted to a clarification of the effect of the islands in the statistical properties of the Chirikov map, for values of the parameters where the islands surrounding $p_1^{1,2}$ play a key role.

# Chapter 3

# Effect of islands in the diffusive properties of the standard map, for large parameter values

In this chapter we review, based on massive, long term, numerical simulations, the effect of islands on the statistical properties of the standard map for large parameter values. Different sources of discrepancy with respect to typical diffusion are identified. We relate them to the geometrical dynamical structures. The individual roles of them are compared and explained in terms of available limit models.

The content of this chapter is already published in [106].

## 3.1 Introduction

One of the main goals of Dynamical Systems is the description, explanation and prediction of the properties of the orbits of a given system. In some cases the individual orbits behave in a seemingly random way, with different properties in different domains of the phase space.

This occurs already in simple models, like area preserving maps. One of the typical models which displays many of the general properties of this class of maps is the Chirikov standard map [26]. For large enough values of the parameter the behavior of the orbits seems like a diffusive process. But this is far from being true for some ranges of the parameter, as noticed by many authors in the past. See, for instance [26, 118, 69, 68] and [149] and references therein.

The purpose of the present chapter is to present the results of massive simulations for large sets of values of the parameter and to explain the different phenomena that lead to the destruction of the diffusive character. This is done using quantitative and qualitative approaches. The results are compared to some limit theoretical models which deal with several of the involved phenomena.

In Section 3.3 we consider simple approaches to the diffusive properties of the standard map: the quasi-linear approximation and the Fourier methods to take into account the correlation effects. These methods are useful for many of the values of the parameter when it is large enough.

Section 3.4 is devoted to methods and results obtained from massive simulations. After looking at the problem for a large set of values of the parameter, we consider narrower and

narrower ranges to focus on the main difficulties. A scaling effect shows up and, hence, details on the dynamics in a narrow parameter domain allow us to understand the behavior at all the other places where the standard diffusion is no longer valid.

Quantitative and qualitative explanations of the numerical results, as well as a comparison with limit renormalisation schemes are the contents of Section 3.5. The main result concerns the behaviour of the standard deviation of the iterates of points, initially in a given ensemble in the chaotic domain, as a function of the number of iterates $T$. While for a typical diffusive process it behaves as the square root of $T$, for some intervals, in the domain of large parameter values, it behaves as a larger power of $T$, whose exponents range, approximately, between 0.7 and 1.

A description of what the orbits do, which explains the main features of the plots which summarize the numerical results, is presented at the end of Section 3.5.7.

The contribution of this chapter has to be seen as an attempt to find quantitative explanations to the results of a large number of simulations, so that one could find the main theoretical reasons which allow to predict, accurately, which should be the observed behaviour of the diffusive properties of the standard map for some special ranges, near integer values, when the parameter is large.

## 3.2 On the destruction of rotational invariant curves

Before starting to deal with diffusive phenomena of $M_k$, it is important to do some remarks on how invariant curves are destroyed, since once destroyed, in the form of Cantori, they are one of the objects that play a key role in diffusion, since they can slow this process down due to the small size of their gaps. To do so, we are going to use as example, the island of stability around the accelerator mode that is born at $(1/4, 0)$ for $k = 1$.

In Figures 3.1 and 3.2 we show how the distribution of invariant curves around islands evolves as the parameter changes. We have estimated the values of the pairs $(x, k)$ of $x$ at the right hand side of the hyperbolic periodic point and of parameter $k$ for which there are invariant curves. For the 1/4 hyperbolic periodic point in Figure 3.1 (see Figure 3.5 right for a sketch of the phase space near these parameter values) and for the 3/13 and 2/9 hyperbolic periodic points in Figure 3.2. In the last case the points are taken to the left of the corresponding periodic hyperbolic point.

We have proceeded as follows: for a fixed value of $k$, we consider a grid of points with spacing $10^{-6}$ on the $y = 0$ line. For each of these points, we have computed an approximation of the Lyapunov exponent. If considered zero, it was a candidate to invariant curve so its rotation number was approximated via the method explained in the appendix of [123]. If it could be considered irrational, we plotted this pair $(x, k)$.

In these figures we observe black bands emanating from the horizontal axis. The white strips in these bands correspond to islands which are perfectly identifiable. In the black bands, one can see "tongues" which, when zooming, reach the $x$ axis: they correspond to instability zones produced by the splitting of the separatrices of hyperbolic periodic points.

For $k = 1.051$, at the bottom of Figure 3.1 one can observe relatively large gaps in the Cantor structure of invariant curves. They correspond to the existence of islands. The rightmost gap, for $x \in [0.314050, 0.314312]$, corresponds to a rotation number $\rho = 10/41$, while the leftmost one, for $x \in [0.309577, 0.309634]$, corresponds to $\rho = 30/121$. The rotation numbers of the islands in the largest gaps are of the form $2j/(8j + 1), j = 5, \ldots, 15$. Due to

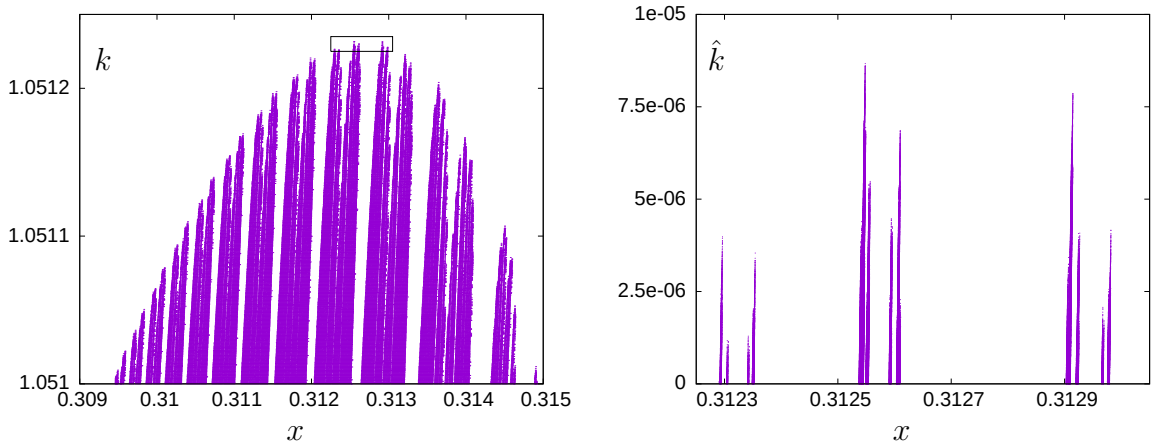


Figure 3.1: Initial conditions in the $(x, k)$ plane taken on $y = 0$ for which there exist rotational invariant curves surrounding the accelerator mode island. The right plot is a magnification of the box in the left plot. Computations for values of the parameter after the 1/4 resonance. The parameter $\hat{k}$ in the right plot is related to $k$ by $\hat{k} = k - 1.051225$.

the symmetry properties of $M_k$, islands with $\rho$ of the form $p/q$ with $p$ even appear to the right of the fixed point, while if $p$ is odd they appear to the left.

Furthermore, to the right of the displayed domain for $k = 1.051$ an island with $\rho = 8/33$ appears for $x \in [0.315087, 0.315453]$ and one to the left, with $\rho = 32/129$, is found for $x \in [0.309386, 0.309443]$.

It is also easy to identify some periodic hyperbolic points, which are born close to the destruction of nearby invariant curves. For instance, for the approximate values $x = 0.309508$, $0.313708$ and $0.314701$ periodic orbits with $\rho = 31/125$, $11/45$ and $9/37$, respectively, are found.

For each elliptic periodic point, one can see that there are 2 invariant curves, one to the right and one to the left, surrounding a chain of islands. They both have similar rotation number, but their destruction is not simultaneous. In particular, the continued fraction expansion of the rotation numbers of the two highest tips which are shown in the magnification of Figure 3.1 are

$$[4, 14, 1, 1, 1, 1, 1, \ldots] \text{ and } [4, 13, 1, 1, 1, 1, 1, \ldots],$$

for the tips located near $x = 0.3125$ and $x = 0.3129$ respectively.

Finally, we note the quadratic shape of the envelope of the purple points in the Figures 3.1 and 3.2. This can be explained as follows. To study the dynamics in the chaotic zone between the 1/4-periodic island surrounding the accelerator mode island and the last invariant curve (if exists) one can use a separatrix map model, see [26, 135]. At some (fixed) distance $y_0$ from the separatrices bounding the 1/4 islands, the separatrix map can be approximated by a standard map $M_k$ with $k \sim 1/|y_0|$. This explains why the boundary of the black points in Figures 3.1 and 3.2 resembles the critical function of the standard map $M_k$. We recall that the critical function (also referred as fractal diagram) relates the frequency $\omega$ with the value of $k = k(\omega)$ for which the invariant curve with frequency $\omega$ breaks down. In our plots we represent $x$ instead of $\omega$ as the $x$-coordinate, but there is a one-to-one correspondence guaranteed by the non-vanishing twist property. As we will see in Chap. 4, the breakdown of invariant curves can be investigated using a renormalisation scheme approach, see [89]. The renormalisation scheme implies that the locally most robust invariant curves correspond to noble rotation numbers. Hence the maxima observed in the figures are related to noble

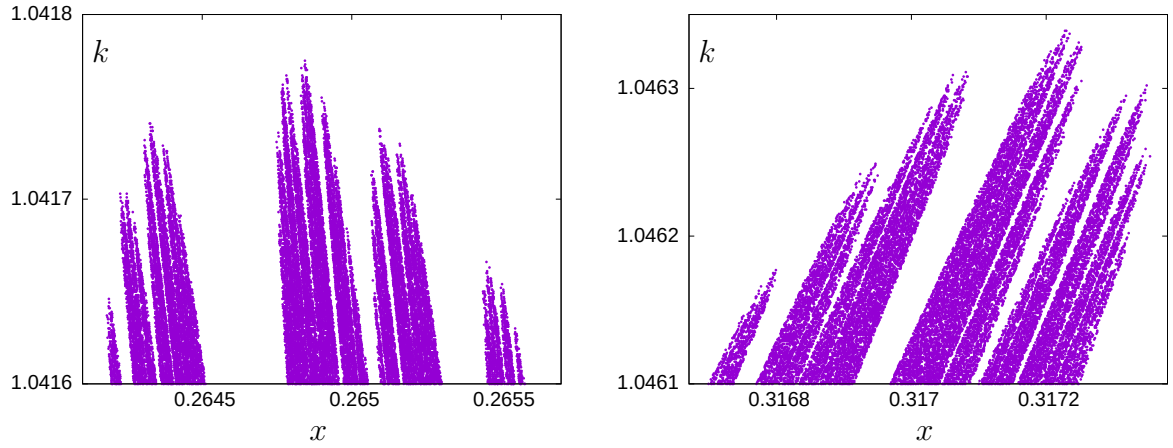


Figure 3.2: Initial conditions in the $(x, k)$ plane taken on $y = 0$ for which there exist a rotational invariant curve with respect to the accelerator mode. Computations for values of the parameter after the: Left: 2/9 resonance. Right: 3/13 resonance.

numbers, as was noticed above for the two highest tips. Moreover, for the golden rotation number $g$ the corresponding renormalisation operator implies that the distance $\Delta\omega$ to the nearby noble numbers scales as

$$\Delta k \sim -|\Delta\omega|^{\eta},$$

where $\eta = |\log(\delta)/(2\log(g))| \approx 0.5063$, see [89]. Here $\delta$ refers to the inverse of the convergence ratio of the renormalisation scheme, see (3.6) in Sect. 3.5.7. See Sect. 4.2. See also related comments in [90]. Moreover, a similar behaviour is expected for any noble number. This implies that each of the tips shown is expected to have (locally) a quadratic shape again. We remark that the renormalisation process gives local information around the most robust noble in a given interval. Nevertheless, in the figures one observes that the quadratic shape has a more global character (although the considered range of $x$ is relatively small).

## 3.3 Elementary approaches to the diffusion properties

We start here with simple approaches to the diffusion properties of the standard map $M_k$, the lift to the cylinder $\mathbb{S}^1 \times \mathbb{R}$ of (1.13) for large $k$. In fact these approaches provide a good idea of the diffusion for most of the values of the parameters if they are sufficiently large. Then we shall compare with a better measure of the properties of the dynamics. Concrete details and explanations will be given in the next sections.

We consider here the diffusion in the $y$ variable for $M_k$. The main conclusion will be that there are ranges of the parameter where the behaviour is not of diffusive type, even starting in the chaotic domain. But the width of these ranges tends to zero as $k \to \infty$.

### 3.3.1 The quasi-linear approximation

For large $k$ the statistical description of the dynamics in the chaotic zone, assuming that the measure of the regular zone is negligible in front of the one of the chaotic zone, can be done via the simplest (homogeneous) diffusion equation [27]

$$\frac{\partial f}{\partial t} = \frac{1}{2} D(k) \frac{\partial^2 f}{\partial y^2}, \tag{3.1}$$

where $f = f(y,t)$ is the density of points, $t$ denotes the number of iterations and $y$ is the momentum. The transition density of a Brownian motion starting at 0 with variance $\sigma^2 = 1$ satisfies the previous heat equation, that is, the infinitesimal generator of the underlying Feller process is $\frac{1}{2}\frac{\partial^2 f}{\partial y^2}$. Note that this approach assumes that the effect of the angles $x$ averages properly, and then the diffusion equation describes the dynamics in the $y$ direction. An improvement to take into account the influence of $x$ will be given in Section 3.3.4.

Let us denote as $(x_j, y_j) = M_k^j(x_0, y_0)$ the values of the successive iterates of a point $(x_0, y_0) \in \mathbb{S}^1 \times \mathbb{R}^1$. Let $\Delta^j y = y_j - y_0$ be the difference in actions after $j$ iterates. The average diffusion rate for $M_k$, $D(k)$, can be evaluated as the limit

$$D(k) = \lim_{n\to\infty} \frac{\langle (\Delta^n y)^2 \rangle}{n}. \tag{3.2}$$

where $\langle\cdot\rangle$ stands for the ensemble average. It is worth stressing that the value of $D(k)$ strongly depends on $k$, and that for each value of $k$, it is a constant in (3.1). Note that in this definition the mean $\langle (\Delta^n y) \rangle$ is assumed to be zero, so it is not included in (3.2). Despite this fact holds true in our setting, when we compute $D(k)$ or some variant of it, to obtain the variance we include that missing term: $\sigma^2 = \langle (\Delta^n y)^2 \rangle - \langle (\Delta^n y) \rangle^2$.

Under the assumption that we can average out the effect of the angles in $M_k$, and no accelerator modes show up in the phase space, the mean value of $D(k)$ after one single iteration is

$$D_{ql}(k) = \int_{\mathbb{S}^1} (y_1 - y_0)^2 \, d\xi = \int_{\mathbb{S}^1} (k \sin(2\pi\xi))^2 \, d\xi = \frac{k^2}{2}, \tag{3.3}$$

which is usually referred to as the quasi-linear value. If we normalize (3.3), to skip the effect of $k$, one should obtain the normalized value $D_{ql,N} = 1/2$, where the subscript $N$ refers to this value as being normalized.

### 3.3.2 Selecting initial points

An important point, for this section and for the rest of similar massive numerical simulations in this thesis, is the selection of initial points to be iterated under $M_k$, to measure the diffusion properties. We want to make sure that these points are taken on the "chaotic sea", i.e., outside any island. To this end we have used the following method to select initial points:

a) Compute an approximation of the unstable manifold $W^u_{k,p}$ of some periodic hyperbolic orbit of period $p$. This can be done in an efficient way via the parametrisation method (see [126]) at some high order (typically between 20 and 50). Except in the case $p = 1$ (i.e., for the hyperbolic fixed point) one has to compute first the Taylor expansion of $M_k^p$ around the chosen point.

b) Let $z$ be a parameter of the manifold and $g(z)$ the corresponding point in $W^u_{k,p}$. The invariance condition reads $M_k^p(g(z)) = g(\lambda z)$, where $\lambda$ is the dominant eigenvalue at the chosen point and $z$ has been normalized so that the linear term in $g(z)$ has modulus 1. Select a fundamental domain in $U = [z_0/\lambda, z_0]$ in which the invariance condition is satisfied with a prescribed tolerance (typically $10^{-20}$).

c) Choose points in $U$, e.g. with uniform step in log scale, and iterate them $n_0$ times under $M_k$ as a transient. These will be the selected initial points.

### 3.3.3 Results and interpretation

An idea on the goodness of the quasi-linear approximation $D_{ql,N}(k)$ can be obtained by computing the first term $\langle(\Delta^1 y)^2\rangle$ in the limit (3.2) via the method just described. We have used $p = 1$ in subsection 3.3.2 a), $N = 250,000$ points in $U$ and have done $T = 10^6$ iterates. Note that, since we recorded $\Delta^1 y$ and $(\Delta^1 y)^2$ at each iterate, assuming uncorrelation, it is equivalent to take just one initial point and iterating it $T = 2.5 \times 10^{11}$ times.

We have considered the values of the parameter $k = 0.72(0.001)6.1$, for which the phase space is filled with what seems to be a chaotic sea, except for the islands appearing near integer and half-integer values of the parameter studied in Section 2.4. After skipping the effect of $k$, the obtained approximation $\tilde{D}_{ql,n}(k)$ of $D_{ql,N}(k)$ differs from $1/2$ by less than $2 \times 10^{-6}$ for most values of $k$.

However, there are parameters for which the computed value $\tilde{D}_{ql,n}(k)$ differs in a significant way from $1/2$ and it is below the expected value. The parameters $k$ for which this occurs are seen to coincide with the ones for which islands are detected for $M_k$, as described in Section 2.5.

In Figure 3.3 we display the values of $1/2 - \tilde{D}_{ql,n}(k)$ as a function of $k$ in the range mentioned above. Compare the left plot with Figure 2.13 in Section 2.4.1. Further details can be seen on the right plot, with $k \in [1.87, 2.13]$. No differences have been observed if we replace the unstable manifold of the fixed point by unstable manifolds of other periodic hyperbolic orbits to select the initial conditions.

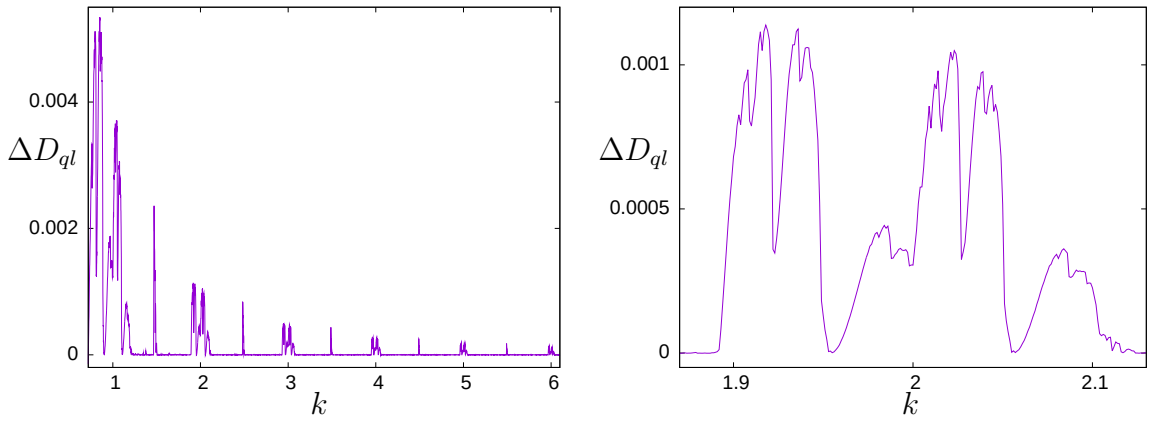


Figure 3.3: Values of $\Delta D_{ql} = 1/2 - \tilde{D}_{ql,n}(k)$, where $\tilde{D}_{ql,n}(k)$ is the numerically estimated average one step diffusion rate, as a function of $k$. Left: results for $k \in [0.72, 6.1]$. Right: a magnification for $k \in [1.87, 2.13]$.

There is an easy interpretation to the results. The places where some islands are located, according to Section 2.4, are close to $x = 1/4$ and $x = 3/4$. The iterates of points in the chaotic zone can not enter into them. Hence, as in these domains the value of $(\Delta y)^2$ is, approximately, equal to $k^2$ and close to maximal, the contribution to the average is missing. This produces a decrease in the value of $\tilde{D}_{ql,n}(k)$ roughly proportional to the size of the island.

Note that this first term in the limit (3.2) is significantly different form all other terms. When one considers more than one single iterate, the value of $\langle(\Delta^n y)^2\rangle$ can not be easily averaged since functions like $k \sin(2\pi(x + y + k \sin(2\pi(x + \cdots))))$ appear. This kind of expressions are typically expanded in $k$ by sums of Bessel functions as will be done in the next Section, producing larger oscillations, as noted in [27].

### 3.3.4 A first improvement

A first improvement with respect to the quasi-linear approximation consists in taking into account the effects of the correlations between successive iterates. A nice description can be found in [75] and references therein. These effects can be studied using Fourier techniques. A simple correction factor, adapted to the notation and normalisations we use in this work, follows from formula (5.5.21) in [75] and the comments that follow after that formula. See also [102] and [144].

Hence, we should expect a corrected value for the normalized average diffusion rate given by

$$D_{cc}(k) = \frac{1}{2}\left[1 - J_2(2\pi k) + (J_2(2\pi k))^2\right], \tag{3.4}$$

where $D_{cc}$ stand for "correlation corrected" and $J_2$ denotes the second Bessel function. The values of $D_{cc}(k) - 1/2$ tend to 0 as $k^{-1/2}$ when $k \to \infty$ with sinusoidal oscillations around 0.

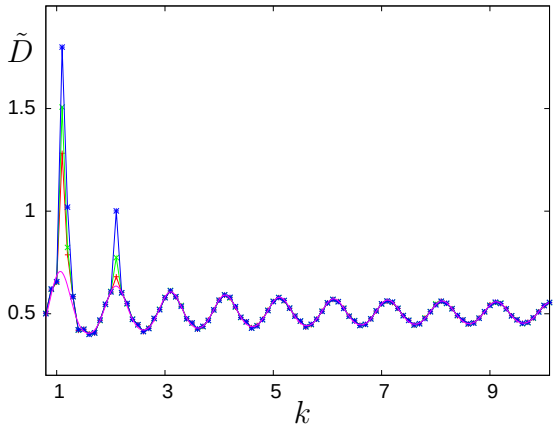


Figure 3.4: For a range of values of $k$, as horizontal variable, and using a large step in $k$, we show the values of the estimated diffusive properties of $M_k$, after $10^3, 10^4$ and $10^5$ iterates (in red, green and blue, respectively), for a sample of $10^5$ initial conditions. The magenta curve shows the values of $D_{cc}(k)$ as given by (3.4). Here $\tilde{D}$ simply denotes the values for the different number of iterates including the normalization mentioned at the end of subsection 3.3.1.

In Section 3.4 we provide a method to estimate the true diffusive properties of $M_k$. We shall see that the results depend on the number of iterates, $T$, after the transient. Explanations for these results will be provided in Section 3.5. For the moment being we display, in Figure 3.4, the comparison between the results using a sample of $10^5$ initial conditions and values of $T$ equal to $10^3, 10^4$ and $10^5$ (in red, green and blue, respectively) and the ones using (3.4) (in magenta). Even taking into account that we have used the values of $k = 0.8(0.1)10.1$, one can observe big differences, mainly near 1 and 2, depending on the value of $T$. In fact, these differences appear shortly after every integer value of $k$ in domains which become narrower as $1/k$ when $k$ increases. Outside these domains, to be discussed in next section, the approximation provided by (3.4) is quite good. The two peaks seen in Figure 3.4 are just a preliminary indication of the richness that in subsection 3.4.2 will be shown to exist. This is one of the main motivations of this work.

## 3.4 Numerical evidences on the real diffusion properties

To have a correct estimate of the diffusive properties of $M_k$ we should take into account how the "diffusion" depends on time, that is, on the number of iterates $T$ and check that it is essentially independent on the size of the sample $N$, i.e. the number of initial points which are iterated under the map.

It is well-known that in a diffusive process, with constant diffusion coefficient, a sample of $N$ points starting at a given value of $y$ (or nearby values) after $T$ iterates has a standard deviation $\sigma_T$ which behaves as $\sqrt{T}$. Hence, when dividing $\sigma_T$ by $\sqrt{T}$ it should tend to a constant, the diffusion coefficient, when $T$ increases and, to minimize the effect of $N$, when the size of the sample also increases.

Consider a given initial value of $y$, say $y_0$ after the transient and reducing it to $\mathbb{T}^2$, that is $0 \le y_0 \le 1$ (or, equivalently, $-1/2 \le y_0 \le 1/2$). Let $y_T$ the value after $T$ iterates, without any further reduction to $\mathbb{T}^2$, that is, using $\tilde{M}_k$. The standard deviation can be measured for the jump in $y$: $\Delta^T y = y_T - y_0$.

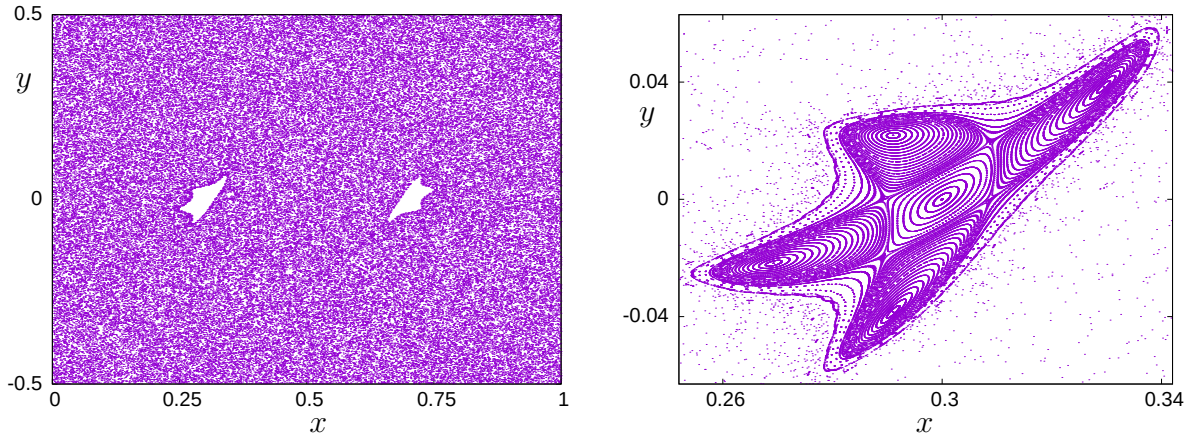


Figure 3.5: For $k = 1.05123$ the left plot shows an orbit of an initial point in the chaotic zone, reducing $y$ to the range $[-1/2, 1/2)$. Two domains, around fixed points of $M_k$, are seen to be non accessible. The right plot shows details on the dynamics around the fixed points on the "left" island.

A typical orbit of a point in the chaotic zone is shown, reducing it to $\mathbb{T}^2$, in Figure 3.5 left. We see that it avoids a couple of islands located, approximately, around $(0.3, 0)$ and $(0.8, 0)$, where there are fixed points of $\tilde{M}_k$. The value used for the figure is $k = 1.05123$ and reasons for that choice of $k$ will be given later. Compare also with the results shown in Figure 3.1. The right plot in Figure 3.5 shows a detail on the dynamics near the left fixed point. As points near the fixed point jump up by an amount close to one unit under iteration by $M_k$, we call it "the positive island". In a similar way, the island on the right side of Figure 3.5 left will be denoted "the negative island". Accordingly, the fixed points inside these islands will be denoted as $E_+$ and $E_-$, respectively. Around the fixed point one can see several KAM curves, then a hyperbolic periodic orbit of period 4, the related islands of period 4 and, as given by the evidence in Figure 3.1 there are still invariant curves around these period-4 islands.

According to Figure 3.1 right, these curves persist until a value of $k = k_{c,1/4}$ located in the range $(1.05123, 1.05124)$. Hence, the iterates of initial points in the chaotic domain can

not enter inside the islands, because of the existence of these invariant curves.

The reason why we have selected values of $k$ near the destruction of the invariant curves around the period-4 islands, as it can be seen in the details shown in Figure 3.9, relies on the measure of the confined chaotic domains for the Hénon map, see Figure 2.4 right. For period 4 it turns out that this measure is one of the largest ones. See more details in Figure 2.5. However, a detailed inspection of the diffusive properties shortly after the destruction of the last invariant curve around islands with other rotation numbers (like 1/5, 1/6, 1/7,...,2/9, 2/11, ...,3/13,...) shows the same properties that will be described for rotation number 1/4. But to go deeply into some of the details of the phenomena for these rotation numbers the number of iterations has to be increased.

The results of the computations of $\sigma_T/\sqrt{T}$ show a strong dependence in $T$ when period-1 islands exist, independently of the size of $N$ if this one is large enough to provide a good estimate of $\sigma_T$. The methods used (some of them to be used also in Section 3.5.2) and which kind of data are recorded, are presented in Section 3.4.1, with results shown in Section 3.4.2.

### 3.4.1 Methods

As mentioned in Section 3.3.2 we have used initial data in $\mathbb{T}^2$ after a transient of $n_0 = 10^3$ starting in a fundamental domain of the unstable manifold $W^u_{k,1}$. Most of the results have been checked using also starting points in $W^u_{k,2}$, having an excellent agreement.

After the transient every initial point is iterated $T$ times. The current values of $y_T$ for different values of $T$ (typically for powers of 2) are stored. At the end of the computation, for each selected value of $k$ and each value of $T$, one has the standard deviation of a sample of $N$ initial points, which is scaled by the current value of $\sqrt{T}$ and also by $k$ to obtain a normalized value, as described in Section 3.3.1. Concretely, if a value $\sigma_T(k)$ has been obtained as standard deviation, we record the value

$$\sigma_{T,k} = \sigma_T(k)/(k\sqrt{2T}), \qquad \sigma_T^2(k) = \left\langle (\Delta^T y)^2 \right\rangle - \left\langle (\Delta^T y) \right\rangle^2 \tag{3.5}$$

The additional $\sqrt{2}$ has been introduced to allow for comparisons with the normalized quasi-linear value $D_{ql,N}$.

It has been checked that the iterates of initial points can remain close to the islands for many iterations. Suitable explanations are given in Section 3.5.

One of the quantitative questions to decide is how to give a concrete meaning to the sentence "to remain close to the islands". This has been used for the computations whose results are shown in Figure 3.9, i.e., for a very narrow range of values of $k$. Looking at Figure 3.5 right we decide to consider as "close to the islands" points which pass at a distance less than some amount $r_b$ (fixed as 0.0775 for the data shown in Figure 3.9) from either $E_+$ or $E_-$. But it is clear that there are points in the chaotic zone that enter this domain. Hence, to consider that the orbit of a point passes close to, say, the positive island, we require to be at a distance less than $r_b$ from $E_+$ for, at least $n_b$ consecutive iterates. As suitable value for $n_b$ we have taken $2^7$. The set of points where these two conditions are satisfied (proximity and permanence) will be denoted as "the vicinity of the island" and represented as $\mathcal{W}_{E_+}$ or $\mathcal{W}_{E_-}$. We will say that the iterates of an initial points are temporarily captured by the island if they spend at least $2^7$ consecutive iterates either in $\mathcal{W}_{E_+}$ or in $\mathcal{W}_{E_-}$.

This will allow us to have average estimates on the "trips" of the different initial points, that is, how many iterates they spend in the chaotic domain, how many close to the positive

or negative islands, the probability to pass from the chaotic domain to $\mathcal{W}_{E_+} \cup \mathcal{W}_{E_-}$ and the mean time spent in these vicinities. All these data will be useful to understand the global dynamics, as described in Section 3.5.

Note that after the transient of $10^3$ iterates it can happen that some point is already in $\mathcal{W}_{E_+}$ or in $\mathcal{W}_{E_-}$. This really does happen but the fraction of points in each one of these vicinities is below 1.5%.

### 3.4.2 Results

Figure 3.6 shows the results for $\sigma_{T,k}$ for $T = 2^{18}$, a sample size $N = 250,000$ and $k = 0.8(0.001)$ 10.1. Beyond the oscillations around 0.5, already observed in Figure 3.4, sufficiently well modeled by the values in (3.4), we see some wild behavior with several large peaks shortly after integer values of $k$. The size of the peaks and also the width of the ranges where this occurs behave, approximately, like $1/k$. A similar type of results can be found in [144].

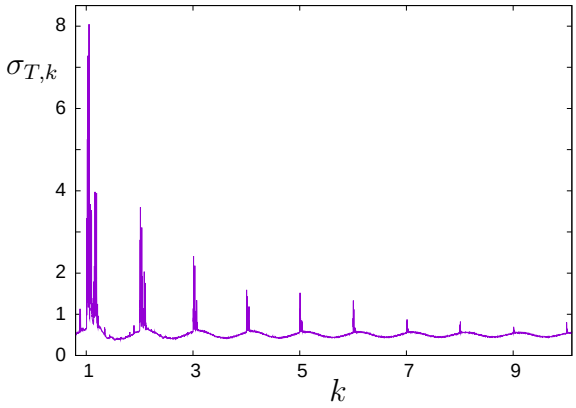


Figure 3.6: For $k = 0.8(0.001)10.1$ as horizontal variable, we represent the values of the estimates of $\sigma_{T,k}$, as vertical variable. See the text for the values of $T$ and $N$.

Note that these ranges correspond to part of the intervals in $k$ where $M_k$ has fixed points (in $\mathbb{T}^2$), but not to the ranges where period-2, period-4 and several other periodic islands are found, recall Sect. 2.6. The reason for this different behavior is elementary and will be given in Sect. 3.5.

In Figure 3.7 we show a detailed view of the previous result shortly after $k = 1$ and $k = 4$. Similar results have been obtained for many other ranges of $k$ following integer values. The corresponding values have been obtained using $N = 10^6$ and for $T = 2^j, j = 16, 18, 20$ are displayed in different colors. The values of $\sigma_{T,k}$ increase with $T$.

Both parts of Figure 3.7 are quite similar, except by the different scaling in both the horizontal and vertical variables and minor details. The peaks are almost gone for $k$ near 1.06 in the left plot and for $k$ near 4.015 in the right one. For these values the elliptic fixed points of $M_k$ have rotation number close to 1/3. According to the study of the standard map islands, and based on the properties of the Hénon map presented in Section 2.2, the islands around $E_+$ have a negligible size.

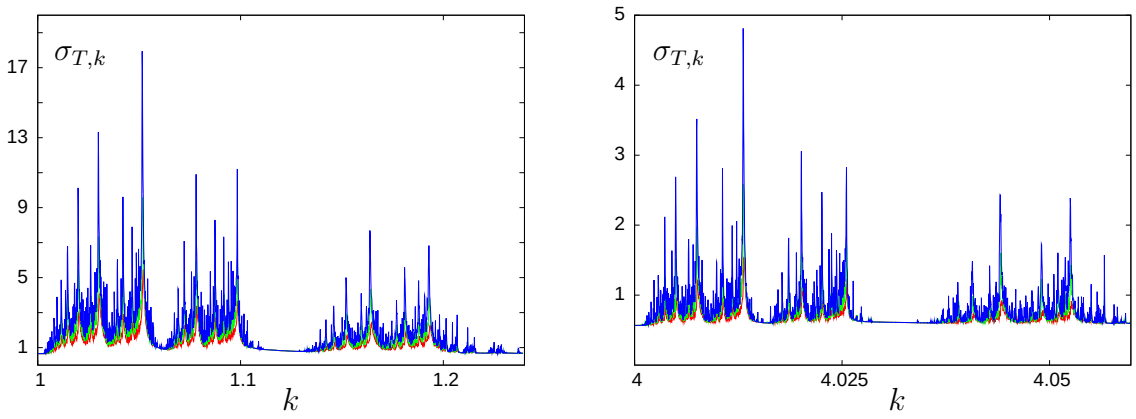


Figure 3.7: Details on the behavior of $\sigma_{T,k}$ near $k = 1$ (left) and $k = 4$ (right) for three increasing values of $T$. The concrete ranges of $k$ are $1(0.0001)1.24$ and $4(0.00003)4.06$. See the text for the values of $N$ and the different values of $T$ used in the computations.

In Figure 3.8 we restrict our attention to the $k$ intervals $[1, 1.06]$ and $[4, 4.015]$. As expected, both plots are quite similar. The values of $N$ and the steps in $k$ are the same as before, but the values used for $T$ are now $2^j, j = 18, 20, 22$. Comparing with the parts of Figure 3.7 corresponding to the same intervals, we realize that the peaks have, roughly, the double value when $T$ increases by a factor 4.

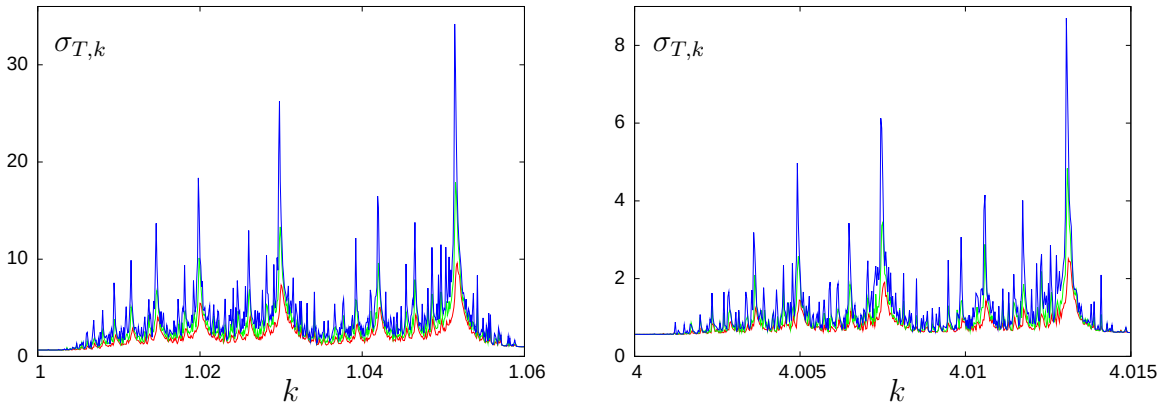


Figure 3.8: Further details on $\sigma_{T,k}$ in narrower ranges near $k = 1$ (left) and $k = 4$ (right). The values used for $T$ have been increased by a factor 4 with respect to Figure 3.7.

Each one of the peaks seen in Figure 3.8 occurs shortly after the breakdown of all the outermost invariant curves surrounding the islands around $E_+$ and $E_-$ with a given rotation number, $\rho$, which occurs for a critical value to be denoted as $k_{c,\rho}$. Approximate values of the location of the peaks in that figure and the corresponding rotation numbers are given in Table 3.1.

| $10^4(k-1)$ | 514 | 465 | 419 | 392 | 298 | 260 | 198 | 146 | 115 | 94 | 80 | 69 | 61 |
|---|---|---|---|---|---|---|---|---|---|---|---|---|---|
| $\rho$ | 1/4 | 3/13 | 2/9 | 3/14 | 1/5 | 2/11 | 1/6 | 1/7 | 1/8 | 1/9 | 1/10 | 1/11 | 1/12 |

Table 3.1: A sample of the values of $k$ for which large peaks appear in Figure 3.8. For each value of $k$ we give the rotation number of the islands such that the outermost invariant curve surrounding them has been destroyed for a nearby, smaller, value of $k$, that we rename as $k_{c,\rho}$.

From now on we concentrate on the vicinity of the largest peak in Figure 3.8 using a large number of iterates. That is, for $k$ around $k_{c,1/4}$. A similar behavior has been observed

for other major peaks. It is apparent that the peak that we consider is the largest one for all $k > 1$.

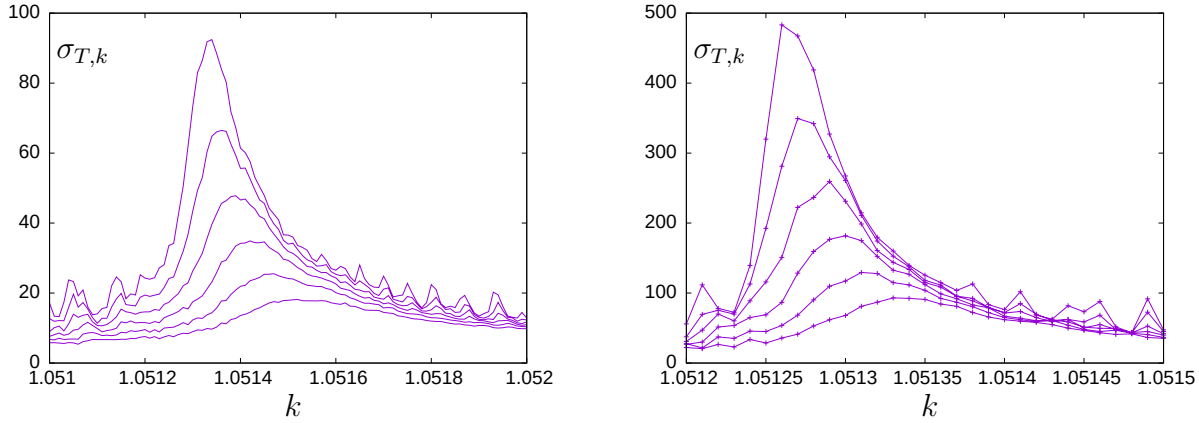


Figure 3.9: A sample of results near the largest peak in Figure 3.8 for large values of $T$. In the left plot the values of $T$ go up to $2^{25}$ and in the right one they reach $2^{30}$. See the text for additional details.

In Figure 3.9 the results in narrow domains around $k = 1.0514$ are shown. In the left plot the number of initial points is $N = 10^6$ while the values of $\sigma_{T,k}$ are shown for $T = 2^j, j = 20(1)25$. We have used $k = 1.051(10^{-5})1.052$. In the right plot one has used $N = 10^5$ and the values of $T = 2^j, j = 25(1)30$. The step in $k$ is the same as in the left plot, but the range is reduced to $[1.0512, 1.0515]$.

The upper curve in the left plot, which reaches a value slightly larger than 92, can be identified with the lower one that can be seen in the right plot. The upper one in the right plot reaches a value slightly larger than 483. The ratio of these values is 5.25, a little bit below the square root of the ratio of the number of iterates ($T = 2^{30}$ on the right, $T = 2^{25}$ on the left).

We can summarize the observed results near a peak of $\sigma_{T,k}$ related to the breakdown of the invariant curves around an island of rotation number $\rho$ as follows. Recall that $\sigma_{T,k} = \sigma_T(k)/(k\sqrt{2T})$ so we already scaled it by $\sqrt{T}$. Hence, in a diffusive setting one expects $\sigma_{T,k}$ to behave as constant times the periodic corrections in (3.4). But

1. The maximal value of $\sigma_{T,k}$, for a given $T$, occurs for values of $k = k(T)$, where $k(T)$ is a decreasing function which tends to $k_{c,\rho}$ as $T \to \infty$.

2. The values of $\sigma_{T,k(T)}$ tend to scale as $\sqrt{T}$. That is, the non-scaled standard deviation $\sigma_T(k)$, see (3.5), reaches a linear dependence in $T$, at least selecting the values of $k$ in a way which depends on $T$. This implies that the dynamics in $y$ is not Gaussian and the diffusion coefficient diverges. Otherwise, $\sigma_{T,k}$ would have finite limit. This is related to the fact that the escape time distribution from the stickiness region around the accelerator modes has infinite variance, see related comments in Section 3.5.6. At the end of Section 3.5.2 we return to this key point, and in Section 3.5.7 we will give a theoretical justification of it.

Note also that for large $T$ the effect of little islands starts to be visible, see Figure 3.9.

To check the role of the arithmetics on the computations we have reproduced, using quadruple precision, the results in a sub-interval of Figure 3.9 left. Concretely, we have taken a reduced set of values of the parameter $k = 1.0512(2 \times 10^{-5})1.0516$, a number of

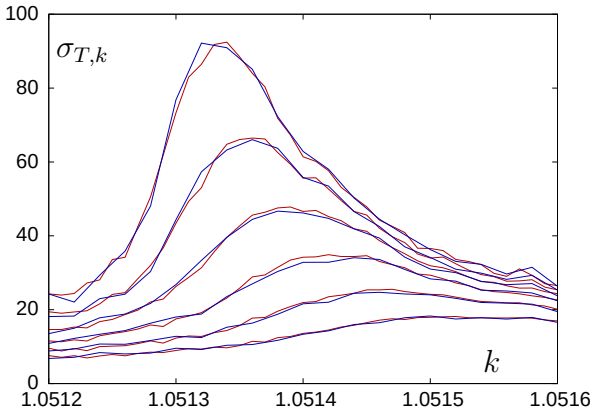


Figure 3.10: Comparison of the results for $T = 2^m, m = 20(1)25$ and a reduced set of values of $k$ using double precision (in red, part of Figure 3.9, with a sample of $10^6$ points) and quadruple precision (in blue, with a sample of $2 \times 10^5$ points).

iterations of the form $T = 2^m$, $m = 20(1)25$ and a smaller size of the sample, $N = 2 \times 10^5$. The results, displayed in Figure 3.10, show a good agreement with the ones that have been produced with double precision.

## 3.5 Qualitative and quantitative approaches to the interpretation of the numerical results

In this section we first comment on the role that different invariant objects have on the statistical properties. Then we provide additional numerical information, mainly extracted from the computations leading to Figure 3.9. To compare with this information we include a study of the breakdown of the last rotational invariant curve (the one with golden rotation number) at the Greene's critical value of the parameter. After a presentation of some theoretical limit renormalisation results, we are in condition to explain the shapes seen in the previous figures, concerning the behavior of the standard deviation as a function of $T$ and $N$.

### 3.5.1 The role of different objects and phenomena

i) The accelerator modes.

For $k$ integer the fixed point $E_+$ of $M_k$, located at $(1/4, 0)$, jumps $k$ units up under $M_k$. Despite starting at the chaotic sea, when entering $\mathcal{W}_{E_+}$ the orbit can mimic the behavior of $E_+$ for many iterates. Going away from $y = 0$ it will produce a major contribution to the standard deviation. The same is true for points entering $\mathcal{W}_{E_-}$, or even if an orbit visits $\mathcal{W}_{E_+}$ for a while, then it visits $\mathcal{W}_{E_-}$ (or, perhaps, $\mathcal{W}_{E_+}$ again) and successive visits to both domains are produced.

As we expected and explained in Sect. 2.6, the situation is different when an orbit approaches the islands of period 2 or 4 (or higher periods). After visiting the vicinity of an island going up, the orbit visits the vicinity of one island going down in next iterate, having close to zero average (after 2 or 4) iterations. This explains the qualitative differences between Figures 2.13 and 3.6.

ii) The Cantor sets.

Consider, first, $k \leq k_{c,1/4}$, that is a value such that there still exist invariant curves around the period-4 islands. Orbits in the chaotic sea can not cross these curves to become trapped by the island. But when they break down, they are replaced by Cantor sets, the iterates can penetrate inside the domain that was bounded by the previous invariant curves, approach the period-4 islands, spend some time near tiny islands, even entering the narrow chaotic channels between the main island and the period-4 islands, created by the very small inner splitting [134], where they can spend many iterates. Eventually, they leave the domain through the gaps of the Cantorus.

If $k > k_{c,1/4}$ the size of the gaps increases with the difference $k - k_{c,1/4}$. It becomes easier "to enter", but also the residence time in that domain decreases. This phenomenon is repeated at different scales around all the tiny islands visited by the iterates. In Chap. 4 we will study the escape rates across a golden Cantorus, with special emphasis on the change of statistics as one tends to the breakdown, and hence the gaps of the Cantorus become narrower.

The effects can be seen on the "bumps" presented in Figure 3.11 and, in a cleaner way, in Figure 3.12.

iii) The stickiness.

In fact one should not only consider the breakdown of the last invariant curve around the period-4 islands. For $k \leq k_{c,1/4}$ there are other curves, inside and outside, which were broken before. See Figures 3.1 and 3.2. For $k > k_{c,1/4}$, before penetrating through the narrow gaps of the "last created" Cantor set, they should enter the previously created Cantor sets, spend some time around the remnant islands, etc. This collective phenomenon, which is the geometrical meaning of stickiness in this setting, tells us that it is difficult to approach an island from outside: there are several gaps to cross. But when the orbit is inside it can remain there for a long time. Upper bounds on the speed of diffusion go back to the pioneer work of Nekhorosev [110], where the author assumed that no channels of dynamics blocked at resonance exist, a requirement which is formulated in terms of a steepness condition. Similar bounds, based on estimates of the remainder of the normal form around a totally elliptic fixed point with an application to the triangular Lagrangian points can be found in [53]. For multiple examples, discussions on fast and slow escape and many illustrations on the dynamics, see [31].

These collective effects can be seen in the linear behavior (in $\log_{10} - \log_{10}$ scale) of part of the plot shown in Figure 3.11.

### 3.5.2 Trapping time statistics around accelerator modes

From the last numerical simulations in Section 3.4, more concretely, the ones illustrated in Figure 3.9, for $N = 10^5$ and $T = 2^{30}$, we can extract valuable additional information. We have collected data on the "trips" of the $N$ initial points. In particular the trapping time $\mathcal{I}(t)$ in the domains $\mathcal{W}_{E_+}$ and $\mathcal{W}_{E_-}$. Recall Sect. 1.1.4. That is, when we have detected that an iterate approaches, say, the positive island (see end of Section 3.4.1), we count for how many iterates, $m$, it remains in $\mathcal{W}_{E_+}$ until leaving it. We introduce some intervals, of the form $I_j = [2^{j/2}, 2^{(j+1)/2}), j = 14, \ldots, 60$, and if $m \in I_j$ we add one unit to a counter $C_j$. At

the end of the computations we collect the counts in each box. This gives an estimate of the average "residence time" in the vicinity of the islands.

The results are shown in Figure 3.11 left. In it we plot all the curves corresponding to data for $k = 1.0512(10^{-5})1.0515$ simultaneously (a total of 31 curves). For the data in each counter $C_j$ we display, on the horizontal axis, the value of $\log_{10}(2^{j/2})$ and on the vertical axis the final value of $\log_{10}(C_j)$, adding the visits to $\mathcal{W}_{E_+}$ and $\mathcal{W}_{E_-}$. For instance we can read, from the left upper corner of the plot, that for all used values of $k$, the number of visits with a stay between 128 and 181 consecutive iterates exceeds the value of $10^8$. Note that in very few cases the length of the stays exceeds the value $2^{29}$ and they occur, mainly, for $k = 1.05125$ and $k = 1.05126$.

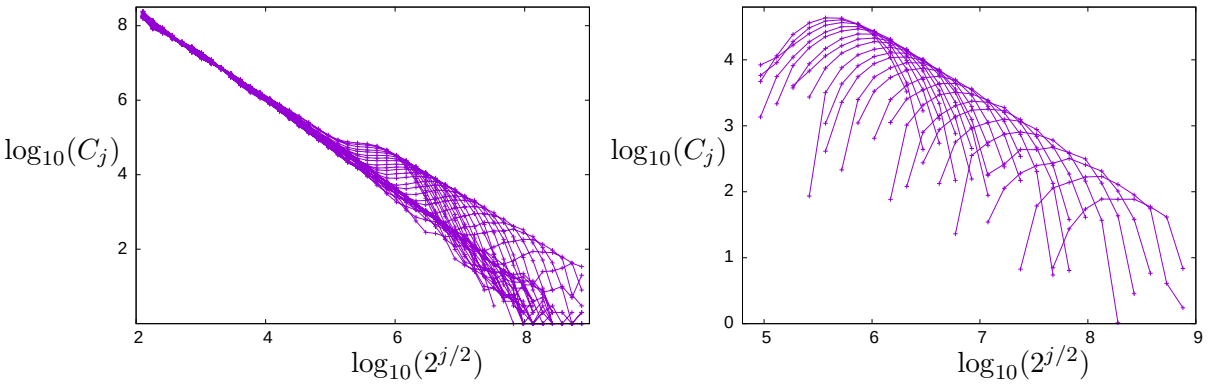


Figure 3.11: Left: number of times that the iterates visit $\mathcal{W}_{E_+} \cup \mathcal{W}_{E_-}$ with a stay in the range $I_j$ as a function of $2^{j/2}$. For both variables the $\log_{10}$ scale has been used. All the values of $k = 1.05120(10^{-5})1.05150$ are plotted simultaneously. Right: A measure of the size of the bumps in the left plot. See the text for details.

In the plot we see two distinctive phenomena: First, on top left, some monotonous decrease until a value of $j$ which depends of $k$. The smaller the value of $k$ is, the larger the value of $j$ up to which the decrease holds. And second, for a each value of $k$ shown, after the monotonous, close to linear, decrease until some value of $j$, one can see a "bump" in the value of $\log_{10}(C_j)$. These two effects are related to each other, namely as items ii) and iii) in the enumeration in Subsect. 3.5.1, but they seem to be visible in different scales of time.

### 3.5.3 Power law statistics

Here we want to do a simple remark to clarify the numerical results in Fig. 3.11, left. In this picture, we can clearly see that the histogram of the trapping times behaves as a power law, and that for all the parameter values shown it seems to be a limit of the value of the slope as the appearance of the bumps move right (that is, it goes outside the range where we can detect it). Actually these bumps only show up for $k > 1.05126$.

For each value of $k$, the behaviour in log-log scale seems to be linear up to some value $j_c$ of $j$. If we do a linear fit of the data for $j \in [14, j_c]$, for decreasing values of $k$ from 1.05150 to 1.05127, the approximate values of the slopes decrease monotonically from -1.11 to -1.21. But we expected a power-law behaviour $\mathcal{I}(t) \sim t^{-b}$, with $2 < b < 3$. This is what we actually get. If what we observed followed such a power law, in each bin $I_j = [2^{j/2}, 2^{(j+1)/2})$ we expect $C_j$ to be a multiple of the probability that the length of a stay $m \in I_j$, namely

$$\int_{2^{j/2}}^{2^{(j+1)/2}} t^{-b}\, dt = \frac{\left(2^{1/2}\right)^{1-b} - 1}{1-b} \left(2^{j/2}\right)^{1-b}.$$

Hence, in a log-log plot, a histogram of a power law $\mathcal{I}(t) \sim t^{-b}$ where the lengths of the bins are equispaced in logarithmic scale is seen as a straight line with slope $1-b$. Hence, the power law we see in Fig. 3.11, left, has actually an exponent $b$ ranging between 2.11 and 2.21.

### 3.5.4 The shape of the bumps

To analyze the bumps seen in Figure 3.11 left, we proceed as follows. For each value of $k$, we subtract from the counts $C_j$ the values predicted by the linear fit for $j > j_c$ explained above in Subsect. 3.5.3. The results are shown in Figure 3.11 right. Again in $\log_{10}$ scale for both variables, we plot in the horizontal direction the value of $2^{j/2}$ and in the vertical one the difference between the value of $C_j$ and the one predicted by the fit. This is a way to obtain a nice representation of the behaviour of the bumps in the left plot.

Note that for larger values of $k$ the height of the bumps is larger. This is natural, because they remain for less iterates in the "linear" regime of Figure 3.11 left, before entering into the bump.

The study of the source of the bumps is actually the contents of Chap. 4. But a brief explanation on our approach to study this effect is added here both to have a self-contained chapter and to motivate the next one. To investigate the shape seen in Figure 3.11 right, we place our study in a different range of values of $k$ for the $M_k$, concretely around the destruction of the last rotational invariant curve (RIC) for Greene's value $\bar{k}_G \approx 0.9716354061062$ [80, 83]. The parameter in classical formulations of the standard map is denoted as $\bar{k}$, which is related to the parameter $k$ we use in this work as $\bar{k} = 2\pi k$.

The last RIC appears for a rotation number $\rho = \omega := (\sqrt{5}-1)/2$ and, by symmetry, also for $1-\omega = (3-\sqrt{5})/2$. Let us denote them as the upper $\mathcal{W}_u$ and lower $\mathcal{W}_l$ last RIC. For values $\bar{k} < \bar{k}_G$ global diffusion is impossible. For $\bar{k} > \bar{k}_G$, close to $\bar{k}_G$, initial points located on a strip between $\mathcal{W}_u$ and $\mathcal{W}_l$ can move away.

The method given in Section 3.3.2 has been used to generate initial points in the unstable manifold of the period-2 hyperbolic orbit. Then these points are iterated until they "escape" from the previous strip. To detect the escape several methods can be used. The simplest one is to check if, in the formulation $M_k$ of the standard map, they cross either $y = 0$ or $y = 1$. Another method looks for an approximate representation of $\mathcal{W}_u$ and then this curve is slightly shifted up (down for $\mathcal{W}_l$). When an iterate crosses some of these shifted curves it is considered as escaped. Both methods agree very well for parameters close to the critical one.

For a decreasing set of values of $\bar{k}$ tending to $\bar{k}_G$ we have taken $10^7$ initial points, for every value of $\bar{k}$, and performed up to $10^{10}$ iterates of each of them until escape is detected. From the more than $2 \times 10^9$ initial points tested for many values of $\bar{k}$, only 46 have not yet escaped for $10^{10}$ iterates.

The Figure 3.12 shows some statistics of escapes for $\bar{k} = 0.98(0.005)1.04$. To this end we count, in a similar way to what has been described to obtain Figure 3.11, how many points, $C_j$, escape after a number of iterates $T$ in the interval $I_j = [10^{0.02j}, 10^{0.02(j+1)}), j = 100, \ldots, 500$. The top left plot in Figure 3.12 displays the values of $C_j$ as a function of $0.02j$. Obviously, the closer $\bar{k}$ is to $\bar{k}_G$, the larger the number of iterates is. In the top right plot the representation is similar, but instead of $C_j$ we display $\log_{10}(C_j)$. From one side, it is remarkable to see that, beyond a shift and a small deformation, the curves are very similar. On the other hand there is a strong similitude between the top right plot and the one that

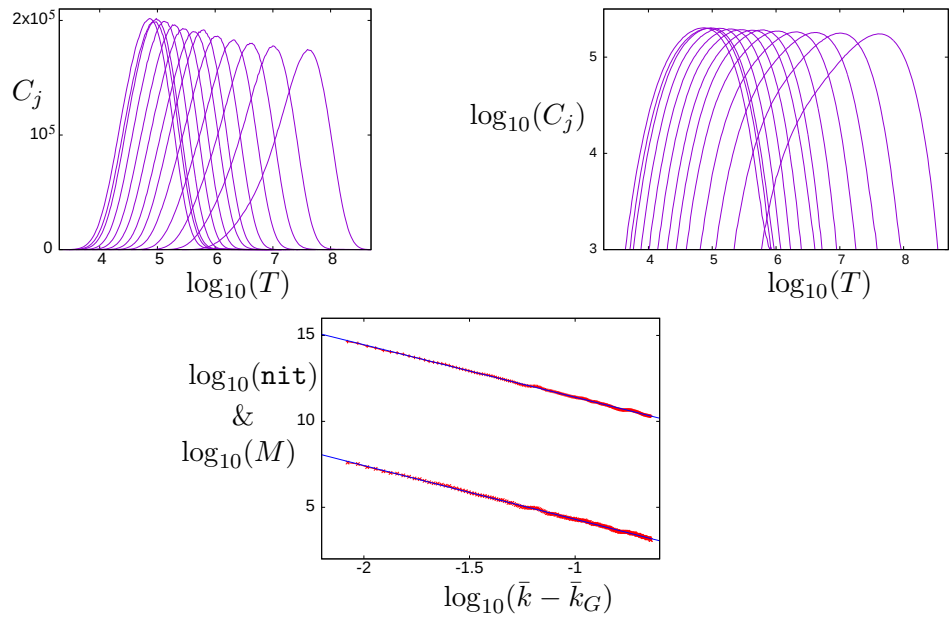


Figure 3.12: Statistics concerning the number of iterates to escape from an initially confined strip when the parameter $\bar{k}$ becomes larger than the critical Greene's value $\bar{k}_G$. In the top left and right plots the horizontal scale is $\log_{10}(T)$. The data on the left are represented in true scale and in the top right in $\log_{10}$ scale. Bottom: total number of iterates `nit` to have escape of all initial points (upper set) and maxima $M$ of the previous plots (lower set), both in $\log_{10}$ scale, as a function of $\log_{10}(\bar{k}-\bar{k}_G)$. Both sets have a behavior close to linear in these scales. For these plots we have used $\bar{k} = 0.980(0.001)1.200$. See the text for additional details. For values of $k$ closer to $k_G$ from above, the histograms on the top appear shifted to the right. See Sect. 4.5.3.

we have seen in Figure 3.11 right. This shows that the bumps in Figure 3.11 are due to the effect of the Cantori gaps surrounding the stability regions of $E_+$ and $E_-$. See Section 3.5.1 for further details.

To complete the information displayed in Figure 3.12, top, we can display, as a function of $\log_{10}(\bar{k}-\bar{k}_G)$, both the total number of iterates to have escape of (essentially) all the points, and the location of the maxima in the previous two plots, both numbers in $\log_{10}$ scale. This is shown in Figure 3.12 bottom. The straight lines show the corresponding linear fits. The slope for the upper data (iterates) is $\approx -3.05$ while the one for the lower data (maxima) is $\approx -3.13$. They are in good agreement with the expectations from renormalization theory around the golden rotation number curve breakdown, see Section 3.5.7, specially with (3.6). To get these slopes we fitted all the data displayed in Fig. 3.12, bottom. But if we get closer values to $k_G$ we expect it to change. In Sect. 4.5 we revisit this problem and give more accurate values of these slopes.

For completeness we have also computed, from the data shown in Figure 3.12, the average and standard deviation of the number of iterates to escape, as a function of $\bar{k}$. We found a good agreement with a power law of the form $(\bar{k}-\bar{k}_G)^{-\beta}$, for the value of $\beta$ in (3.6), both for the mean and for the standard deviation. Furthermore, as it is well-known from renormalisation theory [83], these two values tend to coincide when $\bar{k}$ tends to $\bar{k}_G$ and the numerical computations show this tendency.

### 3.5.5 Some additional numerical results

We return now to $M_k$ for $k$ slightly greater than 1, with the same set of values of $k$ used in Figure 3.9 right and in Figure 3.11.

**The probability to enter the islands zone**. As mentioned in Section 3.4.1 we can count how many times a temporary capture, i.e., entrance in $\mathcal{W}_{E_+} \cup \mathcal{W}_{E_-}$, is produced. This can be divided by the total number of iterates ($10^5 \times 2^{30}$ for each value of $k$). This gives an estimate of the probability that a point in the chaotic domain is temporary captured by an island. The results are represented in Figure 3.13 top left as a function of $k$.

**The fraction of time spent in the islands zone**. On the other hand we can check how many iterations are spent in these temporary captures. The results are shown in Figure 3.13 top middle. Note, however, that for the contribution to the standard deviation $\sigma_{T,k}$ for the present $T = 2^{30}$ it is not just the total number of iterates in $\mathcal{W}_{E_+} \cup \mathcal{W}_{E_-}$ what matters, but how long are the "stays" near the islands. A stay $10^6$ units long counts as much as 100 stays $10^5$ units long. Furthermore, to check that what really matters are the iterates and "stays" in $\mathcal{W}_{E_+} \cup \mathcal{W}_{E_-}$, for the set of values of $k$ used in Figure 3.13, we have computed the standard deviation looking only to the stays in $\mathcal{W}_{E_+} \cup \mathcal{W}_{E_-}$. Concretely, if some initial point has visited $m_+$ times $\mathcal{W}_{E_+}$ and $m_-$ times $\mathcal{W}_{E_-}$, it contributes as $m_+ - m_-$ to the computation of the standard deviation. All the iterates in the chaotic domain are discarded. The values of the $\sigma_{T,k}$ computed in that way have a relative error below 0.0005 with respect to the correct values for $k = 1.05120(0.00001)1.05150$.

**The growth of the diffusion coefficient as we iterate**. Finally we plot at the top right part of Figure 3.13 the evolution of the estimated value of the non-normalized standard deviation $\sigma_T(k)$, see (3.5), as a function of $T$ for the values of $k$ used to produce Figure 3.9 right. We use $\log_{10}$ scales. Globally one can see that up to $T \approx 10^4$ the behavior is close to linear, with a slope larger than 1/2. Concretely, it is close to 0.63, due already to the effect of the points near the islands. From that value of $T$ on, there is a change and the values of $\sigma_T(k)$ lie between two lines of slopes 0.7 and 1, say the lower and the upper lines. If we look at the individual behavior of the lines for the different values of $k$, see the details in the magnification shown in the bottom plot, it is checked that up to $k = 1.05123$ the curves stay near the lower line. For $k = 1.05124$ the curve ends in the middle of the lower and upper lines, with $\sigma_T(k) \approx 10^7$ for $T = 2^{30}$. For $k = 1.05126$ it reaches the upper line at the end of the $T$ domain. From that value of $k$ on, the curve has a tangency with the upper line, for values of $T$ which decrease as $k$ increases (compare with Figure 3.11), and then it decreases approaching the lower curve. The curves shown with thick blue lines illustrate this behavior.

Up to this point we have commented on the numerical results obtained. These results show that for a generic area-preserving map with a divided phase space the diffusion properties are far from trivial. Despite of the difficulties, and motivated by the interest in applications, many authors have investigated the diffusive properties both from numerical and theoretical points of view. Next subsection relates the numerical results obtained with the available theoretical approaches to the diffusive properties in the different regimes observed.

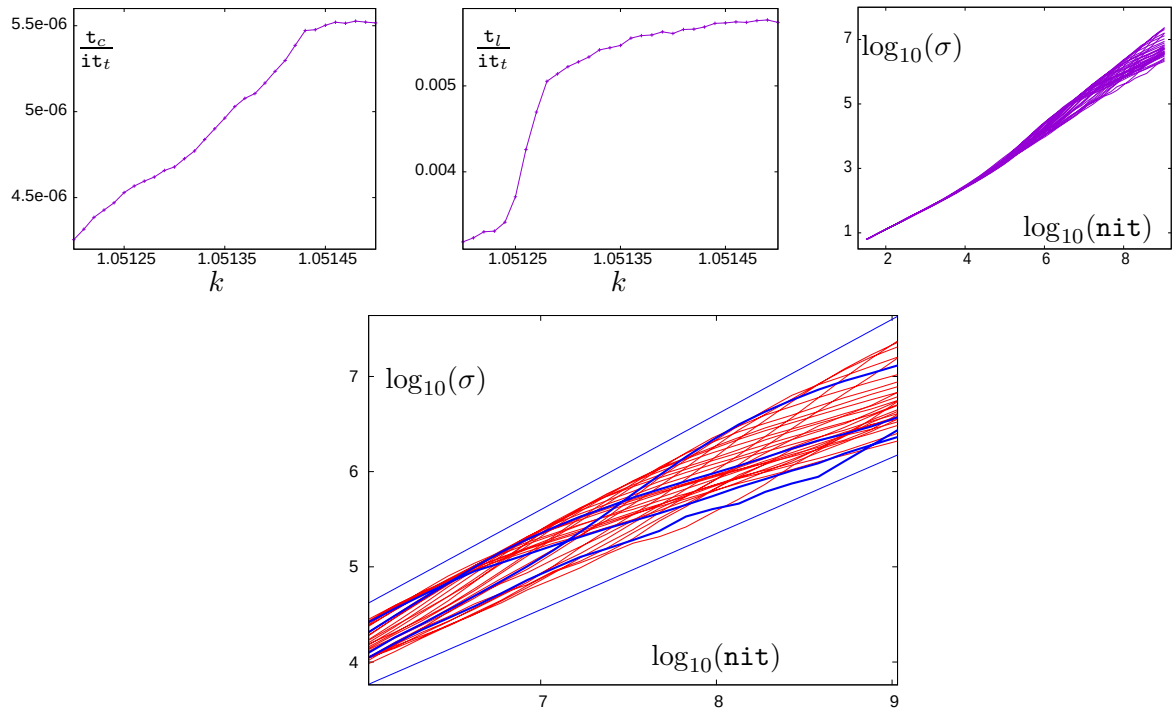


Figure 3.13: Top left: Number of temporary captures $\mathtt{t}_c$ in the $\mathcal{W}_{E_+} \cup \mathcal{W}_{E_-}$ domains divided by the total number $\mathtt{it}_t$ of iterates of all the initial points. Top middle: total lengths $\mathtt{tl}$ of the stays near islands divided by the same quantity. Both data are represented as a function of $k$. Top right: For all the $k$ values of the previous plots the standard deviation $\sigma$ is represented as a function of the number $\mathtt{nit}$ of iterates in $\log_{10}$ scale. Bottom: A magnification of the top right plot for $\mathtt{nit}$ between $2^{20}$ and $2^{30}$ with the lines for $k = 1.0512(0.0001)1.0515$ shown as thick blue lines. For reference two straight lines with slopes 0.7 and 1, mentioned as lower and upper lines in the text, are also shown.

### 3.5.6 Available theoretical frameworks from renormalisation schemes

In what follows we briefly present the theoretical frameworks that either support or even explain some of the numerical results shown.

**Concerning the power law statistics**. The correlation function is related to the probability $\mathcal{I}(t)$, the recurrence time in some fixed region of the phase space. To fix ideas, consider the accelerator mode islands of $M_k$. The probability $\mathcal{I}(t)$ relative to these islands was shown in Figure 3.11 left. First we note that in a purely diffusive regime the correlation function decays exponentially in time, see [75] and references therein ("time" here means "number of iterates of the map"). That would mean that the points can escape from the chaotic region easily as time evolves. However, we observed a power-law decay of $\mathcal{I}(t)$ for the region. Similar results were obtained in many other works, see [27, 29, 30, 68] for example. This means that trajectories are expected to be for a large number of iterates in the neighbourhood of the accelerator mode island, as confirmed by the numerical experiment in Section 3.4. See also [50, 51] for more recent computations on the statistics of the Poincaré recurrences using the Ulam method.

What causes the power-law decay and the stickiness effect has been analysed from differ-

ent points of view. The analysis performed in [27] derived a power-law behaviour in terms of the non-homogeneous diffusion coefficient $D(y)$ of the separatrix map. The analysis of self-similar solutions of the diffusion equation (which was suggested to include a suitable exponent $\alpha$) lead to the power-law probability distribution. This self-similarity was then related with suitable scalings in time and space of the island-around-island structure, meaning that for long-time evolution this hierarchy is the responsible of the behaviour of $\mathcal{I}(t)$. Further developments of this point of view were done by Zaslavsky and collaborators, giving rise to a renormalisation approach related to the hierarchical islands, see [148]. Let us give some details of this approach.

The presence of accelerator modes causes the divergence of the diffusion coefficient since the variance of a power-law distribution grows to infinity. Assume that the density of probability is of the form $f_{\mathcal{I}} \sim a/T^b$. For $2 < b \leq 3$ the expected value exists but the variance diverges. According to the Zaslavsky renormalisation scheme, see [149], one has

$$b = 1 + \frac{\log \lambda_s}{\log \lambda_T},$$

where $\lambda_s$ is the corresponding scaling factor of the area of two consecutive islands in the hierarchical structure and $\lambda_T$ is the scaling factor related to the period of the last invariant curves of these islands. These scalings are assumed to hold approximately and obtained from computations of the first islands in the structure. Several computations for the web map and the standard map for different hierarchies of islands show that $b \approx 2.2$. It is worth noting that the same factor was numerically observed in [97] for the Mather's $\Delta W$ [94] measured in different consecutive islands of a hierarchy (referred there by a class, see [97]), concretely it was observed that $\Delta W_c = \Delta W_{c-1} q^{-\psi}$, with $\psi = 2.2$ and where $p/q$, $p, q \in \mathbb{Z}$ is the frequency of the periodic point of the class $c$ orbit. We refer to [149] and references therein for further details. On the other hand, in [149] it was also observed that the variance of the fractional Fokker-Planck-Kolmogorov equation

$$\frac{\partial^\beta f}{\partial t^\beta} = \frac{1}{2} \frac{\partial^\alpha}{\partial(-x)^\alpha} \left( \frac{\partial^\alpha (Bf)}{\partial(-x)^\alpha} - \frac{\partial^\alpha B}{\partial(-x)^\alpha} f \right),$$

behaves like $t^{\beta/\alpha}$, which provides an explicit relation with the scalings $\lambda_s$ and $\lambda_T$ of the renormalisation scheme. Further discussions on scaling laws can be found in [145].

**Concerning the bumps**. In our experiments we also observed the stickiness effect of Cantori. To analyse this phenomenon MacKay in [80], and in an extended version in [83], defines a renormalisation operator in a class of area preserving twist maps. Here we summarize an extended version of the required explanation that can be found in Chap. 4. The nature of all the constants that appear here will be clarified there.

Let $\omega$ be an irrational number whose continued fraction expansion and rational convergents are

$$\omega = a_0 + 1/(a_1 + 1/(a_2 + \cdots)) \equiv [a_0, a_1, a_2, \ldots], \quad a_i \geq 1, i > 0; \quad p_n/q_n = [a_0, \ldots, a_n].$$

Then $p_n/q_n \to \omega$ as $n \to \infty$. Let $F_\mu : (I, \theta) = (\bar{I}, \bar{\theta})$ be a twist APM 1-periodic in $\theta$ and having a critical invariant circle of rotation number $\omega$ for $\mu = 0$, and $R(I, \theta) = (I, \theta - 1)$. The results obtained suggest that there are scalings $\Lambda_n$ such that the sequence

$$\Lambda_n^{-1} F_{\mu\delta^{-n}}^{q_n} R^{p_n} \Lambda_n$$

converges to a universal map $F^\star$, where $\Lambda_n \simeq \Lambda\Lambda_{n-1}$, $\Lambda(x,y) = (\alpha x, \beta y)$ and it does geometrically with ratio $1/\delta$. In particular he did computations for noble rotation numbers, that is, for which $a_i = 1$ for $i > i_0, i_0 \geq 0$ obtaining

$$\delta = 1.62795, \qquad \alpha = -1.4148360, \qquad \beta = -3.0668882\,. \tag{3.6}$$

The impact of these results in transport properties of the map in the vicinity of the just broken invariant circle are worth noting. One of the consequences of these scalings is that Mather's $\Delta W$ (recall Sect. 1.1.2 and Sect. 1.2) scales as follows. If $\Delta k$ is some small quantity,

$$\Delta W_\omega(k_c + \Delta k/\delta) \approx \Delta W_\omega(k_c + \Delta k)/(\alpha\beta),$$

so that there exists a 1-periodic universal function $U(x) = U(x+1)$ such that

$$\Delta W_\omega(k_c + \Delta k) \approx A(\Delta k)^B U(\log_\delta(\Delta k)), \qquad B = \log_\delta(\alpha\beta) \approx 3.0117220\,.$$

The quantity $\Delta W_{p,q}$, as is proved in [86] is exactly the *flux*, the area per iterate that crosses through the gaps in a periodic orbit (as explained at the end of Sect. 1.2), and $\Delta W_\omega$ is the area that crosses through a Cantorus (when it is an invariant curve the flux is zero, as expected). As a function of the parameter $k$ in the case of $M_k$ (1.13), the time to cross an invariant Cantor set $\langle N\rangle(k)$, conditioned to do it eventually, is related to the flux and the accessible area $\mathcal{A}(k)$ via the Kac formula [99]

$$\langle N\rangle(k) \times \Delta_\omega W(k) = \mathcal{A}(k), \tag{3.7}$$

where $\mathcal{A}(k)$ can be assumed to be bounded between two close positive constants for small enough variations of $k$ so that the time to cross an Aubry-Mather set, sufficiently close to the breakdown, behaves as

$$\langle N\rangle(k) \sim \frac{1}{\Delta k^B},$$

where $\log_\delta$-periodic fluctuations are expected. Note that this law is exactly the same observed by Chirikov in [26]. In order to be able to use this approach to the escape from an island, the effects of islands-around-islands should be included, as in the Markov tree model in [103].

### 3.5.7 Comparing with limit theoretical predictions

Now we are in situation to explain the changes observed on the behavior of the standard deviation, for different values of $k, T$ and $N$, at the light of the previous theoretical considerations.

For a given initial point, located in the chaotic domain, there is some small probability, say $\varepsilon_1$, to enter $\mathcal{W}_{E_+} \cup \mathcal{W}_{E_-}$. This is illustrated in Figure 3.13 top left. Note that even for $k < k_{c,1/4}$ one has $\varepsilon_1 > 0$. The iterates can enter in $\mathcal{W}_{E_+}$, say, but can not cross the still existing invariant curves. When increasing $k$, the value of $\varepsilon_1$ increases up to some saturation. This is due to the fact that the gaps of the more external Cantori are larger.

For $k < k_{c,1/4}$ the only contribution to $\sigma_T(k)$ is the "residence" in $\mathcal{W}_{E_+}$ but outside the invariant curves. Hence, the values of the standard deviation, either scaled or not, are not so large, as illustrated in Figure 3.9 (skip the effect of the small peaks). According to [149] one should have a power law with exponent $\approx -2.2$ in the residence time inside $\mathcal{W}_{E_+}$. Our

numerical results illustrated in Figure 3.11 are in very good agreement with these predictions, as explained in Subsect. 3.5.3.

Now assume $k > k_{c,1/4}$. Immediately after $k_{c,1/4}$ the gaps on the Cantor set which replaces the last invariant curve, are so small that they produce almost no effect. This can be seen, both in Figure 3.11, where the bumps displayed on the right start at $k = 1.05127$, and in the description of the bottom plot in Figure 3.13.

Further increase of $k$ leads to an increased probability to enter inside the last Cantorus. When inside, they remain there for an average number of iterates of the form $c(k - k_{c,1/4})^\beta$ for some $c > 0$ and $\beta$ as given in (3.6). For a given $T$ there exists a value of $k$, say $k^*(T)$ such that the mean residence time inside the last Cantorus equals $T$. In other words: some points enter inside that Cantorus and for the full number of iterates they remain inside. The final value of the jump $\Delta^T y = y_T - y_0$ equals $T$. Even if the fraction of points is not so large, there is a contribution to $\sigma_T(k)$ of the order of $T$.

Increasing $k$ from $k^*(T)$ on, should produce a decrease in $\sigma_T(k)$, because the probability to enter the last Cantorus is larger, the mean residence time is less or much less than $T$. Hence, the "large contributions" to $\sigma_T(k)$ are no longer present. It is clear that the iterates of a point which enter the last Cantorus and leave it, can reenter later (after many additional iterations), but the global effect will be less important. One would need many more iterates (i.e., a larger $T$) and this will decrease the slope in Figure 3.13 bottom.

This reasoning also explains the tangencies mentioned concerning Figure 3.13 bottom. When $k$ increases, the value of $T$ at the tangency decreases: the function $k^*(T)$ decreases if $T$ increases and tends to $k_{c,1/4}$ when $T \to \infty$. This is also related to the fact that, in many previous figures, using the scaled standard deviation, the maximum appears multiplied by a factor $\gamma$ when $T$ is increased by a factor $\gamma^2$.

Finally we can comment on the behaviour of $\sigma_T(k)$, for a fixed $k$ around $k_{c,1/4}$ for very large values of $T$, producing a lower bound of the standard deviation. We start by stating several simplifying assumptions. For concreteness we denote the domain $\mathcal{W}_{E_+} \cup \mathcal{W}_{E_-}$ as the islands zone, and the complement as the chaotic zone.

Assumptions:

a) A point in the chaotic zone has a probability $1 - \varepsilon$ to remain there after one iteration, and equal probabilities, $\varepsilon/2$, to enter either $\mathcal{W}_{E_+}$ or $\mathcal{W}_{E_-}$. Hence, the probability to remain for $m$ consecutive iterations in the chaotic zone and then to enter into the islands zone, is $(1 - \varepsilon)^m \varepsilon$. Both the average and standard deviation are $1/\varepsilon + \mathcal{O}(1)$. According to the data in Figure 3.13 top left, the values of $\varepsilon$ for $k$ around $k_{c,1/4}$ are close to $5 \times 10^{-6}$.

b) A point inside the islands zone remains inside at least for $m_0$ iterates. The probability to go out after $m > m_0$ iterates is of the form $c/m^b$ where $c > 0$ and $2 < b < 3$. From the normalization, requiring $\int_{m_0}^{\infty} c m^{-b}\, dm = 1$, it follows $c = (b-1) m_0^{b-1}(1 + o(1))$. The distribution has average $\approx \frac{b-1}{b-2} m_0$. The value of $b$ can be estimated from Figure 3.11 to be around 2.2 and $m_0$ can then be estimated from the average length of the stays in the islands zone, which follows from the plots in Figure 3.13 top, and the expression above for the average. The values of $m_0$ derived in this way range from 128 to 170, approximately.

The probability that the number of iterates in the islands zone exceeds a value $M$ is given by $(m_0/M)^{b-1}$. We recall, as already said, that the variance of this distribution becomes unbounded.

c) We assume that the different events (remaining in the chaotic zone, entering one or the other islands zones and remaining a given number of iterates in it) are independent. As commented in subsection 3.3.4 and illustrated in Figure 3.4, this is not true, but the correction factor obtained for the diffusion coefficient due to the correlation is not too far from one, so this is a reasonable hypothesis.

Under the above assumptions one has the following

**Proposition 2.** *The standard deviation of a sample of initial points after $T$ iterations, with $T$ large enough, is bounded from below by $T^{2-(b+1/b)/2}$.*

Proof. Let $\gamma > 0, \delta > 0$, to be selected during the proof. We consider the iteration of a given initial point. Assume, first, that until an iterate such that the total number of iterates in the chaotic zone is $T^\gamma$, all the entrances in the islands zones have lengths bounded by $T^\delta$ until a long stay entrance occurs.

From the central limit theorem applied to the distribution in the chaotic zone, one has that the number of times that an iterate enters the islands zone is $\varepsilon T^\gamma(1 + o(1))$. The probability that each of the lengths of the stays in the islands zone is bounded by $T^\delta$, is bounded by

$$\left[1 - \left(\frac{m_0}{T^\delta}\right)^{b-1}\right]^{\varepsilon T^\gamma} (1 + o(1)),$$

that behaves like $\exp(-\varepsilon m_0^{b-1} T^{\gamma-\delta(b-1)})$. This quantity is very close to 1, if we choose $\gamma - \delta(b-1) \leq 0$, taking into account the ranges of $\varepsilon, m_0, b$ that we are considering.

Now assume that a long stay in the islands zone occurs and the point remains there for, at least, $T$ iterates. The probability of such an event is $(m_0/T)^{b-1}$, and it can happen $\varepsilon T^\gamma(1 + o(1))$ times. The computation is stopped as soon as the total number of iterates exceeds $T$. If we assume that this long stay occurs in the positive island, even if the other stays are in the negative one, and neglecting the contribution $\mathcal{O}(T^{\gamma/2})$ due to the stays on the chaotic zone, the final value of $|y|$ is bounded from below by $T - 2\varepsilon T^\gamma T^\delta(1 + o(1)) > 0.999T$, provided $\gamma + \delta \leq 1$.

From the two conditions we get for $\gamma$ and $\delta$, the optimal choice is attained if

$$\gamma = \delta(b-1) \quad \text{and} \quad \gamma + \delta = 1 \quad \Leftrightarrow \quad \gamma = 1 - \frac{1}{b}, \quad \delta = \frac{1}{b}.$$

Under these conditions, the contribution to the sum of squares of the changes in $y$ is bounded from below by

$$\varepsilon T^\gamma(1 + o(1)) \left(\frac{m_0}{T}\right)^{b-1} (0.999T)^2. \tag{3.8}$$

This gives as exponent of $T$ in (3.8) equal to $4 - b - 1/b$. By the assumptions on the equal probabilities to enter $\mathcal{W}_{E_+}$ or $\mathcal{W}_{E_-}$, the average of $y$ is negligible in front of this quantity and the Proposition follows. □

Figure 3.14 shows an illustration similar to Figure 3.13 bottom, for $k = 1.0515$, a number of initial points $N = 10^4$ and a final number of iterations $T = 2^{40}$. For reference a line with

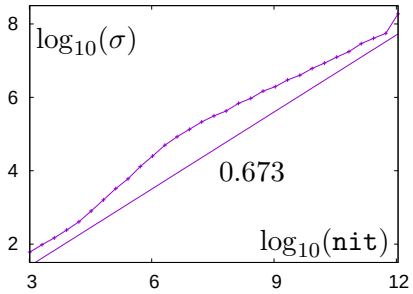


Figure 3.14: The standard deviation $\sigma$ as a function of the number of iterates $T$ for $k = 1.0515$, for large values of $T$. Both variables shown in $\log_{10}$ scale.

slope 0.7 is also shown. We note that, assuming $b = 2.2$, the lower limit of the slope predicted by proposition 2 is $\approx 0.673$. The contributions of other stays in the islands zones are responsible of the difference of limit slopes for $T$ very large. We should mention that for $T = 2^{38}$ and $T = 2^{39}$ the results are below what we expected, while for $T = 2^{40}$ are a little bit larger than expected. Looking at the behavior of the iterates of the initial points one checks that for $T = 2^{38}, 2^{39}$ the largest values of $|y|$ are slightly larger than $1.1 \times 10^9$, a little bit more than the value already reached for $T = 2^{37}$ iterates. On the other hand, for $T = 2^{40}$ one of the points reaches $y = 1.327 \times 10^{10}$. This single point gives half of the total contribution to $\sigma$. But this anomaly is nothing else than a consequence of the reduced size of the sample.

Next chapter is devoted to the study of the role of a single Cantorus in the phase space: we will extend the illustrative numerical results for the standard map for values of the parameter close to Greene's of Subsect. 3.5.4 and review the theory of Subsect. 3.5.6 to give an exhaustive explanation of which effects in diffusion should be attributed to Cantori. We will be mainly focused in understanding and describing the geometry of the phase space in a neighborhood of the Cantorus, for each fixed value of the parameter and as the parameter evolves towards the breakdown of the curve. And all the assertions will be accompanied with detailed massive numerical evaluations of escape rates.

# Chapter 4

# Escape times across a Cantorus

While RIC are complete transport barriers, Cantori have gaps that allow orbits to leak across them. But the number of iterates to do so can be extremely large due to the small size of the gaps. In this chapter we study escape rates across a golden Cantorus. As a main example, we use the Chirikov standard map for values of the parameter close to Greene's $k_G$, where the phase space shows self-similarity properties that can be explained via the Greene-MacKay renormalisation theory for the golden mean RIC. More concretely, this self-similarity implies that if we consider $k > k_G$ and we denote the mean to cross the Cantorus as $\langle N_k \rangle$, while $\langle N_k \rangle \to \infty$ as $k \to k_G$, for a suitable $B < 0$, $\langle N_k \rangle (k - k_G)^B$ is bounded. Moreover, it is actually 1-periodic in a suitable logarithmic scale. In this chapter we are going to give evidence of the shape of this periodic function and to interpret the results obtained for the escape rates by analysing the role of stability islands close to the Cantorus.

## 4.1 Introduction

The prediction of the actual transport properties of chaotic orbits in area-preserving maps (APM) requires the comprehension and description of the main invariant objects in the phase space, their relative position and size and how do they interact with each other.

KAM curves in APM are co-dimension one and hence confine the dynamics. In a perturbative setting, if the perturbation is large enough so that a RIC is destroyed, Aubry-Mather theory (recall Sect. 1.1.2) asserts that there exists a set in the phase space with the same rotation number of the destroyed curve, in the form of a Cantor set. These sets are usually referred to as *Cantori*. Since these Cantori have gaps, orbits can leak through, but one may expect the transit time to be extremely large if these gaps are small. Recall that, apart from these gaps, there are other phenomena that can play a leading role, such as the stickiness effect or even the small chaotic channels between an island of stability and its satellites.

The purpose of this chapter is to study quantitatively the escape rates across a Cantorus whose rotation number is the golden mean $\omega = (\sqrt{5} - 1)/2$. And this will be done by studying the phase space of the Chirikov standard map (4.1) for values of the parameter close to Greene's $k_G$, recall Sect. 1.2. The standard map is a meaningful example since it captures some relevant features of a universal 1-parameter family of maps that comes from the so-called Greene-MacKay renormalisation theory.

In Sect. 4.2 we review the main features of the Greene-MacKay renormalisation theory: the definition and dynamics of the renormalisation operator for golden invariant curves in APM.

In Sect. 4.3 we link the renormalisation operator with the phase space of the standard family of maps, and justify its choice as main example for our simulations. Here we will also explain how to properly scale the phase space close to the golden Cantorus with the aid of the position of periodic points whose rotation number is an approximant of the golden mean.

Sect. 4.4 is devoted to the study of the geometry of the phase space close to the Cantorus. We pay special attention to the local dynamics of elliptic/reflection-hyperbolic periodic orbits whose rotation number is an approximant of the golden mean, and to the area of the stability domain that surrounds them, if any. We argue that these objects are key to explain the transport rates across the Cantorus.

In Sect. 4.5 we present a numerical study of escape rates based on massive simulations inspired in those of the previous chapter. The available theoretical frameworks predict an inverse potential behaviour of the escape rates in a parameter that measures the distance to the breakdown $\Delta k = k - k_G,\ k > k_G$, plus some periodic fluctuations in logarithmic scale of $\Delta k$. Note that this potential behaviour is of different nature as the one we studied in Chap. 3. Here we show the shape of this periodic function and link it to the existence and evolution of the islands of stability we dealt with in Sect. 4.4. We finish by studying the probability law of the escape rates for each fixed value of $k$ considered, with special attention to the behaviour as $k \to k_G$.

And finally, in Sect. 4.5.4 we summarize the results obtained and the future directions one should consider that can lead to a better comprehension of the escape rates through Cantori.

In contrast to the chapters 2 and 3, in this chapter we will use the standard map in the original scale for the parameter. So, when working in the torus, we shall consider

$$\tilde{M}_k : \mathbb{T}^2 \to \mathbb{T}^2, \qquad \tilde{M}_k : \begin{pmatrix} x \\ y \end{pmatrix} \mapsto \begin{pmatrix} \bar{x} \\ \bar{y} \end{pmatrix} = \begin{pmatrix} x + \bar{y} \\ y + \frac{k}{2\pi} \sin(2\pi x) \end{pmatrix} \tag{4.1}$$

And $M_k$ will denote the lift to $\mathbb{S}^1 \times \mathbb{R}$. Throughout this section we are going to use $k_G \approx 0.971635406$.

## 4.2 Renormalisation for invariant curves. A review

Renormalisation in dynamical systems is a tool to deal with asymptotic self-similarity. In the discrete context, this is done by studying the system in smaller scales, by considering a conveniently scaled version of the original phase variables and in longer scales of time, by considering an iterate of the map instead of the original map. Note that, in order to be able to renormalise, we need the iterate of the map we have to consider to be a return map to a region that is similar to the whole phase space.

Kadanoff and Shenker [67] were the first to introduce a renormalisation approach to deal with RIC. Later, MacKay [83, 80] refined the idea by linking in a more precise way the renormalisation operator and RIC, by taking into account the pioneering work of Greene [63]. This approach is usually referred to as Greene-MacKay renormalisation theory.

It consists in the following: if $\rho$ is the rotation number of the RIC under study, the idea is to zoom in regions in the phase space chosen according to the relative positions of elliptic and hyperbolic periodic orbits whose periods are $p_j/q_j$ and $p_{j+1}/q_{j+1}$, two consecutive approximants of $\rho$, and to consider the $q_j$th iterate of the map in this region. Recall that from the twist condition (that implies the vertical ordering of orbits according to their rotation

number) and the fact that approximants alternate around $\rho$, the regions where the zoom is applied always contain part of either a RIC or a Cantorus with rotation number $\rho$. This procedure is inspired by the link between the linear stability of elliptic periodic orbits whose rotation number is an approximant $p_j/q_j$ and the existence of a RIC with rotation number $\omega$ as suggested by Greene in [63].

This section is a compendium of well known facts about the Greene-Mackay renormalisation theory for invariant curves in APM. The reader familiarized with this topic can skip this section. We summarize the main properties which will be used in the forthcoming sections in Subsubsect. 4.2.1.

**Notation**. In this chapter we will systematically deal with periodic orbits whose rotation number is an approximant $p_j/q_j$ of some irrational real number $\omega \in (0,1)$. From now on, we will refer to elliptic or reflection-hyperbolic orbits with $p_j/q_j$ as rotation number simply as *elliptic approximating orbits*, and in case they were hyperbolic, we will refer to them as *hyperbolic approximating orbits*. Moreover, we will refer to the stability domain $\mathrm{DS}(p_j/q_j)$ (recall Def. 7) surrounding elliptic approximating orbits as *approximating islands*.

### 4.2.1 Renormalisation for invariant curves

For an APM $\tilde{F} : \mathbb{T}^2 \to \mathbb{T}^2$ satisfying a twist condition, assume that it has a RIC with rotation number $\rho$ and that $(x_0, y_0)$ belongs to it. Denote the successive iterates under a lift $\bar{F}$ of $\tilde{F}$ to the plane, of the point $(x_0, y_0) \in \mathbb{R}^2$ as $\bar{F}^n(x_0, y_0) = (x_n, y_n)$. If $\{n_j/m_j\}_j$ is any sequence of rationals tending to $\omega$ as $j \to \infty$, then

$$\pi_1 \bar{F}^{m_j} R^{n_j}(x_0, y_0) = x_{m_j} - n_j \to 0,$$

where $\pi_1$ is the projection onto the first variable and $R(x, y) = (x - 1, y)$. This suggests that the study of the dynamics near the invariant curve can be approached by considering a sequence of maps of the form $\Lambda \bar{F}^{m_j} R^{n_j} \Lambda^{-1}$, where $\Lambda$ is a change of variables that is meant to scale the phase space in a way that will be explained later on.

The setting introduced by MacKay [83, 80] consists in embedding this sequence as iterates of some operator in a suitable functional space. The dissipative case was solved by Rand in [117] using the same techniques.

The renormalisation operator defined by MacKay [83, 80] is the following:

$$\mathcal{R}_m(U, T) = \Lambda(T, T^m U)\Lambda^{-1}, \qquad m \in \mathbb{Z},$$

where we have used the notation $\Lambda(A, B)\Lambda' = (\Lambda A \Lambda', \Lambda B \Lambda')$. This is an operator acting on commuting pairs of orientation-preserving diffeomorphisms: $(U, T)$ from $\mathbb{R} \times \mathbb{R}$ to ranges on it, that commute where the compositions $UT$ and $TU$ are defined. Note that if we apply $\mathcal{R}_{l_i}$ successively to a pair of commuting maps, where $l_i$, $i \geq 0$ are the integers of the continued fraction expansion of an irrational real number $\omega = [l_0, l_1, l_2, \ldots]$, we obtain the following:

$$\mathcal{R}_{l_j} \cdots \mathcal{R}_{l_0}(U, T) = \Lambda_{j+1}(U^{q_j} T^{p_j},\ U^{q_{j+1}} T^{p_{j+1}}) \Lambda_{j+1}^{-1},$$

where $\Lambda_{j+1}$ is the composition of successive shifted scalings. This follows from properties of continued fraction expansions.

**Remark 6.** *1.* On the assumptions for the pair of commuting maps $U$ and $T$. *It is not necessary to assume twist properties nor area-preservation for the definition of $\mathcal{R}_m$. MacKay in [84] proved the existence of invariant curves for infinitely renormalisable commuting pairs (meaning those for which one can apply infinitely many times $\mathcal{R}_m$, for convenient $m$) without using any of these two assumptions. But usually area-preservedness is implicit when using the generating functions of $U$ and $T$ instead of the maps themselves, see [83, 139, 140, 1, 73], for instance.*

*2.* On the existence of a symmetry. *The whole setting requires the existence of a preferred symmetry line. Despite not being the most general setting, it is usually assumed to hold. Note that the most common and paradigmatic examples of maps like the Hénon map or the Chirikov standard map have such a symmetry.*

The link between this setting and ours, that is, for area-preserving twist maps $F$ (now with some symmetry line) is just to consider the pair $(F, FR)$, where $R(x, y) = (x - 1, y)$. If, for example, we iterate this pair under $\mathcal{R}_1$, since $F$ and $R$ commute, we obtain

$$(F, FR) \mapsto \Lambda_1(FR, F^2R)\Lambda_1^{-1} \mapsto \Lambda_2(F^2R, F^3R^2)\Lambda_2^{-1} \mapsto \Lambda_3(F^3R^2, F^5R^3)\Lambda_3^{-1} \cdots \qquad (4.2)$$

where again $\Lambda_j$ means the composition of successive shifted scalings, which may change for each iteration, and in some cases it may tend to a limit $\Lambda$. The existence of such a limit is a necessary requirement for the existence of fixed points, and is a key feature in renormalisation theory.

### Observables related to orbits under renormalisation

One can easily translate the concepts of orbits, periodic orbits and invariant curves to (proper) iterates of commuting pairs, see [83]. But we are mostly interested in the following quantities, that are either conserved or nicely transformed under the action of the renormalisaton operator. We will not deal with commuting pairs but with twist APM $F$. If we want to study the RIC with rotation number $\rho = [l_0, l_1, l_2, \ldots]$ of $F$, we have to deal with the $n$th iterate of $F$ under the renormalisation operator. It suffices to study the first component of $\mathcal{R}_{l_n} \cdots \mathcal{R}_{l_0}(F, FR)$, $\Lambda F^{q_n} R^{p_n} \Lambda^{-1}$. If $m > 0$ is an integer, we will refer to the first component of $\mathcal{R}_m(F, FR)$ simply as $\mathcal{R}_m[F]$.

So, let $m > 0$ be an integer,

1. Rotation number. If a map $F$ has an orbit with rotation number $\rho = [l_0, l_1, l_2, \ldots]$, then $\mathcal{R}_{l_n} \cdots \mathcal{R}_{l_0}(F, FR)$ has an orbit with rotation number $\rho' = [l_n, l_{n+1}, \ldots]$. In particular, if $\omega = (\sqrt{5} - 1)/2 = [1, 1, 1, \ldots]$, and $p_j/q_j$ are its approximants, if $F$ has an orbit with rotation number $p_j/q_j$ then $\mathcal{R}_1[F]$ has an orbit with rotation number $p_{j-1}/q_{j-1}$, the previous approximant; and if $F$ has a golden RIC (resp. Cantorus) then $\mathcal{R}_1[F]$ has a golden RIC (resp. Cantorus).

2. Linear stability of periodic orbits. For a $q$-periodic orbit for an APM $F$, its linear stability is determined by the trace
$$\tau = \mathrm{tr} DF^q(x_0, y_0),$$
where $(x_0, y_0)$ is any point in the orbit. Then, if $F$ has an orbit with rotation number $\rho = p/q$ with $\tau$ as trace, then the corresponding periodic orbit with rotation number $\rho' = p'/q'$ of $\mathcal{R}_1[F]$ has also trace $\tau$. This follows from the fact that $\mathcal{R}_1$ consists in iterating $F$ conveniently.

### 4.2.2 Dynamics of the renormalisation operator

From now on, unless otherwise stated, the golden mean will be denoted as $\omega = (\sqrt{5}-1)/2 = [1,1,1,\ldots]$. Recall that its approximants are quotients of successive Fibonacci numbers. We will denote them as $p_j/q_j$, and by $j$th approximant we will refer to the element with subscript $j$ in the sequence

$$q_{j+1} = q_j + q_{j-1}, \quad p_{j+1} = p_j + p_{j-1}, \qquad p_0 = 0, \quad p_1 = q_0 = q_1 = 1.$$

Since the continued fraction expansion of $\omega$ is constant and has all the quotients equal to 1, the study of golden invariant curves is done via the operator

$$\mathcal{R}_1(U,T) = \Lambda(T, TU)\Lambda^{-1},$$

(recall that we choose $U = F$ and $T = FR$), where $\Lambda : \mathbb{R}^2 \to \mathbb{R}^2$ has the following form

$$\Lambda : \begin{pmatrix} \xi \\ \eta \end{pmatrix} \mapsto \begin{pmatrix} \alpha\xi + c \\ \beta\eta + p(\xi) \end{pmatrix} \tag{4.3}$$

being $\alpha, \beta \in \mathbb{R}$ the phase scaling factors, $c \in \mathbb{R}$ is a constant and $p(x)$ is a real polynomial that we shall consider to be of degree 3, see Sect. 4.3.1.

The dynamics of the renormalisation operator $\mathcal{R}_1$ was first studied in MacKay's Thesis [83, 80], where he described the most important features of its phase space. Some of them have been already proven, but some essential questions that have a reasonable conjectural solution remain still open, [78].

Essentially, when acting on the area preserving zero flux class of maps, the most relevant part of the phase space of $\mathcal{R}_1$ is characterized by the existence of two fixed points:

1. $R_T$, the trivial fixed point, which corresponds to an integrable linear shear

$$R_T \begin{pmatrix} x \\ y \end{pmatrix} = \begin{pmatrix} x + (\omega+1)y + \omega \\ y \end{pmatrix}.$$

   Note that it is just a translation of the standard map for $k = 0$. It is an attracting fixed point in the area-preserving class of maps, see [83].

   Furthermore, all the periodic orbits in the phase space of $R_T$ are parabolic ($\tau = 2$).

2. $R_C$, the critical fixed point, that is a map having a critical golden invariant curve. In [83], MacKay computed it very convincingly ($R_C$ and a 1-parameter family that travelled along $W^u(R_C)$), and gave numerical evidence of the fact that it is a saddle, with a single unstable eigenvalue $\delta$. The existence of $R_C$ was finally proven in [1] by Arioli and Koch and the fact that it was hyperbolic with a single unstable direction with eigenvalue $\delta$ was proven by Koch in [73].

   All elliptic approximating orbits of $R_C$ have the same trace, $\tau = \tau^\star$, see (4.7).

MacKay conjectured that the dynamics in a neighborhood of these two fixed points was as sketched in Fig. 4.1. In this figure we also added in red the conjectured relative position of the standard family in this functional phase space.

Note that $W^s(R_C)$ is a co-dimension 1 invariant manifold of maps with a critical golden RIC, so locally separates maps with a golden RIC and maps with a golden Cantorus. Hence

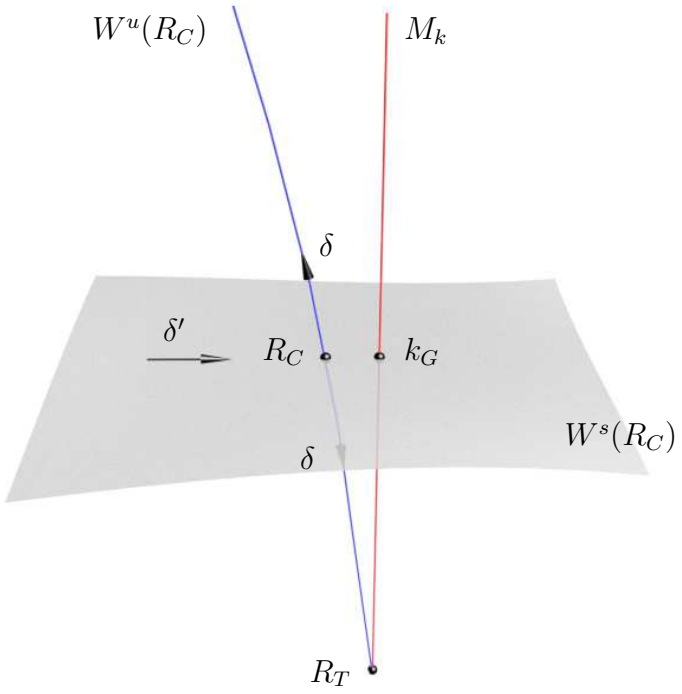


Figure 4.1: Sketch of the conjectured skeleton of $\mathcal{R}_1$.

$W^u(R_C) \setminus \{R_C\}$ has two components. Denote the one that consists in maps with a golden RIC as $W^{u,-}(R_C)$, and the other component as $W^{u,+}(R_C)$. A conjecture related to Fig. 4.1 that is still open is if $W^{u,-}(R_C)$ is a heteroclinic connection between $R_T$ and $R_C$, that is, if this whole branch is contained in the basin of attraction of the trivial fixed point $R_T$. In fact, it was the original motivation of the renormalisation operator: the goal was to prove that all maps with a golden RIC converged to $R_T$ under $\mathcal{R}_1$. For results in this direction one can see, for instance, [64, 139, 140].

## 4.3 The standard family in the phase space of $\mathcal{R}_1$

All numerical experiments dealing with approximating periodic orbits of the golden RIC carried out for the standard map suggest that this family of maps is close to $W^u(R_C)$, as depicted in Fig. 4.1. Namely, the approximations of the phase space scalings $\alpha$ and $\beta$ (4.3) and the eigenvalue $\delta$ given in [1, 73] in the proofs of the existence and hyperbolicity of $R_C$ agree with the corresponding quantities found experimentally in the standard map [67, 80, 83].

The constants $\alpha, \beta$ and $\delta$ are essential for the rest of the chapter. So it is worth recalling how they were first obtained. Here we will use that all monotone elliptic periodic points in the standard map (4.1) have a point on the symmetry line $\{x = 1/2\}$ [83]. Let $k_j$ denote the value of the parameter at which the $j$th elliptic approximating orbit is at a period-doubling bifurcation[1]. Let $(1/2, y_j)$ denote the position of the point of this orbit on the symmetry line for $k = k_j$. And if $j$ is odd (resp. even), let $x_j$ be the $x$-coordinate of the point in the

[1]We will slightly change this notation in Sect. 4.4.

$j$th hyperbolic approximating orbit closest to the right (resp. left) to $\{x = 1/2\}$. From the symmetries of the standard map, the points in the hyperbolic orbit that are the closest to the left or to the right to the symmetry line are exactly at the same distance to the symmetry line.

1. The eigenvalue $\delta$ was first approximated in [83] as the rate of convergence of the sequence $\{k_j\}_j$:

$$\lim_{n\to\infty} \frac{k_n - k_{n-1}}{k_{n+1} - k_n} = \delta \approx 1.627950064984581616762404257349 86. \tag{4.4}$$

   The value we provide here in (4.4) is the one found by Koch in his proof [73], of the hyperbolicity of $R_C$ under $\mathcal{R}_1$.

2. The phase scaling $\beta$ measures the rate of convergence to 0 of the relative distance between consecutive elliptic approximating orbits on the symmetry line

$$\lim_{n\to\infty} \frac{y_n - y_{n-1}}{y_{n+1} - y_n} = \beta \approx (-0.32606339662500148530812206358643)^{-1}, \tag{4.5}$$

   and $\alpha$ measures the rate of convergence to 0 of the relative distance between elliptic and hyperbolic orbits of the same rotation number

$$\lim_{n\to\infty} \frac{(x_n - 0.5) - (x_{n-1} - 0.5)}{(x_{n+1} - 0.5) - (x_n - 0.5)} = \alpha \approx (-0.706795669179637278164917314 16)^{-1}. \tag{4.6}$$

   Again, these are the most accurate values of these constants available in the literature, and can be found in [1, 73]. Furthermore, they agree with the actual values for the standard map [67, 83].

3. There are two other constants that is worth to take into account. MacKay in [83, 80] noticed that, if we denote by $\mathrm{tr}_j(k) = \text{trace } DM_k^{q_j}(1/2, y_j(k))$, where $y_j(k)$ is the position on the symmetry line $\{x = 1/2\}$ of the $j$th elliptic approximating orbit at the value of the parameter $k$, one gets the limit

$$\lim_{n\to\infty} \mathrm{tr}_j(k_G) = \tau^\star \approx 0.999644. \tag{4.7}$$

   MacKay also approximated the convergence rate of the sequence $\{\mathrm{tr}_j(k_G)\}_j$,

$$\lim_{n\to\infty} \frac{\mathrm{tr}_n(k_G) - \mathrm{tr}_{n-1}(k_G)}{\mathrm{tr}_{n+1}(k_G) - \mathrm{tr}_n(k_G)} = \delta' \approx -(0.6108)^{-1}. \tag{4.8}$$

   Moreover, this is the dominant eigenvalue in $W^s(R_C)$, see [83, 80].

As a final remark, note that, despite the standard family captures the behaviour of $W^u(R_C)$, the family of maps $M_k$ is not invariant under $\mathcal{R}_1$. Namely, if $k > k_G$ the orbit of $M_k$ under $\mathcal{R}_1$ will have some iterates close to $W^{u,+}(R_C)$ due to the hyperbolic character of $R_C$ in the functional space. And after some iterates, the maps one obtains behave as maps with a seemingly fully chaotic phase space. If $k < k_G$ then the iterates are conjectured to tend to $R_T$. And if $k = k_G$, since $M_{k_G} \in W^s(R_C)$, it will tend to $R_C$ under iteration of $\mathcal{R}_1$.

We strongly suggest [78] for a full and comprehensive explanation on the dynamics of $\mathcal{R}_1$, the open questions related to the renormalisation operator and its relationship with Greene's criterion [63] and with Olvera and Simó's Obstruction criterion [112].

Note the scaling factors and eigenvalues $\alpha, \beta, \delta$ and $\delta'$, and even $\tau^\star$ depend strongly on the continued fraction of the rotation number of the RIC under study. Namely, for noble rotation number the set of parameters we should eventually find are $\alpha, \beta, \delta, \delta'$ and $\tau^\star$, but not necessarily for metallic irrational numbers (those whose quotients in their continued fraction expansion are equal or eventually equal to $a \in \mathbb{N}$, $a > 1$). Moreover, if the corresponding continued fraction expansion is $n$ periodic, one expects the corresponding renormalisation operator to have a critical $n$-periodic orbit and a set of $n$ different values of $\tau^\star$, and of course different scalings. See [15].

### 4.3.1 Choice of the successive scalings $\Lambda_j$

As commented above, the way the scalings $\Lambda_j$ are chosen is related to the positions of the approximating periodic orbits. Approximating orbits are not generically on straight horizontal lines, so one can not expect to find examples of maps where $\Lambda_j$ is a diagonal scaling (that is, $c = 0$ and $p(x) = 0$ for all $x$ in (4.3)). But if we assume that we have a preferred symmetry line where all elliptic monotone orbits have a point on, we can reduce $\Lambda_j$ to be of the form (4.3). Since in practice we will study elliptic periodic orbits in the standard map, this symmetry line is $\{x = 1/2\}$. Hence $c = 0$ in (4.3). And we are going to use the coordinate $\xi = x - 1/2$ instead of $x$.

Let us consider the $j$th approximant of $\omega$. The way to renormalise the domains around the golden invariant curve or Cantorus between the orbits with rotation number $p_j/q_j$ and $p_{j+1}/q_{j+1}$ is to consider scalings defined as follows:

1. Compute the following orbits and points:
   - 1.1 The elliptic (or reflection-hyperbolic) orbit on the symmetry line with $p_j/q_j$ as rotation number. Call it $P_e^j$.
   - 1.2 If $j$ is odd (resp. even), the point in the orbit of $P_e^j$ closest to the right (resp. left) of it. Call it[2] $Q_e^j$.
   - 1.3 The elliptic (or reflection-hyperbolic) orbit on $\{x = 1/2\}$ with $p_{j+1}/q_{j+1}$ as rotation number. Call it $P_e^{j+1}$. It can be either above or under $P_e^j$, depending on the parity of $j$.
   - 1.4 The hyperbolic orbit with $p_j/q_j$ as rotation number[3]. Call the points in this orbit closest to $P_e^j$ to the left and to the right as $L_h^j$ and $R_h^j$, respectively.
2. Let $p^{(j)}(\zeta) = s_1^{(j)}\zeta + s_2^{(j)}\zeta^2 + s_3^{(j)}\zeta^3$ the cubic interpolating polynomial of the 4 points $L_h^j, P_e^j, R_h^j, Q_e^j$, after moving their abscissas $-0.5$, that is, in such a way that the $x$-coordinate of $P_e^j$ is 0.
3. Let $d_x^{(j)} = \max\left(|\pi_1(P_e^j - L_h^j)|, |\pi_1(P_e^j - R_h^j)|\right)$, and $d_y^{(j)} = |\pi_2(P_e^j - P_e^{j+1})|$, where $\pi_1$ and $\pi_2$ are the projections onto the first and second variable.

[2] This point has to be chosen in different sides of the symmetry line depending on the parity due to the fact that two periodic orbits with consecutive approximants as rotation number lie on different sides of the invariant curve or Cantorus.

[3] In the case of the standard map (4.1), it can be found on the lines $\{y = 2x\}$ or $\{y = 2x - 1\}$.

After all these computations, consider the sequence of changes of variables obtained as the composition of, first, scaling around $P_e^j$ by $d_x^{(j)}$ in the $x$ direction and by $d_y^{(j)}$ in the $y$ direction, then subtracting $p^{(j)}(\zeta)$ in the second variable and finally shifting the coordinates to translate $P_e^j$ to the origin. This altogether reads (suppressing some dependencies on $j$ to lighten the notation)

$$\Lambda_j : \begin{pmatrix} \xi \\ \eta \end{pmatrix} \mapsto \begin{pmatrix} d_x\xi + 1/2 \\ d_y\eta + \pi_2(P_e^j) + s_1 d_x\xi + s_2(d_x\xi)^2 + s_3(d_x\xi)^3 \end{pmatrix} = \begin{pmatrix} x \\ y \end{pmatrix}, \tag{4.9}$$

and transforms the rectangle $[-1,1]\times[0,1]$, where the island is centered in the origin and the next approximant is at $(0,1)$, into the variables of the standard map, see Figures 4.2 and 4.3 for some examples. Before continuing, we must take into account the following.

**Remark 7.** *1. Concerning $d_x^{(j)}$, the symmetries of the standard map imply that, actually $|\pi_1(P_e^j - L_h^j)| = |\pi_1(P_e^j - R_h^j)|$. Hence in the box $[-1,1]\times[-1,1]$ we will have $(-1,0)$ and $(1,0)$ as hyperbolic fixed points and $(0,0)$ as a fixed elliptic or reflection-hyperbolic fixed point.*

*2. The sequences $d_x^{(j)}$ and $d_y^{(j)}$ go to zero geometrically with rates $\alpha$ and $\beta$, respectively.*

*3. The fact that the polynomial $p(\zeta)$ has been chosen as cubic is enough [84, 73], since there is numerical evidence that this condition guarantees that after $q_j$ iterates of points in some compact domain around $P_e^j$ return to the desired domain.*

*We want the renormalised domain close to $\eta = 0$ to be a map on a cylinder, that is, to be able to identify the segments of points with coordinates $(-1,\eta)$ and $(1,\eta)$ where $\eta \in (-\kappa,\kappa)$, $\kappa > 0$ but small. To do so, the right branches of the invariant manifolds of $(1,0)$ should be the same as the right branches of the invariant manifolds of $(-1,0)$, but horizontally shifted by 2 units. And we get this by imposing that $\Lambda_j^{-1}(Q_e^j)$ also lies on $\eta = 0$.*

**Symmetries of the Standard map**. The cubic polynomial $p^{(j)}(\zeta)$ has a relationship with the symmetries of the standard map. Recall the De Vogelaere decomposition of $M_k$ in involutions [63]:

$$I_1 : \begin{pmatrix} x \\ y \end{pmatrix} \mapsto \begin{pmatrix} -x+y \\ y \end{pmatrix}, \quad I_2 : \begin{pmatrix} x \\ y \end{pmatrix} \mapsto \begin{pmatrix} -x \\ y + \frac{k}{2\pi}\sin(2\pi x) \end{pmatrix}, \qquad M_k = I_1 \circ I_2.$$

Since all the orbits we are dealing with are symmetric, they are their own reflection under $I_1$ and $I_2$. Moreover, we are dealing with points in invariant sets under $I_2$ that are near the set of fixed points of $I_2$, $\{x = 1/2\}$, and actually are closer by a factor $\alpha$ as we increase $j$. Hence, in the limit $j \to \infty$ the set of 4 points we are interested in should be on some invariant of $I_2$.

If we set $y = g(x) = g_0 + g_1 x + g_2 x^2 + g_3 x^3 + \cdots$ and impose that $g(x)$ is invariant under $I_2$ locally around $x = 1/2$, we get the following necessary conditions:

$$2g_i = (-1)^{i+1} k \frac{(2\pi)^i}{i!}, \quad \text{where } i \text{ is even},$$

but this argument does not give any information on the odd coefficients. Since $p^{(j)}(\zeta)$ is a cubic polynomial, for each fixed value of $k$ one gets

$$\lim_{j\to\infty} s_1^{(j)} = \frac{k}{2}, \qquad \lim_{j\to\infty} s_3^{(j)} = -\frac{\pi^2}{3}k. \tag{4.10}$$

In Sect. 4.4 we will deal with some special sequences of values of the parameter $k$: we will denote by $k_j(\tau)$ the value of the parameter for which $P_e^j$ has trace $\tau$. We will provide with evidence that regardless of the value of $\tau < 2$, the sequence $\{k_j(\tau)\}_j$ tends to $k_G$. Hence, we expect the polynomials $p^{(j)}(\zeta)$ to have limit coefficients $s_1 = k_G/2$, $s_3 = -\frac{\pi^2}{3}k_G$ and some value for $s_2$ that cannot be predicted from the symmetries of $M_k$. In Sect. 4.4 we will provide with numerical evidence on the limit values of the coefficients $s_1, s_2$ and $s_3$ one obtains when travelling along the sequence $\{k_j(-1)\}_j$, see Tab. 4.1.

### 4.3.2 Iterating $M_k$ under $\mathcal{R}_1$. An example

Before studying with more detail how is the phase space around a Cantorus, it is worth showing how do renormalised domains in the standard map look like. Here we show the part of the phase space transformed under the changes of variables $\Lambda_j$ that we just outlined how to derive.

In Fig. 4.2 and Fig. 4.3 we show the phase space of $\mathcal{R}_1^j[M_k] = \Lambda_j^{-1} \circ M_k^{q_j} \circ \Lambda_j$ in $(\xi, \eta) \in [-1, 1] \times [0, 1.2]$. We considered an equispaced $512 \times 512$ grid and we indicate in light grey those pixels whose center can be considered regular by approximating the maximal Lyapunov exponent. In black, we highlight the positions of the 0/1, 1/2 and 2/3-periodic orbits of $\mathcal{R}_1^j[M_k]$. More concretely,

1. In Fig. 4.2 we show how does $\mathcal{R}_1$ act on $M_k$, for $k = 0.9716$. Recall that for this value of the parameter the golden RIC exists, see [45]. Hence, as conjectured [80, 83] (recall Fig. 4.1) we expect the iterates under $\mathcal{R}_1$ to tend to $R_T$. On top left, we can see the domain defined between the original 1/2-periodic orbit (that appears as the fixed point at the origin) and the original 2/3-periodic orbit (that appears as the 2-periodic orbit at $(0, 1)$). Recall that in this top left picture we are showing the dynamics around the golden RIC under $M_k^2$. We have highlighted the points in the orbits that are going to define the next domain where to zoom, and this zoomed phase space ($M_k^3$ between the 2/3 and the 5/8 periodic orbits of the original map $M_k$, and changing signs both in $\xi$ and $\eta$) is shown on the right. We show 16 iterates of the map. The title in each picture indicates the number of iterate. Note that, as we iterate, we tend to a more regular phase space, as conjectured in [83]; in fact in the phase space of the 17th iterate (not shown), in the resolution used for these plots, we do not detect a single chaotic orbit.

2. And in Fig. 4.3 we show how does $\mathcal{R}_1$ act on $M_k$, for $k = 0.98$. The pictures are produced exactly the same way as for $k = 0.9716$. But here note that as we iterate $\mathcal{R}_1$, the phase space seems to become more and more chaotic. This is the expected behaviour once the golden RIC is destroyed, see Fig. 4.1. To reach a seemingly fully chaotic phase space (in the resolution used here) for $k = 0.98$ one only needs 11 iterates (not shown in the figure).

## 4.4 The phase space near a Cantorus

In this section we want to describe the phase space around a broken invariant curve. It turns out that the Greene-MacKay renormalisation theory allows to make predictions on the

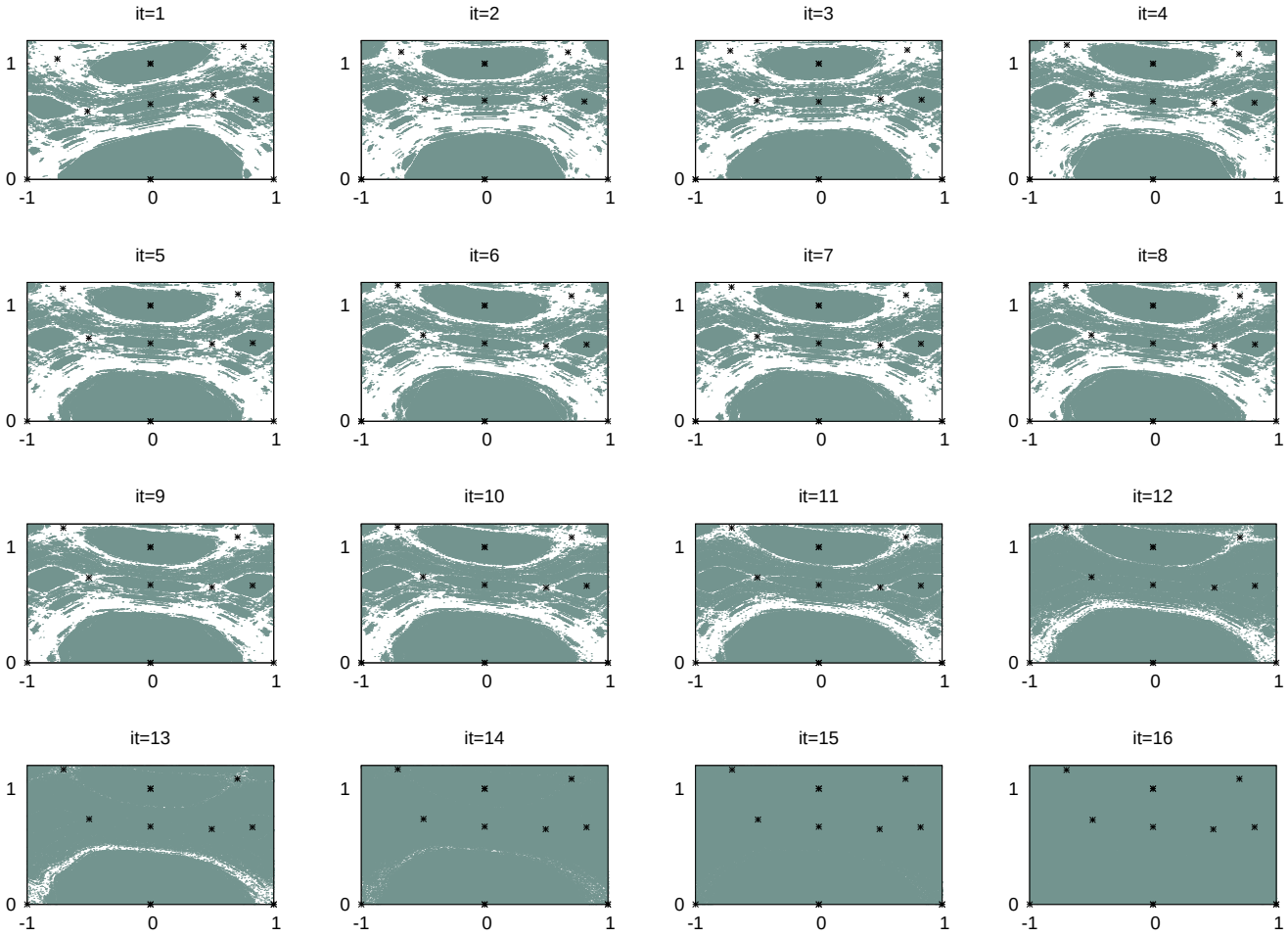


Figure 4.2: Iterates of $M_k$, $k = 0.9716$ under $\mathcal{R}_1$. See the first item in the enumeration in Subsect. 4.3.2 for further explanations.

relative position and relative size of the most prominent objects that play a leading role: approximating islands.

We will study approximating islands of the standard map (4.1) numerically from two different points of view.

1. First locally, by studying the linear stability of elliptic approximating orbits. For the $j$th, it can be determined via the trace

$$\mathrm{tr}_j(k) \quad = \quad \text{trace } DM_k^{q_j}(x_0, y_0), \tag{4.11}$$

where $(x_0, y_0)$ is any point in the periodic orbit. Also denote by $k_j(\tau)$ the value of the parameter $k$ for which the $j$th elliptic approximating orbit has $\mathrm{tr}_j(k_j(\tau)) = \tau$. Recall that the multiplier $\nu_j(k)$ can be recovered by $\mathrm{tr}_j(k) = 2\cos(2\pi\nu_j(k))$, when $\mathrm{tr}_j \in [-2, 2]$.

This is actually the parameter we will use to study approximating islands, since it is invariant under the renormalisation operator (in the sense of Subsubsect. 4.2.1, item 3) and allows to relate all approximating islands to each other.

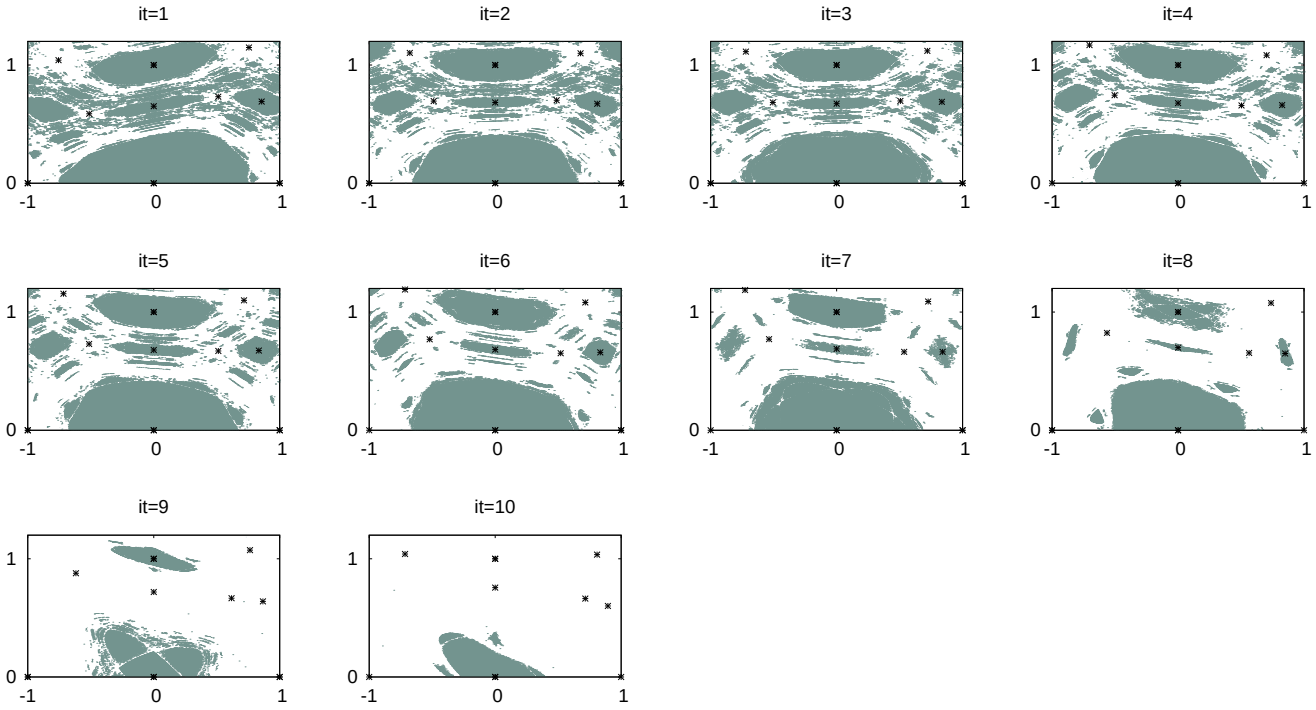


Figure 4.3: Iterates of $M_k$, $k = 0.98$ under $\mathcal{R}_1$. See the second item in the enumeration in Subsect. 4.3.2 for further explanations.

2. And second, in suitable fundamental domains containing a representative part of $\mathrm{DS}(p_j/q_j)$ (see Def. 7), we will measure

$$\mu_j(k) \quad = \quad \text{meas } \mathrm{DS}(p_j/q_j)/q_j. \tag{4.12}$$

Recall that $\mathrm{DS}(p_j/q_j)$ does not only contain the main connected islands that surround the elliptic or reflection-hyperbolic orbit, but also the whole island-around-island structure around them and tiny chaotic confined zones. It consists in $q_j$ pendulum-like structures whose regular zone has exactly the same measure. Note that the set $\mathrm{DS}(p_j/q_j)$ also contains hyperbolic orbits and their stable invariant manifolds, but these have zero measure.

We want to perform a simplified version of the analysis we did in Chap. 2 for the area preserving quadratic Hénon maps, but for the approximating islands of the standard map. Namely, we want to give numerical evidence that the traces $\mathrm{tr}_j$ of elliptic approximating orbits change monotonically in the parameter, and that there exists a limit behaviour of the approximating islands as $j \to \infty$ similarly to the accelerator modes in the standard map we saw in Chap. 2. Here the scaling factors that will allow to relate the islands to each other are the eigenvalues $\delta$ and $\delta'$ for the parameter and $\alpha$ and $\beta$ for the phase variables.

### 4.4.1 Numerical study of the local dynamics of elliptic approximating orbits

In this subsection we will study numerically the dependence of the traces $\mathrm{tr}_j$ on the value of the parameter $k$. Here we will only deal with orbits whose trace is in $\mathrm{tr}_j \in [-2, 2)$, that is

we will only deal with elliptic periodic points, not beyond the period-doubling bifurcation.

We are interested in the ranges of the parameter $k$ where elliptic islands evolve from parabolic to the period-doubling bifurcation. The pioneering numerical studies of Greene [63] suggested that the sequence $\{k_j(-2)\}_j$ is monotonically decreasing with limit $\lim_{j\to\infty} k_j(-2) = k_G$. Here we will study numerically the behaviour of $k_j(\tau)$, both as a function of $\tau$ and as a sequence $\{k_j(\tau)\}_j$ for each fixed value of $\tau \in [-2, 2)$. First, the results we show in Fig. 4.4, left, for $k_j(\tau)$, $j = 1, \ldots, 17$ allow us to state the following:

**Conjecture 1.** *The function $k_j(\tau)$ is strictly decreasing in $\tau$, for all $j > 0$.*

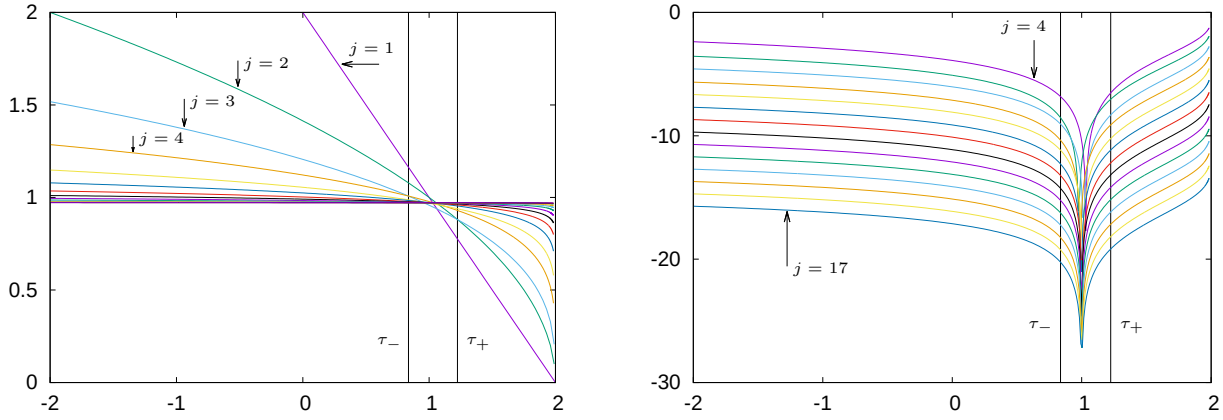


Figure 4.4: Left: Evolution of the value $k_j(\tau)$, for $\tau \in [-2, 2)$ for $j = 1, \ldots, 17$. Right: $\log_\delta(k_j(\tau) - k_G)$ as a function of $\tau \in [-2, 2)$ for $j = 4, \ldots, 17$. Here we only show values of $j$ that are visibly equispaced in some ranges of $\tau$. See the text for the definition of the highlighted values $\tau_+$ and $\tau_-$, see (4.16).

This actually tells us that, for all $j$, the multiplier of the $j$th elliptic approximating orbit has a full passage through resonances. And in case Greene's criterion holds, that the golden RIC can not reappear after $k_G$. We would not expect such monotonicity in cases where RIC can reappear after their destruction, as happens, for instance, in standard-like maps with two harmonics $V(x) = \kappa\,(a\sin(2\pi x) + b\sin(4\pi x))$ as in (1.14), where $\kappa$ measures the distance-to-integrability and $a^2 + b^2 = 1$, see [43, 44, 22, 91].

Back to Fig. 4.4, left, we can see that, as $j$ increases, the graphs $k_j(\tau)$ tend point-wise to be a constant function, and hence we can extend the numerical result of Greene to

$$\lim_{j\to\infty} k_j(\tau) = k_G, \qquad \text{if } \tau < 2, \tag{4.13}$$

The assertion (4.13) includes values of $k$ where the golden RIC still exists, shown in Fig. 4.4, left. Here we give evidence for $\tau > -2$, but we also have evidence for some values of $\tau$ such that $\tau < -2$. For these values, the sequence $\{k_j(\tau)\}_j$ behaves as in the interval $\tau \in [-2, \tau_-]$, see (4.16).

The convergence of $\{k_j(\tau)\}_j$ to $k_G$ implies the convergence of the coefficients $s_1^{(j)}$ and $s_3^{(j)}$ of the cubical change of variables (4.9) to the limit values (4.10). Consider, for a sequence $\{a_j\}_j$ that has limit $a_\infty$ as $j \to \infty$, the following associated sequences:

$$\text{rate}_j(a) = \frac{a_{j-1} - a_j}{a_{j-2} - a_{j-1}}, \quad a_j^{ait} = \frac{a_j a_{j-2} - a_{j-1}^2}{a_j - 2a_{j-1} + a_{j-2}}. \tag{4.14}$$

The sequence $\{\text{rate}_j(a)\}_j$ has, as limit, the rate of convergence of $\{a_j\}_j$ to $a_\infty$ in case the convergence is geometric. And the sequence $\{a_j^{ait}\} \to a_\infty$ as $j \to \infty$ but at a faster rate: it is the Aitken accelerated sequence.

In Table 4.1 we show the numerically evaluated values of the three coefficients $s_i^{(j)}$, $i = 1, 2, 3$ along the sequence $\{k_j(-1)\}_j$, that is, following the 1:3 resonances of approximating elliptic points. To the right of each of these coefficients, we show the approximate rate of convergence. The very last line corresponds to the last value (30th) of the values obtained in each corresponding Aitken accelerated sequence. We show values of these coefficients and rates for convergents $j = 3, \ldots, 30$, that is, from the 2/3 to the 832040/1346269 elliptic periodic point. For the data shown in this table, the positions $P_e^j$ and the values $k_j(-1)$ were determined with 75 correct decimal figures. The same simulation has been carried out for $\tau = -2, 0$. The results obtained are extremely similar.

The results obtained suggest that $s_1^{(j)}$ converges to $k_G/2$ with ratio $\delta$, that $s_2^{(j)}$ has some limit $0.130207\ldots$ and the convergence rate seems to be $\beta/\alpha^2 \approx 1.532095$; and $s_3^{(j)}$ converges to $-\pi^2 k_G/3$ with ratio $\beta/\alpha^3 \approx 1.082878$. Since this last is very close to 1 the convergence is very slow, and one should go further in $j$ to get values of $s_3^{(j)}$ closer to the expected limit.

Moreover, all 3 numerically obtained sequences $\{k_j(\tau)\}_j$ for $\tau = -2, -1, 0$ seem to tend to $k_G$ with converge rate $\delta$. Instead of these sequences, we will show the leading terms of a sequence of values of $k$ that converge to $k_G$ with a faster rate later on.

For different ranges of $\tau$ the sequence $\{k_j(\tau)\}_j$ appears to be either eventually increasing or decreasing or alternating. In Fig. 4.4, left and right, we have added two vertical lines that separate the regions where we can see different behaviours.

Concerning the convergence rate of these sequences, for $\tau = -2$, MacKay in [83] gave numerical evidence that the convergence rate was $\delta$, the only unstable eigenvalue of $D\mathcal{R}_1$ at the critical fixed point $R_C$. To estimate numerically the convergence rate of the sequence $\{k_j(\tau)\}_j$ for all values of $\tau$ considered, it is convenient to change the scale in the parameter (ordinates in Fig. 4.4, left) to be

$$\tilde{k}_j(\tau) = \log_\delta(k_j(\tau) - k_G).$$

This is precisely what we plot in Fig. 4.4, right, $\tilde{k}_j(\tau)$, for $j = 4, \ldots, 17$. Hence, concerning the convergence rate of these sequences, in each of the three ranges $\tau \in [-2, 2) = [-2, \tau_-) \cup [\tau_-, \tau_+] \cup (\tau_+, 2)$ where $\tau^\star \in [\tau_-, \tau_+]$,

1. If $\tau \in [-2, \tau_-) \cup (\tau_+, 2)$ the graphs seem to be vertically equispaced by 1 unit, so in this ranges the convergence rate of the sequence $\{k_j(\tau)\}_j$ seems to be $\delta$, and

2. If $\tau \in [\tau_-, \tau_+]$ the sequence $\{k_j(\tau)\}_j$ seems to alternate around $k_G$ and becomes eventually monotone, but it requires further detailed numerical investigations.

Let us introduce the following quantity. In Fig. 4.4, left, the graphs $k_j(\tau)$ are strictly decreasing functions and seem to cross each other once. So, if $k_j(\tau)$ and $k_l(\tau)$, $1 \le j < l$, let us denote the intersection value of the trace

$$\tau = \tau_{j,l} \quad \text{such that} \quad k_j(\tau_{j,l}) = k_l(\tau_{j,l}). \tag{4.15}$$

A closer look in Fig. 4.4, left allows to see that, actually,

$$\begin{aligned} \tau_- = \tau_{3,4} &= 0.836316630998899379064771402918493203122884569070177\ldots \\ \tau_+ = \tau_{2,3} &= 1.224105134257633758347076577736673021132619783370115\ldots \end{aligned} \tag{4.16}$$

| $j$ | $s_1^{(j)}$ | $\text{rate}_j(s_1)$ | $s_2^{(j)}$ | $\text{rate}_j(s_2)$ | $s_3^{(j)}$ | $\text{rate}_j(s_3)$ |
|---|---|---|---|---|---|---|
| 3 | 0.697659863315635 | | 0.221326141020018 | | -4.188335267344281 | |
| 4 | 0.609345784896336 | | 0.058237119936942 | | -3.851346566856803 | |
| 5 | 0.565289098639612 | 2.004555 | 0.173580338748888 | -1.413945 | -4.297385336445072 | -0.755514 |
| 6 | 0.531833289533581 | 1.316862 | 0.097543583254370 | -1.516940 | -3.946576187700749 | -1.271457 |
| 7 | 0.513486068491566 | 1.823481 | 0.148473166165693 | -1.492978 | -4.060221875905774 | -3.086867 |
| 8 | 0.502260376389276 | 1.634395 | 0.116066222805876 | -1.571563 | -3.849200903849310 | -0.538551 |
| 9 | 0.495719261233143 | 1.716174 | 0.137894977949387 | -1.484598 | -3.870601021185747 | -9.860739 |
| 10 | 0.491794333165289 | 1.666556 | 0.124199667062718 | -1.593885 | -3.746746265573998 | -0.172783 |
| 11 | 0.489444131744877 | 1.670039 | 0.133508783699062 | -1.471171 | -3.738553957951232 | 15.118421 |
| 12 | 0.488024703359202 | 1.655737 | 0.127704958690826 | -1.603962 | -3.661920959946125 | 0.106903 |
| 13 | 0.487163984334194 | 1.649119 | 0.131670420324641 | -1.463593 | -3.643398136155891 | 4.137220 |
| 14 | 0.486640548658096 | 1.644364 | 0.129203051818511 | -1.607162 | -3.592217094360501 | 0.361907 |
| 15 | 0.486321203980256 | 1.639093 | 0.130891098207180 | -1.461671 | -3.570712591753437 | 2.380015 |
| 16 | 0.486126140327378 | 1.637130 | 0.129839991352946 | -1.605970 | -3.533865724718989 | 0.583618 |
| 17 | 0.486006763067780 | 1.634010 | 0.130558194098780 | -1.463523 | -3.512566115675540 | 1.729931 |
| 18 | 0.485933660286107 | 1.633005 | 0.130109916058626 | -1.602136 | -3.484394449999408 | 0.756064 |
| 19 | 0.485888848021360 | 1.631311 | 0.130415382748912 | -1.467518 | -3.464680315636385 | 1.429008 |
| 20 | 0.485861368123777 | 1.630728 | 0.130224098052741 | -1.596921 | -3.442214916728004 | 0.877533 |
| 21 | 0.485844507584827 | 1.629835 | 0.130353999072141 | -1.472541 | -3.424594835706842 | 1.274988 |
| 22 | 0.485834160408368 | 1.629482 | 0.130272359925435 | -1.591160 | -3.406188639710572 | 0.957290 |
| 23 | 0.485827808598866 | 1.629012 | 0.130327599618011 | -1.477907 | -3.390744371084808 | 1.191781 |
| 24 | 0.485823908908457 | 1.628798 | 0.130292756080382 | -1.585364 | -3.375412843186684 | 1.007353 |
| 25 | 0.485821514330261 | 1.628550 | 0.130316247924068 | -1.483218 | -3.362027486622180 | 1.145395 |
| 26 | 0.485820043840145 | 1.628421 | 0.130301377945121 | -1.579816 | -3.349131197871720 | 1.037923 |
| 27 | 0.485819140751071 | 1.628289 | 0.130311369450145 | -1.488262 | -3.337606799505980 | 1.119042 |
| 28 | 0.485818586100744 | 1.628213 | 0.130305024277803 | -1.574662 | -3.326696478971233 | 1.056284 |
| 29 | 0.485818245436085 | 1.628141 | 0.130309274409527 | -1.492935 | -3.316813011423716 | 1.103896 |
| 30 | 0.485818036195133 | 1.628097 | 0.130306567247816 | -1.569958 | -3.307551929395354 | 1.067204 |
| $\bigstar_{30}^{ait}$ | 0.485817703060594 | **1.62**8026 | 0.130307620635113 | -1.**532**588 | -3.**1**69747244523398 | 1.**08**3173 |

Table 4.1: Values of the coefficients $s_i^{(j)}$, $i = 1, 2, 3$, and their approximate rates of convergence, evaluated along the sequence $\{k_j(-1)\}_j$, that is, at values of $k$ where approximating elliptic points are exactly at the $1:3$ resonance. The last line is the 30th coefficient of the sequence $\bigstar_{30}^{ait}$, see (4.14). See text for further information.

The values of $\tau_{2,3}$ and $\tau_{3,4}$ have been computed with 50 correct decimal figures.

From our numerical simulations we can assert the following concerning the convergence of the sequences $\{k_j(\tau)\}_j$.

**Conjecture 2.** *For all values of the trace $\tau \in [-2, 2)$, the sequence $\{k_j(\tau)\}_j$ converges to $k_G$ geometrically. If $\tau = \tau^\star$, the convergence rate is $\delta'$, and $\delta$ otherwise. Furthermore,*

1. *If $\tau \in [-2, \tau_-)$ the sequence $\{k_j(\tau)\}_j$ is strictly decreasing,*
2. *If $\tau \in (\tau_+, 2)$ the sequence $\{k_j(\tau)\}_j$ is strictly increasing,*
3. *If $\tau \in [\tau_-, \tau_+] \setminus \{\tau^\star\}$, if $\tau < \tau^\star$ it is eventually decreasing, if $\tau > \tau^\star$ it is eventually increasing, and*

*If $\tau = \tau^\star$ it alternates around $k_G$. Moreover the sequence of pairs of points*

$$\{(\tau_{j-1,j}, k_j(\tau_{j-1,j})), (\tau_{j,j+1}, k_j(\tau_{j,j+1}))\}_j,$$

*define domains around the limit point $(\tau^\star, k_G)$ that scale as $1/\delta'$ in $\tau$ and as $\delta/\delta'$ in $k$.*

Note that the fact that both the limit value of the parameter $k_G$ and the convergence rate $\delta$ of $\{k_j(\tau)\}_j$, are the same for all $\tau \in [-2, 2) \setminus \{\tau^\star\}$ makes perfect sense with renormalisation theory. From Subsubsect. 4.2.1 the critical fixed point $R_C$ is a map where all approximating elliptic orbits have $\mathrm{tr}_j = \tau^\star$, so as we approach $R_C$ from the upper branch of $W^u(R_C)$ all the values of these traces have to collapse to the limit value at the same rate $\delta$. The standard map inherits this behaviour. And the dynamics of the standard map in a length 1 interval in $\tilde{k} = \log_\delta(k - k_G)$ for values of $k > k_G$ but very close, has to be similar to the dynamics of a one-parameter family of maps $L_\kappa$ that is a fundamental domain of $W^u(R_C)$.

Further, note that the study of the sequences

$$\{\tau_{j-1,j}\}_{j\geq 2} \xrightarrow{\delta'} \tau^\star \qquad \text{and} \qquad \{k_j(\tau_{j-1,j})\}_{j\geq 2} \xrightarrow{\delta/\delta'} k_G \tag{4.17}$$

does not rely on the knowledge of either of the limits. In fact, the right limit in (4.17) converges faster than the sequence $\{k_j(\tau)\}_j$ for fixed $\tau$. Note that MacKay already suggested in [83, 80] to study the sequence $\{k_j(\tau^\star)\}_j$ that converges to $k_G$ with ratio $\delta/\delta'$. But the numerical study of this sequence depends on the value of $\tau^\star$, and without a good approximation of this value one can not go far in the sequence.

We used this method to approximate $k_G$. We computed the pairs $(\tau_{j,j+1}, k_j(\tau_{j,j+1}))$ for $j$ all the way up to 35, that is, where at the elliptic periodic orbits with rotation number 9227465/14930352 and 14930352/24157817 the trace is the same. The computations have been carried up to 50 decimal correct digits, but we only show the first relevant ones in Table 4.2. Using the Aitken acceleration method we get the first 21 digits of $k_G$ and the first 12 digits of $\tau^\star$

$$k_G = 0.971635406047502179389\ldots \tag{4.18}$$
$$\tau^\star = 0.999644540920\ldots \tag{4.19}$$

The first numerical support for Conjecture 2 we show deals with the character and the convergence rate of $\{k_j(\tau)\}_j$. We show it in Fig. 4.5, where the left column corresponds to $k_j(\tau)$ and the right one to $\tilde{k}_j(\tau)$, for fixed $\tau$ as a function of $j$. On top, middle and

| $j$ | $k_j(\tau_{j,j+1})$ | $k_j^{ait}(\tau_{j,j+1})$ | $\text{rate}_j(k)$ | $\tau_{j,j+1}$ | $\tau_{j,j+1}^{ait}$ | $\text{rate}_j(\tau)$ |
|---|---|---|---|---|---|---|
| 10 | 0.**971**579623947541 | 0.**97163548906293571684861** | -2.**6**43591639 | 1.00705752 | 0.**999**563657806180 | -0.**61**9539046 |
| 11 | 0.**9716**56408460215 | 0.**97163537691356153647198** | -2.**6**50920873 | 0.99507268 | 0.**9996**21800604375 | -0.**61**1791440 |
| 12 | 0.**9716**27508716779 | 0.**97163541145651967361861** | -2.**6**56927140 | 1.00243312 | 0.**9996**32644782672 | -0.**61**4145492 |
| 13 | 0.**9716**38373119950 | 0.**97163540**473595812007681 | -2.**66**0039671 | 0.99793497 | 0.**9996**41192274422 | -0.**61**1125489 |
| 14 | 0.**9716**34291898006 | 0.**97163540**636276960286678 | -2.**66**2046641 | 1.00068818 | 0.**9996**42841596845 | -0.**61**2077818 |
| 15 | 0.**97163**5824298498 | 0.**97163540**598549375155581 | -2.**66**3286761 | 0.99900617 | 0.**9996**44061428328 | -0.**61**0927226 |
| 16 | 0.**97163**5249069514 | 0.**97163540606**503364885326 | -2.**66**3983447 | 1.00003438 | 0.**9996**44301175183 | -0.**61**1297203 |
| 17 | 0.**97163**5464958773 | 0.**97163540604**448017229180 | -2.**66**4463190 | 0.**999**40628 | 0.**9996**44473088878 | -0.**61**0863230 |
| 18 | 0.**97163**5383940866 | 0.**97163540604**845431623019 | -2.**66**4710398 | 0.**999**79005 | 0.**99644**507293241 | -0.**61**1004552 |
| 19 | 0.**971635**14342801 | 0.**97163540604**735203532353 | -2.**66**4893129 | 0.**999**55563 | 0.**99644**531380433 | -0.**610**841673 |
| 20 | 0.**971635402**934868 | 0.**97163540604**755320627224 | -2.**66**4982007 | 0.**9996**9884 | 0.**99644**536217867 | -0.**610**895220 |
| 21 | 0.**971635407**215436 | 0.**97163540604**749462387702 | -2.**665**050985 | 0.**9996**1136 | 0.**99644**539582657 | -0.**610**834251 |
| 22 | 0.**971635405**609270 | 0.**97163540604750**489180559 | -2.**665**083207 | 0.**9996**6480 | 0.**99644540**263673 | -0.**610**854452 |
| 23 | 0.**971635406**211934 | 0.**97163540604750**179582084 | -2.**665**109100 | 0.**9996**3216 | 0.**99644540**732907 | -0.**6108**31666 |
| 24 | 0.**971635405**985804 | 0.**97163540604750**232280975 | -2.**665**120846 | 0.**9996**5210 | 0.**99644540**828525 | -0.**6108**39268 |
| 25 | 0.**9716354060**70652 | 0.**97163540604750215**979502 | -2.**665**130530 | 0.**9996**3992 | 0.**99644540**893893 | -0.**6108**30761 |
| 26 | 0.**9716354060**38815 | 0.**97163540604750218**694598 | -2.**665**134828 | 0.**99964**736 | 0.**99644540**907295 | -0.**6108**33616 |
| 27 | 0.**9716354060**50761 | 0.**97163540604750217**838424 | -2.**665**138441 | 0.**99964**281 | 0.**99644540**916395 | -0.**6108**30442 |
| 28 | 0.**9716354060**46279 | 0.**97163540604750217**978690 | -2.**665**140018 | 0.**99964**559 | 0.**99644540**918272 | -0.**6108**31514 |
| 29 | 0.**971635406047**961 | 0.**97163540604750217**933802 | -2.**665141**364 | 0.**99964**389 | 0.**99644540**919538 | -0.**610830**330 |
| 30 | 0.**971635406047**330 | 0.**97163540604750217**941062 | -2.**665141**944 | 0.**99964**493 | 0.**99644540**919800 | -0.**610830**732 |
| 31 | 0.**971635406047**566 | 0.**97163540604750217**938712 | -2.**665142**444 | 0.**99964**430 | 0.**99644540**919977 | -0.**610830**290 |
| 32 | 0.**971635406047**477 | 0.**97163540604750217**939088 | -2.**665142**658 | 0.**99964**468 | 0.**99644540920**013 | -0.**610830**441 |
| 33 | 0.**971635406047**511 | 0.**97163540604750217938**965 | -2.**665142**844 | 0.**99964**445 | 0.**99644540920**038 | -0.**610830**277 |
| 34 | 0.**971635406047**498 | 0.**97163540604750217938**985 | -2.**665142**922 | 0.**99964**459 | 0.**99644540920**043 | -0.**610830**333 |
| 35 | 0.**971635406047**503 | 0.**97163540604750217938**978 | -2.**665142**991 | 0.**99964**450 | 0.**99644540920**046 | -0.**610830**272 |

Table 4.2: Approximation of the sequences $\{k_j(\tau_{j,j+1})\}_j$ and $\{\tau_{j,j+1}\}_j$, and their corresponding Aitken accelerated sequence and approximate rate of convergence. The computations are carried out up to 50 decimal figures.

bottom we show examples $\tau \in [-2, \tau_-)$, $\tau \in (\tau_-, \tau_+)$ and $\tau \in (\tau_+, 2)$, respectively (see the caption in Fig. 4.5 for the actual values of $\tau$ shown). On the left we clearly see the decreasing, alternating and increasing character of the sequences predicted in Conj. 2. On the right we show $\log_\delta(k_j(\tau) - k_G)$ also as a function of $j$, where we added a piece of a straight line corresponding to $\delta^{-j}$, to stress out the fact that the rate of convergence of all the sequences shown is $\delta$. In the middle right plot we highlighted the behaviour of the case $\tau = 2\cos(\pi/3) = 1$, the 1:6 resonance. Since this value of $\tau$ is very close to $\tau^\star$ we checked that the sequence increases once $j \geq 19$.

Concerning the second part of the conjecture, the numerical evidence is shown in Fig. 4.6: these are just convenient magnifications of Fig. 4.4, left. The fact that these domains present these scalings may be useful to eventually derive a limit approximation of the dynamics of these islands of stability.

**Numerical support of Greene's criterion**. Up to here we have been concerned about the behaviour of $k_j$ as a function of $\tau$. We want to stress that our results are not contradictory with Greene's criterion, since it deals with the converse: the behaviour of the traces $\mathrm{tr}_j$ as a function of $k$. In our plots, the evidence for this conjecture is recovered by fixing a value of $k = k^*$ and considering the sequence of intersections of the horizontal line $\{k = k^*\}$ with the graphs of $k_j(\tau)$ in Fig. 4.4. So, what we get is the following:

1. if $k^* < k_G$, the sequence $\{\mathrm{tr}_j(k^*)\}_j$ is bounded and tends to 2 (sub-critical case),
2. if $k^* = k_G$, the sequence $\{\mathrm{tr}_j(k^*)\}_j$ is bounded and tends to $\tau^\star$ (critical case),
3. and if $k^* > k_G$, the sequence $\{\mathrm{tr}_j(k^*)\}_j$ tends to $-\infty$ (super-critical case).

We depict this behaviour in Fig. 4.7 for some approximants up to the 23th. Note also that the behaviour of the first item implies the existence of an analytic RIC, see [43, 82].

**Local behaviour of $\mathrm{tr}_j(k)$ close to $k_G$.** An interesting question is how does $\mathrm{tr}_j(k)$ behave locally around $k_G$ under small changes in $k$. Since for each value of $-2 \leq \tau < 2$, the sequence $\{k_j(\tau)\}_j$ converges to $k_G$ with ratio $\delta$, we expect the first derivative $d\mathrm{tr}_j(k)/dk$ at $k_G$ to be proportional to $\delta^j$.

As above, let $P_e^j$ be the coordinates of the elliptic approximating periodic point on $\{x = 1/2\}$ for $k = k_G$. Since we return exactly to $x = 1/2$, a formal Taylor expansion of the return map around $P_e^j$ with respect to $k$ and $y$ is of the form

$$M_{k_G+\Delta k}^{q_j}\left(P_e^j + (0, \Delta y)^\top\right) = P_e^j + \begin{pmatrix} a_{00}\Delta y + a_{01}\Delta k \\ a_{10}\Delta y + a_{11}\Delta k \end{pmatrix} + \mathcal{O}(\Delta y^2, \Delta k^2).$$

Moreover $a_{00}\Delta y + a_{01}\Delta k = 0$, giving a first order approximation of $\Delta y = \Delta y(\Delta k)$. The previous expansion can be computed numerically using symbolic manipulations, from which we get concrete values of the parameters $a_{00}, a_{01}, a_{10}$ and $a_{11}$. Namely, using Aitken's acceleration method we get that

$$\frac{a_{01}}{a_{00}} \to 0.12060221802966\ldots \text{ as } j \to \infty \text{ with rate } \frac{\beta}{\delta}.$$

Hence, we can compute $\mathrm{tr}_j(k_G + \Delta k)$ as a polynomial in $\Delta k$. We get a linear dependence

$$\mathrm{tr}_j(k_G + \Delta k) = \tau^\star + c_j\Delta k + \mathcal{O}(\Delta k^2). \tag{4.20}$$

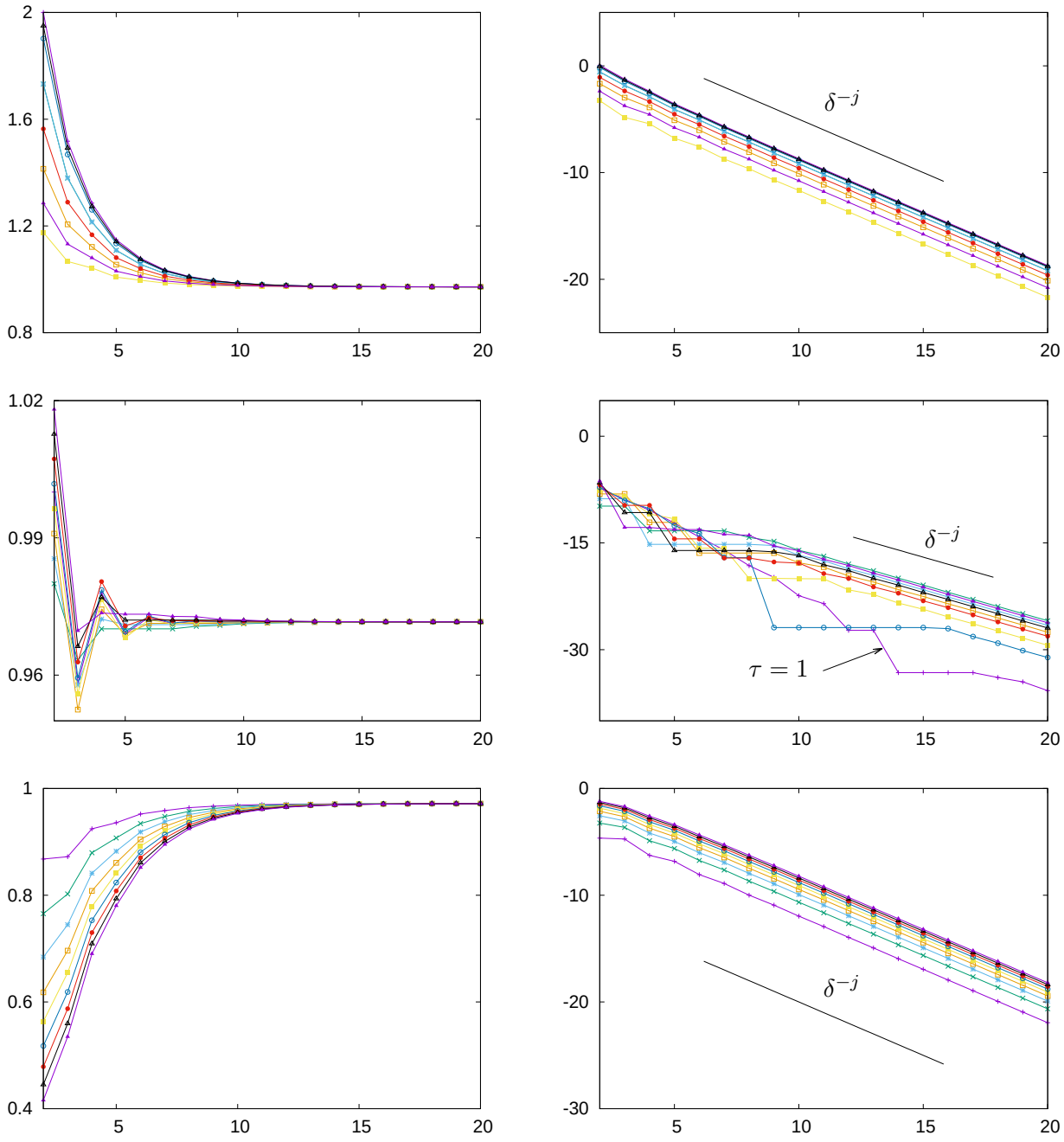


Figure 4.5: Left column: $k_j(\tau)$ as a function of $j$. Right column: $\tilde{k}_j(\tau) = \log_\delta(k_j(\tau) - k_G) + \log_\delta(2\pi)$. The values of the trace are $\tau = 2\cos(2\pi p/q)$. Top: $p/q = 1/2, 1/3, 2/3, 1/4, 1/5, 2/5, 2/7, 2/9$, all of them give $\tau \in [-2, \tau_-)$. Middle: $p/q = 1/6, 163/1000, 164/1000, 165/1000, 166/1000, 167/1000, 168/1000, 169/1000, 170/1000$, they give $\tau \in (\tau_-, \tau_+)$. Bottom: $p/q = 1/7, 1/8, 1/9, 1/10, 1/11, 1/12, 1/13, 1/14, 1/15$, that give $\tau \in (\tau_+, 2)]$.

We have computed $c_j$ for the approximants for $2 \leq j \leq 31$. The results can be seen in Fig. 4.7, right. If we plot $c_j$ as a function of $j$ in log-linear scale, we get what seems to be a straight line, showing that there is some potential dependence $c_j = b\exp(aj) < 0$. The fact

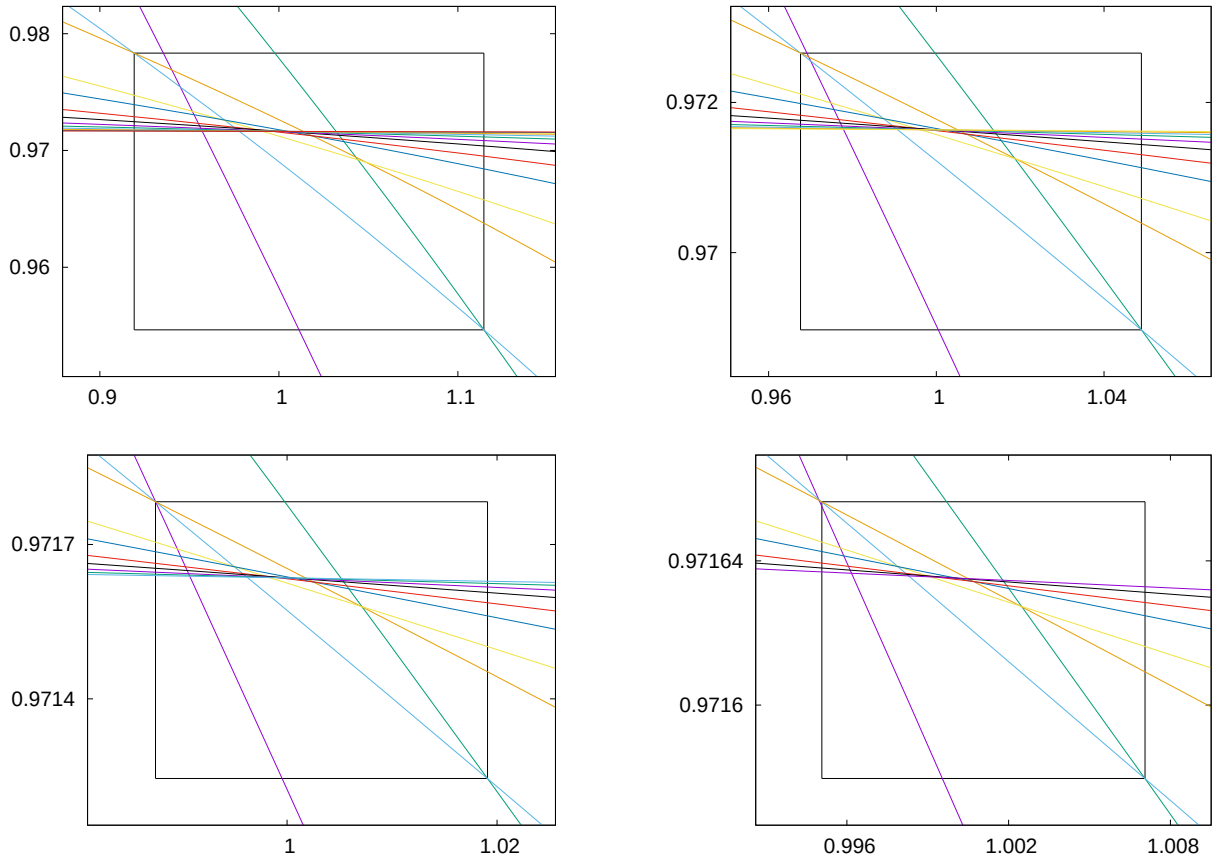


Figure 4.6: Magnifications of Fig. 4.4, left, $2\pi k_j(\tau)$ for different values of $j$. The upper left and lower right vertices of the inner box are of the form $(\tau_{n,n+1}, 2\pi k_n(\tau_{n,n+1}))$ and $(\tau_{n-1,n}, 2\pi k_n(\tau_{n-1,n}))$. The corresponding $n$ and the $j$'s shown in each figure are: Top left: $n = 5$, $j = 3, \ldots, 17$. Top right: $n = 7$, $j = 5, \ldots, 17$. Bottom left: $n = 9$, $j = 7, \ldots, 17$. Bottom right: $n = 11$, $j = 7, \ldots, 17$.

that this constant is negative agrees with the behaviour shown in Fig. 4.4. A least squares fit, done only with the data corresponding to $j = 20, \ldots, 31$, gives the value

$$a = 0.4873220 \pm 5 \cdot 10^{-7} \text{ hence } \exp(a) = 1.6279507 \pm 8 \cdot 10^{-7}, \tag{4.21}$$

This is, as expected, the rate of convergence $\delta$, the unstable eigenvalue of $D\mathcal{R}_1(R_C)$. This means that locally around the periodic point, the changes in the trace scale as $\delta^j$, if $j$ is the number of approximant we are dealing with.

### 4.4.2 The area of approximating islands

For the critical fixed point of $\mathcal{R}_1$, $R_C$, all approximating islands have trace $\mathrm{tr}_j = \tau^\star$. Recall that, for the standard map, this is the limit trace of approximating elliptic periodic orbits at $k = k_G$: $\mathrm{tr}_j(k_G) \to \tau^\star$ as $j \to \infty$. But we are not interested in what happens in a prescribed value of the parameter $k$, but on the evolution of the area of all the approximating islands in the range where they are detectable.

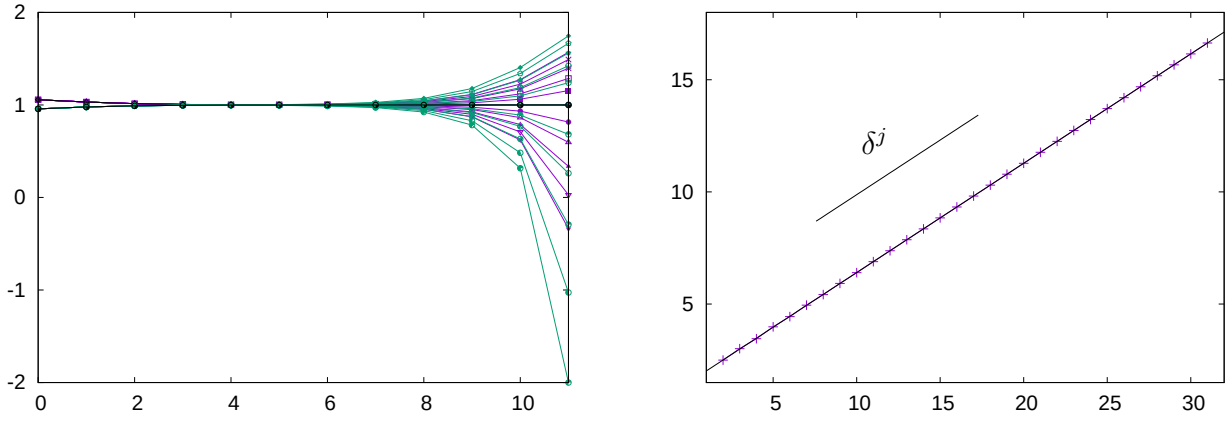


Figure 4.7: Left: Trace $\mathrm{tr}_j(k)$ as a function of $n = [j/2]$ where $[\cdot]$ means flooring. We chose ten equispaced values of $k$ in $[2k_G - k_{23}(-2), k_{23}(-2)]$. We plot in green odd values of $j$ and in purple even values of $j$. In black we show $\mathrm{tr}_j(k_G)$. We see that, if $k < k_G$, $\mathrm{tr}_j \to 2$ and if $k > k_G$, $\mathrm{tr}_j \to -\infty$. Right: Coefficient $\log(c_j)$ as a function of $j$, see (4.20). Red: odd approximants. Green: Even approximants. Blue: fitted line $y = ax + b$, see (4.21).

In the last Section we gave evidence of the fact that, if we choose a value of $\tau < 2$, then the sequence $k_j(\tau) \to k_G$ as $j \to \infty$, and this happens with ratio $\delta$. Despite all this evolution collapses to $k_G$, we expect that, if we scale conveniently the phase space, approximating islands have a limit shape and area as $j \to \infty$. This is what we are going to investigate in this section.

For the standard map, at $k = 0$ there are no islands of stability, but they appear once $k > 0$. For each approximant $j$, this area will be detectable (in some fine grid) up to some value of $k$, call it $k_j^f = k_j(\tau_f)$. Let $\tilde{k}_j^f = \log_\delta(k_j^f - k_G)$. Here $\tau_f$ is an upper bound of the values of the trace where all approximating islands are no longer detectable (they are deep in the period-doubling cascade). We will show that this value is far beyond the period-doubling bifurcation. Namely up to the pixel resolution we will use here, it suffices to consider $\tau_f = -4.5$. Note the difference, for instance, with the Hénon map (2.2): no area around the main elliptic island is detectable once $c > 2.3$. Since the trace $\tau = 2 - 2c$, then no area is detectable for $\tau < -2.6$.

Since there is numerical evidence that the standard family is close to $W^u(R_C)$, we expect the area of these approximating islands to scale as the phase space does: $(\alpha\beta)^{-j}$ for the $j$th approximant, if $j$ is large enough.

**Scaled areas.** Here we will give numerical evidence of the fact that there is a limit shape of the approximating islands, as $j \to \infty$. Each limit will be taken by fixing $\tau \in [-4.5, 2)$. By scaled area we will refer to the area that a single island in the chain occupies in the scaled coordinates $(\xi, \eta)$, see (4.9). In this system of coordinates, we measure

$$\tilde{\mu}_j(k) = \frac{\mu_j(k)}{d_x^{(j)} d_y^{(j)}}, \quad k = k_j(\tau), \tag{4.22}$$

recall (4.12) and Sect. 4.3.1. When $k > k_G$, we can either consider $\tilde{\mu}$ to depend either on $k$ or $\tilde{k}$. We consider a $800 \times 800$ equispaced grid in $(\xi, \eta) \in [-1, 1] \times [-0.6, 0.6]$. A pixel is

considered to correspond to a point in $\mathrm{DS}(p_j/q_j)$ if it stays in $[-1,1]\times[-0.6,0.6]$ for at least $10^5$ iterates. This includes both regular and confined chaotic orbits in the island. Note that, an orbit that we consider to be confined actually remains stuck close to the whole island chain of the standard map for at least $10^5 \times q_j$ iterates.

In Fig. 4.8 we show the evolution of the scaled areas $\tilde{\mu}_j(k_j(\tau))$ as a function of the trace. On the left we show the areas from $j=1$ to $j=10$, that is, from the main elliptic island to those with period $p_{10}/q_{10}=55/89$. On the right we see a magnification where we have labelled the period each area function corresponds to. Note that the area does not decrease to a limit as we increase $j$, but it seems to alternate around the limit. As we commented above, here we show that the period-doubling cascade of these islands seems to be no longer detectable for some value of the trace close to $-4.5$, the leftmost value shown in the plot.

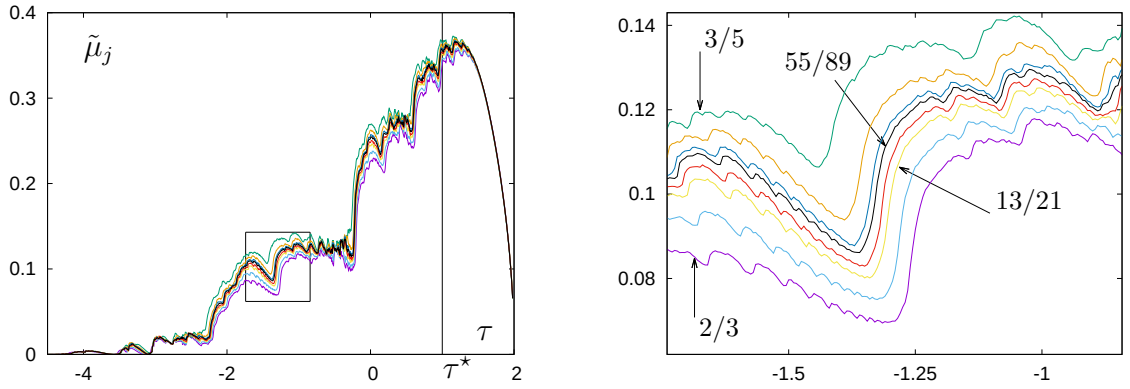


Figure 4.8: Left: Confined scaled area $\tilde{\mu}_j(k_j(\tau))$, $\tau\in[-4.5,2]$, around $P_e^j$ for $j=1,\dots 9$, from the main island to an island with period 34/55, as a function of the trace, $\tau$. The vertical line corresponds to the limit value of the trace $\tau^\star$. Right: Magnification of the left plot, labelled. To generate the shown data we considered a $800\times 800$ equispaced grid in $(\xi,\eta)\in[-1,1]\times[-0.6,0.6]$.

We also computed the corresponding turnstile area $\Delta W_{p_j/q_j}$. To get it we first labelled all pixels with $\eta>0$ such that were mapped to some point with $\eta<0$. Let us denote the scaled values of $\Delta W$ as

$$\Delta\tilde{W}_{p_j/q_j}=\frac{\Delta W_{p_j/q_j}}{d_x^{(j)}d_y^{(j)}}=\frac{\Delta W^c_{p_j/q_j}+\Delta W^{nc}_{p_j/q_j}}{d_x^{(j)}d_y^{(j)}}, \tag{4.23}$$

And similarly for $\Delta\tilde{W}^c_{p_j/q_j}$ and $\Delta\tilde{W}^{nc}_{p_j/q_j}$. Recall that we defined these quantities in pages 16 and 26. In Fig. 4.9 we show, from left to right, $\Delta\tilde{W}_{p_j,q_j}$, $\Delta\tilde{W}^{nc}_{p_j/q_j}$ and $\Delta\tilde{W}^c_{p_j/q_j}$, respectively, as a function of $k$. Comparing the left and middle plots we see that most of the turnstile area is $\Delta\tilde{W}^{nc}_{p_j/q_j}$, but there is still some part of the island that is included here $\Delta\tilde{W}_{p_j/q_j}$. Compare the right plot in Fig. 4.9 with the left plot in Fig. 4.8.

**Total area after $k_G$.** To study escape rates across the golden Cantorus we need information about the amount of area occupied by the approximating islands in the phase space once the golden invariant curve is broken, that is, when $k>k_G$. So, we will use again $k$ as parameter, instead of $\tau$.

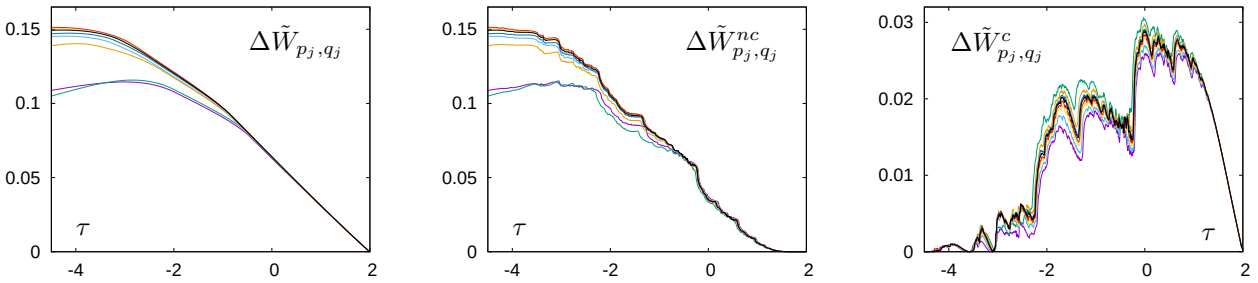


Figure 4.9: We show, as a function of $\tau \in (-4.5, 2)$, left: $\Delta\tilde{W}_{p_j/q_j}$, middle: $\Delta\tilde{W}^{nc}_{p_j/q_j}$ and right: $\Delta\tilde{W}^{c}_{p_j/q_j}$, see (4.23).

In Subsect. 4.4.1 we saw that if $\tau < \tau_-$, then the sequence $\{k_j(\tau)\}_j$ converges monotonically and geometrically to $k_G$ with ratio $\delta$. So, if we plot the scaled areas $\tilde{\mu}_j$ for large enough $j$, as a function of $\tilde{k} = \log_\delta(k - k_G)$ instead of $k$ itself, we should see, as $\tilde{k} \to -\infty$ (that means approaching the breakdown from the right $k \to k_G$) the same behaviour but shifted by one unit in $\tilde{k}$. In the ranges of $k$ we will investigate, the corresponding value of the trace of all approximants will satisfy $\mathrm{tr}_j(k) < \tau^\star$, that is, we are on the left of the vertical line of Fig. 4.8, left, that corresponds to $\tau^\star$.

We have recomputed the areas shown in Fig. 4.8, but in equispaced values of $\tilde{k} < 0$, that is, for $k > k_G$. We also used a $800 \times 800$ equispaced grid in $(\xi, \eta) \in [-1, 1] \times [-0.6, 0.6]$, and considered that a point in this region is non-escaping (and hence belongs to $\mathrm{DS}(p_j/q_j)$) if it remains in this box for, at least $10^5$ iterations of the map $\Lambda_j^{-1} \circ M_k^{q_j} \circ \Lambda_j$. The results can be seen in Fig. 4.10. There we show $\tilde{\mu}_j(\tilde{k})$ for $j = 2$ (period 1/2) to $j = 13$ (period 233/377). The 14th approximating island, that with rotation number 377/610 has no detectable area surrounding it in the range of $\tilde{k}$ shown in the used resolution. There are some distinctive features of this plot that will be taken into account later on:

1. As said before, in this logarithmic scale of $k$, as $\tilde{k}$ decreases, approximating islands appear in values of $\tilde{k}$ that are equispaced by 1 unit. In Fig. 4.10, approximating islands seem to disappear near integer values of $\tilde{k}$, but we did not choose this normalisation.

2. As $j$ increases the shape of the curves seems to get closer to a limit shape, as in Fig. 4.8. By this we mean that
$$\lim_{j\to\infty} \left|\tilde{\mu}_j(\tilde{k}+1) - \tilde{\mu}_{j+1}(\tilde{k})\right| = 0.$$

3. For each $j$, as $\tilde{k}$ decreases, the functions $\tilde{\mu}_j(\tilde{k})$ tend to the limit $\lim_{\tilde{k}\to-\infty} \tilde{\mu}_j(\tilde{k}) = \tilde{\mu}_j(k_G)$. And it seems that $\tilde{\mu}_j(\tilde{k})$ start to behave as if they were a constant equal to $\tilde{\mu}_j(k_G)$. So, let $\nu > 0$ be a small value, and define $\tilde{k} = \tilde{k}^l_j = \tilde{k}^l_j(\nu)$ in such a way that $|\tilde{\mu}_j(\tilde{k}) - \tilde{\mu}_j(k_G)| < \nu$ for all $\tilde{k} < \tilde{k}^l_j$. Recall that at the beginning of Sect. 4.4.2 we defined $\tilde{k}^f_j$ as the value of $\tilde{k}$ for which the $j$th approximating island is no longer detectable, in the resolution used. As $j$ increases, the difference $\tilde{k}^f_j - \tilde{k}^l_j$ tends to a constant. Note that $\tilde{k}^l_j$ depends on $\nu$ but $\tilde{k}^f_j$ does not. It only depends on the resolution we use to measure the area of approximating islands.

The fact that we detect a smooth approach to the limit is because as $\tilde{k} \to -\infty$, a change by 1 unit in $\tilde{k}$ represents an extremely narrow change $\delta^{\tilde{k}}$ in the original scale of $k$, so we expect approximating islands to eventually change slowly in $\tilde{k}$.

4. This last item gives rise, for each value of $\tilde{k}$, to the distinction between 3 different kinds of islands depending on the relative position of $\tilde{k}$ with respect to $\tilde{k}_j^f$ and $\tilde{k}_j^l$:

   (a) We will say that the $j$th approximating island is *evolving* if $\tilde{k} \in [\tilde{k}_j^l, \tilde{k}_j^f]$,

   (b) That the $j$th approximating island is *at its limit*, if $\tilde{k} \leq \tilde{k}_j^l$, and

   (c) That the $j$th approximating island is still *invisible*, if it has not appeared yet, that is, $\tilde{k} \geq \tilde{k}_j^f$.

   Moreover, since $\tilde{k}_j^f - \tilde{k}_j^l$ tends to be constant as $j$ increases, for large enough $j$ there is a fixed finite number of evolving islands, $m_e$, a finite number of islands at their limit, $m_l$, that increase by 1 unit every time $\tilde{k}$ decreases by 1 unit, and countably infinitely many that have not yet appeared. For the standard map, it is plausible to consider $m_e = 5$, but to obtain an accurate value of $m_e$ one should get closer to $k_G$.

   Hence, concerning the area that approximating islands occupy in the original $(x, y)$ coordinates in the standard map, if we change $\tilde{k}$ for $\tilde{k} - 1$, one of the invisible orbits will become part of the $m_e$ evolving ones and one of these evolving islands will reach their limit. Plus, the traces of each of the evolving islands at $\tilde{k}$ are the same of those islands present in the renormalised domain for $\tilde{k} - 1$; and the area that all these $m_e$ islands occupy will be the same but scaled by $\alpha\beta$. Note that this behaviour is 1-periodic, that is, related to the dynamics in a fundamental domain of $W^{u,+}(R_C)$.

In Fig. 4.10 we show the evolution of the scaled areas $\tilde{\mu}_j$ for $j = 3, \ldots, 13$ in a range $\tilde{k} \in [-12, -3]$ that corresponds to a range in the actual scale

$$k \in [0.974521477288362, 1.20341583474535].$$

On top left of Fig. 4.10 we can see that for each $j$, $\tilde{\mu}_j(\tilde{k})$ seems to tend to a different limit value as $\tilde{k} \to -\infty$. This is consistent with the results in Fig. 4.8, where we saw that the scaled areas of consecutive approximants alternate around the limit.

Similar to Fig. 4.9, we plot the corresponding total, non-confined and confined turnstile areas of the islands shown in Fig. 4.10 in Fig. 4.11. These turnstile areas are those that actually play a role in transport properties.

We illustrate the change of the shape of some scaled stability islands in Tab. 4.3 in a length 1 interval of $\tilde{k}$, $\tilde{k} = [-10, -9)$. We plot the islands of rotation number 13/21 up to the ones with rotation number 89/144 (a total of 5 approximants) for $k = -9.125(-0.125) - 10.000$. We can see that the top one (the one with rotation number 13/21) does not change much in this interval, while as we increase the period they do in a faster rate. Even the last one shown (that with rotation number 89/144) disappears in this range of $\tilde{k}$. The scaled area that these islands occupy can be seen in Fig. 4.10. Each column in Tab. 4.3 corresponds to a fixed value of $\tilde{k}$.

In Fig. 4.10 we can see sudden decreases in the scaled confined area. From the displayed evolutions in Tab. 4.3 we can guess to which satellite islands these correspond to. Recall that the sudden decreases confined area are related to the breakdown of an invariant curve

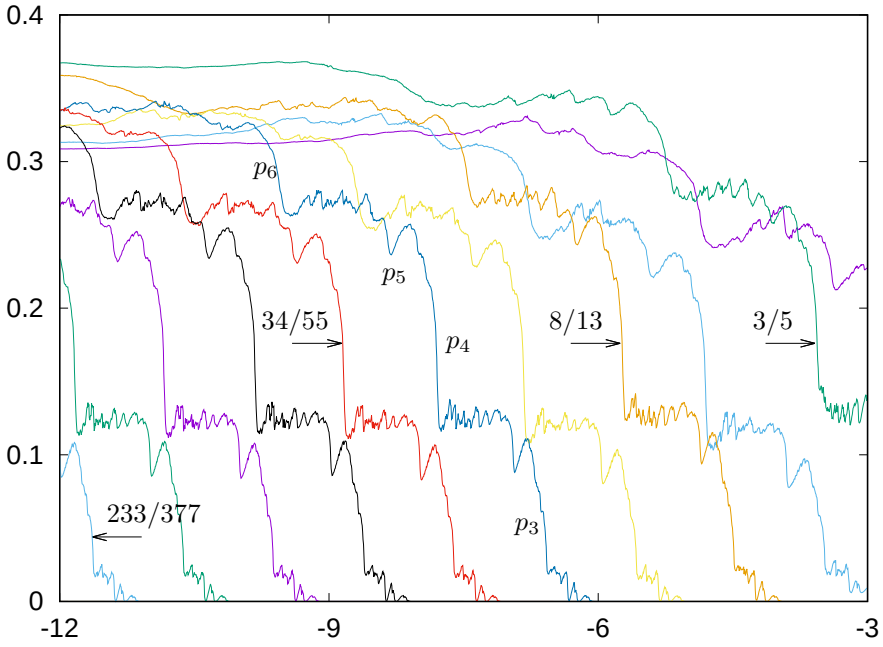


Figure 4.10: Scaled areas of approximating islands $\tilde{\mu}_j(\tilde{k})$, where $\tilde{k} = \log_\delta(k - k_G)$ for $j = 3, \ldots, 13$. Some of the curves are labelled with the rotation number they correspond to. This figure is related to Fig 4.8. Here $\tilde{k}$ is used as parameter instead of $\tau$, and only the data on the left of $\tau^\star$ in Fig 4.8, left, is shown. Note that the value $\tau = \tau^\star$ will appear for $\tilde{k} = -\infty$. See text for further explanations.

that allows previously chaotic confined region to escape from a compact set that contains the whole island. At this global bifurcation satellite islands leave the connected component of the domain of stability. We labelled some of the jumps in Fig. 4.10 as $p_3$, $p_4$, $p_5$ and $p_6$ to refer to the effect of the breakdown of the invariant curves surrounding the islands of rotation number 1/3, 1/4, 1/5 and 1/6, respectively.

### 4.4.3 Expectations for escape rates. Subsect. 3.5.6 revisited

In Subsect. 3.5.6 we referred to renormalisation theory as explanation of the bumps that we observed when dealing with trapping statistics in the vicinity of a stability island. The scaling law for the quantity $\Delta W$, when related to approximating islands gives a first explanation of the power law and the expected 1-periodic fluctuations. After the numerical study just performed, we can make sense on the contents of Subsect. 3.5.6, relating it to approximating islands.

Fix a value of $\tilde{k}^* \ll -1$. Let $j$ be the number of approximant of the last evolving island, meaning the one that for $\tilde{k}^* - 1$ will be promoted to be at its limit.

According to transport theory, the main obstruction to cross the zone where the Cantorus lies is the region of the phase space that has periodic orbits with the smallest $\Delta W$ possible. A quantity that plays a relevant role is $\Delta W^{nc}$. Consider the dynamics of $\mathcal{R}_1^j[M_k]$, where the phase space looks like those in the first iterates shown in Fig. 4.3. Since there are only $m_e + m_l$ present chains of islands, we can assume that they define a partition of the zone

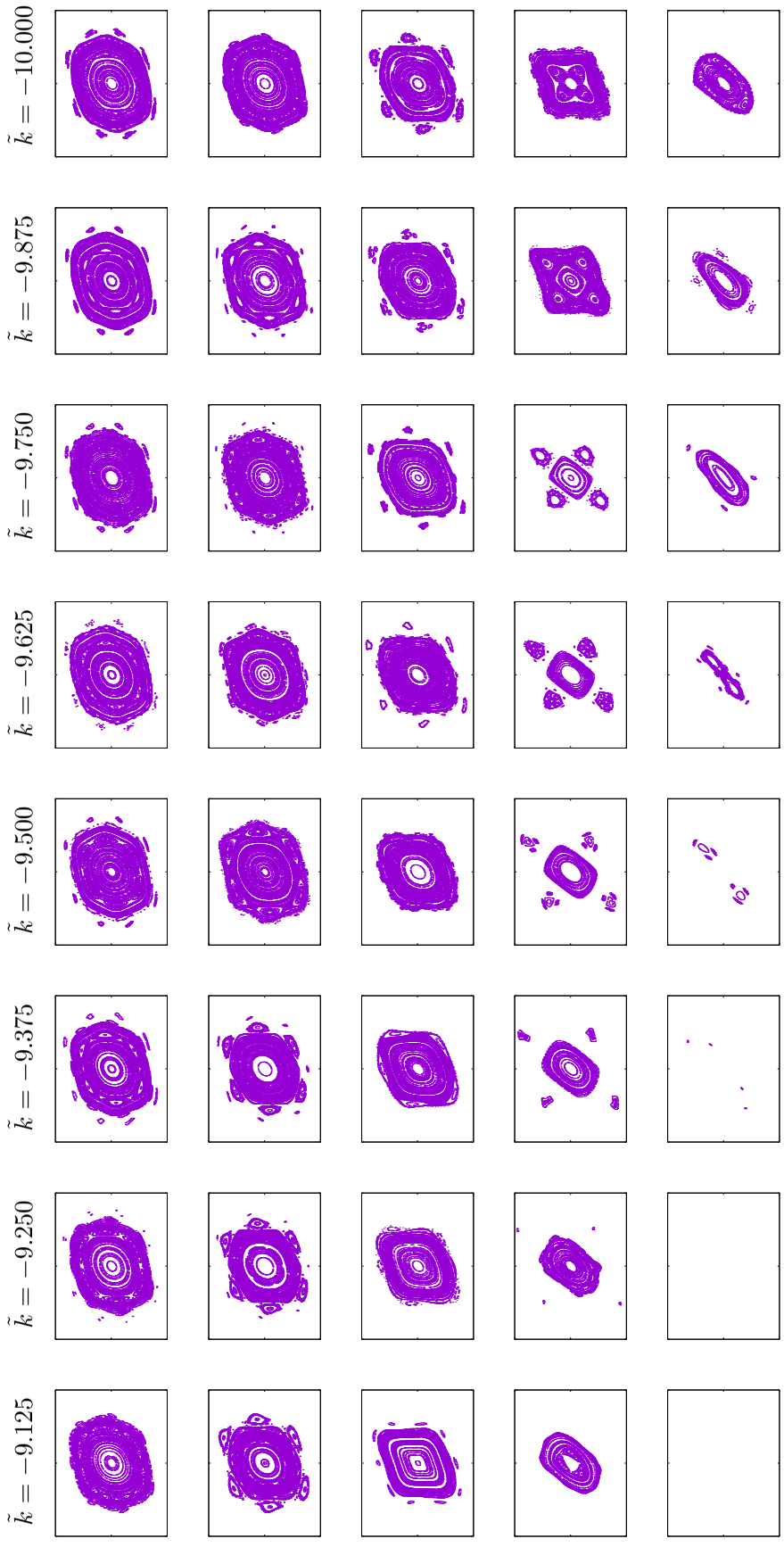


Table 4.3: Evolution of the shape of approximating islands with rotation numbers $13/21, 21/34, 34/55, 55/89$ and $89/144$ in the interval $\tilde{k} \in [-10, -9)$. We show the shape of these islands for the eight values $\tilde{k} = -9.125(-0.125) - 10.000$. See text for further explanations.

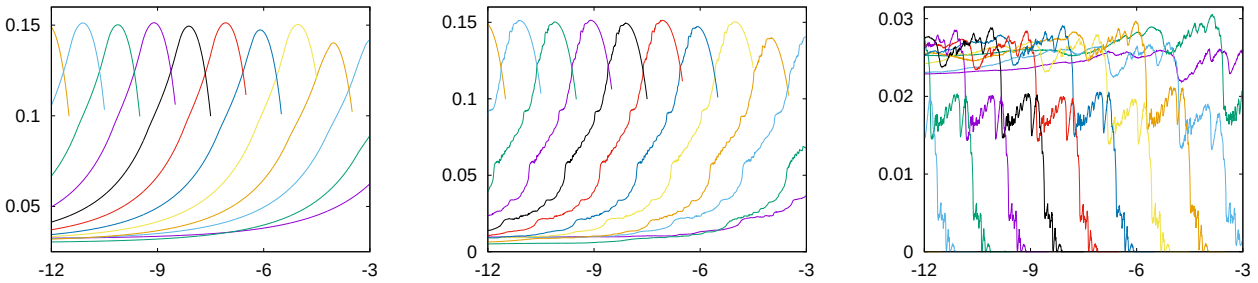


Figure 4.11: We show, as a function of $\tilde{k} \in [-12, -3]$, left: $\Delta\tilde{W}_{p_j/q_j}$, middle: $\Delta\tilde{W}^{nc}_{p_j/q_j}$ and right: $\Delta\tilde{W}^{c}_{p_j/q_j}$, see (4.23).

accessible to chaotic non-confined orbits, and the transport across this zone can be modelled as a nearest neighbour Markov process where the transition probabilities between neighbour regions are those given by

$$\Delta W^{nc}_{p_i,q_i}(\tilde{k}^*), \qquad i = j, \dots, j + m_e.$$

In the region where there are only 'invisible' islands orbits are assumed to behave as if they followed a diffusive process. Note that, since renormalisation applies, one has that the orders of magnitude of these quantities satisfy

$$\mathcal{O}(\Delta W^{nc}_{p_i,q_i}(\tilde{k}^*)) = \mathcal{O}(\Delta W^{nc}_{p_j,q_j}(\tilde{k}^*))(\alpha\beta)^{j-i}, \qquad i = j + 1, \dots, j + m_e,$$

see Fig. 4.11, but since $M_k$ for $k > k_G$ has a golden Cantorus (beyond other Cantori that have rotation number close to $\omega$), each iterate of $M_k$ under $\mathcal{R}_1$ has the origin $(0, 0)$ as fixed point and one expects each iterate to have different decreasing values of the trace at the origin, and a different value of $\Delta W$. Hence one has to think of the set $\{\Delta W^{nc}_{p_i,q_i}(\tilde{k}^*),\ i = j, \dots, j + m_e\}$, as a whole. Let us refer to it as a configuration of transition probabilities. Recall the construction of successive domains in Sect. 4.3.1.

Now, if we shift $\tilde{k}^* \to \tilde{k}^* - 1$, that is, we change $k_G + \Delta k$ to $k_G + \Delta k/\delta$, if $\tilde{k}^*$ is negative enough, and hence we are close enough to the limit, we would have an extremely similar phase space, but scaled by $(\alpha\beta)$. And the configuration of transition probabilities would be $\{\Delta W^{nc}_{p_i,q_i}(\tilde{k}^* - 1),\ i = j + 1, \dots, j + 1 + m_e\}$, but

$$\Delta W^{nc}_{p_{i+1},q_{i+1}}(\tilde{k}^* - 1) \approx \Delta W^{nc}_{p_i,q_i}(\tilde{k}^*)(\alpha\beta)^{-1}, \qquad i = j, \dots, j + m_e. \tag{4.24}$$

Hence, according to the Kac formula (3.7), if we denote the mean time to cross the Cantorus for $\tilde{k}$ as[4] $\langle N_{\tilde{k}} \rangle$, then we expect a mean value $\langle N_{\tilde{k}-1} \rangle = \alpha\beta \langle N_{\tilde{k}} \rangle$ for $\tilde{k} - 1$.

Since the configurations are related to each other like in (4.24) for values of $\tilde{k}$ at distance 1, the 1-periodic fluctuations $U(\log_\delta(\Delta k))$ can be explained as the different configurations of transition probabilities that one has in an interval of the form $[\tilde{k}^* - 1, \tilde{k}^*)$ for negative enough $\tilde{k}^*$. Such an interval can be understood as a fundamental domain in the parameter such that in the coordinates given by the change of scale $\Lambda_j$ one captures the leading dynamics around the golden Cantorus. The study of such a fundamental domain requires the knowledge of the limit dynamics of approximating islands of stability.

[4]This notation will be introduced in Subsect. 4.5.1.

## 4.5 Transport across a golden Cantorus

In this section we study escape rates across a golden Cantorus. In our context the Cantorus under study is the remnant of a RIC that has been destroyed due to perturbation. Unlike RIC, that are complete barriers to transport, Cantori have gaps that allow orbits to leak across them. But the time to cross them can be extremely large. The size of these gaps is exponentially small close to the breakdown. And we can make sense of this fact via renormalisation and the Olvera-Simó criterion for the destruction of invariant curves.

**Theorem 3. Olvera-Simó, [112].** *If an APM $F$ of the cylinder $\mathbb{S}^1 \times \mathbb{R}$ has two hyperbolic periodic orbits $o_1$ and $o_2$ with rotation number $m_1/n_1 > m_2/n_2$, respectively, and the stable invariant manifold of $o_1$ intersects the unstable invariant manifold of $o_2$, then $F$ has no RIC with rotation number $\rho$, $\rho \in (m_2/n_2, m_1/n_1)$.*

This result gives a geometric connection between the existence of RIC for a prescribed rotation number and the relative position of invariant manifolds. We are going to study transport across Cantori, and this theorem allows to do some heuristic considerations on the evolution of the size of their gaps.

Assume that, for the standard map at some value of $k = k_G + \Delta k$ the invariant manifolds (IM) of the hyperbolic periodic orbits (HPO) with rotation number $p_j/q_j$ and $p_{j+1}/q_{j+1}$ have an heteroclinic tangency, and that they do not intersect for any smaller value of $k$. Note that this condition is impossible to be checked numerically. In practice one is lead to consider moderate length pieces of the invariant manifolds. Then, if $i > j$ all IM of HPO with rotation number $p_i/q_i$ and $p_{i+1}/q_{i+1}$ cross transversally giving rise to lobes, but they do not intersect for $i < j$.

The heteroclinic lobes bounded by the IM of the the points nearest to $x = 0.5$ of the HPO of rotation number $p_{n+1}/q_{n+1}$ and $p_{n+2}/q_{n+2}$ have the largest size when projected onto the $x$ axis. Hence, the $x$ projection of size of the largest gap in the Cantorus at $k$, $\Delta x(k)$ is bounded from above by $2d_x^{(j+1)}$, the distance between the points of the $(j+1)$th hyperbolic approximating orbit closest to the symmetry line. Recall Subsect. 4.3.1.

Now consider $k' = k_G + \Delta k/\delta$. Note that $|\log_\delta(k - k_G) - \log_\delta(k' - k_G)| = 1$. According to the renormalisation scheme, if $j \gg 1$, we are close to a tangency between the IM of the HPO of rotation number $p_{j+1}/q_{j+1}$ and $p_{j+2}/q_{j+2}$, and the largest gap now is bounded from above by $d_x^{(j+2)} \approx d_x^{(j+1)}/\alpha$. See [78]. Similarly to the escape rates, a reduction by a factor $\delta$ in $\Delta k$ produces a re-scaling of the gap size by a factor $\alpha$, hence we expect

$$\Delta x(k) \sim (\Delta k)^\nu, \qquad \nu = \frac{\log(\alpha)}{\log(\delta)} \approx 0.712083498531404.$$

One expects the crossing rate across a Cantorus to be related to the area of these lobes that impede the existence of RIC. One always has to take into account that other phenomena like stickiness may play a leading role, see Chap. 3. Moreover, the routes to cross Cantori are those that follow the invariant manifolds that impede the existence of RIC, and these trajectories usually have passages close to saddles, that can also contribute to the slowdown of the escape rates.

In this section we will continue to study the standard map for values of $k > k_G$, but close to $k_G$. The problem of escape rates will be considered from two points of view. First, we will deal with the behaviour of the mean escape rate as $k \to k_G$, and to its standard deviation.

And these results will be crucial for the second point of view: the study of the probability law that an initial condition in the chaotic zone escapes in a prescribed number of iterates, conditioned to be able to escape.

### 4.5.1 Escape rates

Let us start by fixing our escaping rule and by explaining the way we will proceed to study escape rates experimentally. As usual, denote the successive iterates of a point in the cylinder $(x_0, y_0) \in \mathbb{S}^1 \times \mathbb{R}$ under $M_k$ as

$$M_k^n(x_0, y_0) = M_k(x_{n-1}, y_{n-1}) = (x_n, y_n).$$

We will consider that an initial condition in $\mathbb{S}^1 \times (0,1)$ but not confined in any island of stability escapes after $n$ iterations under $M_k$ if either $y_n > 1$ or $y_n < 0$, but $y_i \in (0,1)$ for all $0 \leq i < n$. The choice of the limits $y_n = 0, 1$ is done for simplicity. Instead of that, one could choose a rotational curve above the RIC with rotation number $\omega$ and another curve below the RIC with rotation number $1 - \omega$. In such a case, we obtain similar results.

**Notation.** From now on, we will denote $\Delta k = k - k_G$, for some $k > 0$; $\tilde{k} = \log_\delta(\Delta k) = \log_\delta(k - k_G)$. By $\mathcal{A}(k) \subset \mathbb{S}^1 \times (0,1)$ we will refer to the main zone in the phase space of the standard map (4.1) that can be considered to be chaotic. Here chaotic zones confined inside islands of stability are excluded, as not being accessible from outside.

So, for all values of $k$ considered, and for each initial condition chosen $(x_0, y_0) \in \mathbb{S}^1 \times (0,1) \subset \mathbb{S}^1 \times \mathbb{R}$, we will compute the quantity

$$n(x_0, y_0) = \min\{m \in \mathbb{N} \text{ such that } y_m > 1 \text{ or } y_m < 0\},$$

One of the main aims of this chapter is to study the probability of an orbit escaping in a prescribed number of iterates, conditioned to be able to escape, or

$$N_k(m) \quad = \quad P\left(n(x_0, y_0) = m \mid (x_0, y_0) \in \mathcal{A}(k)\right). \tag{4.25}$$

In Sect. 4.5.2 we will study the average and standard deviation of $N_k$, $\langle N_k \rangle$ and $\sigma_k$ respectively. In particular we will be mainly focused on how do these quantities change as we move the parameter towards $k_G$. More precisely, if we denote by $U(k)$ the set of initial conditions chosen as in Subsect. 3.3.2, and by `ic` the number of initial conditions in $U(k)$, then we will study the behaviour of

$$\langle N_k \rangle = \frac{1}{\texttt{ic}} \sum_{u \in U(k)} n(u) \qquad \text{and} \qquad \sigma_k^2 = \frac{1}{\texttt{ic}} \sum_{u \in U(k)} (n(u))^2 - \langle N_k \rangle^2 . \tag{4.26}$$

Since we are restricting ourselves to $k > k_G$, depending on our purpose, we will either use $k$ or $\tilde{k} = \log_\delta(k - k_G)$, and this will be indicated in the subscripts $\langle N_{\tilde{k}} \rangle$ and $\sigma_{\tilde{k}}$.

In Subsect. 4.5.3 we will use the results for the observables (4.26) to motivate the candidates to probability laws of $N_k$.

For all our experiments, we need to make sure that both the initial condition and values of the parameter chosen are representative, hence

1. To study the statistics of escaping orbits, we will iterate a large number of initial conditions chosen as is explained in Subsect. 3.3.2 until all of them escape. The way these initial conditions are chosen guarantees that they are not inside islands of stability. But the number of initial conditions considered for each value of $k$ depends on how close we are to the breakdown. Namely, one has to considerably reduce the number of initial conditions `ic` as $k \to k_G$, since the mean number of iterates one needs to escape increases fast.

   For our purposes, we can choose initial conditions on the unstable invariant manifold of any point in a Birkhoff hyperbolic periodic orbit with rotation number between $1-\omega$ and $\omega$. In the standard map, they can be found either on $y = 2x$ or $y = 2x-1$, see [83]. For our computations, we chose the 1/2-periodic orbit hyperbolic orbit ($j = 2$). This orbit has a point on $y = 2x$. The region where initial conditions chosen in this way lie is between the Cantori with rotation number $1-\omega$ and $\omega$, and for a long number of iterates they will be confined there (roughly the $y$ component will be in $[1-\omega, \omega]$). So first, the main obstruction to escape will be these Cantori. Once crossed, we expect the orbits to escape the region $y \in (0, 1)$ in a much smaller number of iterates. This has been checked numerically by using other values of $y$ closer to the Cantori under consideration instead of $y = 0$ and $y = 1$. The performed experiments do not show any relevant difference.

2. The values of the parameter $k$ will be chosen accordingly to the linear stability of the critical fixed point $R_C$ of $\mathcal{R}_1$: since $R_C$ has only one unstable direction with eigenvalue $\delta$, it is convenient to choose equispaced values of $k$ in $\log_\delta$-scale.

**Details on the data used.** We have computed the mean escaping time for 1101 values of the parameter $k$ in an equispaced grid in $\log_\delta$-scale. We have considered $\tilde{k} = -3(-0.01)-14$. Since we expect the mean escaping time to behave as a negative power law in $k-k_G$, we have considered less initial conditions as we approached the breakdown value of the parameter $k_G$. Namely $10^4$ initial conditions for $\tilde{k} = -12(-0.01) - 14$ (but for some of them in this range up to $10^5$), $10^5$ initial conditions for $\tilde{k} = -9(-0.01) - 11.99$, $10^6$ for $\tilde{k} = -6(-0.01) - 8.99$ and $10^7$ for $\tilde{k} = -3(-0.01) - 5.99$.

### 4.5.2 Results for the mean escape rate and its standard deviation

Our results on the evolution of the mean $\langle N_k \rangle$ as a function of $k$ can be seen in Fig. 4.12. There we show the same data in different scales. First, on top left, one can see the direct results for the mean as $k \to k_G$. As expected, we observe substantial increase in the mean escaping time as we approach $k_G$ (highlighted as a vertical line in this plot). There we show $\langle N_k \rangle \times 10^{-9}$. The value of $k$ closest to $k_G$ shown in Fig. 4.12, top left, corresponds to $k = 0.972724398546588 \approx k_G + \delta^{-14}$, being $\delta^{-14} \approx 1.089 \cdot 10^{-3}$. In average, for this value of $k$ each initial condition needs over $1.5 \times 10^{10}$ iterates to leave $y \in [0, 1]$. And for the closest value of $k$ we have computed $\langle N_k \rangle$, $k = k_G + \delta^{-15} \approx 0.972304340876959$, being $\delta^{-15} \approx 0.669 \cdot 10^{-3}$ (not shown in Fig. 4.12), the mean value exceeds $8 \times 10^{10}$ iterates.

As explained in Subsect. 3.5.6, from renormalisation and transport theories, we expect

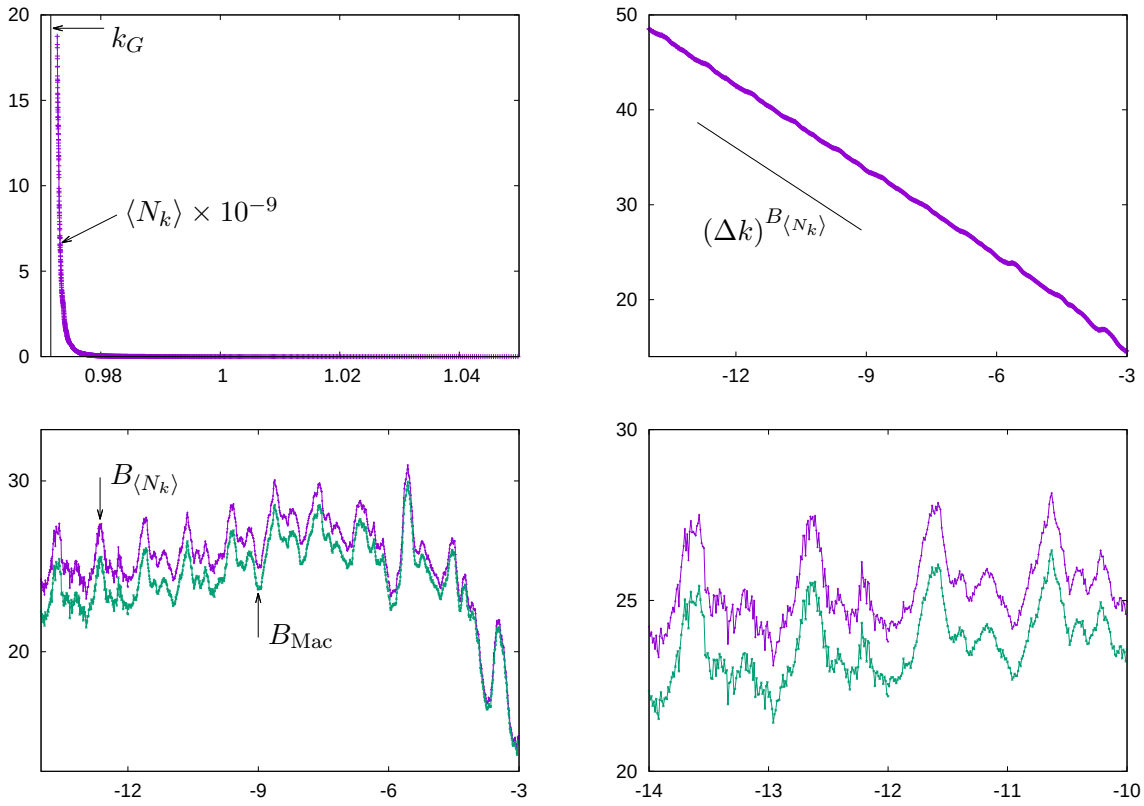


Figure 4.12: Statistics of $\langle N_k\rangle$, the mean escaping time of orbits of the Chirikov standard map (4.1), for values of the parameter near $k_G$. Top left: $\langle N_k\rangle \times 10^{-9}$ as a function of $k$ (purple), $\{k = k_G\}$ (black). Top right: $\log_\delta \langle N_k\rangle$ as a function of $\tilde{k}$ (purple), and the slope $B_{\langle N_k\rangle}$ (black). Bottom left: $\langle N_k\rangle \times (k - k_G)^{-B}$, with $B = B_{\langle N_k\rangle}$ (purple, top) and $B = B_{\rm Mac}$ (green, bottom), as a function of $\tilde{k}$, see (4.29). Bottom right: Detail of Bottom left. Compare with Fig. 4.10 and Fig. 4.11. See text for further explanations.

the mean escape rate $\langle N_k\rangle$ to behave as an inverse power law in $\Delta k$. To fix notation, write

$$\langle N_k\rangle = A(\Delta k)^B, \text{ and taking logarithms } \log(\langle N_k\rangle) = B\log(\Delta k) + \log(A). \tag{4.27}$$

In Fig. 4.12, top right, we show the data in the left plot but in $\log_\delta - \log_\delta$ scale to fit (4.27). Namely, we plot $\log_\delta \langle N_{\tilde{k}}\rangle$. Recall that $\tilde{k} = \log_\delta(\Delta k)$. Note that, as $k \to k_G$ this slope seems to change slightly. Some least squares fits of the data in different ranges of $\tilde{k}$ give

| Interval | $B$ | $A$ |
|---|---|---|
| $[-14, -12]$ | $-3.00 \pm 0.01$ | $25 \pm 1$ |
| $[-14, -11]$ | $-2.978 \pm 0.005$ | $28 \pm 1$ |
| $[-14, -10]$ | $-2.978 \pm 0.003$ | $28.7 \pm 0.5$ |

(4.28)

In Fig. 4.12, top right, the slope shown is $B_{\langle N_k\rangle} = -3.00$, the one corresponding to the data of the interval $\tilde{k} \in [-14, -12]$. This value has to be compared with theoretical one

proposed in [83],

$$B = B_{\text{Mac}} = -\log_\delta(\alpha\beta) \approx -3.01172189133849. \tag{4.29}$$

Our numerical results show that, as we approach the breakdown, we seem to get closer to the expected theoretical value $B_{\text{Mac}}$.

In the large, the diffusive process seems to follow a power law, yet there are some visible fluctuations. To study them, we have to subtract the fitted power law behaviour. In Fig. 4.12 bottom we show $\langle N_k \rangle \times (k - k_G)^{-B}$, as a function of $\tilde{k}$. As labelled in the left figure, the top graph corresponds to choosing $B = B_{\langle N_k \rangle}$ while the one below corresponds to $B = B_{\text{Mac}}$. The right plot is a magnification of the leftmost oscillations of the left plot. The oscillations in $\tilde{k} \in [-14, -12]$ are less smooth since we had to consider 10 times less initial conditions than in $\tilde{k} \in [-12, -10]$.

After subtracting the power-law tendency, we are left with what seems to be a 1-periodic behaviour as we approach the breakdown. See comments in Subsect. 3.5.6, where we referred to this periodic behaviour as the existence of a 1-periodic function $U(\log_\delta(k - k_G))$. The fluctuations far from $k_G$ ($\tilde{k} > -6$ in Fig. 4.12, bottom left) seem to be related to this 1-periodic behaviour close to $k_G$, but strongly deformed. As far as we are aware of, this is the first time where the shape of these 1-periodic fluctuations is shown. The main goal of this chapter is to interpret these fluctuations from the point of view of approximating periodic orbits. The main candidates of their appearance are the shape and area of approximating islands (see Fig. 4.10), the turnstile area (see Fig. 4.11 and compare it with Fig. 4.12: minima in Fig. 4.12 approximately correspond to maxima in Fig. 4.11, left and middle), the area of the lobes created by the invariant manifolds of hyperbolic approximating periodic orbits, and stickiness effects due to stability islands.

In Fig. 4.13 we show that the standard deviation $\sigma_k$ seems to behave similarly to the mean. On the left of this figure, we plot $\sigma_k$ as a function of $k$, and on the right we plot $\log_\delta(\sigma_{\tilde{k}})$ as a function of $\tilde{k}$ and the slope $B_{\langle N_k \rangle}$. Compare with Fig. 4.12, top.

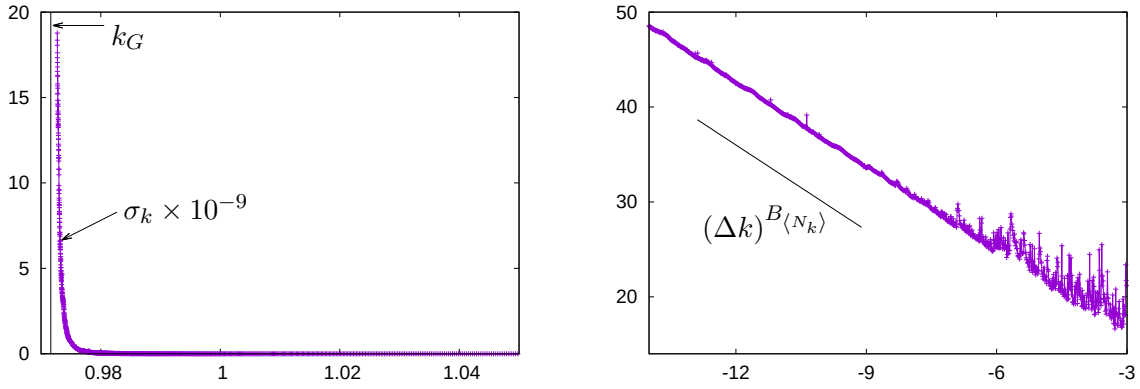


Figure 4.13: Statistics of $\sigma_k$, the standard deviation of $\langle N_{\tilde{k}} \rangle$. Left: $\sigma_k \times 10^{-9}$ as a function of $k$ (purple), $\{k = k_G\}$ (black). Right: $\log_\delta(\sigma_{\tilde{k}})$ as a function of $\tilde{k}$ (purple), and the slope $B_{\langle N_{\tilde{k}} \rangle}$ (black).

Despite having a similar behaviour as $k \to k_G$, as an inverse power law in $\Delta k$ with the same power, the main difference between the two observables is the existence of peaks in

$\sigma_k$, that are much more prominent far from the breakdown. Namely, as one can observe in Fig. 4.13, right, despite we can see some small peaks near $\tilde{k} \approx -10$, the largest deviations from the straight line appear for $\tilde{k} > -8$.

To show the existence and nature of these peaks it is convenient to study how does the standard deviation vary with respect to the mean. This is the contents of Fig. 4.14, where we plot $\sigma_{\tilde{k}}/\langle N_{\tilde{k}}\rangle$ as a function of $\tilde{k}$. On top left we see the behaviour in the whole range considered, $\tilde{k} \in [-14, -3]$, while the other figures are magnifications of this first one. These magnifications allow to see the actual shape of the peaks. In all the plots, we show a black horizontal line that corresponds to $\sigma_{\tilde{k}}/\langle N_{\tilde{k}}\rangle = 1$. It is remarkable that besides the peaks, the statistics of escape rates seem to have close values of the mean and the standard deviation.

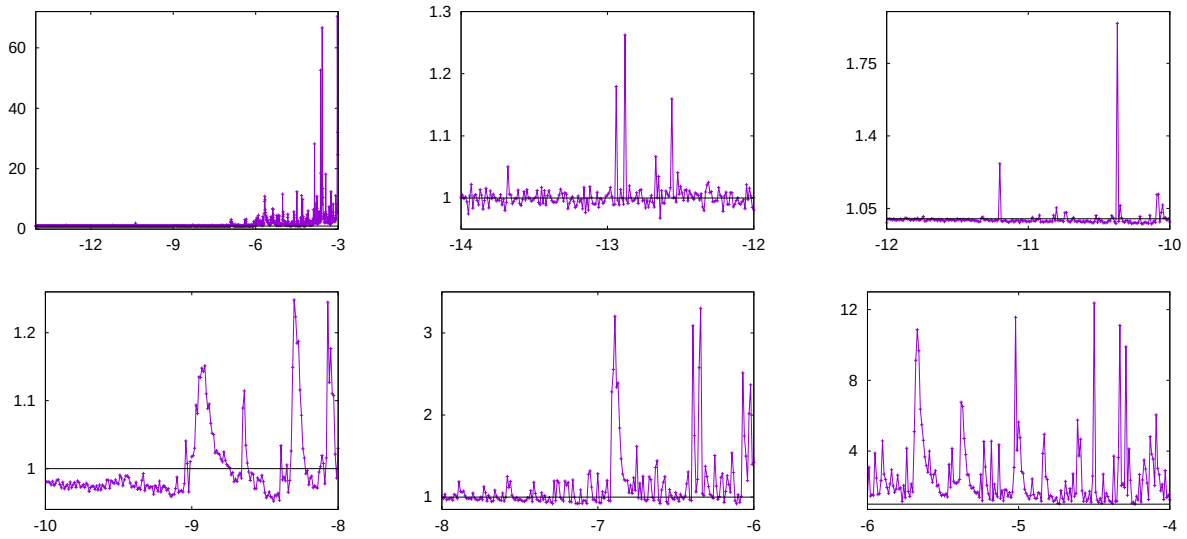


Figure 4.14: Top left: $\sigma_{\tilde{k}}/\langle N_{\tilde{k}}\rangle$ as a function of $\tilde{k}$ in $\tilde{k} \in [-14, -3]$. The other plots are magnifications in: top middle: $[-14, -12]$, top right: $[-12, -10]$, bottom left: $[-10, -8]$, bottom middle: $[-8, -6]$ and bottom right: $[-6, -4]$.

### Interpretation of the results

So far we have presented the results of a massive evaluation of the mean escaping time across the golden Cantorus of the standard map. Our numerical results fit within the available theories of renormalisation and transport. Yet we show that there are still some open questions concerning escape rates: there are phenomena playing a leading role that should be taken into account. Here we enumerate and discuss the numerical results obtained.

1. The power law behaviour $\langle N_{\tilde{k}}\rangle \sim (\Delta k)^{-B_{\mathrm{Mac}}}$. As we first explained in Subsect. 3.5.6 and later in Subsect. 4.4.3, the interpretation of Mather's $\Delta W$ as an area and the renormalisation theory justify that the escape rates have to behave like an inverse power law in $\Delta k$. In our simulations we approached the breakdown by $\delta^{-14} \approx 0.00108$ and got a difference between the theoretical value and our experimental approximation $|B_{\mathrm{Mac}} - B_{\langle N_{\tilde{k}}\rangle}| = \mathcal{O}(10^{-2})$. This means that we are still far from the limit, but computing representative statistics for values of $\tilde{k}$ smaller than $-14$ is still far from

practical. Note further that if we were close enough to the limit, the oscillations in Fig. 4.12 should take place around a horizontal line. But we expect this to happen closer to the limit, that is, as $\tilde{k} \to -\infty$.

2. The tendency $\sigma_{\tilde{k}}/\langle N_{\tilde{k}}\rangle \to 1$ as $\tilde{k} \to -\infty$. This behaviour might suggest that the transport rates behave as if they followed a Gamma distribution. Recall that the pdf of a Gamma distribution has the form

$$G(x;\kappa,\lambda) = \frac{\lambda^\kappa}{\Gamma(\kappa)} x^{\kappa-1}\exp(-\lambda x), \qquad \kappa \geq 1 \text{ (shape)}\ , \quad \lambda > 0 \text{ (rate)}\ . \tag{4.30}$$

This distribution has mean $\kappa/\lambda$ and standard deviation $\sqrt{\kappa}/\lambda$, so for values of $\kappa$ close to one we would see such a behaviour. Note that if one chooses $\kappa = 1$ in (4.30) one recovers the pdf with exponential distribution with rate $\lambda$. But in Sect. 4.5.3 we will argue that this is not the case for our actual statistics since the maximal value of the numerically approximated pdf's is not at $x = 0$. The determination of which is the underlying probability law still requires clarification from the point of view of which is the role of approximating islands. See also the comments at the end of Sect. 4.5.3.

3. The visible peaks in $\sigma_{\tilde{k}}/\langle N_{\tilde{k}}\rangle$ and the stickiness effect of islands of stability. In Fig. 4.14 there are many visible peaks, that seem to be more prominent for $\tilde{k} > -8$. Their shape resembles that of the effect of the accelerator modes in the standard map in Chap. 3. Recall Figures 3.7, 3.8 and 3.9, where we also show, for that problem, the behaviour of the standard deviation relative to the mean. Note that in the range of $k$ we are dealing with there are always visible islands so it is more than plausible to notice their effect.

   As shown in Chap. 3, the power law behaviour of the trapping time statistics has finite mean but unbounded variance. So, we expect $N_k$ to have a bounded mean, regardless of the value of $k$. But $\langle N_{\tilde{k}}\rangle$ has to depend strongly on the effect of islands of stability and the stickiness effect they produce. Furthermore, note that the way initial conditions are chosen ensures that all of them will eventually escape. This is one of the main differences between the experiments we did in Chap. 3 and the ones in this chapter. Hence, despite the trapping statistics in islands have unbounded variance, here $\sigma_k$ will be also bounded, but strongly dependent on the number of initial conditions, $\sigma_k = \sigma_k(\texttt{ic})$. In Fig. 4.15 we show examples of this strong dependence: we plot $\sigma_{\tilde{k}}(\texttt{ic})$ for $\tilde{k} \in [-5,-3]$ and $\texttt{ic} = 10^5, 5\times10^5, 10^6, 5\times10^6$ and $10^7$. Note that the values of $\sigma_{\tilde{k}}(\texttt{ic})$ do not increase as ic does. Here, the initial conditions of the case $\texttt{ic} = 5\times10^5$ are those of $\texttt{ic} = 10^5$ plus $4\times10^5$ extra initial conditions, and so on. So, we are adding initial conditions at each evaluation.

   Coming back to Fig. 4.14, for values of $\tilde{k} < -8$ we see that there is little effect due to the stickiness of stability islands, if any. This is mainly due to the fact that the time to cross the Cantorus is of an order of magnitude larger than the mean trapping time in any of the islands that are present in the phase space. This means, in particular, that as we get closer to $k_G$ the data obtained in simulations better reflects the effect of a single Cantorus.

4. The limit 1-periodic oscillations $U(\log_\delta(k-k_G))$. The power-law behaviour comes from the scaling in area and in parameter, but yet it needs to be clarified which are the objects responsible for the actual transport probabilities. One expects the oscillations

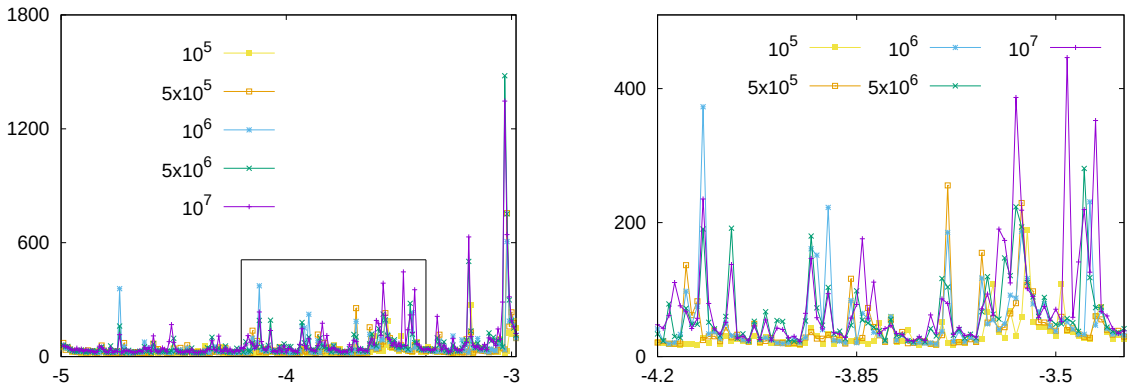


Figure 4.15: Left: $\sigma_{\tilde{k}} \times (k - k_G)^{B_{\text{Mac}}}$ as a function of $\tilde{k} \in [-5, -3]$, obtained for different values of `ic`, see the key in the plots. Right: Magnification of the square in the left plot.

to be strongly related to the area of the heteroclinic lobes of intersecting IM of HPO and the turnstile areas of approximating orbits. Namely, as $k$ varies, the area in the phase space that is accessible to orbits that can escape changes as the islands of stability do, and not in a monotone way in $\tilde{k}$, but if we conveniently scale the phase space, the area occupied by evolving islands varies in a periodic way, recall Sect. 4.4.2, and also Figs. 4.10 and 4.11.

**Discussion on previous literature**

The very first computations similar to the ones we present here were done by Chirikov in [26]. In this review, he iterated 100 orbits starting at $\{y = 0\}$ of (4.1) for at most $10^7$ times, keeping track on the number of iterates needed to eventually cross the line $\{y = 0.5\}$. By doing this, he obtained an approximation of Greene's critical value $k_{\text{Chi}} = 0.989/(2\pi)$. Furthermore, he fitted the behaviour of the mean to

$$T = \frac{A_{\text{Chi}}}{(k - k_{\text{Chi}})^{B_{\text{Chi}}}}, \qquad \text{where} \qquad A_{\text{Chi}} = 103, \quad B_{\text{Chi}} = 2.55. \tag{4.31}$$

The values of $k$ Chirikov dealt with were from close to $k_{\text{Chi}}$ until almost $k = 2\pi$. For the largest values for which he computed the statistics, there are almost no visible stability islands in the phase space, and in this situation $D(k)$ grows as $k^2$, recall Chap. 3. This may be the reason why he got a value of $A$ in (4.27) almost 3 times larger than ours.

This power law behaviour was theoretically justified by MacKay, Meiss and Percival in [86]. In this work, the authors fixed $B = B_{\text{Mac}}$ as theoretical value and fitted the value of $A$ in (4.27) to be $A_{\text{MMP}} = 25$, close to our results. See (4.28).

The last paper we want to mention here is that of Dana and Fishman [34]. There the authors were the first to give numerical evidence of the predictions from renormalisation theory [83, 80] and transport theory [86]. Namely, they looked for ranges in the parameter $k$ where the behaviour (3.7) was good enough. They computed the diffusion coefficient $D(k)$, averaged among 5000 initial conditions. They restricted themselves to $1/(2\pi) \leq k \leq 2.5/(2\pi)$, and in this range they were able to get satisfactory results for the exponent $B = B_{DF}$. In

the whole range, they got $B_{DF} = 3.24$. In $1/(2\pi) \leq k \leq 1.4/(2\pi)$ they got $B_{DF} = 3.16$ and in $1.4/(2\pi) \leq k \leq 2.5/(2\pi)$ numerical simulations gave $B_{DF} = 2.96$, which is closer both to theoretical result $B_{\mathrm{MMP}}$ and ours, $B_{\bar{T}}$ and $B_\sigma$. In this reference the authors gave no information on the value of the constant $A$ in (4.27).

As a final remark, we want to note that the computation of escape rates near Greene's critical values is still a hard computational issue. To obtain the results shown in Figures 4.12 and 4.13 we had to perform over $8.33 \times 10^{15}$ iterations of the standard map (4.1). And the computations for the case $\tilde{k} = -15$, $k = k_G + \delta^{-15}$ alone required over $8 \times 10^{15}$ iterations. So, the sharpness of the results of the previous literature is remarkable.

### 4.5.3 The probability law of escape rates

In this subsection we deal with the probability law $N_k$ (4.25), for $\tilde{k} < -5$. Recall that the size of the samples (number of initial conditions we iterated) we are dealing with are $10^5$ for $\tilde{k} = -9(-0.01) - 12.00$ and $\tilde{k} = -13, -14, -15$, $10^6$ for $\tilde{k} = -6(-0.01) - 8.99$, and $10^7$ for $\tilde{k} = -5(-0.01) - 5.99$. Since we expect escaping times to be increasingly large as we approach $k_G$, to get an approximation of the probability density function (pdf) of $N_k$ it is convenient to compute histograms with bins of constant length in decimal logarithmic scale, similar to what we did in Subsect. 3.5.2 when dealing with trapping times of accelerator modes.

More concretely, for each $k$, assume that we can set a time interval $T = [t_0, t_1]$ where we can assure that most initial conditions will escape in a number of iterations that is contained in $T$. We say most because we expect, due to the results of Chap. 3, that if an orbit gets trapped around a stability island, the escaping time for this orbit can become extremely large. Then we consider $n_i$ sub-intervals $I_j = [t_0\lambda^j, t_0\lambda^{j+1})$, where $\lambda = \exp\left(\log_{10}(t_1/t_0)\log(10)/n_i\right)$, and a counter $C_j$ initially set to 0, $j = 0, \ldots, n_i - 1$. Each initial condition adds a unit to $C_j$ if escapes in $m$ iterates, where $m \in I_j$. To recover the pdf from the histogram we only have to divide each counter by the length of the interval and by the total number of initial conditions, `ic`, that is, to consider $C_j/((n_i + 1)\mathtt{ic})$ instead of $C_j$ itself.

A sample of the pdf's obtained can be seen in Fig. 4.16. On the left we can see the pdf $N_k$ in the actual scale time for $\tilde{k} = -5(-0.5) - 12$, and on the right we display these same pdf's, but in decimal logarithmic scale in time, that is, we plot

$$N_k'(\xi) = \log(10)10^\xi N_k(10^\xi). \tag{4.32}$$

We have labelled some pdf's according to the value of $\tilde{k}$ they correspond to. In both plots, left and right, one can follow $N_k$ for decreasing values of $\tilde{k}$ by following the maximum of each pdf from left to right. In the left plot, one observes that the pdf's accumulate to 0 as $k$ goes further apart from $k_G$. To see what happens for $k \to k_G$, the right plot is more convenient. The pdf's in $\log_{10}$-scale in the number of iterates appear to be equispaced since they correspond to equispaced values of $\tilde{k}$ and $\langle N_k \rangle \sim (\Delta k)^B$. It is remarkable that in $\log_{10}$ scale for the number of iterates, the pdf's seem to go from a seemingly symmetric shape to some asymmetric limit behaviour that resembles that of a gamma distribution (4.30)in log scale in time.

In item 2 in the enumeration in page 118 we commented on the possibility that the pdf's displayed in Fig. 2 followed a gamma distribution if the corresponding estimated value for

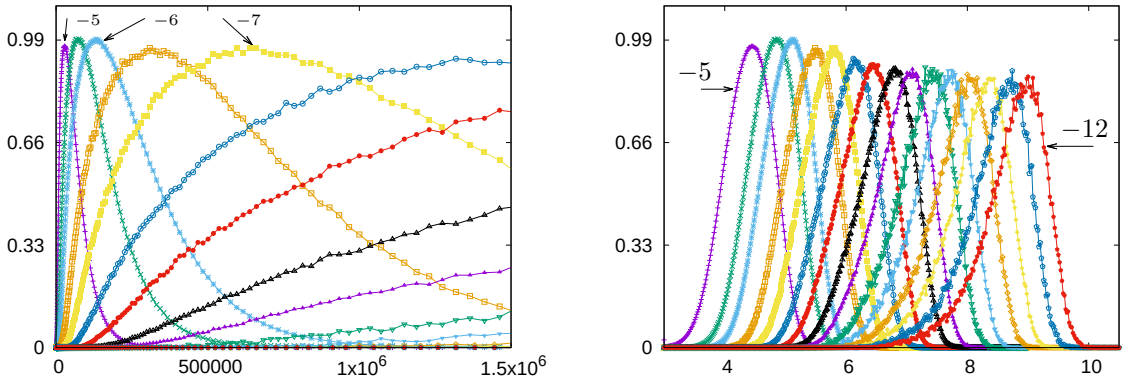


Figure 4.16: Estimates of the probability density function (pdf) of the number of iterates needed to escape, $N_k$, for different values of $\tilde{k}$. Left: $N_k$ in the original scale of time. Right: $N'_k$ vs $\xi$, see (4.32). Here we show the pdf's for $\tilde{k} = -5.0(-0.5) - 12.0$.

the shape $\kappa$, see (4.30), was close to one. That is, the behaviour is close to exponential, but not exponential, since the maxima of the numerically computed pdf's are not located at $x = 0$ but increase as the mean escape rate does.

Again back to (4.30), a rough estimation of both shape $\kappa$ and rate $\lambda$ parameters can be done by taking into account the fact that the potential factor plays a leading role for small values of the number of iterates, $t$, and that the exponential factor does for larger values of $t$. Namely, for large $t$, one would expect an exponential decay of the pdf, that is detected as a straight line in some range of $t$ in a $\log - \log$ plot. See Fig. 4.16, right. The first estimation of $\lambda$ allows to estimate the value of $\kappa$. This procedure has been carried out for the results of some of the values of the parameter shown, followed by a least squares fit to better adjust the values of the parameters.

Despite we found that as $\tilde{k}$ decreased, the agreement became better, the adjustment was not completely satisfactory. A Kolmogorov-Smirnov test of adjustment was performed to see if the experimental data followed the hypothetical gamma pdf with the adjusted parameters. In all cases studied, the statistic $D$ (the largest vertical distance between the experimental cumulative distribution function (cdf) and the cdf of the theoretical distribution) was $D \approx 0.02$. For `ic` $= 10^5$, it is way larger than the minimum to accept that the data follows a gamma distribution.

Hence, other means have to be adopted in order to study transport rates across Cantori. The previous study on approximating stability islands suggests to construct a nearest neighbour Markov chain taking into account different layers. The corresponding transition probabilities between different stages have to be related to the turnstile areas, [86]. This will be done elsewhere.

### 4.5.4 Summary and remarks

In this chapter we have presented a detailed study of the escape rates in the standard map (4.1) for values of the parameter close but larger than $k_G$. We have first reviewed the Greene-MacKay renormalisation theory and how does the dynamics of the renormalisation operator for invariant curves explain the geometry of phase space of the standard map close to the

golden RIC.

We have performed a detailed study of approximating islands, both from a local point of view (around the elliptic/reflection hyperbolic orbit) and more globally in adequate compact sets containing islands of stability. This study has lead to a classification of these islands that allows to give an explanation of the periodic fluctuations around the mean inverse potential behaviour of the escape rates one observes as $k \to k_G$. We have also given evidence of the shape of the periodic function $\langle N_k \rangle (k - k_G)^B$ that has period 1 in $\log_\delta$ scale.

We finished the chapter by addressing the problem of determining the probability law of escape rates. We have given numerical evidence that a Gamma distribution can not fully explain the shown behaviour. Instead of that, a nearest neighbour Markov process with different states (as many as relevant approximating islands appear near the Cantorus) has been suggested. We will deal with this problem with more detail in forthcoming contributions.

We hope that the contents of this chapter contributes to the comprehension of the phase space near the breakdown so that the probability laws of escape rates can be better understood, by taking into account as many phenomena as possible. We have argued that one only needs to study a conveniently scaled version of the phase space in a length 1 interval in $\tilde{k}$. We have also explained how to properly scale the phase space and choose $\tilde{k}$ to get representative results.

# Chapter 5

# Stickiness effect due to a resonance bubble emerging from a Hopf-zero bifurcation in 3D volume preserving maps

In this chapter we study the trapping statistics around a stability bubble that arises after a Hopf-zero (or Hopf-Saddle-Center) bifurcation. We construct a proper 3D volume preserving map on the 3-torus $\mathbb{T}^3$ with accelerator modes, by mimicking some features of the Chirikov standard map.

The results of preliminary massive numerical simulations (inspired in those performed in Chap. 3) give evidence that the bubbles are responsible for anomalous diffusive properties of lifts of the VPM model to the cylinder $\mathbb{T}^2 \times \mathbb{R}$, and that the trapping statistics exhibit an algebraic decay. We pay special attention to the geometry of the outermost invariant objects in the bubble, as they are the main responsibles for the stickiness effect.

## 5.1 Introduction

While the geometry and relative position of invariant objects in twist APM is fairly well understood, this is not the case in the VPM case, even if these maps satisfy the non-degeneracy conditions of KAM-like results [24, 147], recall Sect. 1.1.1. From now on, we will restrict ourselves to VPM such as $H_\varepsilon^{(2)}$ see, (5.1): maps depending on $(\theta, r)$ where $\theta \in \mathbb{T}^2$ can be interpreted as angles and $r \in [0,1]$ as an action variable. That is, we will consider 2-angles and 1-action maps. For convenience, let us recall the form of the VPM that we are going to deal with:

$$H_\varepsilon^{(2)} : \mathbb{T}^2 \times [0,1] \to \mathbb{T}^2 \times [0,1],$$
$$H_\varepsilon^{(2)} : \begin{pmatrix} \theta \\ r \end{pmatrix} \mapsto \begin{pmatrix} \bar{\theta} \\ \bar{r} \end{pmatrix} = \begin{pmatrix} \theta + g^{(2)}(r) \\ r \end{pmatrix} + \varepsilon \begin{pmatrix} f_1^{(2)}(\theta, r) \\ f_2(\theta, r) \end{pmatrix}, \quad (5.1)$$

where $f_2$ is going to be assumed to have zero average with respect to $\theta$.

For this kind of maps, in the near-integrable case $\varepsilon > 0$ small, as we discussed with more detail in page 14, the dynamics near rank one and rank two resonances can be explained via averaging theory [41]: near a rank one resonance, in some suitable region close to it the

dynamics can be approximated by the area-preserving twist or non-twist standard map times some rotation; and near a double resonance the dynamics can be approximated by a "quasi-periodic pendulum". But in contrast to the twist APM setting, there is local analogue of the Poincaré-Birkhoff theorem in the volume preserving case for invariant curves [25] but not for periodic orbits [48]: one can not predict, a priori, which periodic orbits will be present in the phase space by means of boundary conditions, for instance, as the existence and invariance of two rotational 2D invariant tori (RIT) defining an invariant region in the phase space. Moreover, despite there has been recent efforts to deal with the destruction of RIT, this phenomenon is not yet completely understood: one does not know if there is a remnant of these RIT after their breakdown, an analogue of Cantori for twist APM, and in case such remnants exist, how is this set embedded in the phase space, see [100, 48].

Concerning transport in chaotic regions, as usual, one expects them to be strongly affected due to regular components in the phase space, recall Sect. 1.1.4. It is surprising that, in 3D maps, there are examples for which there is numerical evidence that the trapping times decay in different ways. First, algebraically, meaning that the statistics of stays in compact sets containing some invariant object behaves as $t^{-b}$, $b > 0$ where $t$ denotes the number of iterates, see [109]. This is the observed behaviour in the 2D setting (see Chap. 3). And second, in other examples, this decay seems to behave in an exponential way, see [141].

In this chapter we are going to perform a preliminary study of the stickiness effect of a stability bubble, see [18, 19, 20, 40], that arises from a Hopf-zero (or Hopf-Saddle-Center) bifurcation in a family of VPM of the three-torus $\mathbb{T}^3$. The family of VPM that we will use as example is going to be constructed in such a way that it mimics some features of the standard map for large values of $k$, so that we can use the methods we introduced in Chapter 3.

This chapter is organized as follows. Sect. 5.2 is devoted to the construction of the family of VPM we are going to use for our simulations, and to the study of the local dynamics around some of the Hopf-zero bifurcations that occur for the constructed family. In Sect. 5.3 we are going to review the main known facts about the Michelson system, specially those concerning the volume of bounded orbits. In particular, we will discuss on parameters to ensure that our model exhibits bounded volume right after the Hopf-zero bifurcation. Finally, in Sect. 5.4 we will deal with a case study. A proper choice of parameters will be done so that one can observe the strong effect of the bubble in diffusive properties, and to give numerical evidence of its trapping statistics.

This chapter has to be understood as a preliminary extension of the work performed in the 2D AP setting. The goal is to show that the techniques can be easily transferred to the VP case, where similar phenomena can be also expected. This is work in progress with J. D. Meiss, C. Simó and A. Vieiro.

## 5.2 A family of maps of $\mathbb{T}^3$ with accelerator modes

In this section we motivate the choice of the model we are going to work with. Roughly speaking, we want to consider a setting analogous to the one we dealt with in Chap 3: we want to study the stickiness effect due to a bubble embedded in a seemingly fully chaotic phase space. To do so, we will construct a family $\bar{f}_\varepsilon$ of VPM of $\mathbb{T}^3$ such that, for large values of $\varepsilon$, its corresponding phase space is seemingly fully chaotic, but presents some moderate bounded volume mainly due to bubbles that appear periodically in the parameter $\varepsilon$. By

bounded volume we refer to a set of orbits contained in a compact set $K$ that never leave $K$ under iteration. Note that these orbits can be either regular or confined chaotic. Moreover, this bubble is going to be an accelerator mode, so if one lifts $\bar{f}_\varepsilon$ to the cylinder $\mathbb{T}^2 \times \mathbb{R}$, say $f_\varepsilon$, the stickiness effect of the bubble will give rise to anomalous diffusion in the lifted variable.

More concretely, we are going to consider a family of VPM $(x', y', z') = f_\varepsilon(x, y, z)$ where $(x, y) \in \mathbb{T}^2$ are angles and $z \in \mathbb{R}$ is an action. The map $\bar{f}_\varepsilon$ above is the projection of $f_\varepsilon$ in the 3-torus. The family $f_\varepsilon$ will be written as compositions of 3 shears, recall Sect. 1.3.2. Since the dynamics in the third component will be $z' = z + f_2(x, y)$, where $f_2$ is periodic in $x$ and $y$ and has zero average, we will be able to smoothly project the map to the three torus $\mathbb{T}^3$. Note that we still only explicitly stress the dependence on a parameter $\varepsilon$, which is going to be the 'distance-to-integrable' parameter, but $f_\varepsilon$ will depend on more.

If we want to translate the setting that we dealt with in Chap. 3 to the 3D VPM case, we should choose $f_\varepsilon$ in such a way that it fulfills the following three main requirements:

**R1** The map $f_0$ has to be integrable as defined in Def. 1, see page 10. This will be imposed by choosing $f_0$ so that its phase space is foliated by horizontal RIT $\{z = \text{const}\}$. Moreover, the restriction of the dynamics on each such 2-torus has to be conjugated to a rigid rotation. Furthermore, we want some of this structure, that is, the existence of RIT, to be preserved for small values of $\varepsilon > 0$, but not too small, as happens in the Chirikov standard map.

**R2** For integer values of $\varepsilon = n \in \mathbb{Z} \setminus \{0\}$, the origin $P_+ = (0, 0, 0)$ is a fixed point of $\bar{f}_n$. But for $f_n$, $P_+$ is no longer fixed. It jumps upwards a distance $n$ in the $z$ variable per iterate:

$$f_n^q(0, 0, m) = (0, 0, m + nq), \quad m \in \mathbb{Z}.$$

Hence, the origin is an accelerator mode, see Def. 8.

**R3** The local parameter $\kappa = \varepsilon - n$ unfolds a Hopf-zero (also known as Hopf-Saddle-Center) bifurcation at $P_+$. Moreover, for $\kappa > 0$ small, there appears some moderate bounded volume around it. To fix ideas, we will define the family $f_\varepsilon$ in such a way that the Taylor expansion around $P_+$ for $\varepsilon = n + \kappa$, $n \in \mathbb{Z} \setminus \{0\}$ is locally conjugated to a map that consists in a discretisation of the Michelson system (5.3), see [104], plus higher order terms that depend on $n$ in such a way that they tend to vanish as $n \to \infty$, see Prop. 3.

We aim to detect the effect of the orbits that get trapped around the bubble as anomalous diffusion in the statistical behaviour of the $z$ component of non-bounded chaotic orbits. Due to the accelerating character of the whole bubble, we expect this effect to give rise to super-diffusive phenomena, see Sect. 1.1.5 in page 22.

### 5.2.1 A choice of the shearing functions

First, concerning the first requirement **R1**, the KAM theorem in the VP setting [24, 147], holds if the image of any 2-torus under the map intersects itself (intersection property) and if the following twist condition holds

$$\det\left(D_r g^{(2)}, D_r^2 g^{(2)}\right) \neq 0, \text{ for all } r, \quad \text{see equation (5.1).} \tag{5.2}$$

Note that the intersection property is guaranteed by choosing $f_2$ with zero average with respect to the angles $(x, y)$.

Concerning the third requirement **R3**, we want the local dynamics around the origin near integer values of $\varepsilon$ to be close to a discretisation of a flow in a suitable compact domain in $\mathbb{R}^3$. Namely to be close to the so-called Michelson system

$$\left\{ \begin{array}{rcl} \dot{x} & = & y \\ \dot{y} & = & z \\ \dot{z} & = & 1 - x^2 + ay \end{array} \right. , \quad \text{where} \quad a < 0. \tag{5.3}$$

We are concerned about the set of bounded orbits of (5.3). This set will be described in Sect. 5.3. The flow (5.3) arises as the equation for travelling wave solutions of the Kuramoto-Sivashinsky nonlinear PDE

$$u_t + u_{xxxx} + u_{xx} + \frac{1}{2} u_x^2 = 0, \qquad t \geq 0, \quad x \in \mathbb{R},$$

see [104] for the derivation of (5.3) from the equation of the PDE. We will consider the following discretisation of (5.3):

$$\mathrm{Mic}_{\varphi,a} : \begin{pmatrix} u \\ v \\ w \end{pmatrix} \mapsto \begin{pmatrix} u' \\ v' \\ w' \end{pmatrix} = \begin{pmatrix} u + \varphi v \\ v + \varphi w' \\ w + \varphi \left( 1 - u^2 + \frac{a}{\varphi^2} v \right) \end{pmatrix} \tag{5.4}$$

Note that it is written as a composition of 3 shears as (1.25) in page 32: first in $w$, then in $u$ and finally in $v$. We have changed the form of the coefficient in $v$ in the representation of $w'$ for aesthetic purposes that are going to be clarified in Prop. 3, see item 2 in Rem. 9.

Taking these considerations into account, we can consider the following family of maps of $\mathbb{T}^2 \times \mathbb{R}$:

$$f_\varepsilon : \begin{pmatrix} x \\ y \\ z \end{pmatrix} \mapsto \begin{pmatrix} x' \\ y' \\ z' \end{pmatrix} = \begin{pmatrix} x + \mu \sin(2\pi y) + \psi(z') \\ y + \nu \sin(2\pi z') \\ z + \varepsilon \left( \cos(2\pi x) + b \sin(2\pi y) \right) \end{pmatrix}, \tag{5.5}$$
$$\mu, \nu, \varepsilon \text{ and } b \in \mathbb{R},$$

where $\psi$ is a 1-periodic function in $z$. This map fulfills part of the requirement **R1**: for $\varepsilon = 0$, all horizontal 2-tori $\{z = \text{const}\}$ are invariant and have rotation vector $\omega = (\psi(z), \nu \sin(2\pi z))$. This is true regardless of the term $\mu \sin(2\pi y)$ that appears in the first component of $f_\varepsilon$, since it is averaged out under iteration.

If $\psi(0) = 0$, then **R2** is also fulfilled, since if $\varepsilon = n \in \mathbb{Z}$, $f_2(0, 0) = n$.

Concerning **R3**, if we impose that $\psi'(0) = 0$ and $\psi''(0) = 0$, then the local expansion of $\bar{f}_n$ around $P_+$ can be conveniently scaled to recover, up to terms of order 2, the map (5.4), see Prop. 3.

**Remark 8.** *The intersection property is also a zero-flux condition. This implies that for each upwards jumping accelerator mode $f_\varepsilon$ has, there must exist another downwards jumping accelerator mode. In our case, $P_+$ jumps upwards and the corresponding downwards jumping accelerator mode is located at $P_- = (1/2, 0, 0)$.*

It only remains to choose the summand $\psi(z)$ in the first component. Mimicking the standard map, (1.13), we want $\psi(z') \approx z'$. All the requirements to be imposed to $\psi(z)$, beyond being $\psi(z) - z$ 1-periodic, are summarized as follows:

$$\psi(z) = -\psi(-z), \quad \psi(1) = 1, \quad \psi'(0) = 0, \quad \psi''(0) = 0, \tag{5.6}$$

and $\psi(z)$ has to be close to the identity $z$ near $z = 1/2$. Furthermore, we need $\psi'(z)$ to be non-vanishing in some ranges of $z \in [0, 1]$ so that the KAM theorem [24, 147] can be applied and some RIT persist for small values of $\varepsilon > 0$.

**A choice for $\psi(z)$**

For our concrete example, we chose $\psi$ as follows. Consider for the moment a function $\tilde{\psi}(z) = -z + c_3 z^3$, defined on $[0, 1]$. If $c_3 \geq 4$ there is a unique $z_c \leq 1/2$ such that $m_c = \tilde{\psi}'(z_c)$ is the slope of the straight line between $(z_c, \tilde{\psi}(z_c))$ and $(1/2, 0)$. The value $z_c$ is determined as a solution of the cubic equation,

$$\tilde{\psi}'(z_c)(1/2 - z_c) + \tilde{\psi}(z_c) = 0.$$

Define the $C^1$ function

$$\tilde{\psi}_{\text{ext}}(z) = \begin{cases} \tilde{\psi}(z) & \text{if} \quad z \in [0, z_c), \\ m_c(z - 1/2) & \text{if} \quad z \in [z_c, 1 - z_c], \\ -\tilde{\psi}(1 - z) & \text{if} \quad z \in (1 - z_c, 1]. \end{cases}$$

This is an odd function with zero average. We can consider an analytic approximation of it via (a truncated) Fourier series, that will only contain sinus terms with coefficients $\hat{a}_k < 0$. Call such an approximation $\hat{\tilde{\psi}}_{\text{ext}}$. We have chosen $c_3 = 8\pi^2$ and, for this value, it is enough to take the first 7 harmonics to get a fairly good approximation of $\tilde{\psi}_{\text{ext}}$. That is,

$$z + \lambda_c \hat{\tilde{\psi}}_{\text{ext}}(z) \approx z + \lambda_c \sum_{k=1}^{7} \hat{a}_k \sin(2\pi k z),$$

where $\lambda_c = |d\hat{\tilde{\psi}}_{\text{ext}}(0)/dz|^{-1}$ is a correction factor to make sure that $\psi'(0) = 0$. For our map $f_\varepsilon$, we chose

$$\psi(z) = z + \sum_{k=1}^{7} a_k \sin(2\pi k z), \tag{5.7}$$

where

$$\begin{aligned} a_1 &= -0.03172255262410020, & a_5 &= -0.00394622128219923, \\ a_2 &= -0.01500144672104500, & a_6 &= -0.00257376369649251, \\ a_3 &= -0.00909490284466739, & a_7 &= -0.00159954483407287. \\ a_4 &= -0.00594357151581041, \end{aligned}$$

In Fig. 5.1 we can see the graph of $\psi(z)$ in $[0, 1]$ (left), and how much it differs from the identity $z$ (right). Note that for a 1-periodic map $\psi(z)$ as (5.7), the twist condition (5.2) is violated near $z = 0, 1/2$. Indeed: for (5.5), the corresponding $g^{(2)}(z)$ as in (5.1) is $g^{(2)}(z) = (\psi(z), \nu \sin(2\pi z))^\top$. Its second derivative is

$$D^2 g^{(2)}(z) = \left( -4\pi^2 \sum_{k=1}^{7} k^2 a_k \sin(2\pi k z), -4\pi^2 \nu \sin(2\pi z) \right), \tag{5.8}$$

which vanishes identically at $z = 0, 1/2$. Furthermore, (5.8) is still small in $[0,1] \setminus \{0, 1/2\}$. Hence, around $\{z = 0\}$ and $\{z = 1/2\}$ we expect the chaotic zone to be already prominent for small values of $\varepsilon > 0$.

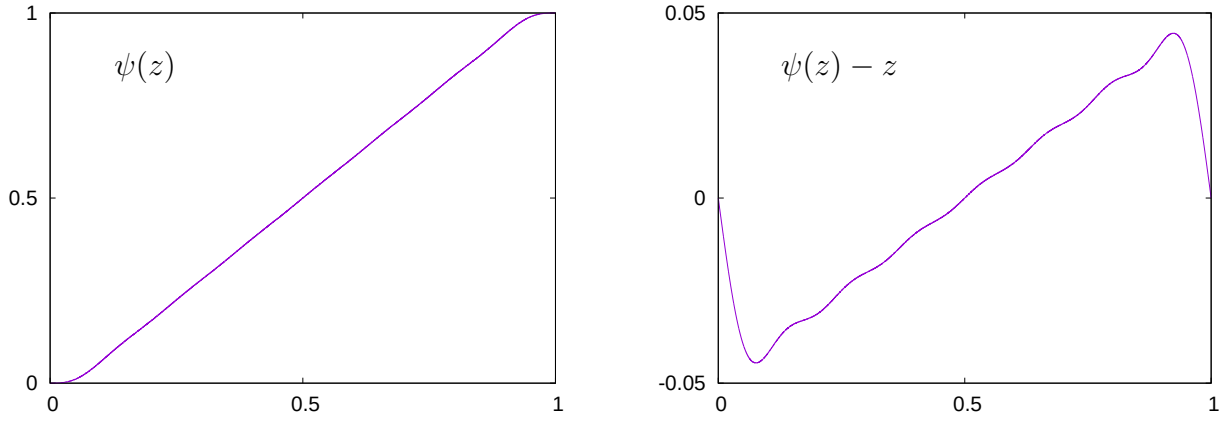


Figure 5.1: Left: function $\psi(z)$ in (5.5), see (5.7). Right: $\psi(z) - z$.

Concerning parameters, $f_\varepsilon$ depends on $\varepsilon$ and on three extra parameters, $\mu, \nu$ and $b$. In Prop. 3 we will prove that for all values of $\mu, \nu$ and $b$, the local dynamics around $P_+$ for $\kappa = \varepsilon - n > 0$ small is close to the dynamics of the discrete Michelson system (5.4) for some suitable values of $\varphi$ and $a$. For the purpose of this chapter, it is enough to study trapping statistics by only varying the value of $\varepsilon$, and to fix the other 3 parameters $\mu, \nu$ and $b$. These will be fixed in such a way that some RIT persist for a value of $\varepsilon$ as large as possible. To get the most suitable model, we will fix them in a way that for $\kappa = \varepsilon - n > 0$ there appears a positive volume bubble and that it is as large as possible, with respect to the volume of $\mathbb{T}^2 \times [0,1]$.

**Fixed points of $f_\varepsilon$.** It is easy to locate the fixed points of $f_\varepsilon$, and to compute their first and second traces $\tau$ and $\sigma$, see Tab. 5.1. Once we fix the values for the parameters $\mu, \nu, b$ we can determine their stability for each value of $\varepsilon$ by locating their corresponding $\tau$ and $\sigma$ in any of the 8 zones of the diagram in Fig. 1.6 in page 34. This will be used later on to generate initial conditions for the diffusion experiments we are going to perform, again as explained in Sect. 3.3.2 in page 65.

| **Position** | $\tau$ | $\sigma$ |
|---|---|---|
| $(1/4, 0, 0)$ | $3 + 4b\pi^2\varepsilon\nu$ | $3 + 4b\pi^2\varepsilon\nu + 8\pi^3\varepsilon\mu\nu$ |
| $(1/4, 1/2, 0)$ | $3 - 4b\pi^2\varepsilon\nu$ | $3 - 4b\pi^2\varepsilon\nu - 8\pi^3\varepsilon\mu\nu$ |
| $(3/4, 0, 0)$ | $3 + 4b\pi^2\varepsilon\nu$ | $3 + 4b\pi^2\varepsilon\nu - 8\pi^3\varepsilon\mu\nu$ |
| $(3/4, 1/2, 0)$ | $3 - 4b\pi^2\varepsilon\nu$ | $3 - 4b\pi^2\varepsilon\nu + 8\pi^3\varepsilon\mu\nu$ |

Table 5.1: Fixed points of the map $f_\varepsilon$ together with their first and second traces, $\tau$ and $\sigma$.

### 5.2.2 Local dynamics around accelerator modes

Let us restrict ourselves to $\varepsilon > 0$. The first accelerator mode of $f_\varepsilon$ appears at $\varepsilon = 1$. According to the stability analysis performed in Sect. 1.3.2, for $\varepsilon = n \in \mathbb{Z} \setminus \{0\}$ the first and

second traces of $Df_n$ at $P_+$ are

$$\tau = \sigma = 3 + g_1^{(2)} g_2^{(1)} = 3,$$

so $\tau$ and $\sigma$ are on the line $\tau = \sigma$ in the bifurcation diagram in Fig. 1.6. In particular, $Df_n(P_+)$ has 1 as triple multiplier. Hence, it corresponds to the point $B$ in Fig. 1.6. Consider values of $\varepsilon$ of the form $\varepsilon = n + \kappa$, where $\kappa > 0$ is small. For these values of $\varepsilon$, the origin ceases to be fixed under $\bar{f}_\varepsilon$ and bifurcates into two other fixed points. These two fixed points still lie on $y = z = 0$, and their $x$ component can be found by setting to zero the forcing $\varepsilon(\cos(2\pi x) + b\sin(2\pi x))$, the coefficient in $\varepsilon$ in the third component in (5.5). This equation reads, in lowest terms,

$$\begin{aligned}(n+\kappa)(1 - 2\pi^2 x^2 + \mathcal{O}(x^4)) = n \quad &\Leftrightarrow \\ x = \pm\frac{\sqrt{\kappa}}{\pi\sqrt{2(n+\kappa)}} + \mathcal{O}(\kappa) &\approx \pm\frac{\sqrt{\kappa}}{\pi\sqrt{2n}} + \mathcal{O}(\kappa).\end{aligned}$$

Hence, for small $\kappa > 0$, their distance is proportional to $\sqrt{\kappa}$. Moreover, for different values of $n$, this distance scales as $1/\sqrt{n}$.

Now we are in position to relate explicitly the maps (5.4) and (5.5) around the origin near integer values of $\varepsilon$. For the purpose of the following result, it is convenient to also stress the dependence of $f_\varepsilon$ also on the parameter $b$, so throughout this section we are going to denote the map (5.5) as $f_{\varepsilon,b}$. Let

$$E(x, y, z) = (\alpha x, \beta y, \gamma z) = (u, v, w). \tag{5.9}$$

**Proposition 3.** *Given $\varepsilon, b, \mu$ and $\nu$, assume that for a suitable $n \in \mathbb{Z} \setminus \{0\}$ we can express $\varepsilon$ as $\varepsilon = n + k/n$, being $0 < k < k_0$ with $k_0 = \mathcal{O}(1)$ (i.e., we are $\mathcal{O}(n^{-1})$ close to the birth of an accelerator mode, and $k = \kappa n$ measures the scaled distance to the bifurcation). Denote $\tilde{b} = b/n$. There exists a phase scaling as (5.9) with scaling factors $\alpha = \alpha(n, k)$, $\beta = \beta(n, k, \mu, \nu)$ and $\gamma = \gamma(n, k, \mu, \nu)$ that are $\mathcal{O}(n)$, such that the Taylor expansion $T_+$ (resp $T_-$) of*

$$E \circ f_{\varepsilon,\tilde{b}} \circ E^{-1} = E \circ f_{n+k/n,b/n} \circ E^{-1}$$

*around $P_+ = (0, 0, 0)$ (resp. $P_- = (1/2, 0, 0)$) verifies that*

$$T_+ \;=\; \mathrm{Mic}_{\varphi,a} + \mathrm{Rem}_n, \qquad (\textit{resp. } T_- = \mathrm{Mic}_{\varphi,a} + \mathrm{Rem}_n), \tag{5.10}$$

*for suitable parameters $\varphi = \varphi(k, \mu, \nu)$ and $a = a(\nu, b)$ that do not depend on $n$, where $\mathrm{Rem}_n$ are terms $\mathcal{O}(n^{-2})$.*

*Proof.* We are only going to perform the proof around $P_+$. The proof around $P_-$ works exactly the same but after translating $P_-$ to the origin.

The scaling $E$ (5.9) relates the $u, v$ and $w$ variables with the $x, y$ and $z$. The Taylor expansion of $E \circ f_{n+k/n,b/n} \circ E^{-1}$ around $P_+$ reads

$$\begin{pmatrix} u' \\ v' \\ w' \end{pmatrix} = \begin{pmatrix} u + \alpha\mu\left(2\pi\frac{v}{\beta}\right) \\ v + \beta\nu\left(2\pi\frac{w'}{\gamma}\right) \\ w + \gamma\left(\left(n + \frac{k}{n}\right)\left(1 - 2\pi^2\frac{u^2}{\alpha^2} + 2\pi\frac{b}{n}\frac{v}{\beta}\right) - n\right) \end{pmatrix} + \mathcal{O}_3(u, v, w), \tag{5.11}$$

where the $-n$ summand in the $z$ component in (5.11) is due to the return to the torus, and $\mathcal{O}_3$ denote terms of global order 3 in $u$, $v$ and $w$.

If the scalings $\alpha, \beta$ and $\gamma$ are chosen to be $\mathcal{O}(n)$, the Taylor expansion $T_+$ (5.10) can be written as $T_+ = L_+ + R_+$, where $L_+$ is a quadratic volume preserving map that does not depend on $n$, and $R_+ = \mathcal{O}(n^{-2})$. In addition, these scalings can be chosen in such a way that $L_+$ is exactly $\mathrm{Mic}_{\varphi,a}$, for suitable values of $\varphi$ and $a$ that depend on $\mu, \nu, b$ and $k$ in a way that is going to be specified later on. We will first determine $\alpha, \beta$ and $\gamma$ in such a way that $L_+ = \mathrm{Mic}_{\varphi,a}$, and then check that any other term in $T_+$ depends on a negative power of $n$ and hence can be included in $R_+$.

**The map $L_+$: a choice of $\alpha, \beta$ and $\gamma$.** Let us impose the leading terms of (5.11) to be of the form of those in (5.4). Consider that $n$ is large enough, so $\kappa = k/n \ll n$: neglect for the moment the monomial in $kv$ and the monomial in $ku^2$ in the third component of (5.11) not in $\mathcal{O}_3$. After choosing $\alpha, \beta$ and $\gamma$ we will see that they can be included in $R_+$.

If we equate the coefficients which are: linear in $v$ in the first component, linear in $w'$ in the second component and linear in $k$, linear in $v$ and quadratic in $u^2$ in the third component, we get, respectively, the following 5 equations which relate our target parameters $\alpha, \beta, \gamma, \varphi$ and $a$ with $n, k, b, \mu$ and $\nu$:

$$\varphi = \frac{2\pi\alpha\mu}{\beta}, \quad \varphi = \frac{2\pi\beta\nu}{\gamma}, \quad \varphi = \frac{\gamma k}{n}, \quad \frac{a}{\varphi} = \frac{2\pi b\gamma}{\beta}, \quad \varphi = \frac{2\pi^2\gamma n}{\alpha^2}. \tag{5.12}$$

We can solve (5.12) for $\alpha, \beta$ and $\gamma$:

$$\alpha = \pi n \left(\frac{2}{k}\right)^{1/2}, \quad \beta = \pi n \left(\frac{4\mu^2}{k^2\nu}\right)^{1/3}, \quad \gamma = \pi n \left(\frac{32\mu^2\nu^2}{k^5}\right)^{1/6}, \tag{5.13}$$

that are obviously $\mathcal{O}(n)$. The parameters $\varphi$ and $a$ read, in the original parameters,

$$\varphi = \pi \left(32\mu^2\nu^2 k\right)^{1/6}, \quad a = 4b\pi^2\nu. \tag{5.14}$$

Note that they do not depend on $n$, and $a$ does not depend on $k$.

**All terms not in $L_+$ are at least $\mathcal{O}(n^{-2})$.** Now we have to deal with the rest of the summands in the expansions we have considered. We will show that the coefficient of each of them depends on a negative power of $n$.

First of all, let us consider the terms we did not take into account before: those in the third component of (5.11) that are not included in the $\mathcal{O}_3(u, v, w)$. They read, from the choice (5.13),

$$\frac{2\pi b\gamma}{n^2\beta} kv - \frac{2\pi^2\gamma}{n\alpha^2} ku^2 = \frac{\pi}{n^2}\left(\left(\frac{128k^5\nu^4}{\mu^2}\right)^{1/6} bv + \left(32k^7\mu^2\nu^2\right)^{1/6} u^2\right).$$

Concerning the $\mathcal{O}_3$ terms, those in $v^j$ in the first component, and those in $(w')^j$ in the second component for odd $j \geq 3$ have the form (in absolute value), respectively,

$$\alpha\mu\frac{(2\pi)^j}{\beta^j \cdot j!} = \mathcal{O}(n^{-j+1}), \qquad \beta\nu\frac{(2\pi)^j}{\gamma^j \cdot j!} = \mathcal{O}(n^{-j+1}),$$

and similarly for all the terms in $(w')^j$ due to the expansions of the sinus functions contained in $\psi$, that appear first at order 3, by construction. Finally, the absolute value of the coefficients of the terms in $\mathcal{O}_3$ in the third component have the form (for $j \geq 4$ even and $i \geq 3$ odd)

$$\gamma n\frac{(2\pi)^j}{\alpha^j \cdot j!} = \mathcal{O}(n^{-j+2}), \quad \gamma\frac{(2\pi)^j}{n\alpha^j \cdot j!} = \mathcal{O}(n^{-j}), \quad \gamma\frac{(2\pi)^i}{\beta^i \cdot i!} = \mathcal{O}(n^{-i+1}), \quad \gamma\frac{(2\pi)^i}{n^2\beta^i \cdot i!} = \mathcal{O}(n^{-i-1}).$$

Hence, the orders of magnitude in $n$ of each of all terms in $R_+$ is $n^{-2}$. □

There are some important aspects within the proof that are worth noting:

**Remark 9.** *1. In the expression of our limit map (5.4), $\varphi = \mathcal{O}(k^{1/6})$.*

*2. The reparametrisation $a = 4b\pi^2\nu$ does not depend on $k$. This is a crucial parameter to take into account, as we are going to see in Subsect. 5.3. This is the reason why we chose the third component in (5.4) to be of the form $w' = w + \varphi - \varphi u^2 + av/\varphi$.*

*3. As $n$ increases, the volume occupied by the bubble around $P_\pm$ scales as $n^{-1-1-1} = n^{-3}$.*

*4. Recall that in Prop. 1 (see page 55), we related the local dynamics around the fixed accelerator modes of the standard map at $(1/4, 0)$ and $(3/4, 0)$ near $k = n \in \mathbb{Z}\setminus\{0\}$ to the Hénon map near $k = n \in \mathbb{Z}\setminus\{0\}$. We proved that, except for terms of order greater than 3, the local dynamics was the same for all $k = n \in \mathbb{Z}\setminus\{0\}$ by scaling the phase variables and the translated parameter $k' = k - n$. In the present case, we also get the same local map but we have to consider the map $f_{\varepsilon,\tilde{b}}$ for decreasing values of $\tilde{b} = b/n$. In practice, we are going to fix $\mu, \nu$ and $b$ and only vary $\varepsilon$. Hence, for different values of $n$, the local dynamics around the origin will be conjugated to that of* $\mathrm{Mic}_{\varphi,a_n}$*, where*

$$\varphi = \pi(32\mu^2\nu^2 n\kappa)^{1/6}, \qquad a_n = 4bn\pi^2\nu.$$

*That is, for each $n$ the corresponding value of $a$ in the local dynamics increases by a factor $n$, and hence is different, and the range in $\varphi$ where the accelerator mode exhibits some bounded volume around it is reduced by a factor $1/n$.*

Before dealing with the set of bounded orbits of the local model $\mathrm{Mic}_{\varphi,a}$ in the next section, it is convenient to summarize the main features of $f_\varepsilon$. We have constructed a family of VPM $f_\varepsilon$ defined on the cylinder $\mathbb{T}^2 \times \mathbb{R}$ (5.5) that smoothly projects on the torus $\mathbb{T}^3$. We have denoted such a projection as $\bar{f}_\varepsilon$. The map $f_\varepsilon$ is a VP perturbation of an integrable map, in the sense that the phase space of $f_0$ is foliated by horizontal RIT, see Def. 1 in page 10. Except around the tori $z = 0, 1/2$ (where a necessary non-degeneracy condition is violated), the VP version of the KAM theorem applies [24, 147] and some of these tori persist for small values of $\varepsilon$. Moreover, the projection at integer values of $n \in \mathbb{Z}\setminus\{0\}$, $\bar{f}_n$, has $P_+ = (0, 0, 0)$ and $P_- = (1/2, 0, 0)$ as fixed points, that are not fixed under $f_n$. Their iterates become unbounded:

$$f_n^j(0, 0, 0) = (0, 0, nj), \quad f_n^j(1/2, 0, 0) = (1/2, 0, -nj), \qquad j > 0, \tag{5.15}$$

hence they are fixed accelerator modes, see Def. 8 in page 29. Moreover, we have proved that, scaling suitably the phase variables and $\kappa = \varepsilon - n$, with scaling factors that depend

on $n$, the dynamics under $\bar{f}_\varepsilon$ around these fixed accelerator modes is that of $\text{Mic}_{\varphi,a}$ for some values of $\varphi, a$ specified in the proof of Prop. 3, plus a remainder that depends on $n$ that tends to vanish as $n \to \infty$. Assume that under $\bar{f}_\varepsilon$, the points $P_+$ and $P_-$ are surrounded by some bounded volume[1]. For any lift $f_\varepsilon$ of $\bar{f}_\varepsilon$ to the cylinder $\mathbb{T}^2 \times \mathbb{R}$, the $z$ component of all such bounded orbits either grows or decreases linearly in the number of iterates if they lie close to $P_+$ or $P_-$, respectively. We also expect that non-bounded chaotic orbits that get temporarily stuck around the bubbles that emanate from either $P_+$ or $P_-$, say for $t$ consecutive iterates, the $z$ component would grow or decrease by a quantity $nt$, respectively. Recall the discussion in Sect. 2.6, in page 59.

### 5.2.3 Other accelerator modes

Apart from $P_+$ and $P_-$ at $\varepsilon = n \in \mathbb{Z} \setminus \{0\}$, $f_\varepsilon$ may have other fixed accelerator modes. If we look for points that jump upwards a distance $n$ at $\varepsilon = n$ (that can be found as the intersection of level sets of the shearing functions), we find 2 isolated points, and from the zero-flux condition, we deduce that there are 4 fixed accelerator modes. These may be taken into account when doing any diffusion study. Note that there might also be higher periodic accelerator modes, but we did not detect any in our numerical studies.

All upwards-jumping accelerator modes that are born at $\varepsilon = n \in \mathbb{Z} \setminus \{0\}$ appear at some point whose $x$ coordinate is zero, and those that jump downwards are born at some point with $x = 1/2$, at the same value of the parameter. The position in the phase space when they are born can be found in the leftmost columns of Tab. 5.2.

One can rewrite the proof of Prop. 3 around any of the points of Tab. 5.2. So, the local dynamics around any of them is also close to the discrete version of the Michelson system $\text{Mic}_{\varphi,a}$. In Tab. 5.2 we show the corresponding values of the parameters $\varphi$ and $a$ obtained after this procedure as a function of $k, n, \mu, \nu$ and $b$. When redoing the proof, the only difference we encounter with the original one are some changes of sign due to expanding sinus terms around $\pi$.

| **Upwards** | **Downwards** | $\varphi$ | $a$ |
|---|---|---|---|
| $(0,0,0)$ | $(1/2,0,0)$ | $\pi\left(32k\mu^2\nu^2\right)^{1/6}$ | $4b\pi^2\nu$ |
| $(0,1/2,0)$ | $(1/2,1/2,0)$ | $-\pi\left(32k\mu^2\nu^2\right)^{1/6}$ | $-4b\pi^2\nu$ |

Table 5.2: Position of the accelerator modes at their birth at $\varepsilon \in \mathbb{Z} \setminus \{0\}$ together with the relevant parameters they depend on, $\varphi$ and $a$, see (5.14).

In the next section we will discuss parameters. We need to choose them so that after the Hopf-zero bifurcation that occurs at $P_+$ and $P_-$ for $\varepsilon = n \in \mathbb{Z} \setminus \{0\}$, the approximated local model (5.4) has bounded orbits. From the analysis in [40],accelerator modes will appear if the corresponding value of $a$ in the local map is negative. Hence, from Tab. 5.2, for any choice of the parameters $b$ and $\nu$, only a pair of accelerator modes will be surrounded by bounded motion.

[1] By bounded volume we mean the set of orbits that do not escape a compact vicinity of $P_+$ or $P_-$ under iteration.

## 5.3 Dynamics of the discrete Michelson map

In this subsection we discuss for which ranges of the parameters $\varphi$ and $a$ the family of VPM $\mathrm{Mic}_{\varphi,a}$ presents some positive volume set of bounded orbits.

The local dynamics around accelerator modes has been chosen to be $\mathrm{Mic}_{\varphi,a}$ mainly because it is a discretisation of the flow (5.3), so when $\varphi \approx 0$ one can explain the shape and evolution of the set of bounded orbits (if any) via (5.3). The dynamics of the flow (5.3) can be completely understood by means of a Poincaré map on a suitable surface of section. Among the well known properties of the Michelson flow written in the form (5.3) the most straightforward are that

1. It preserves volume since it is divergence free,
2. It is reversible under $(x, y, z) \mapsto (-x, y, -z)$ and the time reverse $t \mapsto -t$, and
3. It has 2 fixed points located at $(\pm 1, 0, 0)$ which are both of saddle-focus type, and $\dim W^u(1,0,0) = \dim W^s(-1,0,0) = 2$.

Besides that, if we choose as Poincaré section $z = 0, y \geq 0$, volume preservedness and transversality of orbits to this surface imply the preservation of a measure whose density is proportional to $1 - x^2 + ay$. This measure is absolutely continuous with respect to the Lebesgue measure. Hence the dynamics of (5.3) can be explained as if it was an open symplectic map of the plane (the Poincaré return map on $z = 0, y \geq 0$, call it $\mathcal{P}$) times some angle. This allows to explain the evolution of the whole set of bounded orbits phase space as the parameter $a$ varies as we did in Chap. 2. For instance, fixed or periodic points of $\mathcal{P}$ correspond to periodic orbits of the flow, invariant curves to invariant tori, etc. In particular, the destruction of 2D invariant tori of the flow can be explained by means of obstruction arguments inherited from $\mathcal{P}$. We refer to [42] and references therein for more details on the Hopf-zero singularity. In this referenced work, the authors pay special attention to the Michelson system (5.3).

Movies of the evolution of the set of bounded motion of a scaled version of (5.3) as a function of the parameter $a$ are available in `http://www.maia.ub.es/dsg/moviehsn`. One can see some of the available pictures in Fig. 5.2.

It is important to remark that (5.4) is conjugated to the map

$$g_{\epsilon_1,\epsilon_2} : \begin{pmatrix} \xi \\ \eta \\ \zeta \end{pmatrix} \mapsto \begin{pmatrix} \xi' \\ \eta' \\ \zeta' \end{pmatrix} = \begin{pmatrix} \xi + \eta \\ \eta + \zeta' \\ \zeta + \epsilon_2 \eta + \epsilon_1(-1 + \xi^2) \end{pmatrix} \tag{5.16}$$

via the change of scale and reparametrisation

$$C(\xi, \eta, \zeta) = (-\xi, -\eta\epsilon_1^{-1/3}, -\zeta\epsilon_1^{-2/3}) = (u, v, w), \quad \varphi = \epsilon_1^{1/3}, \quad a = \epsilon_2. \tag{5.17}$$

The map (5.16) is a scaled version of a truncation of the normal form of a triple-one multiplier [39], and its dynamics was studied, with special emphasis on bifurcations of invariant circles, in [40]. In this article, the authors performed a normal form analysis and justified that there is a set of positive volume of bounded motion when $0 < \epsilon_1 < \epsilon_{\max}$ and $\epsilon_2 \in [-4, 0]$, that is, for $0 < \varphi < \epsilon_{\max}^{1/3}$ and $a = 4bn\pi^2\nu \in [-4, 0]$. The value of $\epsilon_{\max}$ depends on the value of $a$, and it can not be estimated a priori. This value $\epsilon_{\max}$ has to be understood in a practical way as follows: for any $\epsilon > \epsilon_{\max}$ for some fixed pixel size, no bounded motion is detectable.

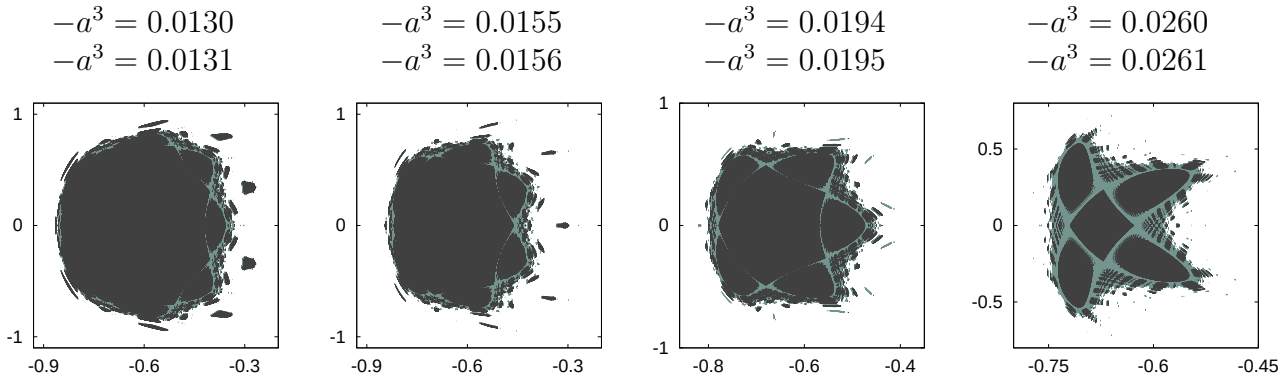


Figure 5.2: Sections of the bubble of the flow (5.3) in $z = 0$, $y \leq 0$. The displayed variables are $y$ in the abscissas and $x$ in the ordinates. In each plot we show the data for two different values of the parameter, before (light gray, smaller value of $a$ in absolute value) and after (dark gray, larger value of $a$ in absolute value) the breakdown of an outermost invariant 2D torus (invariant curve in section). From left to right, in section, they confined 1:7, 1:6, 1:5 and 1:4 periodic islands. The breakdown of these 2-tori allows previously confined orbits to escape to infinity. The corresponding values of the parameter $a$ are displayed on top of each figure.

### 5.3.1 The set of bounded orbits of $g_{\epsilon_1,\epsilon_2}$

Despite all the computations in this section will be performed for the map $g_{\epsilon_1,\epsilon_2}$, we will refer to the volume of its set of bounded orbits as $B_{\varphi,a}$. As usual, we will distinguish between bounded orbits that are either regular or chaotic[2]. The measure of the set of regular (resp. chaotic) bounded orbits will be denoted as $B^r_{\varphi,a}$ (resp. $B^c_{\varphi,a}$). So, in practice $B_{\varphi,a} = B^r_{\varphi,a} + B^c_{\varphi,a}$. For all $\epsilon_1 > 0$, $B_{\varphi,a}$ is contained in a compact set of $\mathbb{R}^3$. Moreover, this set seems to tend to some limit shape when $\epsilon_1 \to 0^+$. Also, $g_{\epsilon_1,\epsilon_2}$ is actually a scaled version of a map of the quadratic family of VPM originally introduced in [39, 40]:

$$\tilde{g}_{\epsilon_1,\epsilon_2} : \begin{pmatrix} \bar{x} \\ \bar{y} \\ \bar{z} \end{pmatrix} \mapsto \begin{pmatrix} \bar{x}' \\ \bar{y}' \\ \bar{z}' \end{pmatrix} = \begin{pmatrix} \bar{x} + \bar{y} \\ \bar{y} + \bar{z}' \\ \bar{z} - \epsilon_1^2 + \epsilon_2 \bar{y} + A\bar{x}^2 + B\bar{x}\bar{y} + C\bar{y}^2 \end{pmatrix}. \tag{5.18}$$

for $A = 1$ and $B = C = 0$. One recovers (5.16) from (5.18) via the change of scale $\bar{x} = \epsilon_1 \xi$, $\bar{y} = \epsilon_1 \eta$, $\bar{z} = \epsilon_1 \zeta$. The difference between these two versions is that $g_{\epsilon_1,\epsilon_2}$ has, for all $\epsilon_1 > 0$, two fixed points located at $(\pm 1, 0, 0)$, while for $\tilde{g}_{\epsilon_1,\epsilon_2}$ these fixed points are located at $(\pm|\epsilon_1|/\sqrt{A}, 0, 0)$, provided $A > 0$.

In [40], the authors mostly restricted themselves to the case $A = 1$ and $B = C = 0.5$. We do not expect major differences between this case and ours. In case the quadratic form $A\bar{x}^2 + B\bar{x}\bar{y} + C\bar{y}^2$ is positive definite, one can prove that all bounded orbits of (5.18) are contained in a cube centered at the origin, see [79, 40]. Since $\mathrm{Mic}_{\varphi,a}$ is conjugated to $\tilde{g}_{\epsilon_1,\epsilon_2}$ with $A = 1$ and $B = C = 0$, the corresponding quadratic form is not positive definite. Yet it

[2]Throughout this chapter, an orbit is considered to be chaotic if after $N$ iterations of the map ($N$ has to be large enough, say, at least $10^5$), the numerically approximated maximal Lyapunov exponent is larger than $5/N$.

is easy to show that all bounded orbits of (5.16) are still contained in a cube that is centered at the origin, by mimicking the procedure introduced in [79].

As inherited from the Michelson system, for $\varphi > 0$ but close to 0, $B_{\varphi,a}$ mostly consists in a Cantor family of nested 2D tori that are, in turn, enclosed by the 2D invariant manifolds of the fixed points at $(\pm 1, 0, 0)$. In Fig. 5.5 one can see, in the section $\zeta = 0$, $\eta \geq 0$, the distinction between regular and chaotic orbits. Note that it resembles the aspect of the set of bounded orbits of a stability island of an APM.

Back to $B_{\varphi,a}$, the theoretical estimations for the compact set where all bounded orbits lie are not practical, and it is convenient to perform a numerical exploration to get better bounds. A rough numerical study suggest that they are all contained in the following box and for the following ranges of parameters

$$\begin{aligned} \mathcal{B}_{\text{prac}} &= \{(\xi, \eta, \zeta) \text{ such that } |\xi| < 3.2, |\eta| < 4.5, |\zeta| < 8.5\}, \\ &\quad \varphi^3 = \epsilon_1 \in [0, 0.60], \quad \epsilon_2 = a \in [-4, 0]. \end{aligned} \tag{5.19}$$

In Fig. 5.3 we plot the relative volumes $B_{\varphi,a}$ (top), $B^r_{\varphi,a}$ (bottom left) and $B^c_{\varphi,a}$ (bottom right), relative to the volume of $\mathcal{B}_{\text{prac}}$ for the values of the parameter in (5.19). To obtain these plots, we used a $800 \times 800 \times 800$ grid in $\mathcal{B}_{\text{prac}}$ and iterated each initial condition at most $10^5$ times. The initial conditions that did not escape from $\mathcal{B}_{\text{prac}}$ in $10^5$ iterates were classified, either as regular or chaotic using an approximation of the maximal Lyapunov exponent. For a better visualisation of the results obtained, we plot $a$ in the abscissas and $\epsilon_1^2$ in the ordinates, and the color of each pixel corresponds to the percentage of the volume in $\mathcal{B}_{\text{prac}}$ that is occupied by the displayed quantity. In this plot, we see that the set of bounded orbits for $g_{\epsilon_1,\epsilon_2}$ tends to some finite non-zero limit as $\varepsilon_1 \to 0$. This suggests that the volume of the bubbles of $\bar{f}_\varepsilon$ that appear at $\varepsilon = n \in \mathbb{Z} \setminus \{0\}$ grows as $\varphi^3$. The position of the vertical lines in the top figure is going to be explained in Sect. 5.4. It is worth noting that the practical set $\mathcal{B}_{\text{prac}}$ is still a lot larger than the set of bounded orbits. This is the reason why only at most 4.5% of $\mathcal{B}_{\text{prac}}$ is occupied by bounded motion. Better estimates of this set can be obtained by considering a larger number of iterates, but it can be time consuming due to the larger total of iterations one should perform. It will be improved in forthcoming contributions.

In Fig. 5.3 we can see the whole picture of the evolution of bounded volume. As commented above, in this chapter we will restrict ourselves to some fixed values of $\mu, \nu$ and $b$ and vary $\varepsilon$. From (5.14), this means that we will just deal with a bubble whose dynamics, in lowest terms, is described by $\text{Mic}_{\varphi,a}$ for some fixed value of $a$, and where $\varphi$ is allowed to vary. Namely, the choice we will justify in Sect. 5.4.1 corresponds to considering $a = a_1 = -0.1152\pi^2$, the rightmost vertical white line in Fig. 5.3, top.

It is interesting to show what happens for this value of $a = a_1$. This will allow us to compare with the actual bubble of $f_\varepsilon$. In Fig. 5.4 we show the evolution of the bounded volumes for $a = a_1$. As in the Michelson system of ode (5.3), the orbits that are bounded appear to cross $\zeta = 0$ transversally. We computed also the area of the intersection in $\zeta = 0$, $\eta \geq 0$, call it $A_{\varphi,a}$. Again, we have distinguished those initial conditions that belong to what seems to be a regular or a chaotic orbit. We denote the respective areas that these sets occupy as $A^r_{\varphi,a}$ and $A^c_{\varphi,a}$.

Again, for a better visualization of the results, and to be able to relate this data to the corresponding data for the actual accelerator mode, we plot $\epsilon_1^2$ in the abscissas instead of $\epsilon_1 = \varphi^3$, the volumes $B_{\varphi,a}, B^r_{\varphi,a}$ and $B^c_{\varphi,a}$ are shown multiplied by a factor $\epsilon_1^3 = \varphi^9$, and the areas $A_{\varphi,a}, A^r_{\varphi,a}$ and $A^c_{\varphi,a}$ appear multiplied by a factor $\epsilon_1^2 = \varphi^6$.

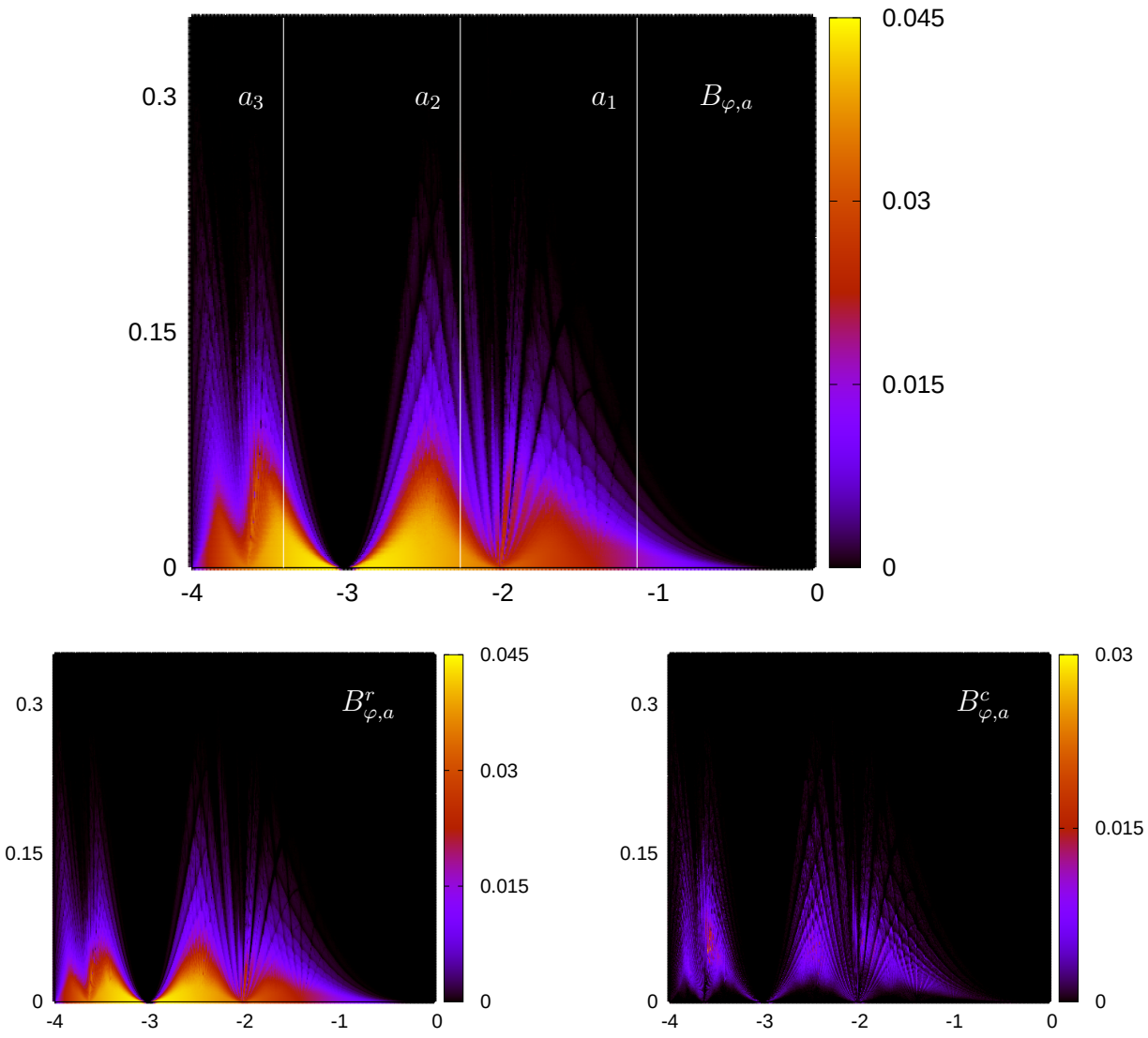


Figure 5.3: Fraction of the volume, relative to $\mathcal{B}_{\text{prac}}$, of: top, $B_{\varphi,a}$, bottom left, $B^r_{\varphi,a}$ and bottom right, $B^c_{\varphi,a}$. In the abscissas we plot $\epsilon_2 = a$ and in the ordinates we plot $\epsilon_1^2 = \varphi^6$. The color of each pixel corresponds to the fraction of bounded orbits, corresponding to the vertical color legend on the right of each plot. For further info on the vertical lines on the top picture, see Sect. 5.4.

For this concrete value of $a = a_1$, we could improve $\mathcal{B}_{\text{prac}}$ to

$$\{(\xi, \eta, \zeta) \text{ such that } |\xi| < 3.2, |\eta| < 3, |\zeta| < 3.2\}, \qquad \varphi^3 = \epsilon_1 \in [0, 0.3],$$

and all bounded orbits intersected $\zeta = 0$, $\eta \geq 0$ in $\xi \in [-1, 1]$ and $\eta \in [0, 2]$. So in Fig. 5.4 we show volumes and areas relative to these sets.

In Fig. 5.4, top, we can see results for the bounded volume and in the bottom we see results for the area in the section $\zeta = 0$, $\eta \geq 0$, relative to the boxes and squares given just above. As in the 2D setting, in either case, it seems that some resonances occur in the central periodic orbit (seen as a fixed point in the section) that give rise to chaotic area inside the whole bounded region. As $\epsilon_1$ increases, some 2D invariant tori are destroyed and

this volume is eventually released and orbits in it can become unbounded. This is seen in the growth of the chaotic volumes and areas $B^c_{\varphi,a}$ and $A^c_{\varphi,a}$ that appear as peaks, and the eventual sudden decreases of the total bounded quantities.

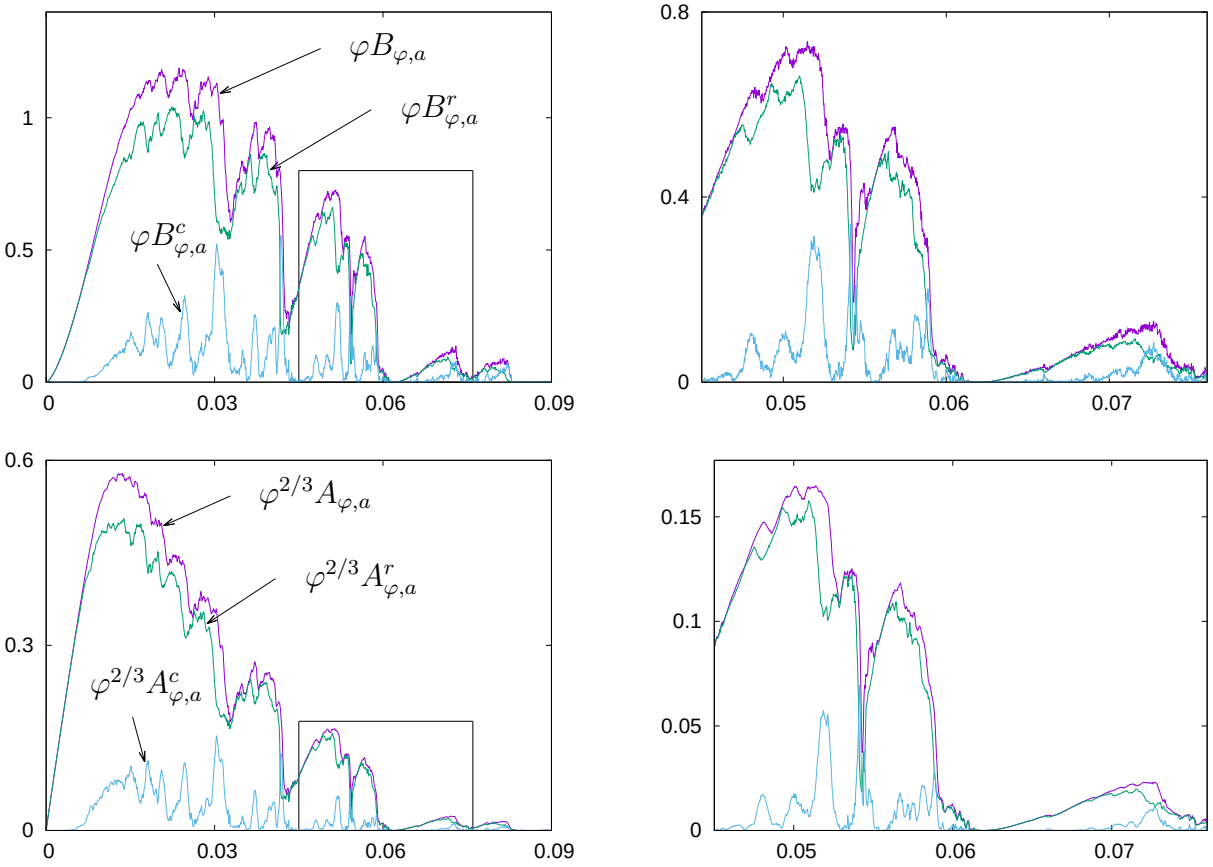


Figure 5.4: For $a = \epsilon_2 = -0.1152\pi^2$, and as a function of $\varepsilon_1^2$: top left: Bounded volume of the bubble $10^4\varphi B_{\varphi,a}$ (purple), $10^4\varphi B^r_{\varphi,a}$ (green) and $10^4\varphi B^c_{\varphi,a}$ (blue). Top right: magnification of the square in the top left plot. Bottom left: bounded area in the section $\zeta = 0$, $\eta \geq 0$. We plot $10^2\varphi^{2/3}A_{\varphi,a}$ (purple), $10^2\varphi^{2/3}A^r_{\varphi,a}$ (green) and $10^2\varphi^{2/3}A^c_{\varphi,a}$ (blue). Bottom right: magnification of the square in the bottom left plot. To obtain these plots we considered an orbit to be non-escaping if it remained bounded for $10^6$ consecutive iterates. The stepsize used in $\varepsilon_1^2$ is, in all figures, $7.5 \cdot 10^{-5}$.

Despite not being equivalent, one is lead to compare the evolution of $A_{\varphi,a}$ and the evolution of the set of bounded area of the orientation preserving Hénon map in Fig. 2.3, page 43. A remarkable difference is found in the evolution of the area of the set of chaotic confined motion, $A^c_{\varphi,a}$ versus the evolution displayed in Fig. 2.4, see page 44. As $\varphi$ changes, it seems that in some ranges, $A^c_{\varphi,a}$ exhibits a large persistent set of chaotic confined motion that occupies a relatively large part of the whole set of bounded motion. Despite having increased the maximal number of iterations to $10^6$ to get rid of orbits that actually unbounded that are stuck outside the bubble for long times, numerical evidence suggests that one has to iterate up to $10^9$ times in order to get rid of most of these orbits (this is what we have done to generate the sections in Fig. 5.5). So we expect that these actually unbounded orbits

that are trapped for long times give a non neglectable contribution to what is shown as $B^c_{\varphi,a}$ and $A^c_{\varphi,a}$. But there is also a large measure of chaotic confined orbits that lies within the structure of nested 2D tori.

In the 2D setting, the main source of chaotic confined orbits is due to the transversal crossing of the invariant manifolds of hyperbolic periodic orbits that are born at the elliptic point. In the 3D VPM setting, if the map has an invariant curve, we can think of two rotation numbers: the longitudinal one $\omega_L$ that is measured along the invariant curve, and a transversal one $\omega_T$. If we fix $a$ and vary $\varphi$, we expect these rotation numbers undergo resonances. In [40] the authors discuss and classify these bifurcations. The VPM case is much richer than the 2D case in the following sense: invariant curves can bifurcate either into invariant curves (whose period does not need to be a multiple of the original invariant curve) or into strings of bubbles as observed in the dissipative setting [18] and in the conservative setting [40]. This first kind of bifurcations give rise, when looking at sections, to the typical pattern of bifurcating pendulum-like structures related to the Poincaré-Birkhoff theorem. But despite looking like a single periodic orbit, they can correspond to sections of periodic normally elliptic invariant curves. The mixture of these two phenomena may be responsible for the abundance of bounded chaotic motion.

In Fig. 5.5 we show the sections of the set of bounded orbits in $\zeta = 0$, $\eta \geq 0$ for some values of $\epsilon_1$. Regular pixels are shown in red, while chaotic confined orbits are shown in blue. To produce these plots we have used a $1250 \times 1250$ grid in $(\xi, \eta)[-1, 1] \times [0, 2]$. First, we have detected if the center of each pixel was in a an orbit that did not escape after $10^5$ iterations. Let $(i_1, i_2)$ one of such pixels. If any pixel of the form $(i_1 + j_1, i_2 + j_2)$, where $j_1, j_2 \in \{-2, -1, 0, 1, 2\}$ did escape in less than $10^5$ iterations, we re-checked the center of the pixel $(i_1, i_2)$ for a larger number of iterates, up to $10^9$ (and $10^{10}$ for the case $\varepsilon_1^2 = 0.031$). After this process, for the initial conditions that were in orbits that we could consider to be bounded, we approximated the maximal Lyapunov exponent. It is important to stress that for $\varepsilon_1^2 = 0.030$, there are isolated blue spots in the outermost part of the section of the bubble that do not seem to be confined by any 2D torus (curve in section). For $\varepsilon_1^2 = 0.031$, if we only iterated at most $10^9$ times, there was a cloud of blue spots surrounding the regular motion. All these initial conditions correspond to unbounded motion that is trapped for long times around the bubble. In order to get rid of this cloud, for $\varepsilon_1^2 = 0.031$, we had to iterate up to $10^{10}$ times.

In section, the apparent similarity between the 2D and 3D cases is visible. We show two pictures where there appear what seems to be a 7-periodic orbit (left), and two where there seems to have a 5-periodic orbit (right). The investigation of whether what shows up in section as islands of stability actually come from a single elliptic invariant curve or several invariant curves (that are mapped periodically) [40] is left for future contributions.

As a final remark, we have to note that for low values of $n$, the dynamics of $\mathrm{Mic}_{\varphi,a}$ and the real local dynamics of the accelerator modes that appear may differ substantially, due to the summand $\mathrm{Rem}_n$ in (5.10). But the accelerator modes that are larger in the phase space are those for smaller $n$ (and hence are the most suitable for studies concerning trapping statistics), since their volume decreases fast as $n$ increases, namely as $n^{-3}$, see Rem. 9.

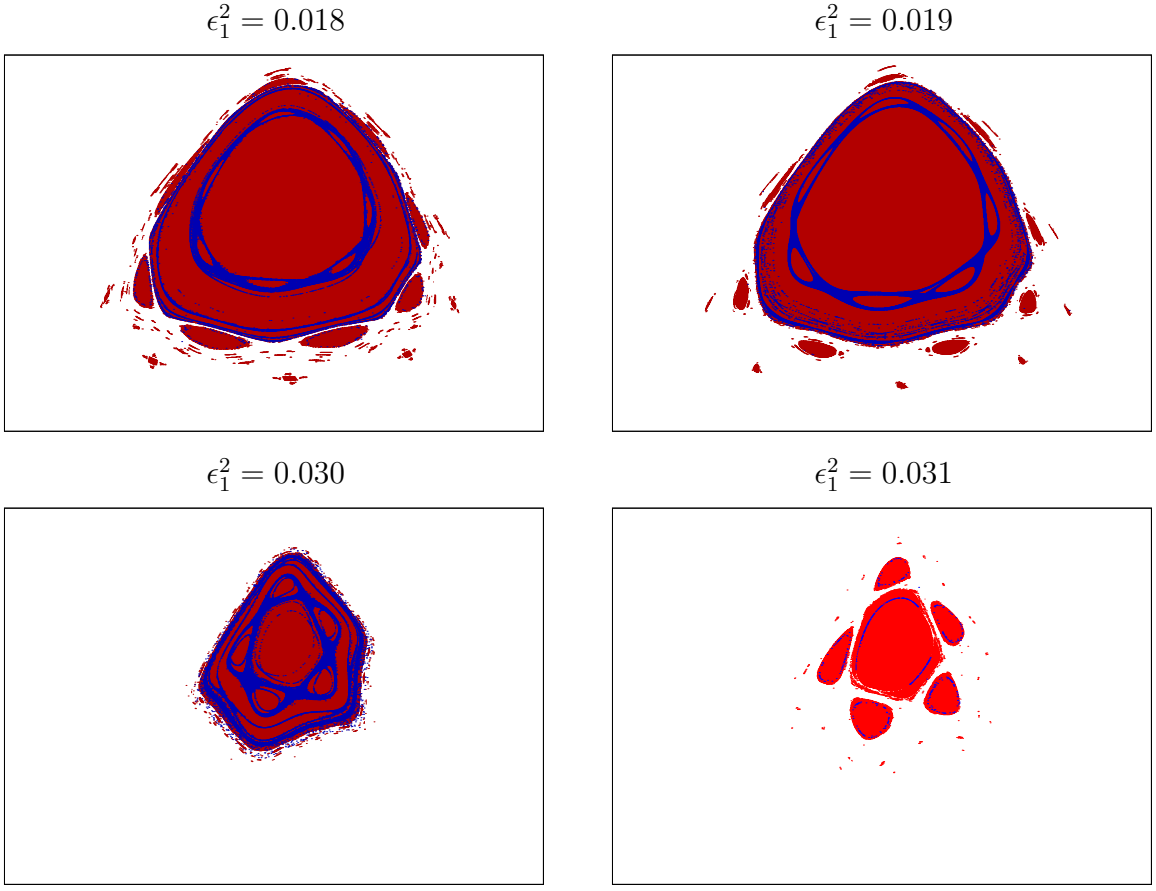


Figure 5.5: Sections of the bubble in $\zeta = 0, \eta \geq 0$, in a $1250 \times 1250$ grid in $(\xi, \eta) \in [-1, 1] \times [0, 2]$. The red pixels correspond to regular orbits and the blue ones to chaotic confined motion. Here by confined we mean that these points do not escape from $\mathcal{B}_{\text{prac}}$ in $10^9$ ($10^{10}$ for $\epsilon_1^2 = 0.031$) iterations, see the text for further information on how we have produced the figures. The corresponding values of $\epsilon_1$ are shown on top of each figure. On the left one can clearly see what in section seem to be 7, 8 and 9-periodic islands of stability, and on the right, the most prominent seem to be 5-periodic.

## 5.4 Diffusion in the presence of a bubble: a case study

The main goal of this section is to analyse the results of some preliminary massive numerical simulations of chaotic orbits of $f_\varepsilon$ to study the role of a moderate size bubble in a seemingly fully chaotic phase space. Here we present the first steps of a larger forthcoming first systematic study on the role of bubbles in the diffusive properties in the $z$ component in the phase space of $f_\varepsilon$ for large values of $\varepsilon$, which is linked to stickiness phenomena. We are going to proceed as we did in Chap. 3.

For our purposes, it is enough to conveniently fix $\mu, \nu$ and $b$, and allow $\varepsilon$ to vary. We recall that near any integer value of $\varepsilon = n + \kappa$, $n \in \mathbb{Z} \setminus \{0\}$, $\kappa$ small, the relationship between the parameters of $f_\varepsilon$ and the local limit dynamics $\text{Mic}_{\varphi,a}$ is

$$\varphi = \pi(32n\mu^2\nu^2\kappa)^{1/6}, \qquad a = 4bn\pi^2\nu.$$

Hence, if we fix all parameters of $f_\varepsilon$ but $\varepsilon$, we will fix the value of $a$ in the limit local map.

This choice can be understood as studying the effect of a bubble along its evolution on single straight vertical line in Fig. 5.3, as the white vertical segments depicted.

### 5.4.1 A choice of $\mu, \nu$ and $b$

We have chosen the values of the parameters $\mu, \nu$ and $b$ in such a way that the value of $\varepsilon$ for which the last RIT of $f_\varepsilon$ is destroyed, say $\varepsilon_{\text{crit}}$, is maximal. This value is analogous to Greene's critical value $k_G$ for the standard map (1.13). Recall that we have already fixed the appearance of the first accelerator mode to be at $\varepsilon = 1$. We want to minimize the distance in the parameter $\varepsilon$ between the destruction of the last RIT and the appearance of the accelerator mode, so that the volume of bounded orbits around the origin right after the Hopf-zero bifurcation is as large as possible.

After a fine exploration, we chose

$$\mu = 0.01, \qquad \nu = 0.24, \qquad b = -0.12, \tag{5.20}$$

and for these values, we conjecture that $\varepsilon_{\text{crit}} \in (0.093, 0.094)$. We have determined this value by iterating a relevant set of initial conditions in $\mathbb{T}^2 \times [0,1]$ (where there is evidence of the existence of RIT) under $f_\varepsilon$ for long times, say $T$, with $T$ up to $2 \cdot 10^7$. Each initial condition was classified first as either escaping or non-escaping from $z \in [0,1]$, if for some number of iterates $t < T$ it escaped $z \in [0,1]$. Those that did not escape were classified as either chaotic or regular using an approximation of the Lyapunov exponent. And if they could be considered to belong to a regular orbit, we checked whether they could be considered to be on a 2D rotational invariant torus or not by iterating them and checking that, in the $x, y$ coordinates, they completely filled all the pixels on a $400 \times 400$ grid.

Note that the value of $\varepsilon_{\text{crit}}$ is approximately 1.65 times smaller than $k_G$, but it is far from being negligible.

### 5.4.2 Bounded region around the actual accelerator mode

After fixing the values of the three parameters $\mu, \nu, b$ to those in (5.20), for each $n$ we get different values of $a$ in $\text{Mic}_{\varphi,a}$, since it does not depend on $\kappa$. We represented the values $a_n$, $n = 1, 2, 3$ where

$$a_n = \epsilon_2 = 4bn\pi^2\nu = -0.1152\pi^2 n,$$

in Fig. 5.3 as vertical white lines. The following is worth noting.

**Remark 10.** *1. A necessary condition for $a = \epsilon_2$ so that there might appear a bubble is that it belongs to $[-4, 0]$, [40]. Hence, for (5.20),*

$$a_n > -4 \quad \Leftrightarrow \quad n < \frac{4}{0.1152\pi^2} \approx 3.52.$$

*Hence, for the present choice of parameters, for $n \geq 4$, no fixed accelerator modes will have bounded volume around them.*

*2. Of course, the choice of the parameters could have been done in the opposite way: for a given $a = a^*$ of interest, we could have chosen $\nu$ and $b$ so that $4b\pi^2\nu = a^*$.*

3. *Concerning other accelerator modes that may appear in the phase space. First, the choice (5.20) implies that only 2 of the listed fixed accelerator modes in Tab. 5.2 can appear since the corresponding value of $a$ in the local dynamics $\mathrm{Mic}_{\varphi,a}$ has to be contained in $[-4,0]$. If this is not the case, we do not expect any bounded volume to show up around them. Second, the dynamics around these accelerator modes is strongly affected by a large remainder $\mathrm{Rem}_n$ (5.10) for small values of $n$. Our numerical studies suggest that actually, for $n=1$, only $P_+$ and $P_-$ have some bounded motion around them. But for $n=2$, there seem to appear more bounded motion for $\bar{f}_\varepsilon$. Namely, there seems to appear a 2-periodic accelerator mode orbit that gives rise to some bounded volume.*

Since we want to study the effect of a single accelerator mode, it is convenient to deal with values of $\varepsilon$ close to 1. Let us now compare the volumes of the set of bounded orbits of the theoretically predicted limit map $\mathrm{Mic}_{\varphi,a}$ and the actual accelerator mode. For $f_\varepsilon$, with $\varepsilon$ near 1, we studied the set of bounded orbits of the accelerator mode, but only in the section $z=0, y\le 0$. In a $400\times 360$ grid in $(x,y)\in[-0.024,0.024]\times[-0.12,0]$ we iterated the centers of the pixels for a maximum number of times $T_{\max}=10^6, 10^7, 3\cdot 10^7$, and considered that we escaped if before reaching $T_{\max}$, either $|x|$, $|y|$ or $|z|$ were larger than 0.25. The range where we looked for bounded orbits was chosen accordingly to the position of the fixed points of $\bar{f}_\varepsilon$ that bifurcate from the origin at $\varepsilon=1$. We did this exploration for $\varepsilon=1+\kappa$, $\kappa=10^{-6}(10^{-6})0.0096$. We show the results obtained in Fig. 5.6.

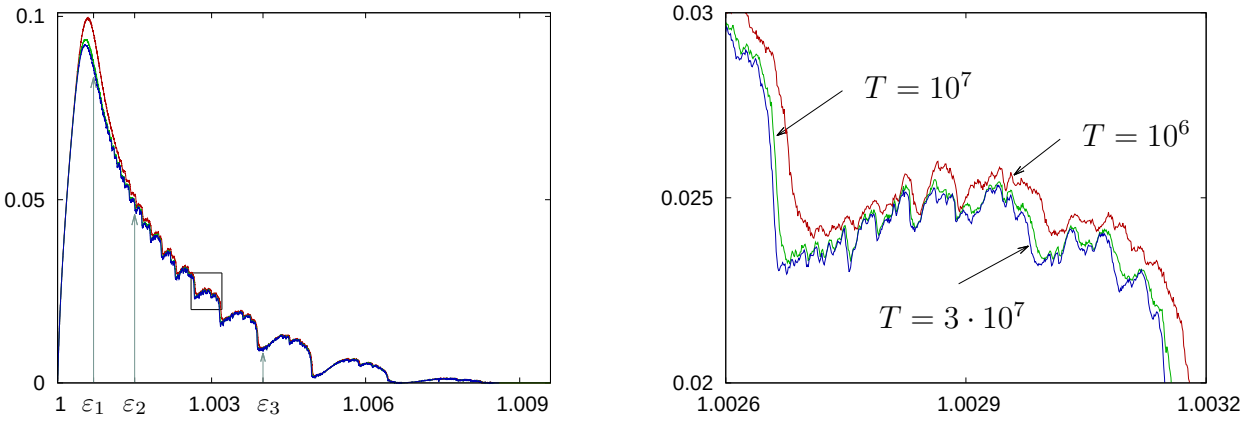


Figure 5.6: Evolution, as a function of $\varepsilon$, of the area of bounded orbits around the accelerator mode of $f_\varepsilon$ that appears at $\varepsilon=1$ in the section $z=0, y\le 0$ relative to $(x,y)\in[-0.024,0.024]\times[-0.12,0]$. The colors indicate different maximal number of iterates: the red line corresponds to $10^6$, the green line to $10^7$ and the blue one to $3\cdot 10^7$. Left: full range of $\kappa$ where an accelerator mode is detected. The labelled values $\varepsilon_1,\varepsilon_2,\varepsilon_3$ are studied later in Sect. 5.4.6. Right: magnification of the box in the left figure. The sudden decreases in bounded area correspond to the breakdown of an outermost invariant 2D torus that allows previously confined motion to escape from a neighborhood of the bubble, recall Fig. 5.2.

We can see how much does $\mathrm{Rem}_1$ affect the dynamics of the actual ball by comparing Fig. 5.6, left and Fig. 5.4, bottom left. The perturbation does not only affect the shape and evolution of the bubble, but also forces it to disappear a lot faster. In Fig. 5.6 we see that

$\kappa \in [0, 0.009]$ and in Fig. 5.4 that $\epsilon_1^2 \in [0, 0.09]$. Let us relate $\epsilon_1$ and $\kappa$. In Prop. 3 we proved the local parameter $\kappa$ was related to that of the limit local dynamics $\varphi$ as

$$\varphi = \pi(32n\mu^2\nu^2)^{1/6}\kappa^{1/6} \quad \Rightarrow \quad \kappa = \frac{\varphi^6}{32\pi^6 n\mu^2\nu^2} \approx 5.64\varphi^6.$$

Note that in Fig. 5.4 we used $\epsilon_1^2 = \varphi^6$ as parameter. Hence, we see that in case $\mathrm{Rem}_1$ was not present, the range of $\kappa$ for which the bubble presented bounded motion would be at least 56 times wider.

For $n = 2$, where 4 fixed accelerator modes show up, the terms in the remainder $\mathrm{Rem}_2$ affect the bubbles in a different way and the two pairs of bubbles that show up seem to be completely different.

### 5.4.3 Diffusion in the chaotic zone: expectations

We have constructed a family of maps $f_\varepsilon$ in a way that we can consider 3 main ranges of the parameter concerning the possibility of vertical drift and the geometry of the phase space, as we did in page 24. For $f_\varepsilon$,

1. If $0 \leq \varepsilon \leq \varepsilon_{\mathrm{crit}} \approx 0.093$ there is no vertical diffusion due to the existence of homotopically nontrivial invariant 2D tori,

2. If $\varepsilon_{\mathrm{crit}} < \varepsilon \leq 1$ there is vertical diffusion but moderate sized regular components in the phase space may still be present. If the size of these regular components is below pixel size we would observe the statistics in the action variable $z$ of orbits in the main chaotic sea to tend to be uniformly distributed under iteration of $\bar{f}_\varepsilon$ (in $\mathbb{T}^3$). We have numerically detected that this is is actually the case for values $\varepsilon > 0.2$. To reach this stage it could require a long transient of iterations.

3. If $\varepsilon \geq 1$, except from three intervals $[1, 1+\kappa_1]$, $[2, 2+\kappa_2]$, $[3, 3+\kappa_3]$ that are related to the ranges of parameter where bubbles around fixed accelerator modes appear, and maybe except from other intervals due to the existence of higher period accelerator modes, we expect that the $z$ component of any chaotic orbit rapidly distributes close to uniformly, because the phase space is seemingly fully chaotic. Note that we can not assure, for any value of the parameter, the absence of other orbits that can strongly affect the diffusive properties of $f_{\varepsilon,b}$, like other smaller fixed or periodic bubbles. But in the ranges we are interested in, we did not detect any of them.

We have numerical evidence that $\kappa_1 \approx 0.009$, see Fig. 5.6, but recall that as we change $n$, the volume of the bubble that appears scales as $1/n^3$ and the range of the parameter $\kappa$ for which it appears scales as $1/n$. Moreover, if we do not also scale $b$ as $1/n$, the parameter $a$ in the local dynamics around accelerator modes changes, so $\kappa_1$, $\kappa_2$ and $\kappa_3$ cannot be a priori related to each other.

Here we will investigate the behaviour in the interval $\varepsilon \in [0.2, 1.009] \supset [1, 1+\kappa_1]$, that contains the interval where first pair of fixed accelerator modes shows up.

As in the 2D case, outside the regime where the accelerator mode appears, if we assume that the phase space is fully chaotic, we expect the diffusion in $z$ to behave as the simplest diffusion equation (recall Sect. 1.1.5)

$$\frac{\partial p}{\partial t} = \frac{1}{2}D(\varepsilon, \mu, \nu, b)\frac{\partial^2 p}{\partial z^2},$$

where $p(z,t)$ is the density of points, $z$ is the angle variable and $t$ the number of iterations. Here $D(\varepsilon,\mu,\nu,b)$ is the diffusion coefficient. The 1-step coefficient, known as the quasi-linear value can be easily evaluated as

$$D_{ql}(\varepsilon,\mu,\nu,b)=\int_{\mathbb{T}^2}(z'-z)^2=\int_{\mathbb{T}^2}(\varepsilon(\cos(2\pi x)+b\sin(2\pi y)))^2=\frac{\varepsilon^2}{2}(1+b^2). \tag{5.21}$$

More accurate versions of $D(\varepsilon,\mu,\nu,b)$, obtained by taking into account the effect of the correlations of more iterations, can not be obtained in a straightforward way. We tested the so-called Fourier-paths technique [118, 75], but in this setting, the dependency of $x'$ and $y'$ of simple trigonometric functions in $z'$ does not allow to obtain such paths in the corresponding Fourier space. Despite that, we expect $D(\varepsilon,\mu,\nu,b)$ to behave quasi-periodically due to effect of more than one angle, but to determine this diffusion coefficient in a more precise way other techniques should be used. We will not address this specific problem here.

It is not clear, though, what will happen inside $[1,\kappa_1]$. In Chap. 3 we dealt with the 2D case with stability islands. Their Hierarchical Island-Around-Island structure gives rise to a power-law behaviour of the lengths of stays which, in turn, gives rise to anomalous diffusion. In contrast, it is not clear how the invariant objects of the bubble are organized according to their rotation numbers $\omega_L$ and $\omega_T$. In next section we are going to give numerical evidence that bubbles also give rise to anomalous diffusive properties in the dynamics along the $z$ variable of $f_\varepsilon$.

### 5.4.4 Methods

We performed a similar massive simulation of orbits for some values of $\varepsilon\in[0.2,1.009]$. For each selected value of the parameter, we chose $\texttt{ic}=10^5$ initial conditions accordingly to the procedure explained in Sect. 3.3.2. We used a linearisation of the 1D unstable manifold of the fixed point $(3/4,0,0)$, which is a fixed unstable saddle with a 1D unstable manifold and a 2D stable manifold, in the ranges of parameters we are dealing with, see Tab. 5.1. The initial conditions chosen are equispaced in log scale, at a distance from the fixed point that is typically $10^{-8}$ and even $10^{-9}$ in some cases. Recall that choosing initial conditions using this procedure prevents them of being confined by sets with regular motion.

Each initial condition was iterated either $10^8$ or $10^9$ times, and in the course of the iteration, we kept track mainly on

1. The standard deviation $\sigma_T=\left(\left\langle(\Delta^T z)^2\right\rangle-\left\langle\Delta^T z\right\rangle^2\right)^{1/2}$ every $10^6$ or $10^7$ iterates, and
2. Captures into bubbles. We have kept track on the number of consecutive iterates that an orbit has remained close to a bubble. By close to a bubble we mean to be in the union of two boxes each containing one of the bubbles around $P_+$ and $P_-$. Our numerical experiments suggest that the bubbles are completely contained in

$$\begin{aligned}\mathcal{W} &= \mathcal{W}_+\cup\mathcal{W}_-, \qquad \text{where}\\ \mathcal{W}_+ &= \{(x,y,z)\ :\ |x|\le 0.024, |y|\le 0.12, |z|\le 0.08\}, \quad \text{and}\\ \mathcal{W}_- &= \{(x,y,z)\ :\ |x-1/2|\le 0.024, |y|\le 0.12, |z|\le 0.08\}.\end{aligned} \tag{5.22}$$

Note that the projection of $\mathcal{W}_+$ onto $z=0$, $y\le 0$ is the region where we studied the set of bounded orbits of the actual accelerator mode around $P_+$. See Fig. 5.6. Furthermore, we have considered an orbit to be trapped in any of these two sets if it did remain at least 128 consecutive iterates inside one of them.

### 5.4.5 Results

Our main observable is the standard deviation $\sigma_T$, and we are mostly interested in its behaviour as $T$ increases. As explained in Sect. 1.1.5, in a phase space that is seemingly fully chaotic, if there are no accelerator mode orbits, we can travel either upwards and downwards in $z$ without restriction, and with equal probabilities. This gives rise to a process that eventually tends to seem to be diffusive. In the presence of accelerator modes, this diffusive behaviour might be destroyed. In case this happens one is lead to study the trapping statistics $\mathcal{I}(t)$ in the set $\mathcal{W} = \mathcal{W}_+ \cup \mathcal{W}_-$. The upwards and downwards accelerator mode bubbles have exactly the same shape and volume. So, the effect of both accelerator modes in the standard deviation and the trapping statistics is the same, despite one jumps upwards and the other one downwards. This is why we consider an orbit to be trapped for $t > 128$ consecutive iterates around accelerator modes if either it has spent $t$ consecutive iterates in $\mathcal{W}_+$ or $\mathcal{W}_-$.

#### Evolution of $\sigma_T$ as a function of $T$ in $[0.2, 1.009]$

Our numerical experiments suggest that the last RIT of $f_\varepsilon$ breaks down near $\varepsilon = 0.1$. We have numerically checked that close to $\varepsilon_{\text{crit}}$, approximately 2% of the phase space is occupied by regular motion, and that in the range $\varepsilon \in [0.2, 1]$ any regular component is below pixel size. Hence, in this range of the parameter, $\sigma_T$ is expected to increase as $\sqrt{T}$. But a drastic change in the statistics is expected for $\varepsilon \in (1, 1.009]$.

In Fig. 5.7 we show some examples on how does $\sigma_T$ behave as we increase the number of iterates. In the left plot we show the evolution for some values of $\varepsilon$ before the appearance of the fixed accelerator modes. These display a growth that fits quite convincingly a behaviour like const $\times\, T^{1/2}$. Moreover, the coefficient seems to grow in a roughly linear way in $\varepsilon$, accordingly to the dependency of $D_{ql}$ (5.21), but one can tell that the effect of correlations (that we expect to be quasi-periodic due to the dependency of two angles) is strong. As shown on Fig. 5.7, this is not the case for $\varepsilon > 1$, in the range where accelerator bubbles exist. Namely one observes sudden and large increases in $\sigma_T$. In some cases, they even seem to fit a straight line for some time. Here we display the behaviour for 14 (non-equispaced) values of $\varepsilon \in [1.0005, 1.0055]$, most of them in light gray. This behaviour is clearly non-uniform in $\varepsilon$, mainly due to random long trapping around the bubbles. We have numerical evidence that the diffusive behaviour is recovered close to $\varepsilon = 1.0085$.

#### Some examples of trapping statistics

Among all the values of $\varepsilon$ for which we have data of, we have observed a similar phenomenon. To illustrate it, we have chosen the following three examples: $\varepsilon_1 = 1.0007$,$\varepsilon_2 = 1.0015$ and $\varepsilon_3 = 1.0040$, see Fig. 5.6. These 3 values are those in blue, green and red in Fig. 5.7, right, respectively.

The displayed results on the evolution of $\sigma_T$ show that in some ranges the standard deviation grows faster than $\sqrt{T}$. Namely linearly for long times. This suggests that the $z$ component of an average orbit grows linearly for some long number of iterates. Of course, by the way we have constructed the family $f_\varepsilon$, we expect this behaviour to be due to large stays close to bubbles. It seems that once an orbit gets trapped in $\mathcal{W}$ (5.22), it may be difficult to escape from this set.

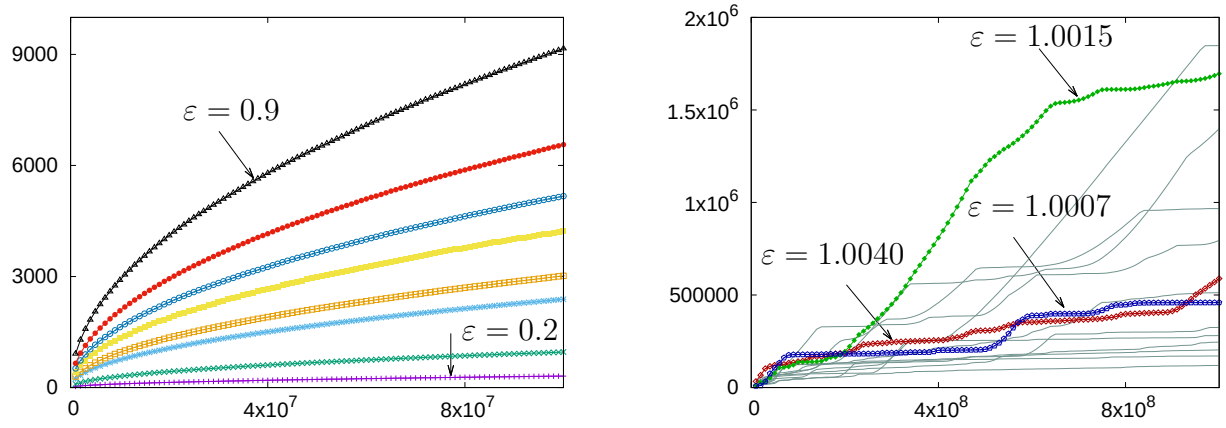


Figure 5.7: Evolution of the standard deviation $\sigma_T$ as a function of the number of iterates $T$. Left: $\varepsilon = 0.2(0.1)0.9$, where one observes a behaviour $\sigma_T \asymp T^{1/2}$. The curves are ordered vertically according to the value of $\varepsilon$ they correspond to. Right: Some values of $\varepsilon \in [1.0005, 1.0040]$, mostly in light grey. The highlighted values plotted with lines and points are $\varepsilon_1 = 1.0007$ (blue), $\varepsilon_2 = 1.0015$ (green) and $\varepsilon_3 = 1.0040$ (red). We will give further information of these 3 cases later on.

Denote by $\mathcal{I}(t)$ the probability that an orbit spends $t$ consecutive iterates in $\mathcal{W}$. If it behaves as an inverse power-law $\mathcal{I}(t) \sim t^{-b}$, $b > 0$, a histogram of trapping times would appear as a straight line in a $\log - \log$-scale plot. We have considered numbers of iterations in the interval $[t_0, t_1) = [2^7, 2^{26})$ and a partition of this interval, in decimal logarithmic scale, in 190 sub-intervals $I_i = [t_i, t_{i+1})$ where $t_{i+1} - t_i = 0.1 \log_{10}(2)$, $i = 70, 260$. For each interval, we considered a counter $C_i$ initially set to 0. For each stay of length $t$, we added 1 to the counter $C_i$ if $i = \text{floor}(0.1 \log_2(t))$. In Fig. 5.8, left, we can see the numerically approximated non-normalized densities. By normalized we mean that its integral (sum, since we have discretised it) is 1. The abscissas correspond to the center of each interval in $\log_{10}$-scale, and in the ordinates we plot the frequencies divided by the amplitude of each bin, $2^{0.1(i+1)} - 2^{0.1i}$. These have been obtained by iterating $10^6$ initial conditions for $10^8$ iterates.

In all non-normalized pdf's shown, we observe several interesting phenomena. First, for small values of $t$, we see some oscillations. These are related to the transversal rotation number of the outermost invariant 2D torus. Each oscillation is related to spending a multiple of the inverse of this rotation number around the torus. That is, once trapped they correspond to perform a complete turn around the outermost torus, then two, etc., before escaping from a vicinity of the bubble. These oscillations become less prominent as $\varepsilon$ increases. For larger $t$, after these oscillations, it is plausible to assume that the trapping times behave as an inverse power law, but we observe that in different ranges we can fit lines with different slopes, the first one being larger (smaller in absolute value) than the second one. On the right of each histogram we display an example of orbit that got stuck around the bubble. In Fig. 5.9, top, we display some points of these orbits close to $z = 0$ projected onto $z = 0$. In the bottom plots of this figure we show also some points in regular orbits (inside the bubble) that are close to $z = 0$, projected onto $z = 0$. See the caption in the figure for further information of the width of the slices considered.

For $\varepsilon_1 = 1.0007$, on top of Fig. 5.8, we observe two slopes in the histogram, $-1.55$ and

$-2.35$, and since this value of $\varepsilon$ is very close to the birth of the bubble (see Fig. 5.6) we guess that the typical trapped orbit entered close the stable 1D manifold of the leftmost fixed point (that at $(x^\star, 0, 0)$ with $x^\star < 0$), then followed a trajectory that seems to fill a 2D torus, and then escapes following the 1D unstable manifold of the rightmost fixed point (that at $(x^\star, 0, 0)$ with $x^\star > 0$). This behaviour is also clear in Fig. 5.9, top left. In the middle, for $\varepsilon_2 = 1.0015$, we find a similar situation, with slopes $-1.83$ and $-2.84$. Here we seem to be far from the birth of the bubble, and we expect orbits to generically get trapped either around an outermost 2D torus or smaller satellite tori. In the example shown in the middle right of Fig. 5.8 the orbit gets stuck around a satellite torus that lies outside the main bubble whose transversal period (in section in $z = 0$, $y \geq 0$) seems to be 12. What we see is actually the section of a 6-periodic invariant curve that is 2-periodic in section, see related comments in 138. This is seen in this plot as a region that is more dense in points. The central region, where there is a smaller density of points, corresponds to those in the central channel, that still seems to play a role for this value of the parameter, see Fig. 5.9, middle. And in the bottom, for $\varepsilon_3 = 1.0040$, we are close to the complete destruction of the bubble, but still we expect, as for $\varepsilon_2$, to get trapped around the main 2D torus or around satellite tori. In Fig. 5.9, top right it seems that the example orbit got trapped around what in section is a 5-periodic orbit. What we see is actually the section of a single elliptic invariant curve.

### 5.4.6 Discussion

In Sect. 3.5.3 we argued that in the kind of histograms we show in Fig. 5.8, if we detect a slope $-b+1$ in double log scale, the pdf of the underlying probability law is an inverse power law like $\mathcal{I}(t) \sim t^{-b}$. Note that we have already divided each frequency by its corresponding bin width, so the given exponent is $-b$.

As $\varepsilon$ changes, the shape of the bubble also does. In some cases, for instance after the breakdown of an outermost 2D torus, the volume of the set of confined orbits suddenly decreases, as seen in Fig. 5.6. For small $\kappa = \varepsilon - n$, the leading objects that rule stickiness are the 2D invariant tori that are close to the 2D invariant manifolds of the two fixed points that appear at the bifurcation. These invariant manifolds enclose the whole bubble, but they do not coincide. The splitting of these manifolds (1D and 2D) is exponentially small in the unfolding parameter, see [10, 11, 12, 42]. Typically an orbit gets trapped into this zone by following a trajectory close to the 1D stable manifold of the leftmost fixed point, and exits following the 1D unstable manifold of the rightmost fixed point. Once trapped, these orbits follow a trajectory that is close to an outermost 2D torus. So, at some point they have to enter the small channel where the other branches of these 1D manifolds lie. The passage through this channel affects the trapping time by slowing it down due to the passage close to the two saddles. The top example in Fig. 5.8 and its corresponding slice around $z = 0$ in Fig. 5.9, top left, is an illustrative example of this situation.

As $\varepsilon$ grows, this small channel becomes larger but for some range may still play a role. See Fig. 5.9, middle, that for $\varepsilon = 1.0015$, where orbits do not only get stuck around a satellite torus but also in a zone with larger volume. But if $\kappa$ is large enough this channel will no longer play a role.

Concerning the fact that we see different slopes in different ranges of the number of iterates, a first plausible conjecture to explain the results shown is that there are different objects in the phase space that play a leading role in different time scales. For instance, they may get stuck either around the main torus or around some satellite tori. Also, if we

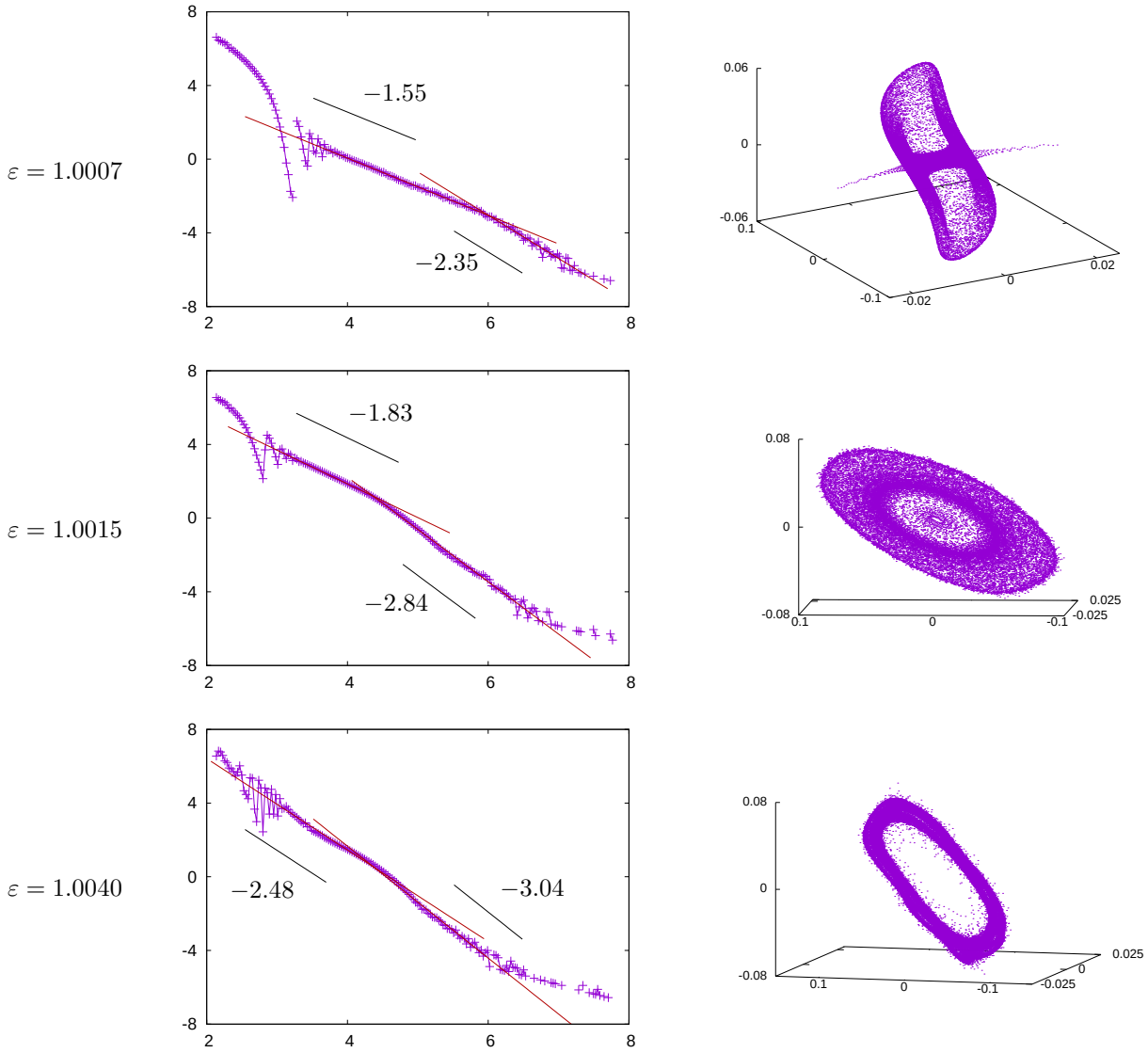


Figure 5.8: From top to bottom, results for $\varepsilon = 1.0007, 1.0015$ and $1.0040$. Left: trapping statistics around the bubble. Right: example of an orbit that got trapped around the bubble, for the corresponding value of $\varepsilon$ on the left. The height and depth (ranging typically $-0.025$ to $0.025$) in the right pictures correspond to the $z$ and $x$ axes, respectively.

take into account the numerical evidence shown in Chap. 3, this change of slope may also be due to a bump caused by the breakdown of an outermost invariant 2D torus. But in the VP 3D setting we do not know the geometrical mechanism of destruction of these 2D tori, so it may require further dedicated investigations. It is important to remark that in a preliminary exploration with a larger number of initial conditions the discrepancy between the visible slopes seems to be reduced.

Finally, concerning the obtained values of the slopes, since we have mimicked the setting in the standard map for large values of $k$, under the hypotheses stated in Sect. 3.5.7 that can be translated into the present setting, we expect a result similar to Prop. 2 to still hold true. This requires further investigations on the mean trapping time. The values of the

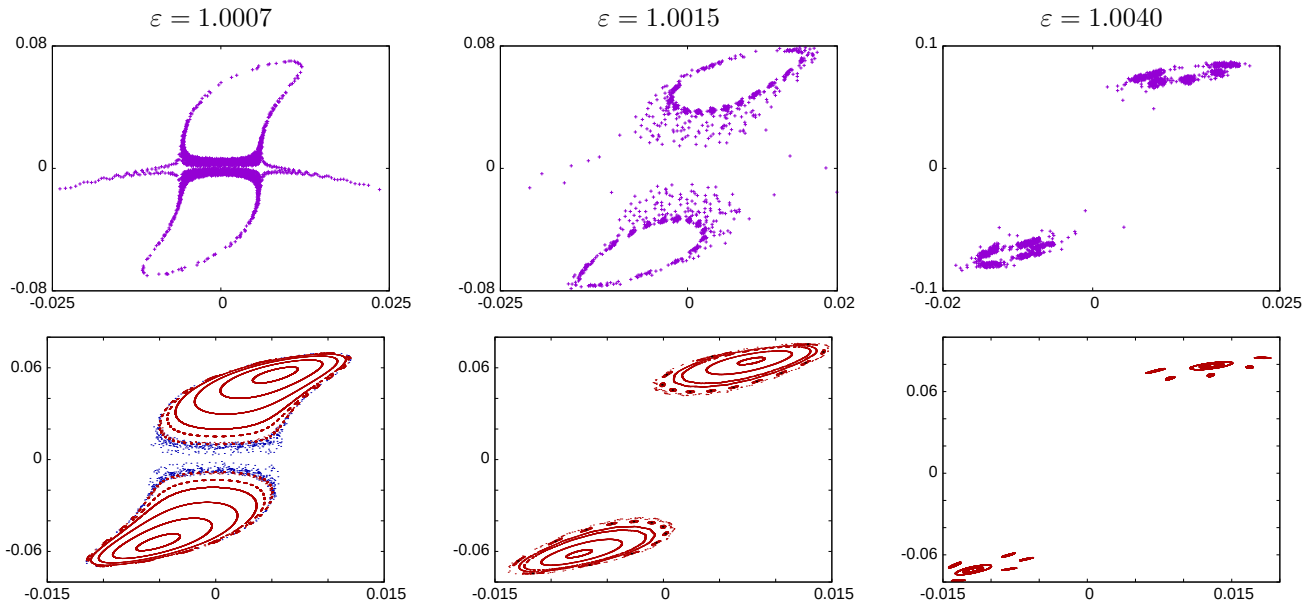


Figure 5.9: For the values of the parameter $\varepsilon$ above the pictures, top: points of the temporarily trapped orbits in Fig. 5.8, right, whose $z$ component lies within $|z| < 0.01$ (left and middle) and $|z| < 0.02$ (right) projected onto $z = 0$. Bottom: points with $|z| < r$ projected onto $z = 0$ of regular orbits inside the bubbles (red, $r = 10^{-4}$) and on escaping orbits (blue, $r = 10^{-4}$). The black dots in the bottom middle plot indicate the intersection of a 6-periodic invariant curves of $\bar{f}_\varepsilon$ with $z = 0$ (on a slice with $r = 10^{-7}$) that look like a 12-periodic elliptic orbit in section (each of the 6 invariant curves intersects twice the plane $z = 0$).

slopes we showed in Fig. 5.8 correspond to exponents that are, in some cases, larger than $-2$ and smaller than $-3$. If the exponent is larger than $-2$, the underlying probability law has unbounded mean. And if it is smaller than $-3$, both mean and variance would be bounded. In both cases, it would still imply the divergence of the diffusion coefficient of $f_\varepsilon$, and hence give rise to anomalous diffusion. This suggests to study higher moments of the statistics in the $z$ variable, and how are they affected by trapping statistics that have some bounded or unbounded momenta.

The remarks of this section give rise to many questions that deserve some specific attention. Some of them are going to be listed in Chap. 6.

# Chapter 6

# Conclusions and future work

This last chapter is devoted to summarize and conclude the studies exposed in this thesis, and to set the future directions of work that are derived from the presented studies.

## 6.1 Summary and conclusions

In Chap. 2 we have given a detailed and complete account of the dynamics of the well-known quadratic orientation-preserving and conservative Hénon map, $HP_c$ with emphasis on the evolution of the measure of the set of bounded orbits, on the confined chaotic orbits and on the splitting properties of the invariant manifolds of fixed and periodic points.

The paradigmatic character of $HP_c$, as a model for many other maps, and the fact that it appears as a relevant model near quadratic tangencies of general APM allowed to explain some features of the diffusion in the standard map for large values of the parameter in Chap. 3, and we hope that the work we presented here will be useful to explain other features in many other maps.

Also, a shorter study of the quadratic orientation-reversing and conservative Hénon map $HR_c$ has been presented.

These two maps are key to understand the behaviour of the dominant islands of stability that appear in the phase space of the Chirikov standard map $M_k$,

$$M_k : \mathbb{T} \times \mathbb{R} \to \mathbb{T} \times \mathbb{R}, \quad M_k : \begin{pmatrix} x \\ y \end{pmatrix} \mapsto \begin{pmatrix} x' \\ y' \end{pmatrix} = \begin{pmatrix} x + y' \\ y + k \sin(2\pi x) \end{pmatrix},$$

that smoothly projects to the 2-torus $\mathbb{T}^2$ as $\bar{M}_k$, for large values of the parameter, $k \geq 1$. We presented both a theoretical approach that related $HP_c$ and $HR_c$ with the local dynamics around fixed points of $\bar{M}_k$ for $k = n \in \mathbb{Z}$, as $n \to \infty$, and numerical evaluations in order to compare the Hénon map and the local model found, that are in good agreement even for $k \approx 1$.

In Chap. 3 we have presented several numerical massive experiments concerning the anomalous diffusion properties of APM. Specifically we focused on the role of the islets studied in Chap. 2 in the standard map. Some of them are accelerator modes (periodic orbits that are fixed for $\bar{M}_k$ but whose momentum $y$ increases linearly in the number of iterates if done under $M_k$), and this fact was used to explore the role of the geometry of the outermost structure of islands of stability in terms of trapping statistics, and how this affected the dynamics in the Chirikov standard map when considered in the cylinder, $M_k$.

Namely, the normal diffusive behaviour observed for most of the parameter values no longer persists for ranges in which these sticky structures appear. In particular, we give extensive numerical evidence that the probability of being trapped for some number of iterates $t$ around islands behave as an inverse power law $\mathcal{I}(t) \sim t^{-b}$. Furthermore, a different power-law decay in $t$, produced by the effect of the gaps of Cantori, was also detected for some parameters, in the form of bumps in the statistics in a $\log - \log$ scale. Both situations have a theoretical framework that reasonably explain the results obtained. In fact, it is possible to understand the numerical results in light of the limit cases described by the available theories.

In Chap. 3 we motivated the need to understand the role of a single Cantorus in order to make predictions of trapping times. Chap. 4 has been devoted to perform an extensive study of transport rates across a single golden Cantorus. For this study, we have used again the Chirikov standard map as main example, but this time for values of the parameter close to (and larger than) the breakdown of the golden invariant curve $k_G \approx 0.1546405777555608265\ldots$. There is a general agreement that the most robust invariant curves are those whose rotation number is eventually golden (meaning that its continued fraction expansion has eventually all quotients equal to 1). The study performed strongly relies on the choice of the rotation number, and even for the standard map, for other rotation numbers one could get substantially different results.

The twist condition implies the vertical ordering of orbits. In particular, it implies that in the neighbourhood of the golden invariant curve one expects to find many periodic orbits. The Greene-MacKay renormalisation theory relates both the position and local dynamics of periodic orbits whose rotation number is an approximant (approximating periodic orbits) of the rotation number of the curve under study. This is reduced to study of the dynamics of the MacKay renormalisation operator for the golden mean invariant curve $\mathcal{R}_1$, that acts in some functional space. It is known to have 2 fixed points: $R_T$, the so-called trivial fixed point, that is a linear shear, and $R_C$, the so-called critical fixed point. Its existence and hyperbolicity were recently proven via computer-assisted techniques. Namely, it is an unstable saddle with a 1D unstable invariant manifold with eigenvalue $\delta$.

We have used the theoretical framework of the Greene-MacKay renormalisation theory to explore approximating periodic orbits that are elliptic, both locally and in suitable compact sets containing the whole islands they may be surrounded with. This allowed us to give explicit account on the consequences of the applicability of this theory for the standard map. In particular, we have focused on describing the phase space close to the invariant curve, from the point of view of which islands of stability appear, and what is the local dynamics around the elliptic or reflection hyperbolic periodic orbit they surround. These are the most prominent objects in the phase space and those who allegedly rule the diffusive properties across Cantori. We have given numerical evidence of the local dynamics (that varies when changing the approximant depending on the eigenvalue $\delta$) and shape of the islands surrounding approximating elliptic periodic points (that scale according to some universal quantities $\alpha < 0$ and $\beta < 0$ in the $x$ and $y$ coordinates, respectively) taking suitable limits. We hope that this work contributes to the comprehension of the dynamics of the renormalisation operator close and after the breakdown. In particular in the comprehension of fundamental domain of $W^u(R_C)$.

Also, as an example, our numerical studies lead to a conjecture that allows to numerically approximate Greene's constant $k_G$ via periodic orbits in a faster rate than applying directly Greene's Conjecture. A similar and related method was already proposed by MacKay in

his thesis, but it relied on the knowledge of some constants that can only be numerically approximated and that only few digits of them were known. We got, using the accelerating method of Aitken, that

$$2\pi k_G = 0.971635406047502179389\ldots$$

After having described the phase space near a Cantorus, we have dealt with massively numerically evaluated escape rates across the golden Cantorus of the standard map. We have given numerical evidence of the evolution of escape rates as a function of $k$ as $k$ approaches the breakdown parameter $k_G$. If $\langle N_k \rangle$ denotes the mean escape rate across a Cantorus for some fixed value of $k$, the MacKay-Meiss-Percival transport theory together with renormalisation theory implies that there exists $B > 0$ that depends exclusively on $\alpha, \beta$ and $\delta$, such that, $\langle N_k \rangle (k - k_G)^B$ is bounded. Moreover, this same theory predicts that in $\log_\delta$-scale, as $k \to k_G$, $\langle N_k \rangle (k - k_G)^B$ is a 1-periodic function. In this work we have given the first numerical evidence of the shape of this periodic function. The study of the standard deviation of $\langle N_k \rangle$ also lead to the detection of the effect of islands of stability, and of ranges in $k$ where they could be neglected. Finally, this 1-periodicity has been again related to the islands around approximating elliptic periodic orbits, that again lead to the study of a single fundamental domain of $W^u(R_C)$.

We finished the chapter by dealing with which is the pdf of escape rates for a fixed value of $k$. We gave evidence of the shape of these corresponding pdf's and checked that the usual hypothesis that they behave as a Gamma distribution fails. We concluded that one should construct a Markov model taking into account the partition that chains of islands define and to study escape rates.

Finally, in Chap. 5 we translated the setting where we dealt with the stickiness effect of a stability island in 2D APM (Chap. 3) to the volume preserving 3D context. We constructed a 4-parameter family of volume preserving maps (VPM) $\bar{f}_\varepsilon$ of the 3-torus $\mathbb{T}^3$ in such a way that it mimicked the Chirikov standard map $\bar{M}_k$

1. The phase space of $\tilde{f}_0$ is foliated by horizontal 2D rotational invariant tori (RIT) and for small $\varepsilon$, some of this structure is preserved for $\tilde{f}_\varepsilon$ in virtue of a KAM-like result,

2. For $\varepsilon = n \in \mathbb{Z}$ the origin is fixed and undergoes a Hopf-zero bifurcation,

3. And if $\tilde{f}_n$ is lifted to the cylinder $\mathbb{T}^2 \times \mathbb{R}$, the origin is no longer fixed but its $z$ component (that can be understood as a momentum) increases linearly in the number of iterates.

In this situation, we are again as in Chap. 3 where we studied the effect of fixed accelerator modes in the destruction of the diffusive behaviour of the $z$ variable under iteration of $f_\varepsilon$ in a seemingly fully chaotic phase space.

We have locally related the map $\tilde{f}_\varepsilon$ for $\varepsilon = n + \kappa$, $\kappa > 0$ small, around the origin with a discretization of the Michelson system that is a quadratic VPM. This map is, in turn, conjugated to the truncated normal form given by Dullin and Meiss. We proved that as $\varepsilon = n \in \mathbb{Z}$ tends to $\infty$, the local dynamics around the origin is reduced to the chosen discretization of the Michelson system.

We studied the Michelson system from the point of view of the set of the evolution of bounded orbits, in order to compare it with the accelerator modes in our family $\bar{f}_\varepsilon$. After that, we performed a preliminary numerical study that gives numerical evidence in many values of the parameter that the trapping statistics around bubbles also behaves as an inverse

power law. These power laws are seen as straight lines in $\log - \log$ plots. We found that in different ranges of $t$ in log scale, one could fit different slopes.

## 6.2 Future work

Taking into account the work here presented, there are many open lines for future research that are a natural continuation.

In the 2D setting,

1. To perform a detailed study of the bumps in trapping statistics in order to explicitly relate them with escape rates across the outermost Cantorus that plays a leading role. This is related to study the interaction between the Greene-MacKay and the Zaslavsky renormalisation approaches.

2. When dealing with anomalous diffusion, to study higher moments of the displacement in the momentum in order to identify further correlations.

3. To propose and test a model inspired in the Markov-Tree model of Meiss and Ott that can effectively explain transport across a Cantorus.

4. To study the area of lobes defined by the invariant manifolds of hyperbolic periodic points with consecutive approximants as rotation number and to test their role in the transport rates across Cantori.

5. To consider different rotation numbers for invariant curves right after their breakdown. For instance, metallic numbers or numbers with $n$-periodic continued fraction expansion.

6. To consider different APM, for instance standard-like maps and maps coming from interesting 2 dof Hamiltonian systems.

And concerning the 3D setting,

1. To perform a geometrical description of the main relevant invariant objects in the proposed models and other related models.

2. To perform a detailed study of escape rates across broken RIT, and to relate these rates with the rotation numbers of the just broken RIT.

3. To study diffusion coefficients in the presence and absence of accelerator modes, in particular to study the effect of correlations in the quasi-linear approximation. Also to investigate higher order moments of the displacement in the action.

4. To refine the study concerning trapping statistics. To identify the sources of the change in slope or bumps, if any.

# Bibliography


[1] Arioli G. and Koch H., The critical renormalization fixed point for commuting pairs of area-preserving maps, Comm. Math. Phys. 295 (2010), no. 2, 415-429

[2] Arnold, V. I., Proof of a theorem of A. N. Kolmogorov on the preservation of conditionally periodic motions under a small perturbation of the Hamiltonian, Uspehi Mat. Nauk 18 1963 no. 5 (113), 1340.

[3] Arnold, V. I, Instability of dynamical systems with many degrees of freedom, Dokl. Akad. Nauk SSSR 156 1964 912.

[4] Arnold, V. I., Chapitres supplémentaires de la théorie des équations différentielles ordinaires. Translated from the Russian by Djilali Embarek. "Mir", Moscow, 1980.

[5] Arnold, V. I., *Mathematical methods of classical mechanics*. Translated from the 1974 Russian original by K. Vogtmann and A. Weinstein. Corrected reprint of the second (1989) edition. Graduate Texts in Mathematics, 60. Springer-Verlag, New York

[6] Arnol'd, V. I. and Avez, A., Problèmes ergodiques de la mécanique classique, Gauthier-Villars, Paris, 1967.

[7] Arnold, V. I., Kozlov, V. V. and Neishtadt, A. I. *Mathematical aspects of classical and celestial mechanics. Dynamical systems. III*. Third edition. Encyclopaedia of Mathematical Sciences, 3. Springer-Verlag, Berlin, 2006

[8] Aubry, S. and Le Daeron, P. Y., The discrete Frenkel-Kontorova model and its extensions: I. Exact results for the ground-states, Phys. 8 D (1983), 381–422

[9] Baesens, C. and MacKay, R. S., Cantori for multiharmonic maps Phys. D 69 (1993), no. 1-2, 5976.

[10] Baldomá, I., Castejón, O. and Seara, T. M., Exponentially small heteroclinic breakdown in the generic Hopf-zero singularity, J. Dynam. Differential Equations 25 (2013), no. 2, 335-392.

[11] Baldomá, I., Castejón, O. and Seara, T. M., Breakdown of a 2D heteroclinic connection in the Hopf-zero singularity (I), arXiv:1608.01115v1 [math.DS]

[12] Baldomá, I., Castejón, O. and Seara, T. M., Breakdown of a 2D heteroclinic connection in the Hopf-zero singularity (II). The generic case, arXiv:1608.01116v1 [math.DS]

[13] Barreira, L. and Pesin, Ya. B. *Lyapunov exponents and smooth ergodic theory*. University Lecture Series, 23. AMS, Providence, RI, 2002

[14] Batut, C., Belabas, K., Bernardi, D., Cohen, H. and Olivier, M., Users' guide to PARI/GP, `http://pari.math.u-bordeaux.fr/`

[15] Berretti, A. and Gentile, G., Scaling of the critical function for the standard map: some numerical results Nonlinearity 17 (2004), no. 2, 649-670.

[16] Birkhoff, G. D., Proof of Poincaré's geometric theorem, Trans. Amer. Math. Soc. 14 (1913), no. 1, 14–22.

[17] Broer, H., Simó, C. and Tatjer, J. C., Towards global models near homoclinic tangencies of dissipative diffeomorphisms, Nonlinearity 11 (1998), no. 3, 667770.

[18] Broer, H., Simó, C. and Vitolo, R., Hopf saddle-node bifurcation for fixed points of 3D-diffeomorphisms: analysis of a resonance 'bubble', Phys. D 237 (2008), no. 13, 17731799.

[19] Broer, H., Simó, C. and Vitolo, R., The Hopf-saddle-node bifurcation for fixed points of 3D-diffeomorphisms: the Arnold resonance web, Bull. Belg. Math. Soc. Simon Stevin 15 (2008), no. 5, Dynamics in perturbations, 769787.

[20] Broer, H., Simó, C. and Vitolo, R., Chaos and quasi-periodicity in diffeomorphisms of the solid torus, Discrete Contin. Dyn. Syst. Ser. B 14 (2010), no. 3, 871905.

[21] Broer, H., Simó, C. and Vitolo, R., Routes to chaos in the Hopf-saddle-node bifurcation for fixed points of 3D-diffeomorphisms, Nonlinearity 23 (2010), no. 8, 19191947.

[22] Calleja, R. and de la Llave, R., A numerically accessible criterion for the breakdown of quasiperiodic solution and its rigorous justification, Nonlinearity 23 (2010), 2029–2058

[23] Cincotta, P. M., Giordano, C. M. and Simó, C., Phase space structure of multi-dimensional systems by means of the mean exponential growth factor of nearby orbits. Phys. D 182 (2003), no. 3-4, 151-178.

[24] Cheng, C. Q. and Sun, Y. S., Existence of invariant tori in three-dimensional measure-preserving mappings. Celestial Mech. Dynam. Astronom. 47 (1989/90), no. 3, 275292.

[25] Cheng, C. Q. and Sun, Y. S., Existence of periodically invariant curves in three-dimensionsl measure-preserving mappings. Celestial Mech. Dynam. Astronom. 47 (1989/90), no. 3, 293303.

[26] Chirikov, B. V., A universal instability of many-dimensional oscillator systems, Phys. Rep., 1979, Vol. 52, no. 5, pp. 264–379.

[27] Chirikov, B. V., Chaotic dynamics in Hamiltonian systems with divided phase space, in *Dynamical Systems and Chaos*, Lecture Notes in Physics, Vol. 179, Springer, 1983.

[28] Chirikov, B. V. and Izraelev, F. M., Some numerical experiments with a nonlinear mapping: stochastic component. In Colloques Internationaux du C.N.R.S. Transformations Ponctuelles et leurs Applications, Toulouse, 1973.

[29] Chirikov, B. V. and Shepelyansky, D. L., Statistics of Poincaré recurrences and the structure of the stochastic layer of a nonlinear resonance, Ninth international conference on nonlinear oscillations, Vol. 2 Kiev, 1981. Translation to English: Plasma physics laboratory, Princeton University, 1983.

[30] Chirikov, B. V. and Shepelyansky, D. L., Correlation properties of dynamical chaos in Hamiltonian systems, Phys. 13 D (1984), 395–400.

[31] Contopoulos, G. and Harsoula, M., Stickiness effects in conservative systems, Internat. J. Bifur. Chaos Appl. Sci. Engrg. 20 (2010), 2005–2043.

[32] Cristadoro, G. and Ketzmerick, R., On universality of algebraic decays in Hamiltonian systems Phys. Rev. Lett. 100, 184101 (2008)

[33] Cushman, R., Examples of nonintegrable analytic Hamiltonian vector fields with no small divisors, Trans. Am. Math. Soc., 238:4555 (1978)

[34] Dana, I. and Fishman, S., Diffusion in the standard map, Phys. 17 D (1985), 63–74

[35] Delshams, A., *Por qué la difusión de Arnol'd aparece genéricamente en los sistemas Hamiltonianos con más de dos grados de libertad*. Tesi Doctoral. Universitat de Barcelona, 1983.

[36] Delshams, A., Gonchenko, S.V., Gonchenko, V.S., Lázaro, J.T. and Sten'kin, O., Abundance of attracting, repelling and elliptic periodic orbits in two-dimensional reversible maps, Nonlinearity, 2013, Vo. 26, pp. 1–33.

[37] Douady, R., Stabilité ou instabilité des points fixes elliptiques, Ann. Sci. École Norm. Sup. (4) 21 (1988), no. 1, 1–46.

[38] Duarte, P., Plenty of elliptic islands for the standard family of area preserving maps, Ann. Inst. H. Poincar Anal. Non Linaire 11 (1994), 359–409.

[39] Dullin H. R. and Meiss, J. D., Nilpotent Normal form for Divergence Free Vector Fields and Volume-Preserving Maps, Phys. D 237(2): 156-166 (2008)

[40] Dullin H. R. and Meiss, J. D., Quadratic Volume-Preserving Maps: Invariant Circles and Bifurcations, SIAM J. Appl. Dyn. Sys. 8 76-128 (2009)

[41] Dullin H. R. and Meiss, J. D., Resonances and Twist in Volume-Preserving Maps, SIAM J. Appl. Dyn. Sys. 11 319-359 (2012)

[42] Dumortier, F., Ibáñez, S., Kokubu, H. and Simó, C., About the unfolding of a Hopf-zero singularity, Discrete Contin. Dyn. Syst. Ser. A, 2013, Vol. 33, pp. 4435–4471.

[43] Falcolini C. and de la Llave R., A rigorous partial justification of Greenes criterion J. Statist. Phys. 67 (1992), 609-643

[44] Falcolini C. and de la Llave R., Numerical calculation of domains of analyticity for perturbation theories in the presence of small divisors, J. Statist. Phys. 67 (1992), 645-666

[45] Figueras, J-Ll., Haro, À. and Luque, A, A Rigorous computer assisted application of KAM theory: a modern approach arXiv:1601.00084v1 [math.DS]

[46] Fontich, E. and Simó, C., Invariant Manifolds for Near Identity Differentiable Maps and Splitting of Separatrices, Ergod. Th. & Dynam. Sys., 1990, Vol. 10, pp. 319–346.

[47] Fontich, E. and Simó, C., The Splitting of Separatrices for Analytic Diffeomorphisms. Ergod. Th. & Dynam. Sys., 1990, Vol. 10, pp. 295–318.

[48] Fox, A. M. and Meiss, J. D., Greene's residue criterion for the breakup of invariant tori of volume-preserving maps, Phys. D 243 (2013), 45-63.

[49] Fox, A. M. and Meiss, J. D., Critical invariant circles in asymmetric and multiharmonic generalized standard maps. Commun. Nonlinear Sci. Numer. Simul. 19 (2014), no. 4, 1004-1026.

[50] Frahm, K. M. and Shepelyansky, D. L., Ulam method for the Chirikov standard map, Eur. Phys. J. B. 76 (2010), 57–68.

[51] Frahm, K. M. and Shepelyansky, D. L., Poincaré recurrences and Ulam method for the Chirikov standard map. Eur. Phys. J. B. 86 (2013), 322–333.

[52] Garrido, L. and Simó, C., Some ideas about strange attractors, in *Dynamical Systems and Chaos*, Lecture Notes in Physics, Vol. 179, Springer, 1983.

[53] Giorgilli, A., Delshams, A, Fontich E., Galgani, L. and Simó, C., Effective stability for a Hamiltonian system near an elliptic equilibrium point, with an application to the restricted three body problem. J. Diff. Eq. 77 (1989), 167–198.

[54] Gelfreich, V. G., A proof of the exponentially small transversality of the separatrices for the standard map, Comm. Math. Phys. 201 (1999), no. 1, 155216.

[55] Gelfreich, V. G. and Simó, C., High-precision computations of divergent asymptotic series and homoclinic phenomena. Discrete Contin. Dyn. Syst. Ser. B, 2008, Vol. 10, pp. 511–536.

[56] Giorgilli, A. and Zehnder, E., Exponential stability for time dependent potentials, Z. Angew. Math. Phys. 43 (1992), no. 5, 827-855.

[57] Giorgilli, A. and Morbidelli, A., Invariant KAM tori and global stability for Hamiltonian systems Z. Angew. Math. Phys. 48 (1997), no. 1, 102–134.

[58] Gómez, A., and Meiss, J. D., Volume-Preserving Maps with an Invariant, Chaos 12 289-299 (2002).

[59] Gonchenko, S. V. and Shilnikov, L. P., On two-dimensional area-preserving mappings with homoclinic tangencies, Russian Math. Dokl., 2001, Vol. 63, no. 3, pp. 395–399.

[60] Gonchenko, S. V. and Shilnikov, L. P., On two-dimensional area-preserving maps with homoclinic tangencies that have infinitely many generic elliptic periodic points, Notes of the S. Petersburg branch of Steklov Math. Inst., 2003, Vol. 300, pp. 155–166.

[61] Gonchenko, S. V. and Gonchenko, V. S., On bifurcations of birth of closed invariant curves in the case of two-dimensional diffeomorphisms with homoclinic tangencies, Trans. of Math.Steklov Inst., Moscow, 2004, Vol. 244.

[62] Gonchenko, M., *Homoclinic phenomena in conservative systems*, Ph.D. Thesis, Universitat Politècnica de Catalunya, 2013.

[63] Greene, J. M., A method for determining stochastic transition. J. Math. Phys., 1979, Vol. 6, no. 20, pp. 1183–1201.

[64] N. Haydn, On invariant curves under renormalisation Nonlinearity 3 (1990), 887–912

[65] Hénon, M., Numerical study of quadratic area-preserving mappings, Quart. Appl. Math., 1969, Vol. 27, pp. 291–312.

[66] Jungreis, I., A method for proving that monotone twist maps have no invariant circles, Ergod. Th. & Dynam. Sys. 11 (1991), 79–84.

[67] Kadanoff, L. P. and Shenker, S. J., Critical Behavior of a KAM Surface: I. Empirical Results, J. Stat. Phys. 27 631 (1982)

[68] Karney, C. F. F. Karney, Long time correlations in the stochastic regime, Phys. D 3 (1983), 360–380.

[69] Karney, C. F. F., Rechester, A. and White, B., Effect of noise on the standard mapping, Phys. D, 1982, Vol. 4, no. 3, pp. 425–438.

[70] Katok A., Some remarks of Birkhoff and Mather twist map theorems. Erg. Th. Dyn. Sys. 2 (1982), no. 2, 185-194

[71] Khanin K. M. and Sinai Ya. G., The renormalisation group method and Kolmogorov-Arnold-Moser Theory, in Nonlinear Phenomena in Plasma Physics and Hydrodynamics. Ed, R. Z. Sagdeev (1986) Mir.

[72] Khinchin A. Ya., *Continued Fractions*, The University of Chicago Press, Chicago, Ill.-London 1964

[73] Koch, H., On hyperbolicity in the renormalization of near-critical area-preserving maps, preprint, mp-arc 06-89.

[74] Ledrappier, F., Shub, M., Simó, C. and Wilkinson, A., Random versus deterministic exponents in a rich family of diffeomorphisms, J. Stat Phys. 113 (2003), 85–149.

[75] Lichtenberg, A. J. and Lieberman, M. A., Regular And Chaotic Dynamics, Applied Mathematical Sciences, 2nd edition, Springer, New York, 1992.

[76] de la Llave, R., A tutorial on KAM theory. In: *Smooth ergodic theory and its applications* (Seattle, WA, 1999), Proc. Sympos. Pure Math. 69. 175–292. Amer. Math. Soc., Providence, RI, 2001

[77] de la Llave, R. and Fox, A. M., Barriers to transport and mixing in volume-preserving maps with nonzero flux, Phys. (295/296) D (2015), 1-10.

[78] de la Llave, R. and Olvera, A., The obstruction criterion for non-existence of invariant circles and renormalization, Nonlinearity 19 (2006), 1907-37

[79] Lomelí, H. E. and Meiss, J. D., Quadratic Volume Preserving Maps, Nonlinearity 11 557-574 (1998)

[80] MacKay, R. S., A renormalisation approach to invariant circles in area-preserving maps, Phys. 7 D (1983), 283–300. Order in chaos (Los Alamos, N.M., 1982).

[81] MacKay, R. S., Hyperbolic Cantori have dimension zero, J. Phys. A: Math. Gen. 20 (1987) L559

[82] MacKay, R. S., Greene's residue criterion, Nonlinearity 5 (1992), 161–187

[83] MacKay, R. S., *Renormalisation in area-preserving maps*, Advanced Series in Nonlinear Dynamics, 6. World Scientific. 1992

[84] R. S. MacKay, Existence of invariant circles for infinitely renormalisable area-preserving maps, in Dynamics, games and science. I, 631636, Springer Proc. Math., 1, Springer, Heidelberg, 2011.

[85] MacKay, R. S. and Meiss, J. D., Linear stability of periodic orbits in Lagrangian systems, Phys. Lett. A 98 (1983), 92-94

[86] MacKay, R. S., Meiss, J. D. and Percival, I. C., Transport in Hamiltonian systems, Phys. 13 D (1984), 55–81.

[87] MacKay, R. S., Meiss, J. D. and Stark, J., Converse KAM Theory for Symplectic Twist Maps, Nonlinearity 2 (1989) 555–570

[88] MacKay, R. S. and Percival, I. C., Converse KAM: theory and practice, Comm. Math. Phys. 98 (1985), 469–512.

[89] MacKay, R. S. and Stark, J., Locally most robust circles and boundary circles for area-preserving maps, Nonlinearity 5 (1992), 867–888.

[90] Marmi, S. and Stark, J., On the standard map critical function, Nonlinearity 5 (1992), 743–761.

[91] Martínez, R. and Simó, C., Invariant manifolds at infinity of the RTBP and the boundaries of bounded motion, Regular and Chaotic Dynamics, (19) (2014), 745–765

[92] Martínez, R. and Simó, C., Return maps, dynamical consequences and applications, Qual. Theory Dyn. Syst. 14 (2015), no. 2, 353–379.

[93] Mather, J. N., Existence of quasiperiodic orbits for twist homeomorphisms of the annulus, Topology 21 (1982), 457–467

[94] Mather, J. N., Nonexistence of invariant circles, Ergod. Th. & Dynam. Sys. 4 (1984), 301–309.

[95] Mather, J. N., A criterion for the nonexistence of invariant circles, IHES Publ. Math 63 (1986), 153–204

[96] Medvedev, A. G., Neishtadt, A. I. and Treschev, D. V., Lagrangian tori near resonances of near-integrable Hamiltonian systems, Nonlinearity 28 (2015), no. 7, 2105–2130.

[97] Meiss, J. D., Class renormalization: Islands around islands, Phys. Rev. A 34 (1986), 2375–2383.

[98] Meiss, J. D., Symplectic Maps, Variational Principles, and Transport, Reviews of Modern Physics 64 (1992) 795–848

[99] Meiss, J. D., Average exit time for volume-preserving maps, Chaos 7 (1997), 139–147.

[100] Meiss, J. D., The destruction of tori in volume-preserving maps, Commun. Nonlinear Sci. Numer. Simul. 17 (2012), no. 5, 2108-2121.

[101] Meiss, J. D., Thirty Years of Turnstiles and Transport, Chaos 25 (2015)

[102] Meiss, J. D., J. R. Cary, C. Grebogi, J. D. Crawford, A. N. Kaufman and H. D. I. Abarbanel, Correlations of Periodic Area-Preserving Maps, Phys. 6 D (1983), 375–384.

[103] Meiss, J. D. and E. Ott, Markov tree model of transport in area-preserving maps, Phys. 20 D (1986), 387–402

[104] Michelson, D., Steady solutions of the Kuramoto-Sivashinsky equation, Phys. D 19 (1986), 89111.

[105] Miguel i Baños, N., Simó, C., and Vieiro, A., From the Hénon conservative map to the Chirikov standard map for large parameter values, Regular and Chaotic Dynamics 20 (2013), 469–489.

[106] Miguel i Baños, N., Simó, C., and Vieiro, A., Effect of Islands in Diffusive Properties of the Standard Map for Large Parameter Values, FoCM 15 (2015), 89–123

[107] Morbidelli, A. and Giorgilli, A., Superexponential stability of KAM tori, J. Statist. Phys. 78 (1995), no. 5-6, 1607–1617.

[108] Moser, J., On invariant curves of area-preserving mappings of an annulus, Nachr. Akad. Wiss. Gttingen Math.-Phys. Kl. II 1962 1962 1-20.

[109] Mullowney, P., Julien, K. and Meiss, J. D., Chaotic Advection in the Küppers-Lortz State, Chaos 18 033104 (2008)

[110] Nekhorosev, N. N. An exponential estimate of the time of stability of nearly-integrable Hamiltonian systems, Russian Mathematical Surveys 32 (1977), 1–65.

[111] Newhouse, S. E., Diffeomorphisms with infinitely many sinks. Topology, 1974, Vol. 13, pp. 9–18.

[112] Olvera, A. and Simó, C., An obstruction method for the destruction of invariant curves. Phys. D, 1987, Vol. 26, pp. 181–192.

[113] Palis, J. and Takens, F., *Hyperbolicity and Sensitive Chaotic Dynamics at Homoclinic Bifurcations*, Cambridge Studies in advanced mathematics, Cambridge University Press, 1995.

[114] Pesin, Ya., Characteristic exponents and smooth ergodic theory, Russian Math. Surveys 32 (1977), 55–114.

[115] Piftankin, G. N. and Treschev, D. V., *Separatrix maps in Hamiltonian systems*, Russian Mathematical Surveys, Volume 62, Number 2, 2007.

[116] Pöschel, J., Integrability of Hamiltonian systems on Cantor sets, Comm. Pure Appl. Math. 35 (1982), no. 5, 653–696.

[117] Rand, D. A., Existence, nonexistence and universal breakdown of dissipative golden invariant tori. III. Invariant circles for mappings of the annulus, Nonlinearity 5 (1992), no. 3, 681-706

[118] Rechester, A. B., Rosenbluth, M. N. and White, R. B., Fourier-space paths applied to the calculation of diffusion for the Chirikov-Taylor model, Phys. Rev. A 23, (1981) 2664

[119] Reichl, L. E., The transition to chaos. Conservative classical systems and quantum manifestations. Second edition. Institute for Nonlinear Science. Springer-Verlag, New York, 2004

[120] Roberts, J. A. G., Escaping orbits in trace maps, Phys. A 228, 295325 (1996)

[121] Roberts, J. A. G. and Baake, M., Trace maps as 3D reversible dynamical systems with an invariant, J. Stat. Phys. 74, 829888 1994

[122] Rom-Kedar, V. and Zaslavsky, G., Islands of accelerator modes and homoclinic tangles. Chaos, 1999, Vol. 9. no. 3, pp. 697–705.

[123] Sánchez, J., Net, M. and Simó, C., Computation of invariant tori by Newton-Krylov methods in large-scale dissipative systems, Phys. D, 2010, Vol. 239, pp. 123–133.

[124] Siegel, C. L. and Moser, J. K., Lectures on Celestial Mechanics, Classics in Mathematics (Reprint of the 1971 Edition), Springer-Verlag, Berlin 1995.

[125] Simó, C., *La variedad de órbitas keplerianas y la teoría general de perturbaciones*. Tesi doctoral. Universitat de Barcelona, 1974.

[126] Simó, C., Analytical and numerical computation of invariant manifolds. In Modern methods in celestial mechanics, Benest, D. et Froeschlé, C., editeurs, Editions Frontières, 1990, pp. 285–330.

[127] Simó, C., Invariant Curves of Perturbations of Non Twist Integrable Area Preserving Maps. Regular and Chaotic Dynamics, 1998, Vol. 3, pp. 180–195.

[128] Simó, C., Analytic and numeric computations of exponentially small phenomena. In Proceedings EQUADIFF 99, Berlin, Fiedler, B., Grögeri, K. and Sprekels, J., editors, World Scientific, Singapore, 2000, pp. 967–976.

[129] Simó, C. Some properties of the global behaviour of conservative low dimensional systems. In Foundations of Computational Mathematics: Hong Kong 2008, Cucker, F. et al. editors, London Math. Soc. Lecture Notes Series, Vol. 363, pp. 163–189, Cambridge Univ. Press, 2009.

[130] Simó, C., Sousa-Silva, P. and Terra, M., Practical Stability Domains near $L_{4,5}$ in the Restricted Three-Body Problem: Some preliminary facts, in Progress and Challenges in Dynamical Systems Vol. 54, Springer, 2013, pp. 367–382.

[131] Simó, C. and Treschev, D., Evolution of the "last" invariant curve in a family of area preserving maps. Preprint, 1998, see `http://www.maia.ub.es/dsg/1998/index.html`

[132] Simó, C. and Treschev, D., Stability islands in the vicinity of separatrices of near-integrable symplectic maps, Discrete Contin. Dyn. Syst. Ser. B, 2008, Vol. 10, pp. 681–698.

[133] Simó, C. and Vieiro, A., A numerical exploration of weakly dissipative two-dimensional maps. In Proceedings of ENOC-2005, Eindhoven, Netherlands, 2005.

[134] Simó, C. and Vieiro, A., Resonant zones, inner and outer splittings in generic and low order resonances of Area Preserving Maps, Nonlinearity, 2009, Vol. 22, pp. 1191–1245.

[135] Simó, C. and Vieiro, A., Dynamics in chaotic zones of area preserving maps: close to separatrix and global instability zones, Phys. D, 2011, Vol. 240, no. 8, pp. 732–753.

[136] Simó, C. and Vieiro, A., Some remarks on the abundance of stable periodic orbits inside homoclinic lobes, Phys. D, 2011, Vol. 240, pp. 1936–1953.

[137] Skokos, Ch., The Lyapunov Characteristic Exponents and Their Computation, in *Dynamics of Small Solar System Bodies and Exoplanets*, Lecture Notes in Physics, vol 790, 63–135, 2009.

[138] Smale, S., Diffeomorphisms with many periodic points. Differential and Combinatorial Topology. Princeton Univ. Press, Princeton N.J., pages 6380, 1965.

[139] Stirnemann, A., Renormalization for golden circles, Commun. Math. Phys. 152 (1993), 369-431

[140] Stirnemann, A., Towards an existence proof of MacKay's fixed point, Commun. Math. Phys. 188 (1997), 723-35

[141] Sun, Y. S. and Zhou, L. Y., Stickiness in three-dimensional volume preserving mappings, Celestial Mech. Dynam. Astronom. 103 (2009), no. 2, 119131.

[142] Treschev, D. Width of stochastic layers in near-integrable two-dimensional symplectic maps. Phys. D 116 (1998), no. 1-2, 2143.

[143] Veerman, J. J. P. and Tangerman, F. M., Intersection Properties of Invariant Maniofolds in Certain Twist Maps. Comm. Math. Phys. 139, (1990), 299–321.

[144] Venegeroles, R., Calculation of superdiffusion for the Chirikov-Taylor model, Phys. Review Letters 101 (2008): 054102.

[145] Venegeroles, R., Universality of Algebraic Laws in Hamiltonian Systems, Phys. Review Letters 102 (2009): 064101.

[146] Wilbrink, J., Erratic behaviour of invariant circles in standard-like mappings, Phys. 26 D (1987), 358–68

[147] Xia, Z., Existence of invariant tori in volume-preserving diffeomorphisms, Ergodic Theory Dynam. Systems 12 (1992), no. 3, 621631.

[148] Zaslavsky, G. M., Dynamical traps, Phys. 168-169 D (2002), 292–304.

[149] Zaslavsky, G. M., Edelman M. and Niyazov, B. A., Self-similarity, renormalization, and phase space nonuniformity of Hamiltonian chaotic dynamics, Chaos 7 (1997), 159–181.

[150] Zaslavsky, G. M., Zakharov, M. Yu., Sagdeev, R. Z., Usikov, D. A. and Chernikov, A. A., Stochastic web and diffusion of particles in magnetic field, Sov. Phys. JETP, 1986, Vol. 64, pp. 294–303.

[151] Zehnder, E., Homoclinic points near elliptic fixed points, Comm. Pure Appl. Math. 26 (1973), 131–182.